EXPERIMENTELLE PHYSIK

Data Analysis in the XENON1T Dark Matter Experiment

INAUGURAL-DISSERTATION
ZUR ERLANGUNG DES DOKTORGRADES DER NATURWISSENSCHAFTER
IM FACHBEREICH PHYSIK
DER MATHEMATISCH-NATURWISSENSCHAFTLICHEN FAKULTÄT
DER WESTFÄLISCHEN WILHELMS-UNIVERSITÄT MÜNSTER

VORGELEGT VON
MIGUEL ÁNGEL VARGAS JARA
AUS BOGOTÁ, COLOMBIA
-2019-

Dekan:	Prof. Dr. Gerhard Wilde
Erster Gutachter:	Prof. Dr. Christian Weinheimer
Zweiter Gutachter:	Prof. Dr. Michael Klasen
Tag der mündlichen Prüfung:	28.05.2019
Tag der Promotion:	28.05.2019

Abstract

To date XENON1T is the world leading dark matter experiment, pursing the direct detection of Weakly Interacting Massive Particles (WIMPs) that present a potential candidate for the so-called dark matter in the Universe. It utilizes a liquid xenon time projection chamber (TPC) with a ton-scale target mass. This thesis is brought forward to improve the understanding and to develop corrections for time-depending detector inefficiencies correlated with the presumably accumulation of charges at the wall of the TPC. Expecting an extremely rare signal rate, a precise understanding of background sources is of outermost importance. Within this work electronic recoil background was studied that is, among others, generated by out-plated and long-lived radon daughters at the TPC surface. In contrast to this, the last part of the thesis addresses electronic recoils as potential signal events of leptophilic dark matter that would manifest itself in an annual event rate modulation. Therefore, the ultra-low electronic recoil rate was monitored, the lowest one ever achieved in a dark matter experiment. In the same context, a framework was developed that is specified on the calculation of scattering rates and sensitivity estimations for any kind of dark matter particles scattering-off electrons of the atomic shell.

Zusammenfassung

Bis heute ist XENON1T das weltweit führende Experiment für die direkte Suche nach Dunkler Materie. Ziel ist der Nachweis von Weakly Interacting Massive Particles (WIMPs), einem möglichen Kandidaten für die Dunkle Materie in unserem Universum. Hierfür wird ein mit flüssigem Xenon gefüllte Zeitprojektionskammer (TPC) mit einem aktiven Detektorvolumen von einer Tonne verwendet. Im Fokus dieser Arbeit steht das Verständnis und die Entwicklung von Korrekturen zeitabhängiger Detektoreffekten im Zusammenhang mit möglicher Ansammlung von Ladungen auf den Wänden der TPC. Auf Grund der extrem niedrigen zu erwartenden Signalrate ist es notwendig ein genaues Verständnis der Untergrundquellen zu erlangen. Im Verlauf dieser Arbeit wurde der Untergrund durch Streuung an Hüllenelektronen (electronic recoil) untersucht, dieser entsteht ähnliche zu anderen Untergründen durch die Ablagerung von langlebigen Radontöchtern an der Oberfläche der TPC. Im Gegensatz dazu befasst sich der letzte Teil der Arbeit mit der Streuung an Hüllenelektronen als potentielle Signatur einer Interaktion von leptophiler Dunkler Materie, die sich in einer jährlichen Modulation der Signalrate manifestieren würde. Daher wurde die extrem niedrige Rate solcher Ereignisse untersucht, die niedrigste, die jemals in einem Dunkle Materie Experiment jemals erreicht wurde. Im gleichen Zusammenhang wurde eine Software spezialisiert auf die Berechnung von Streuraten und Sensitivitäten für alle Arten von Dunkle Materie Teilchen, die an Elektronen der Atomhülle streuen, entwickelt.

Table of contents

Chapter 1

Introduction

Over the past century, numerous and diverse observations from cosmological to astronomical scales have suggested that ordinary baryonic matter contributes only a small fraction to the total energy content in the Universe. The rest is assumed to be made of two mysterious, invisible components called dark energy and dark matter. A well-motivated dark matter candidate beyond the Standard Model of Particle Physics is the Weakly Interacting Massive Particle **WIMP**, which might be directly detectable with Earth-based detectors. The XENON Dark Matter Project aims at a direct detection of WIMPs with a xenon dual-phase time projection chamber. This experiment provides the framework of the present work. For a potential detection of dark matter particles it is an uttermost necessity to have a detailed understanding of the measuring instrument, the XENON1T TPC itself. One requirement is that the created signals are corrected for any detection inefficiency. This subject was studied related to a newly observed effect in the course of the XENON Dark Matter Project. It consists on the hypothesis that charges accumulate at the TPC wall. As result, the electric field is distorted within the TPC, which leads to a time-dependent altering of the position reconstruction of the events, as well as a change in the yield of the signals. Related corrections to these effects were studies in this thesis. Furthermore, for dark matter experiments searching for extremely rare events, a detailed description of all background components is crucial.

In XENON1T backgrounds from interactions of particles with atomic electrons are most dominant. In comparison to the previous generations of detector of the XENON Dark Matter Project, an additional new source of background was observed in XENON1T. It arises from events located at the wall of the TPC. This works aims at a detailed understanding of the electronic recoil background components, including the one generated from the wall events. However, interactions with the xenon electrons are not neccessarily produced only by unwanted background events. Alternative dark matter models suggest that dark matter particles can also interact with the atomic shell. This could be observed by an modulation of the electronic recoil rate over time, correlated to the Earth's motion around the galactic center. This search for an annual event rate modulation is one further subject of this thesis. In the same context, a framework to explore the notion of dark matter scattering-off electrons from the

atomic shell was developed and used to calculate the scattering rate and sensitivity reach for different analyses performed in XENON1T.

The content of this thesis is outlined as follows: Chapter 2 presents an introduction to the basic principles of dark matter, potential candidates and an overview of detection methods together with their results. Chapter 3 reviews the calculations of differential spin-independent WIMP-nucleon interaction rates, presents an introduction to particle detection aspects with liquid xenon and briefly overviews the detector technology of the XENON1T experiment. Chapter 4 overviews the required signal corrections for an accurate characterizes the detector response. Chapter 5 provides a full description of charges accumulating at the PTFE panels inside the TPC, together with the consequences on position reconstruction and signal correction. This chapter presents as well two data-driven methods used to overcome the described challenges. Chapter 6 is on one hand devoted to characterize the electronic recoil background, specifically ^{85}Kr and different radon progenies. Furthermore, it investigates events featuring charge loss near the PTFE wall of the detector. On the other hand, in the context of annual modulation studies, this chapter discusses preliminary results assuming electronic recoil events as being due to dark matter-electron scattering. In the final Chapter 7, the premise of sub-GeV dark matter scattering with atomic electrons, as opposed to nuclei, is explored in the context of the latest 1 year$\times$ton exposure result of XENON1T. Hence a framework to compute differential scattering rates is developed and validated. This chapter concludes by presenting the 90% confidence exclusion limit estimated for dark matter scattering off electrons, when using as input preliminary results from the S2-only analysis performed in XENON1T. Finally, a summary is given in Chapter 8 at the end of this thesis.

Chapter 2

Introduction to Dark Matter

What is our cosmos made of? We do not completely know. In spite of the extraordinary progress made towards answering this question in the last decades, among others the discoveries of the Higgs boson and the measurement of gravitational waves from black hole and neutron star mergers, we still miss to understand at the most fundamental level what the majority of the Universe is made of. This perspective is based on the ΛCDM paradigm, the simplest parametrization of the Big Bang cosmological model broadly consistent with several observations of the Universe. From this model it is known that the sum of the countless of galaxies, planets, stars, atoms, chemical elements and diffuse gases that can be observed constitute merely and only up to 5% of the mass-energy content of the cosmos. Stunned by this conundrum, physicists have come to the realization that they need to understand what is the nature of the 95% missing content. In the context of our current understanding, we have dubbed these remaining hidden constituents as *dark energy* and *dark matter*. While the former is linked to an unknown form of energy that is believed to permeate all of space and which tends to accelerate the expansion of the universe, the latter is associated to an invisible substance that governs the masses of galaxies, clusters and that shapes the observed cosmic structures on largest scales.

This chapter presents an introduction to dark matter, from a collection of observational evidence (section 2.1), to what possible candidates are discussed in literature trying to explain its nature and how do these possibilities fit into the Standard Model of particles (section 2.2). Lastly, it is briefly presented what are the methods explored to detect dark matter and the results of these different efforts (section 2.3).

2.1 Evidence of Dark matter

The puzzle of dark matter dates back to the 1930s, when the astronomer Fritz Zwicky measured the radial velocities of galaxies (back then called nebulae) in the large Coma cluster. By assuming only gravitational interaction for the galaxies in the cluster, and by applying the Virial theorem, Zwicky found evidence of the total mass of the cluster being more than a hundred times larger that the mass of

the stars enclosed in the individual galaxies [1]. The observation of this mass discrepancy, suggesting the existence of a larger abundance of dark matter[1] in comparison to luminous matter, stands as the starting point of a series of cosmological and astrophysical measurements towards understanding the nature of one of the longest outstanding problems in modern physics.

Everything started with the observation that various luminous objects (such as stars, gas clouds, globular clusters, or entire galaxies) move faster than it would be expected if they only felt the gravitational attraction of other visible objects. This observation was followed by the discovery of flat rotation curves in disk galaxies (scale out to tens of kpc[2]) [2], starting with Babcock (1939) and followed by Rubin, Ford, and Kent (1970) [3]. Subsequently, along with Einstein's theory of general relativity, gravitational lensing measurements (out to 200 kpc) together with different studies of hot gas in clusters provided what is labeled as the classical collection of evidence for the existence of an unknown form of non-luminous (section 2.1.1). Further evidence for the case of dark matter comes from the development of a Standard Model for the evolution of cosmic structure that would reproduce large-scale structure observed, and it is based on numerical simulations, redshift surveys and the measurements of temperature fluctuations in the Cosmic Microwave Background. Rooted in different ideas that were once revolutionary, this model describes the geometry and material content of the Universe, explaining how the structure - of different groups of clusters of galaxies and the entire cosmic web of filaments and voids - emerged from the Big Bang [4] (section 2.1.2).

It is worth mentioning that variations of the laws of gravity have been proposed to explain the observations found without introducing any dark matter. For instance, modified Newtonian dynamics **MOND** is a class of theories that states that below a certain level of gravitational acceleration, the gravitational force is no longer proportional to the acceleration, but the acceleration squared [5], thus demonstrating that rotation curves are flat. TeVeS, a relativistic formulation of MOND [6], features success in making contact with gravitational lensing and structure formation observations. Similarly, a new idea called emergent gravity casts gravity as a byproduct of quantum interactions and suggests that the extra gravity attributed to dark matter is an effect of dark energy [7]. Nevertheless, all of these theories face problems to fit simultaneously lensing, rotation curves and the temperature fluctuations of the cosmic microwave background, while requiring parameters that don't generate an unstable Universe. Furthermore, they need to deal with further conceptual problems in light of recent observations of a galaxy that appears to be free of dark matter [8].

2.1.1 At the Scale of Galaxies and Clusters

In the 1960s, measurements of extended rotation curves of stars in spiral galaxies became possible. These measurements were obtained from the Doppler shifts of the 21 cm transition line radiation from

[1] Zwicky's phrase "würde sich also das überraschende Resultat ergeben, dass dunkle Materie in sehr viel grösserer Dichte vorhanden ist als leuchtende Materie" is regarded as the origin for the term Dark Matter (*Dunkle Materie* in German).

[2] A parsec is defined as the distance at which 1 astronomical unit, which is the average distance between Sun and Earth, subtends an angle of 1 arcsecond perpendicular to the line of sight (1 kpc $\equiv 3.08\times10^{19}$ m).

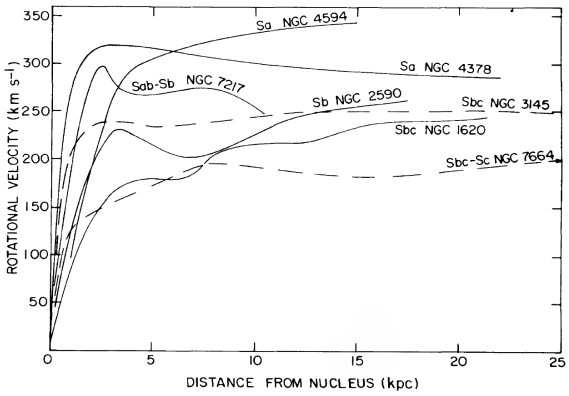

Figure 2.1. Rotational velocities for seven galaxies as a function of distance from nucleus. Early-type galaxies have higher peak velocities than later types, but all curves remain constant out to large distances (taken from Rubin et al. [2]).

Figure 2.2. Galaxy cluster CL0024 1654. This gravitational lens shows strange blue objects stretched, spread in a circle. In reality they are multiple views of a single ring galaxy. Since the likelihood of two appropriately bright and distant objects lining up perfectly is low, distorted galaxies appear as "arclets" [9].

the atomic hydrogen gas, which made evident that stars had the same orbit velocity irrespective of their distance from the center of the galaxy [3].

In Newtonian dynamics, the circular velocity of an object is expected to follow the relation:

$$v(r) = \sqrt{GM(r)/r},$$

where G is the gravitational constant and the mass distribution enclosed in a radius r is expressed as $M(r) = 4\pi \int \rho(r) r^2 dr$ and $\rho(r)$ is the mass density profile. Beyond the optical disk, it would be expected to find a so-called "Keplerian fall-off" of the circular velocity given that the center of the galaxy appears to be more and more point like, leading to a decline of the velocity with growing distance $v \propto 1/\sqrt{r}$. Instead, as shown in Figure 2.1, the striking results from Rubin, Ford and Thonnard when analyzing 10-high-luminosity spiral galaxies beyond the optical disk demonstrated that $v(r)$ is approximately constant [2]. The implication of this observation is presumably the existence of a dark matter halo with $M(r) \propto r$ and density profile $\rho \propto 1/r^2$. Up to date, despite the consensus about the general shape of these halos at large energies, the exact form of their density profiles, especially in their innermost regions, is still heavily debated [10][11].

In the 1970s, following Einstein's general theory of relativity principles, that light propagating along geodesics deviates from straight lines when passing near intense gravitational fields, estimates from gravitational lensing studies helped to check the previous observations made in the galactic scale [12]. By using a distorted galaxy's image as shown in Figure 2.2, and by using the expression for the "Einstein radius" Θ_E[3], which allows to inquire directly the amount of mass causing the observed bending and focusing of light (known as "Einstein rings"), Bergmann *et al.* calculations resulted in

[3] i.e.: $\Theta_E = \sqrt{(4GM/c^2)(d_{LS}/d_L d_S)}$, where M is the mass of the lens, c is the speed of light, and d_{LS}, d_L, and d_S are the distances between the lens and source, the distance to the lens, and the distance to the source, respectively [13].

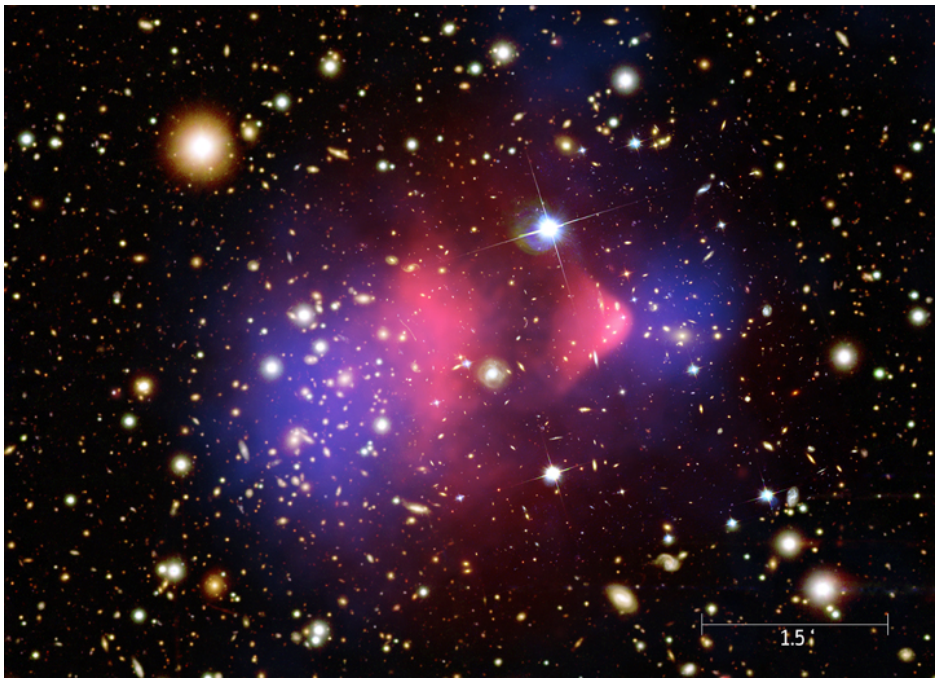

Figure 2.3. The bullet cluster's individual galaxies are seen in the optical image data, but their total mass adds up to far less than the mass of the two clusters clouds of hot X-ray emitting gas shown in red. Representing even more mass than the optical galaxies and X-ray gas combined, the blue hues show the distribution of the majority of the mass in the cluster, clearly non-baryonic. Credit: (X-ray) NASA/CXC/CfA/M.Markevitch *et al* [14]; (Optical and Lensing Map) NASA/STScI; ESO WFI; Magellan/U.Arizona/D.Clowe *et al* [15].

the convincing evidence that galaxy clusters can contain five times as much dark matter than luminous matter.

More recent evidence comes from combining gravitational lensing studies with X-ray measurements by space telescopes. For instance, the particular findings in systems such as the *Bullet Cluster*. Shown in Figure 2.3, this system resulted from the collision of a sub-cluster (the "bullet") with the galaxy cluster 1E 0657-56. During their collision, the galaxies between the cluster passed by each other without interacting. However, since the majority of a cluster's baryonic mass exists as an extremely hot gas between the galaxies, the collision compressed and shock heated this gas, resulting in huge amount of X-ray radiation observed by NASAs Chandra X-ray observatory [16]. When comparing the location of this radiation, which is an indication of the location of the majority of the baryonic mass, to a mapping of the weak gravitational lensing, which is an indication of the location of the total mass, it was found that the majority of the mass in the cluster is not concentrated in the areas of strong X-ray emission. In fact, with 72 similar observed collisions by using the Chandra and Hubble space telescopes, the detection of the existence of dark matter is proven to be at 7.6σ significance [17]. These remarkable results did not just add to the already established notion that most of the mass must be non-baryonic, but also entailed that dark matter interacts gravitationally, maybe weakly, but certainly not electromagnetically.

2.1.2 N-Body Simulations and Cosmological Scale

The thought that galaxies and galaxy clusters could be embedded in massive dark matter halos started to be widely discussed until the 1970's. Within few years, strongly influenced by observations from Ostriker, Peebless, Yahil [18], theoretical arguments started to advocate for the need of these massive halos in order to stabilize spiral galaxy disks [19]. With the purpose of testing this notion, while building up from an analytic model from Press and Schechter that entailed the growth of cosmic structure from a Gaussian initial density field [20], the basis for the first detailed N-body computer simulation were established[4]. Although the original objective of this new tool was to quantitatively explore the evolution of halo populations by examining linear and non-linear structure formation in an expanding Universe, soon many other lines of research benefited from it. Among the most prominent efforts there were those associated to understand if gravitational evolution could explain the properties of the known galaxy distribution at the time, which generated extensive systematic numerical studies based on the growth of large-scale structures.

Despite the fast development of the field, the collection of results from the previous simulations discussed made evident the difficulty of identifying a gravitationally dominant component in the Universe, together with an underlying theory for the evolution of the cosmic structure. Overall, they seemed to suggest the use of too idealized initial conditions due to the lack of a consistent guiding principle. It was only until the confluence of particle physics, astronomy and computing science that two key ideas materialized in a breakthrough. On one hand there was the theory of cosmic inflation proposed by Guth and Linde [21, 22], manifesting that the very early Universe went through a period of accelerated, exponential expansion during the first 10^{-35} seconds after the Big Bang before settling down to the more sedate rate of expansion. The realization of this notion would have inherently promoted the appearance of quantum fluctuations, growing under the influence of gravity, which in turn would have seeded the Universe eventually producing galaxies and the cosmic web [23]. On the other hand there was the conception of dark matter as being composed by new weakly interacting elementary particles having a non-baryonic nature. Together, these ideas set the starting point of several detailed calculations about the Universe's structure evolution: from its genesis until the formation of the expected non-linear objects.

Soon enough the new cosmological methodology based on these two principle found an experimental source of validation in light of the publication of the first extensive 3D survey of galaxies, the Center for Astrophysics **CfA** redshift survey, which provided a first representative picture of the cosmic web through having looked at $\sim$5800 galaxies [24, 25]. By combining the measurement of the distance from astronomical objects (i.e. redshift) with angular position data, generation after generation of surveys started to map each time more accurately the 3D spectra distribution of matter within the sky, as shown in Figure 2.4. In spite of technical computational challenges and several understanding difficulties concerning the treatment of astrophysical uncertainties, testing different

[4]These simulations used Newtonian rather than relativistic gravity given that non-linear large scale structure induces velocities smaller than the speed of light and given that linear structure growth is the same in the matter dominated regime of both theories.

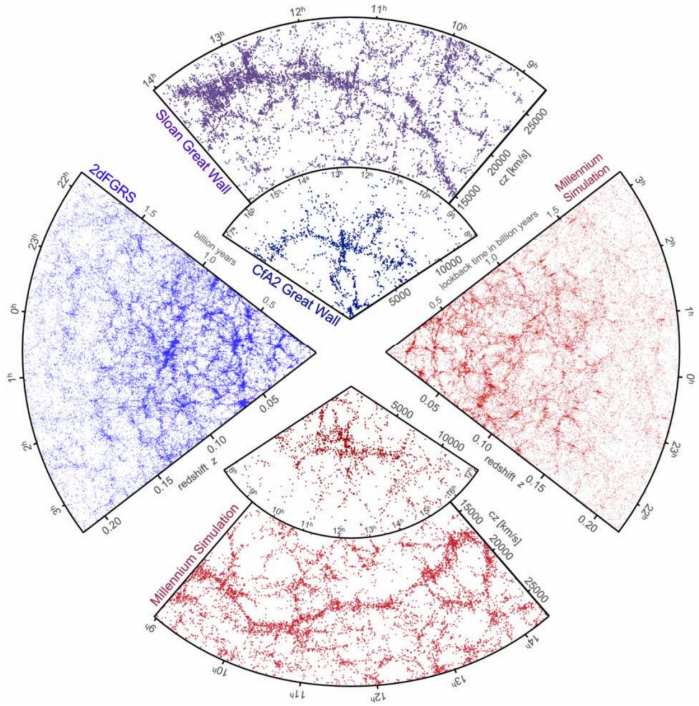

Figure 2.4. Galaxies distribution from redshift surveys and from mock catalogs constructed from cosmological simulations. As discussed in [26], the slice at the top shows the CfA2 "Great Wall" [25] (∼15.000 galaxies by the early 1990s) together with the Coma cluster at the center. Drawn to the same scale there is a small section of the Sloan Digital Sky Survey **SDSS** (∼1 million redshifts by 2007) in which the largest observed structures in the Universe has been identified, the so called "Sloan Great Wall" (over 10.000 galaxies, stretching over more than 1.37 billion light-years long). The wedge on the left shows one-half of the 2dF Galaxy Redshift Survey **2dFGRS** (221.000 redshifts by 2002), which determined distances in the southern sky out to a depth of 2 billion light years. At the bottom and on the right are shown mock galaxy surveys constructed using semi-analytic techniques to simulate the formation and evolution of galaxies within the evolving dark matter distribution of the "Millennium" [27] simulation.

Universe scenarios with simulations of structure growth from the initial conditions predicted by the inflationary model became possible. For instance, as an immediate outcome, a neutrino-dominated Universe was demonstrated to be unlike the observed Universe, consequently ruling out light neutrinos in the mass range of $\sim$ 30 eV as dark matter. This result, in particular, allowed a mindset shift of most of the efforts into the possibility of a Universe dominated by Cold Dark Matter **CDM**, given that hot and warm dark matter simulation at that time showed incompatibility since the relative size of structure formation would be smeared out.

In the 1980's, simulations following the CDM approach started to find better success than before in terms of describing the observed spatial clustering and dynamically induced motion of galaxies compared to the CfA galaxy distribution. This lead to consider that a natural consequence from inflation would be a flat Universe, and also provided a re-interpretation of the cosmological constant as unnatural. However, throughout a decade of considerations, alternatives to the standard CDM needed to be explored in light of different evidence. For instance, there were found stronger than

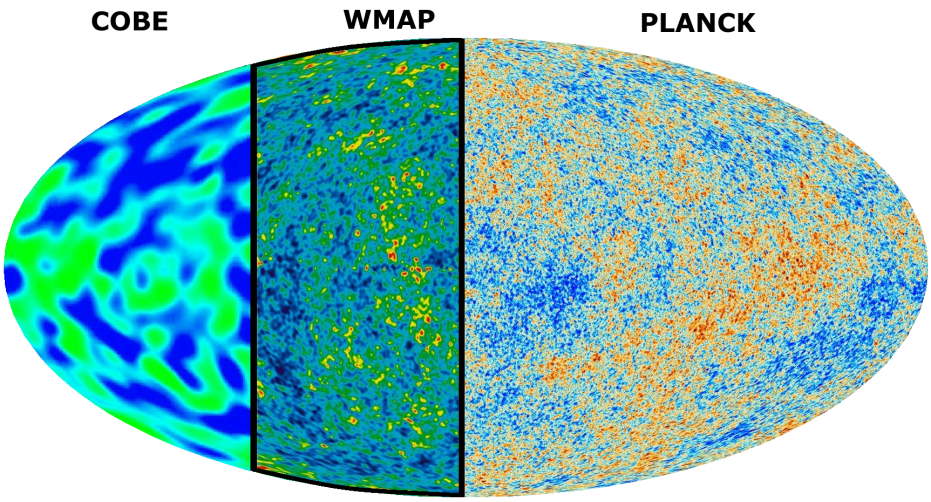

Figure 2.5. Snapshot of the oldest light in the Universe. Here it is shown an all-sky map of the CMB, measured by subsequent generations of satellites, illustrating a tale of increasing resolution and precision in terms of understanding its temperature fluctuations. COBE, the first CMB satellite, measured fluctuations to scales down to 7 degrees. WMAP was able to measure resolutions down to 0.3 degrees, while Planck measured fluctuations down to 0.07 degrees.

predicted galaxy correlations at large scales [28], also an inconsistent baryon fraction in clusters to the expected from Big Bang Nucleosynthesis **BBN**[5] and additionally, measurements of the redshifts from distant type Ia supernovae which showed that cosmic expansion is not only a reality but it was also speeding up [31].

The transition to an upgraded cosmology model capable to estimate the total amount of dark matter in the Universe and to accommodate all observation obtained by the time was established by analyzing and interpreting the Cosmic Microwave Background **CMB**. Predicted by George Gamow 1948 and discovered accidentally by Arno Penzias and Robert Wilson in 1965, the existence of a remnant background radiation originated from the propagation of photons in the early Universe, once they decoupled from matter, was found to be indeed present in all directions of the sky. Although observations made from high altitude balloons confirmed that the cosmic microwave background followed the intensity curve of a thermal blackbody with a temperature of about 3 K, a real breakthrough came only until the discovery by the space-based observer COsmic Background Explorer **COBE** satellite. In 1992, COBE not only confirmed a very uniform thermal background with a temperature of 2.728 K, but also small fluctuations in the temperature of the CMB [32]. Followed by efforts from the Wilkinson Microwave Anisotropy Probe **WMAP** in 2003 and the Planck satellite in 2009, similar maps have established that the CMB is isotropic at the 10^{-5} scale, as shown in Figure 2.5.

[5] Known as well as Primordial nucleosynthesis, one of the main evidences for the Big Bang model, it refers to what happened just minutes after the Universe was expanding and cooling down. In a dense and hot enough for nuclear reactions to take place, deuterium became stable $p+n \rightarrow D+\gamma$ and the BBN produced the so called light nuclei elements ^{4}He, D, ^{34}He and ^{7}Li, together with traces of heavier nuclei [29]. The predictions from the Big Bang are 10^{-5} deuterium, 25% Helium-4 and 10^{-10} Li-7 abundance by mass, which match exactly the data as long as atoms are only 4% of the total constituents of the Universe [30].

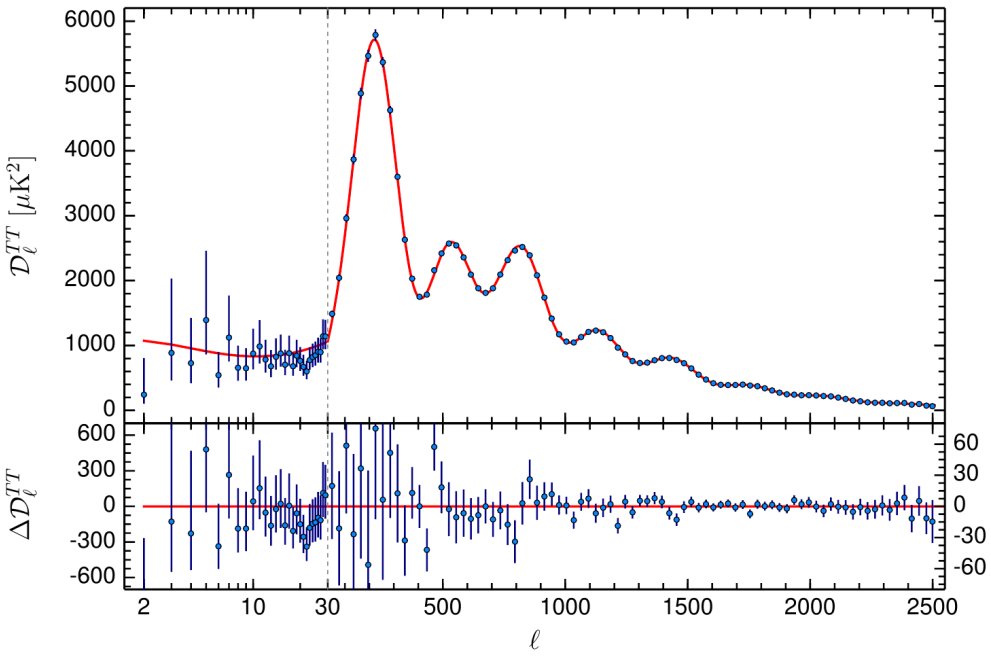

Figure 2.6. Temperature angular power spectrum of the CMB map by Planck 2015. The best-fit case ΛCDM theoretical spectrum is plotted in the upper panel, while the residuals with respect to this model are shown in the lower panel. Figure taken from [33].

As it has been found, the usefulness of such an accurate map is that its power spectrum inherently contains information about the structure and history of the cosmos. In principle, the temperature fluctuation found on it depend on the parameters that end up defining the geometry and content of the Universe and can provide details about the interplay of matter, radiation and dark matter. The methodology to extract this information from the CMB can be consulted in literature [34]. The general idea consists in expanding the temperature anisotropies measured from the sky as:

$$\frac{\delta T}{T}(\theta,\phi) = \sum_{\ell=0}^{+\infty} \sum_{m=-\ell}^{+\ell} a_{\ell m} Y_{\ell m}(\theta,\phi), \tag{2.1}$$

where $Y_{\ell m}(\theta,\phi)$ are spherical harmonics and the variance of $a_{\ell m}$ is given by:

$$\langle |a_{\ell m}|^2 \rangle \equiv C_\ell \equiv \frac{1}{2l+1} \sum_{m=-\ell}^{\ell} |a_{\ell m}|^2. \tag{2.2}$$

As shown in Figure 2.6, the amplitude of the CMB power spectrum $\mathscr{D}_\ell \equiv \ell(\ell+1)C_\ell/2\pi$ is expressed as function of the multipoles ℓ. Then, starting from a cosmological model with a certain number of parameters, the best fit parameters are determined from the peaks found. For instance, the position of the first and the relative heights of the second and third peaks indicate the curvature of the Universe, while also containing information about the amount of baryonic matter and non-baryonic mass density.

Table 2.1. The simplest ΛCDM model is based on the first six parameters showed: the physical baryon density, the physical dark matter density, the age of the Universe, scalar spectral index, curvature fluctuation amplitude and re-ionization optical depth, needed to satisfactory fit current observations while having fixed some parameters at "natural" values [35]. From these six parameters, other model values such as the dark matter and dark energy density can be calculated.

Constrains on Standard cosmological parameters from Planck			
	Symbol	Value	Description
Independent Parameters	$\Omega_b h^2$	0.02230 ± 0.00014	Physical baryon density parameter
	$\Omega_c h^2$	0.1188 ± 0.0010	Physical dark matter density parameter
	t_0	$13.799 \pm 0.021 \times 10^9$ yr	Age of the universe
	n_s	0.9667 ± 0.0040	Scalar spectral index
	Δ^2_R	$2.441^{+0.088}_{-0.092} \times 10^{-9}$	Curvature fluctuation amplitude
	τ	0.066 ± 0.012	Reionization optical depth
Fixed Parameters	Ω_{Tot}	1	Total density parameter
	$\sum_\nu$	0.06 eV/c^2	Sum of three neutrino masses
	N_{eff}	3.046	Effective number of relativistic d.o.f
	w	-1	Equation of state of dark energy
Calculated values	H_0	67.74 ± 0.46 km s^{-1} Mpc^{-1}	Hubble constant
	Ω_b	0.0486 ± 0.0010	Baryon density parameter
	Ω_c	0.2589 ± 0.0057	Dark Matter density parameter
	Ω_m	0.3089 ± 0.0062	Matter density parameter
	Ω_Λ	0.6911 ± 0.0062	Dark energy density parameter

When the data of the Planck mission was fitted with the spatially-flat, six-parameter Lambda-cold dark matter **ΛCDM** cosmological model, it became clear that dark matter is a fundamental ingredient of the Universe along with dark energy, a quantity related to the cosmological constant Λ necessary to explain the accelerated expansion of the Universe. Under the measurements from Planck [33], a summary of different interesting parameters for the ΛCDM model are presented in Table 2.1. Most importantly, the result indicates that the mass-energy content of the Universe contains ∼4.8% ordinary matter, ∼25.8% dark matter and ∼69.1% of dark energy.

Measurements of the matter distribution from the CMB maps combined with spectroscopic surveys such as 2dFGRS, gravitational lensing studies, independent measurements of the total matter content through baryonic acoustic oscillations **BAO** [36], agreement with the primordial abundances of light elements from the predictions of the BBN, and more extensive efforts seem to confirm the validity of the principles of the ΛCDM model. Furthermore, the explicit predictions for the initial conditions for structure formation have been a key input for N-body simulations to provide a link between the early, near-uniform Universe and the rich structure seen at more recent times.

Results from the Millennium Simulation Project [27], as shown in Figure 2.7, have not only confirmed a good agreement between simulated distributions and measurements, but have also provide

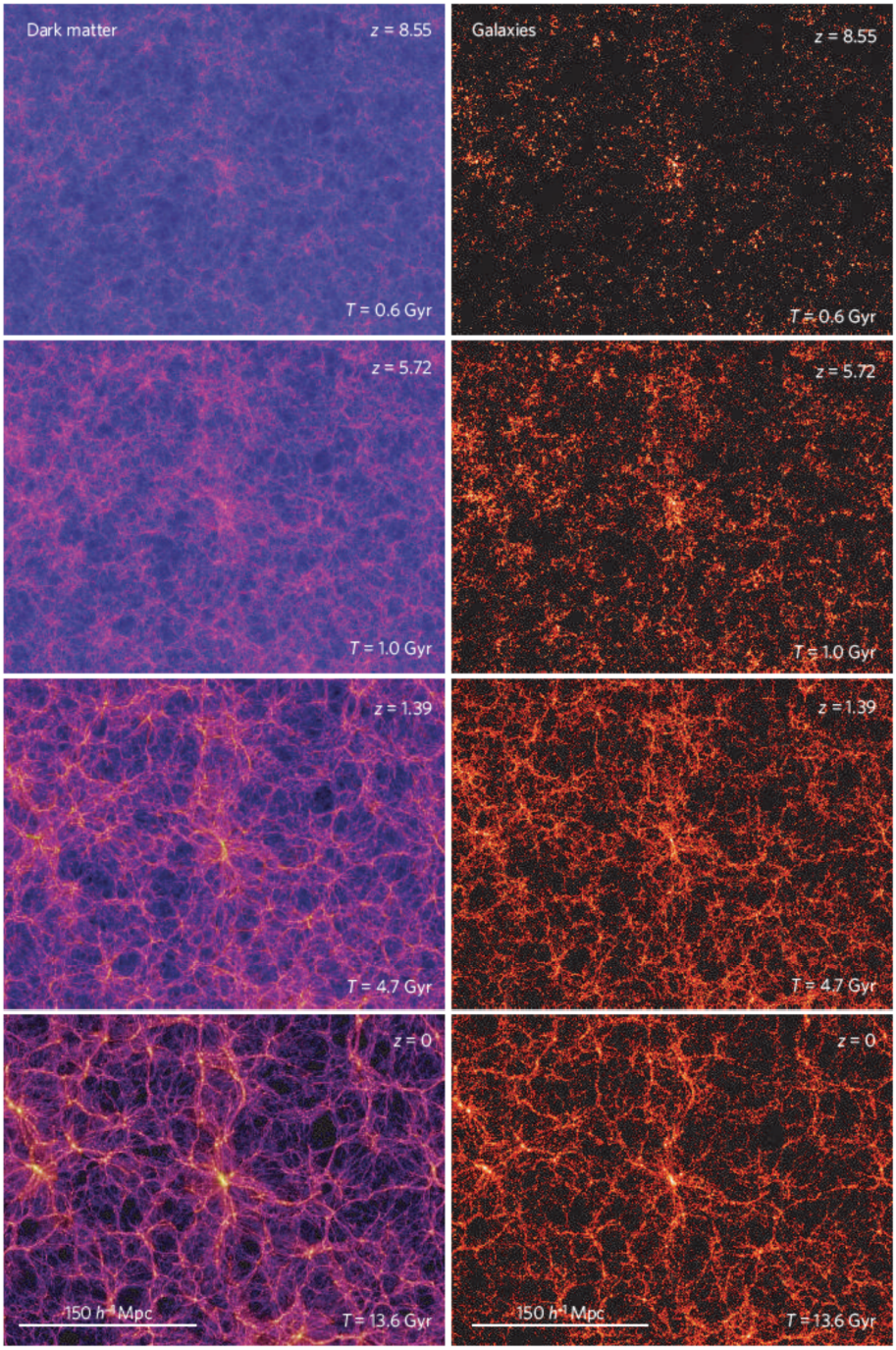

Figure 2.7. Projected dark matter distributions from Millennium N-body simulations after the Big Bang. Each different epoch displays how dark matter evolves from a smooth, nearly uniform distribution into a highly clustered state, unlike galaxies which had showed to be strongly clustered since the beginning [26].

a tool to accurately understand systematic effects found in surveys. Here, the time evolution of the cosmic large scale structure in galaxies and dark matter has been obtained in concordance to ΛCDM

model by the Virgo Consortium, while simulating approximately ten billion particles in a cubic region of the Universe over 2 billion light-years on a side.

2.2 Candidates

The vast amount of astrophysical evidence collected so far at all observational scales sets important constraints for any potential dark matter candidate. However, all evidence is based on its gravitational interactions. Due to the universality of gravity, dark matter's nature is still a puzzle with wide-ranging implications: from dictating how structures form and influence the evolution of the Universe, to serve as one of the strongest empirical evidence that motivates physics beyond the Standard Model. Aside from modification of gravitational laws, as discussed in section 2.1, simplified models following the hypothesis that dark matter is made out of elementary particles is nowadays one of the most common approach studied[6]. This section will introduce some of the candidates discussed in the literature of this assumption.

2.2.1 Standard Model Candidates

Historically, Standard Model particles were the first option to look out for a possible dark matter candidate. For instance, being stable on the scale of the age of the Universe, weakly self-interacting and charge neutral, neutrinos were once thought to constitute a solution for dark matter based on their "undisputed virtue of being known to exist" [37]. However, observed structure formation on the galactic and intergalactic scales[7], cosmological constraints from the CMB, limits in the neutrino mass from tritium β-decay experiments at Troitsk and Mainz [39] and several others experimental efforts have imposed an upper bound on the total neutrino relic density $\Omega_\nu h^2 \leq \sum m_\nu / 93.14$ eV. With the sum of the neutrino masses limit to be $\sum m_\nu < 0.12$-0.72 eV at 95%CL [40], it turned out that neutrinos are not abundant enough and thereby are ruled out as an entire solution (to be more relevant, its mass would need to be larger [41] and its free streaming length lower [42]).

Forward in time, attention was drawn to well known "dark" astrophysical objects made of ordinary baryonic matter, such as brown dwarfs, primordial black holes, neutron stars or unassociated planets as first suspects. Such astronomical bodies called Massive Astrophysical Compact Halo Objects **MACHOs** would be in principle detectable when they pass in front of a star in a nearby galaxy by using gravitational micro-lensing techniques. However, on the basis of observations of more than 35 million stars over eight years, results indicate that MACHOs cannot account for all of the dark matter in spiral galaxies [43].

The fact that dark matter doesn't find a satisfactory explanation on the framework of the Standard Model of particle physics, along with its difficulties to include neutrino masses, an explanation for

[6] Different approaches involve full theories motivated to solve several problems at the time, such as Supersymmetry or extra dimensions, or to try to capture an approximation of the underlying physical theory by using effective field theories.

[7] Since neutrinos are relativistic collision-less particles, they would erase fluctuations below a scale of ~ 40 Mpc, known as the free-streaming length [38].

the matter-antimatter asymmetry observed in the Universe, the strong CP-problem and various other difficulties, has motivated the transition to consider new models beyond the standard model, which ideally would provide a new particle to account for dark matter and solve others of the problems mentioned.

2.2.2 WIMPs

Weakly Interactive Massive Particles **WIMPs** represent a class of dark matter particles popular since the late 1970s because they are naturally produced with a relic density consistent with the one required of dark matter. Predicted to have a mass in the range of the characteristic scale of weak interactions, $m_{weak} \sim$ (GeV - TeV), WIMPs are expected to be stable on the time scale of the Universe, neutral, non-relativistic and due to its observed relic density, measurable through different strategies.

In terms of the production mechanism that generates the well known WIMP dark matter relic abundance from the CMB, the most robust they were produced as a thermal relic of the Big Bang [44] through thermal freeze out. This means that in the dense and hot early Universe, WIMPs were in equilibrium with the thermal plasma. As the Universe expanded, the temperature of the plasma decreased and the number density of created WIMPs started to drop. At some point, WIMPs became so diluted that they could no longer find each other to annihilate. With a number density asymptotically approaching a constant value, their thermal relic density, WIMPs "freeze out" [45]. The freezing-out of the number density depends on the thermally-averaged annihilation cross-section $\langle \sigma_a v \rangle$. Currently, numerical routines such as micrOMEGAs and DarkSUSY are used to perform precise calculations between $\langle \sigma_a v \rangle$ and $\Omega_c h^2$.

2.2.3 Supersymmetry

Proposed by Julius Wess and Bruno Zumino in 1973, Supersymmetry **SUSY** [46] is in principle an extension of the Standard Model that proposes a type of spacetime symmetry relating bosonic and fermionic particles. The motivation of this approach is not only to resolve the Standard Model hierarchy problem within gauge theory (which refers to the enormous difference between the electroweak and Planck energy scales), but also to suggest an unification framework for weak, strong and electromagnetic interactions (which would provide hints towards a Grand Unified Theory that predicts a gauge coupling unification below the Planck scale). The model postulates the existence of a new set of particles associated to each one from the Standard Model, known as superpartners, which are characterized by having similar masses but differ from its partner by a half-integer spin [47].

From all these new and different undiscovered superpartners postulated, three possible dark matter candidates could exist: sneutrino, gravitino and neutralino. The sneutrino, the superpartner of the neutrino, is expected to have a mass defined in the range of 550 to 2300 GeV [48]. Given that direct detection experiments have already probed the sneutrino nucleon cross-section region, this candidate is already ruled out. The gravitino, superpartner of the yet undiscovered graviton, is a less favored candidate at the present moment because no direct detection is possible given that it doesn't couple

weakly. Lastly, made out of a superposition of the partners of the gauge bosons and with a mass in the range of 0.01 - 10 TeV, the lightest of the four neutralinos is currently the most favored dark matter candidates as it is stable, massive and in principle detectable through different strategies. Detailed information can be found in literature [48, 47, 49].

2.2.4 Axions

In contrast to the success found in electroweak theory when measuring the CP violation process $K_L \rightarrow 2\pi$ very well [50], in Quantum Chromodynamics **QCD** there is no reason to conserve CP. However, experimental bounds on the electric dipole momentum of the neutron indicate very small CP violation. In order to solve this problem, Roberto Peccei and Helen Quinn postulated in 1977 a new global symmetry under which a complex scalar field is charged. After this symmetry is spontaneously broken below an energy scale called f_a, the vacuum expectation value obtained from this scalar field leads to find the massless Goldstone boson of this broken symmetry called the axion [51].

Their masses are restricted to the mass range of 1 μeV - 3 meV by astrophysics, cosmology and several laboratory searches [52]. Even though they are very light, axions present a good candidate as they were produced non-thermally in the early Universe. In fact, there are several axion-like particle models that provide a solution to the CP problem, such as KSVZ [53] and DFSZ [54].

2.2.5 Sterile Neutrinos

Experiments such as neutrino oscillation [55–57] have verified by now that neutrinos do have mass, opposite to what is predicted by the Standard Model. This has led to consider subtle extensions in the model so that fundamental problems as the neutrinos mass and its chirality can be solved. Originally proposed in 1993 by Scott Dodelson and Lawrence Widrow to explain the smallness of neutrino masses (with the See-saw mechanism) [58], the idea of sterile neutrinos consists on introducing through the standard electroweak theory additional right-handed neutrinos with typical masses in the range of (10^5 - 10^{12}) GeV.

These particles would have spin-1/2 and would not possess electric or color charge. They would only differ from the standard neutrinos in terms of not carrying weak nuclear charge and hypercharge. Nevertheless, as they would not be associated with either the strong nuclear scale or electroweak symmetry breaking scale, sterile neutrinos could have an arbitrarily large/small mass. Therefore, their existence could be linked to neutrino oscillations, the baryon asymmetry of the Universe and ultimately they would stand as a dark matter candidate.

2.3 Detection Methods

As a mean to test the hypothesis about the particle nature of dark matter, experimental efforts concentrate on three complementary ways based on their possible interaction with Standard Model particles: production at collider searches, indirect detection as the signature coming from products of

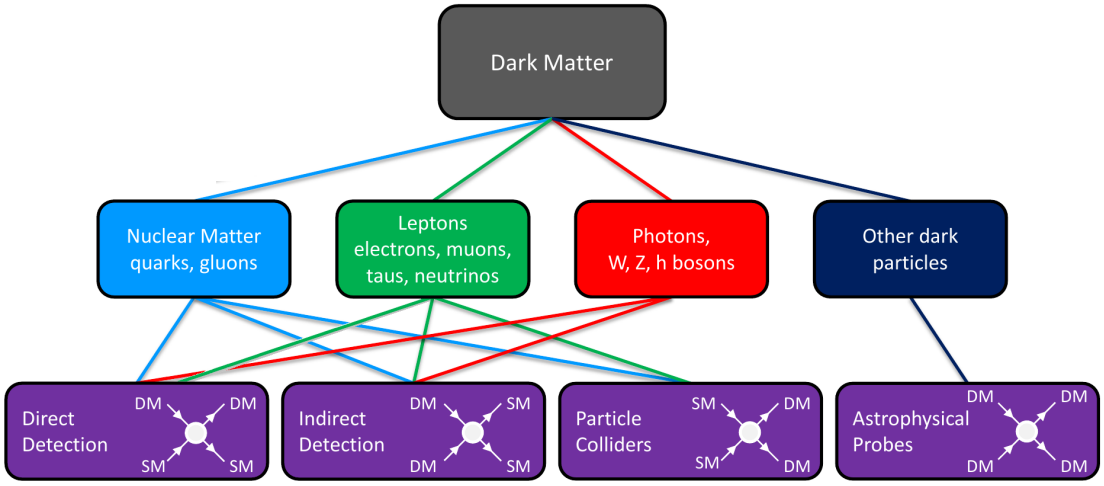

Figure 2.8. Larger context of dark matter detection searches presenting the complementarity methodologies explored. In principle, dark matter could have non-gravitational interactions with any of the already known particles, as well as an unknown dark particles, and these interactions can be probed in several ways. Figure adapted from [59].

the annihilating of dark matter or its decay, and scattering in underground direct detection experiments. In addition, since dark matter could potentially interact with a currently unknown particle, there are different effort searching for of a hidden sector. Illustrated in Figure 2.8, this section will outline the methodology followed in each different approach.

2.3.1 Direct Detection

Given that dark matter permeates the whole Universe, an opportunity to detect these particles directly when they pass through the Earth and scatter off baryonic matter can be exploited, despite how extremely rare those events are expected to be. In the case of WIMPs, a uniformly distributed signal throughout the detector is expected since the local dark matter density is considered to be reasonably homogeneous [48]. The mass energy range from detected particles when recoiling off heavy nuclei will be in the keV-MeV, and therefore constrains on the parameter space of the dark matter-nucleon cross-section in terms of the dark matter mass are placed. Additionally, the rate of the signal is anticipated to vary at different times of the year as the Earth is moving with or against the velocity of dark matter in the galaxy, which provides a further mechanism to reject different sources of background [30].

The interaction of the WIMPs within the detector material depends on the nature of the dark matter particles and is often classified as being spin-dependent or spin-independent, elastic or inelastic, see section 3.1.3. Current experimental techniques include detectors making use of ionization, scintillation light, phonons, bubbles and droplets, as shown in Figure 2.9. In fact, in order to enable signal/background discrimination, some of these detectors take advantage of the interplay of multiple detection channels at the same time.

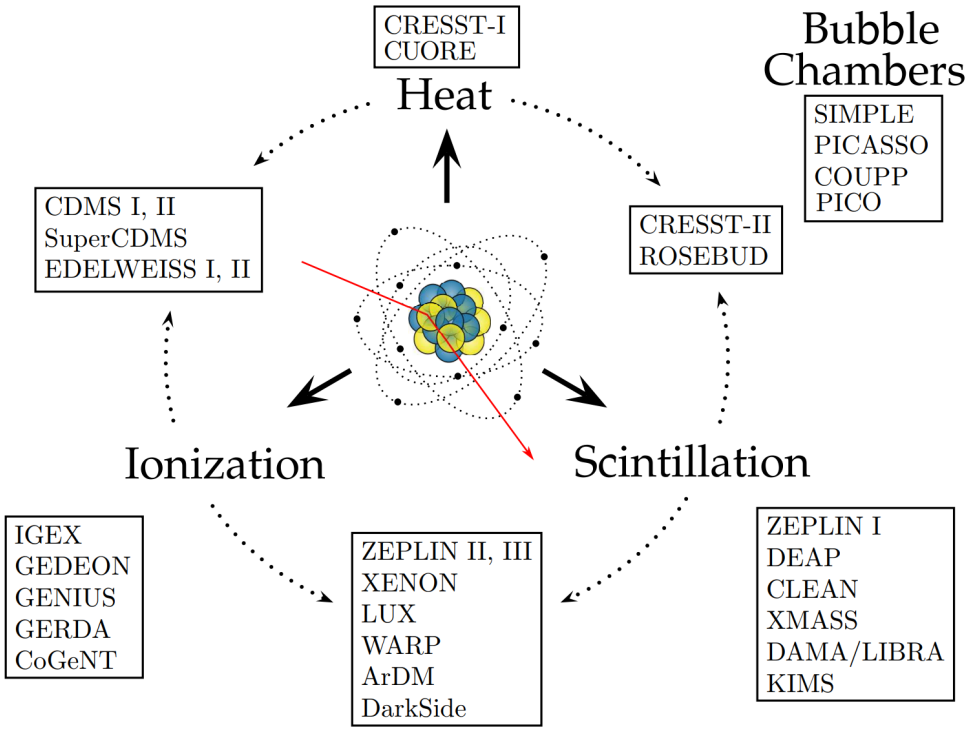

Figure 2.9. Collection of past and present of WIMP direct detection experiments sorted according to their detection technique. Figure adapted from [60].

Detectors searches making use of liquid noble gases, such as argon and xenon, offer the advantage of large and homogeneous targets relatively easy to scale up. The most common approach in the field is to use single-phase/liquid or double-phase/liquid-gas detectors, more details later. The sensitivity of the current generation of detectors is making a rapid progress towards the neutrino floor [61]. Leading efforts at WIMP masses above 5 GeV/c^2 come from projects such as XENON1T [62], LUX [63], PANDA-X [64], DarkSide [65], DEAP [66] and XMASS [67] have established exclusion limits for WIMP-nucleon spin-independent elastic scatter cross-section $\sigma_p^{SI} \sim 10^{-47}$ cm^2 at ~ 50 GeV/c^2. A new generation of multi-ton scale detectors will be lead by XENONnT [68], DARWIN [69], LZ [70], PandaX-30T. In terms of the frontier of lighter WIMPs in the range of a few GeV/c^2, cryogenic detectors such as CRESST [71], CDMS [72], CDEX [73], DAMIC [74], EDELWEISS [75], have established exclusion limits approaching $\sigma_p \sim 10^{-41}$ cm^2 at > 6 GeV/c^2. Currently, the technology developments in the field have enable to lower down progressively the energy threshold of these searches, which has already open the sub-GeV/c^2 regime. The next stage of these efforts will be lead by SuperCDMS [76], DAMIC100 and CDEX-10. Additional to these approaches, there are the long standing results from scintillator crystals at room temperature, mainly from DAMA/LIBRA [77] through their annual-modulated rates, which have caused tension in the community after claimed evidence for low mass WIMPs (this will be discussed in more details in section 6.5.2). On the other

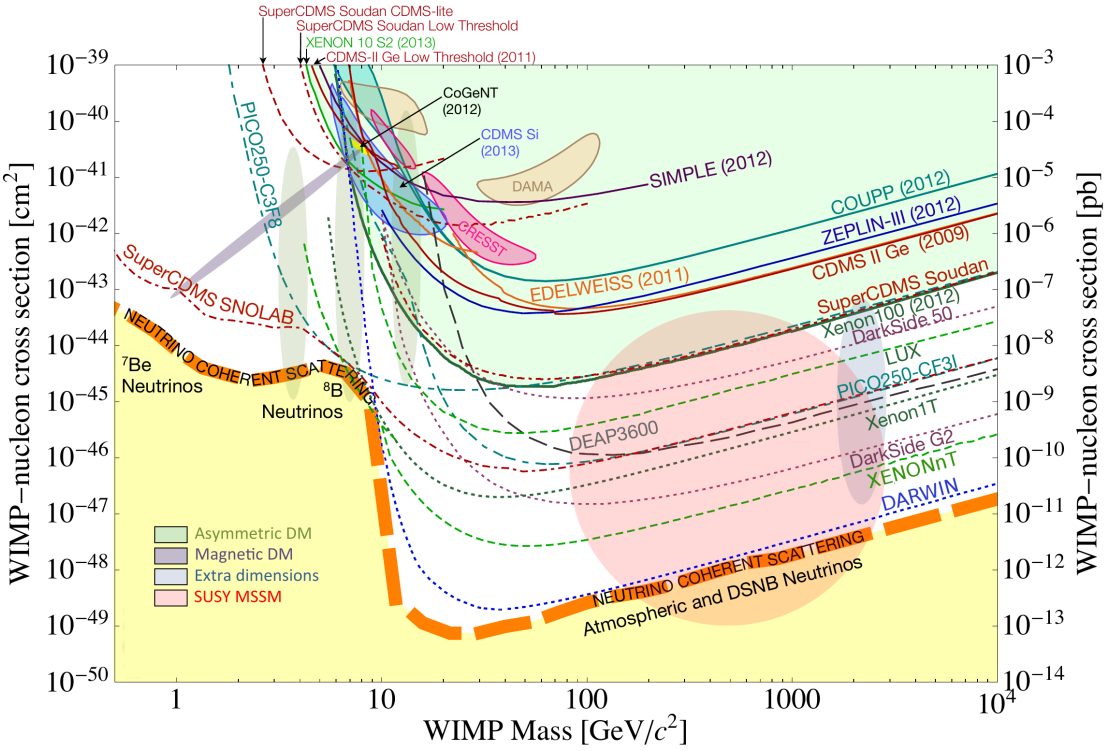

Figure 2.10. Summary of spin-independent WIMP-nucleon scattering results. Shown are upper limits (solid curves), hints for WIMP signals (shaded closed contours) and projections (dot-dashed curves) for experiments expected to operate the next decade. Additionally, the band from coherent scattering of ^8B solar neutrinos, atmospheric neutrinos and diffuse supernova neutrinos with nuclei is shown (yellow region). Lastly, a collection of theoretical model predictions is presented (shaded regions). Figure adapted from [59].

hand, superheated liquid detectors looking for spin-dependent WIMPs signals with bubble chambers have also shown success, from leading efforts from PICO [78].

For different experiments to compare their results, the assumption that WIMPs scatter coherently and elastically off all nucleons in the nucleus is made, such that the interaction does not have nuclear spin nor a proton-neutron dependence. Figure 2.10 summarizes the current direct detection limits on spin-independent WIMP-nucleon cross-section versus the WIMPs mass. Further information can be found in dedicated reviews [59, 79].

2.3.2 Indirect Detection

Indirect dark matter searches aim to find indirect evidence from dark matter annihilation products or decays, originated in the outer space, by searching for stable messenger particles created in the process, such as γ-rays, neutrinos, or even antimatter in the form of antiprotons and positrons. Given that the energy of these messengers can reach up to the mass of the dark matter particle, signals of a few hundred GeV can be expected.

Considering that positrons and electrons are able to give rise to synchrotron radiation detected in the radio band, different detector technologies covering the range of cosmic and X-rays, γ-rays,

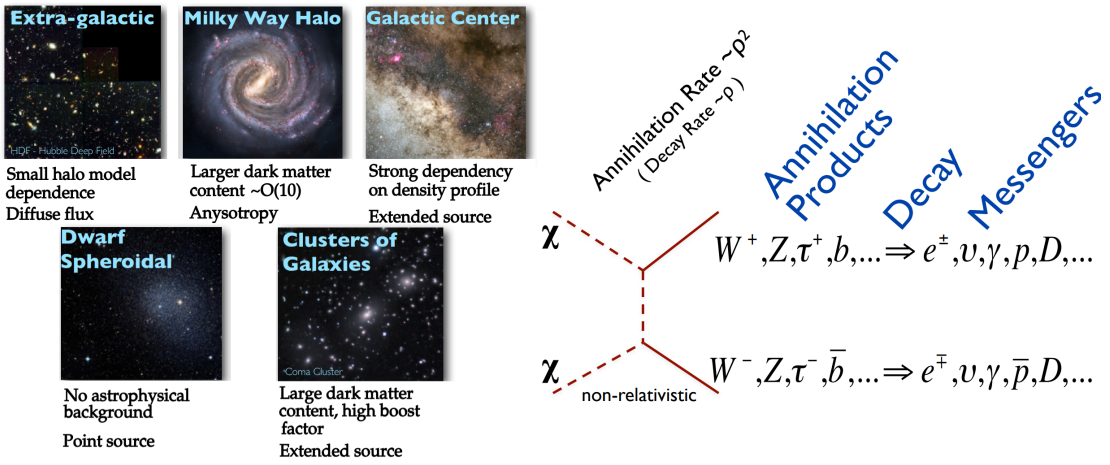

Figure 2.11. **Left** Targets used in indirect detection searches at all scales of the Universe where indirect evidence is expected to be found. **Right** Principle of indirect detection from dark matter annihilation products, decays or messenger particles. Figure adapted from [80].

neutrino telescopes and radio telescopes are used. Furthermore, since dark matter evidence can be found at different scales in the Universe, there are several targets used in these searches, each one having an associated benefit or challenge, as shown in Figure 2.11. In terms of the preferred signal locations to investigate, places where there are objects with larger expected dark matter density and a reasonably large solid angle tend to be the most attractive, such as the Milky Way galactic center, spheriodal dwarfs,Andromeda (being the nearest galaxy), galaxy clusters nearby as Coma or Virgo, and even the Sun.

Experiments with directional sensitivity using neutrinos like AMANDA [81], IceCube [82] and ANTARES [83], use the same target and detection medium (e.g. watter, ice). By means of recording the Cherenkov radiation emitted by the charged leptons created after the interaction of neutrinos with matter takes place, kinematical parameters of the incoming neutrinos try to be reconstructed, along the source of their origin. Gamma detection experiments can be subdivided depending the energy they aim to measure. Detection of high energies γ-rays ($E_\gamma >$100 GeV) by imaging Cherenkov telescopes such as VERITAS [84], MAGIC [85], HESS [86], take place on Earth through measuring Cherenkov light from particle-showers found at the Earth's upper atmosphere. Complementary detection of low energetic γ-rays ($E_\gamma \sim$ 10 MeV - 300 GeV) is done by space satellites such as INTEGRAL [87] or Fermi [88]. Cosmic-ray experiments through satellites such as Pamela [89], Fermi-LAT [90], AMS [91], focus on charged particles e^-/e^+, $p/\overline{p}$ and how are they deflected in interstellar magnetic fields. Lastly, with a detection energy range of $E_X \sim$ (0.1 - 10) keV and using Wolter grazing mirrors, X-ray measurements out from Earth are made at satellites such as XMM-Newton, Chandra [92], because the atmosphere would absorb this radiation.

Many interesting observations in this field have been interpreted as hints of dark matter (e.g. a γ-rays excess from the galactic center or an excess positrons in cosmic rays). Nevertheless, the main complication inherent to any of these observations is that there are multiple astrophysical sources that

could mimic the expected dark matter signal. For a review about the latest results of each research, see [93].

2.3.3 Particle Colliders

As an alternative approach, dark matter may be produced at high-energy particle collisions in experiments such as the Large Hadron Collider **LHC** [94] or the Large Electron–Positron Collider **LEP** [95]. Once produced, due to their non-baryonic nature, weak interaction with Standard Model particles and lack of electromagnetic interactions, created particles would escape a direct detection within the detector. However, they could be inferred due to the imbalance in the transverse momentum measured. The specific signature will depend considerably on the particular dark matter model assumed [48]. Nonetheless, several mechanism can accommodate different production scheme, directly placing bounds in the parameter space of the dark matter mass and interaction strength.

The main advantage of dark matter production at colliders is that the mechanism is independent from astrophysical uncertainties or backgrounds. With a feasible TeV-scale collision center-of-mass energy at the LHC, the sensitivity to several SUSY scenarios has been reached and the validity of several other classes of models is being tested. Currently, null results from different LHC searches for SUSY partners of quarks exclude such particles with masses less than at least 1.5 TeV. On the other hand, LEP has already excluded dark matter masses below 90 GeV for electroweak-size couplings to electrons [96]. Lastly, complementary to any possible discovery from collider searches, a discovery by direct or indirect detection channels would have to confirm the finding.

2.3.4 Astrophysical Probes

Astrophysical probes refer to efforts focused on measuring specific effects of dark matter properties on structure formation in the Universe. Even though predictions from ΛCDM seem to be in good agreement with cosmological data, indications of low central densities at different galactic scales suggest that this assumption may be only an approximation that breaks down on sub-galactic scales. Thus, astrophysical observations aim to give insight about how warm dark matter is and about its self-interaction strength. Results could in principle indicate that dark matter is not entirely cold and collisionless, as conceived nowadays, but rather warm or even strongly self-interacting.

Observatories such as LSST [97] and WFIRST [98] will test the predicted presence of dark sub-halos within the halo of galaxies [99, 100] through strong gravitational lensing systems. The absence of these dark matter self-bound clumps would entail that part of dark matter has to be warm. In fact, although constraints from Lyman-α forest produced from the absorption of neutral hydrogen clouds along the line of sight to quasars prevents warm dark matter to provide a complete explanation to the small scale structure [101], its interplay with light particles from hidden sector dark matter models could lead to similar effects than those observed. In the same way, several model dependent mechanisms of the hidden sector could provide dark matter with self-interactions that consistently would reduce the central density of dark matter halos, as cosmological data suggests [102].

Chapter 3

Direct Dark Matter Detection With Xenon

To this day, large efforts are placed into developing experiments which are able to test the hypothesis of dark matter consisting of new weakly interacting particles. In the context of direct detection of dark matter conceived as WIMPs, the aim in this pursuit is to detect, or set limits on, the cross-section of nuclear recoils **NR** arising from collisions between the detector's target nuclei and the dark matter particles from the dark halo of the Milky Way. Typical nuclear recoil energies in the range of (1 - 100) keV are expected from the elastic scattering of WIMPs having masses of (10 - 1000) GeV/c^2 [103]. The biggest challenge for this detection endeavor has become to achieve a precise understanding on the signal signatures, the particle physics aspects and nuclear physics modelling involved in the scattering of dark matter on Earth when using a specific target.

Focusing on WIMPs, this chapter will begin by reviewing the details of the components needed to calculate nuclear recoil scattering rates, from kinematics of the scattering taking place, to the knowledge about the density and velocity distributions of dark matter particles in the galactic halo. Then, nuclear physics aspects and a discussion of the results that can be obtained (section 3.1). This will be followed by an introduction to particle detection aspects with liquid xenon (section 3.2) and lastly all these detection principles will be discussed in the context of the XENON1T experiment (section 3.3).

3.1 Direct detection strategy

Under the assumption that the Galactic disk (containing the Sun) moves through the Milky Way's non-rotating dark matter halo, the solar system experiences a "WIMP wind" due to the Earth's orbital motion around the Sun. As consequence, billions of WIMPs pass through the Earth each second [104], offering an opportunity for their detection, even though they are expected to very rarely interact with baryonic matter. The standard strategy of direct detection experiments is to search for the signature that these WIMPs create when scattering with atomic nuclei from a detector's material. Specifically,

efforts concentrate on measuring the energy spectrum of dark matter interactions, whereby all possible background sources have to be mitigated and understood in order to have a reliable discrimination between signal and background. The next subsections will describe the procedure to calculate the differential energy spectrum of nuclear recoils from WIMP interactions.

3.1.1 Dark matter density and velocity distributions

To begin with, ρ_χ is an average over a small volume, typically a few hundred parsecs, around the Sun. Although there is a long history of local measurements of it using different data sets and different methodologies (and therefore assumptions), there are two general approaches to estimate this value. The first one consist on local measurements that use the vertical kinematics of stars in the solar neighborhood, called "tracers" (e.g. [105]). The second method consist on global measurements which extrapolate ρ_χ from the rotation curve[1] [107]. An extensive collection of results from different surveys show agreement with each other within their quoted uncertainties. For them, the overall best-fit values found for the Galactic frame range between (0.2 - 0.6) GeV/cm^3 with errors that roughly lie in the range of (0.05 - 0.5) GeV/cm^{-3} (see e.g. [108], Table 4). Nevertheless, recent observations on the local frame suggest that the value lie in the range of (0.22 - 0.33) GeV/cm^3.

In terms of the velocity distribution, the most commonly adopted dark matter halo model is the Standard Halo Model **SHM**. In the galactic rest frame, this model assumes an isothermal, spherical dark matter halo with an isotropic Maxwell-Boltzmann velocity profile distribution:

$$f(\mathbf{v}) = \begin{cases} k\left(\frac{1}{\sqrt{\pi}\upsilon_0}\right)^3 e^{-(\mathbf{v}/\upsilon_0)^2}, & \text{for } |v| < \upsilon_{\text{esc}} \\ 0, & \text{otherwise} \end{cases} \tag{3.1}$$

where $\upsilon_0 = \sqrt{2k_\text{b}T/m}$ (with k_b the Boltzmann constant) is the most likely speed of the dark matter particles and the normalization constant k is defined as [103]:

$$k = \text{erf}\left(\frac{\upsilon_{\text{esc}}}{\upsilon_0}\right) - \frac{2}{\sqrt{\pi}}\left(\frac{\upsilon_{\text{esc}}}{\upsilon_0}\right) e^{-\left(\upsilon_{\text{esc}}/\upsilon_0\right)^2}. \tag{3.2}$$

In order to compare the result between different direct detection dark matter experiments, with the SHM assumption, the local dark matter density $\rho_\chi = 0.3$ GeV/cm^3, υ_0 = 220 km/s and υ_{esc} = 544 km/s are the values often taken. The Earth moves with an average speed υ_e = 232 km/s with respect to the galactic frame (the additional annual modulation due to the Earth's 30 km/s orbital velocity around the sun will be ignored for now).

For non-directional detectors such as XENON1T, Equation 3.1 can be solved to obtain only the observed speed distribution $f(\upsilon)$ [103]. Figure 3.1 illustrates the WIMP speed distribution in the local frame and the inverse mean speed, the velocity-dependent component later needed in the rate

[1] Often this method branches further on the category of studies using the local surface density of matter as a constrain, taking the value from [106], or rather using a prior from the rotation curve that assumes a spherical halo model.

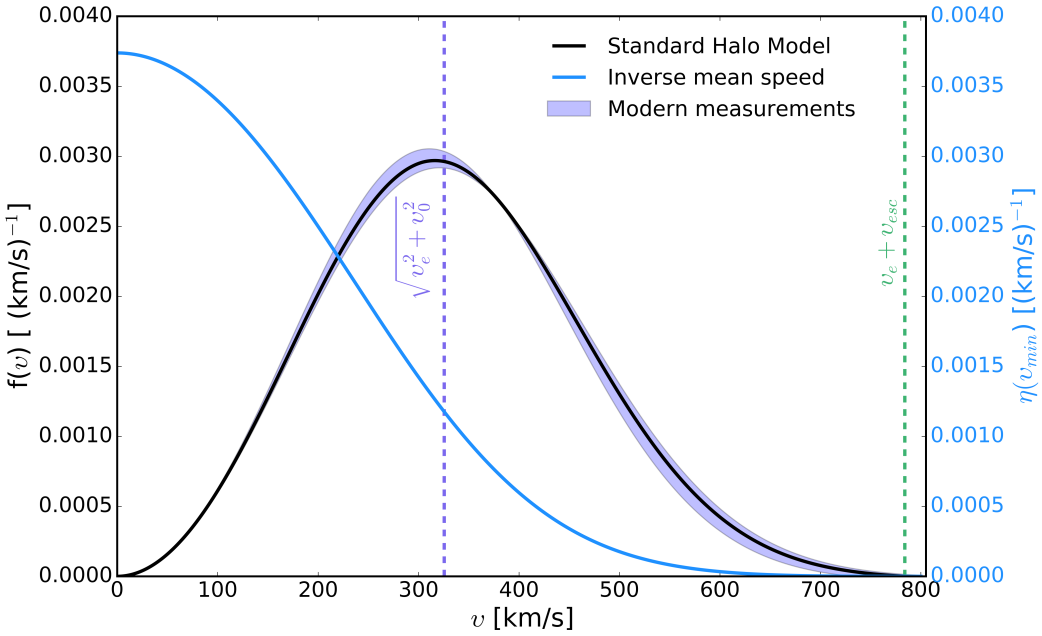

Figure 3.1. Dark matter speed distribution under the Standard Halo Model in the local frame (black). The band surrounding this distribution (purple) illustrates the uncertainties of the local-frame velocity distribution. It is showed as well the mean inverse speed (blue) resulting after having integrated the velocity distribution dependencies. In the local frame, the mean WIMP speed is $\sqrt{\upsilon_e^2+\upsilon_0^2}$ (dashed purple line), with a maximum observable WIMP speed of $\upsilon_e+\upsilon_{esc}$ (dashed green line).

calculations, defined as:

$$\eta(\upsilon_{\min,t}) = \int_{\upsilon>\upsilon_{\min}} d^3\upsilon \frac{f(\mathbf{v},t)}{\upsilon}, \tag{3.3}$$

whose solution is also described in literature [30]. Due to the Earth's motion around the sun, the velocity distribution of dark matter particles detected in a detector located on the Earth is not isotropic. Thus, the mean WIMP velocity in the local detector frame is $\sqrt{\upsilon_e^2+\upsilon_0^2}$, with a maximum observable WIMP of $\upsilon_e+\upsilon_{esc}$.

3.1.2 Scattering kinematics

Since WIMPs velocities are non-relativistic ($\upsilon \sim 10^{-3}$ c), the kinematics of their scattering can be describe by Newtonian mechanics. For a WIMP with velocity v, mass m_χ and incident kinetic energy $E_i = m_\chi \upsilon^2/2$ scattering with a nucleus at angle θ in the center of mass frame, conservation of energy and momentum allows to show that the recoil energy $E_R(\upsilon)$ in the laboratory frame can be expressed as [103]:

$$\begin{aligned} E_R(\upsilon) &= \frac{m_\chi \upsilon^2}{2}\frac{1-\cos\theta}{2}\frac{4m_\chi m_N}{(m_\chi+m_N)^2} \\ &= \frac{\mu_N^2\upsilon^2}{m_N}(1-\cos\theta), \end{aligned} \tag{3.4}$$

where m_N is the mass of the nucleus and thus $\mu_N \equiv m_\chi m_N/(m_\chi + m_N)$ is the reduced mass of the WIMP-nucleus system.

From Equation 3.4 it follows that the maximum achievable recoil energy is obtained in a head-on collision ($\theta = \pi$), i.e.:

$$E_{max}(\upsilon) = 2\frac{\mu_N^2 \upsilon^2}{m_N}. \tag{3.5}$$

As presented in Figure 3.2, where the dark matter mass dependency on the energy is shown, the maximum energy deposition that can be achieved in xenon is found when considering a head-on collision while using the highest possible local-frame dark matter particle speed, i.e. the sum of the Earth velocity and the escape velocity, $\upsilon_{esc}+\upsilon_e$. This corresponds to E_{max} = 1.632 MeV (green line). At the same time, the mean energy deposition (blue line) considers that $\cos\theta$ alters the distribution as being uniformly distributed between -1 and 1, while the mean velocity from the local frame has been used.

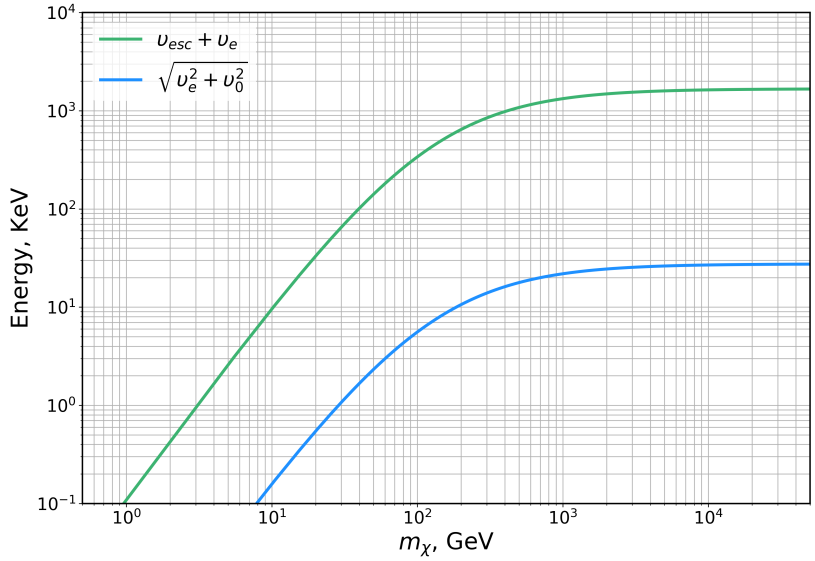

Figure 3.2. Energy deposition as function of dark matter mass. Maximum energy deposition found when considering a head-on collision while using the local-frame dark matter particle speed (green) and average energy deposition (blue).

Lastly, the relation found in Equation 7.10 allows to define the minimum WIMP speed υ_{min} required to produce a recoil energy E in a generalized way as:

$$\upsilon_{min} = \begin{cases} \sqrt{\frac{m_N E}{2\mu_N^2}} & \text{elastic} \\ \frac{1}{\sqrt{2m_N E}}\left(\frac{m_N E}{\mu_N} + \delta\right) & \text{inelastic} \end{cases} \tag{3.6}$$

where δ stands for the mass splitting between the lightest and next to lightest states in the spectrum when the inelastic scattering interaction case is considered [30].

3.1.3 Expected event rate

In the context of particle physics, the expected event rate of interaction R is proportional to the number of target nuclei in the detector N, the flux of WIMPs on Earth Φ_χ and the WIMP-nucleus scattering cross section σ:

$$R = N\Phi_\chi\sigma, \tag{3.7}$$

where the flux of WIMPs can be written as $\Phi_\chi = n_\chi\langle\upsilon\rangle$, $n_\chi = \rho_\chi/m_\chi$ is the WIMP number density, ρ_χ is the local dark matter mass density and $\langle\upsilon\rangle$ is the average WIMP velocity with respect to the rest frame of the detector.

Combining above expressions, the signature of dark matter for direct detection experiments consists on the differential recoil spectrum from dark matter interactions per unit recoil energy E and detector mass. This can be written, following [103], as:

$$\frac{dR}{dE}(E,t) = \frac{N_A}{A}\frac{\rho_\chi}{m_\chi}\cdot\int_{\upsilon_{min}}^{\upsilon_{max}} d^3\mathbf{v} f(\mathbf{v},t)\cdot|\mathbf{v}|\cdot\frac{d\sigma}{dE}(E,\mathbf{v}). \tag{3.8}$$

Here N_A is Avogadro's number, A is the mass-number of the target material, $\frac{d\sigma}{dE}(E,\upsilon)$ represents the differential dark matter-nucleus cross section per unit nuclear recoil energy E for a given $\mathbf{v}$ (particle physics input) and $f(\mathbf{v},t)$ characterizes the WIMP velocity distribution in the detector reference frame (astrophysics input).

Based on Equation 6.6, it follows that detection strategies can exploit the energy, time or direction dependencies of the signal. Nevertheless, in order to make use of this Equation to interpret the data of a dark matter experiment, additional assumptions on the specific particle physics model, as well as on the involved nuclear physics processes, need to be defined. As discussed in [109, 110], and explained in more details in the next sections, the track length for the energies of WIMPs recoils is $\ll$ 100 nm, much smaller than the low energy $\sim$ 10 eV electrons mean thermalization length $\sim 4.6\ \mu s$. This means that in experiments such as XENON1T, track's structure information can't be derived from charge signals and therefore it can't be used as a directional dark matter detector. Therefore Equation 6.6 will be simplified to:

$$\frac{dR}{dE}(E,t) = \frac{N_A}{A}\frac{\rho_\chi}{m_\chi}\cdot\int_{\upsilon_{min}}^{\upsilon_{max}} d\upsilon f(\upsilon,t)\cdot\upsilon\cdot\frac{d\sigma}{dE}(E,\upsilon), \tag{3.9}$$

where the information of the direction is not longer considered but rather the magnitude of any vector expression. From Equation 3.9 it follows that the differential event rate expected depends strongly on the local dark matter density ρ_χ and velocity distribution $f(v,t)$. Hence, an accurate modeling of these quantities is required to obtain reliable constraints on the properties of WIMPs.

3.1.4 Cross-section and nuclear physics aspects

Most common interactions between dark matter particles and target nucleons are considered spin independent/dependent of the target. In the former case, it is assumed that neutrons and protons

contribute equally to the scattering process. In the later, it is assumed that only nuclei with an odd number of protons or neutrons are the ones contributing [79]. Thus, the dark matter-nucleus scattering can be generally expressed as the sum of spin-independent **SI** and spin-dependent **SD** contributions, such that the total cross section can be calculated by adding these terms coherently using nuclear wave functions.

Consequently, the differential WIMP-nucleus cross section can be expressed as:

$$\frac{d\sigma}{dE}(E,\mathbf{v}) = \frac{m_{\mathrm{N}}}{2\mu_{\mathrm{N}}^2 \upsilon^2} \cdot (\sigma_0^{SI} \cdot F_{\mathrm{SI}}^2(E) + \sigma_0^{SD} \cdot F_{\mathrm{SD}}^2(E)), \tag{3.10}$$

where $\sigma_0^{SI,SD}$ are the SI and SD components of the cross sections at zero momentum transfer and $F_{\mathrm{SI,SD}}^2$ are the form factors accounting for the coherence loss found when the momentum transfer is such that the particle wavelength is no longer large compared to the nuclear radius [103].

The nuclear form factor calculations start typically from the Fourier transform of the nuclear density function. As discussed in [103], as first approximation, the Helm parametrization considering the nucleus as a solid sphere allows to express the SI form factor as:

$$\begin{aligned} F_{\mathrm{SI}} &= 3\frac{[\sin(qr) - qr\cos(qr)]}{(qr)^3} e^{-(qs)^2/2}, \\ r^2 &= c^2 + \frac{7}{3}\pi^2 a^2 - 5s^2 \;\; fm^2, \\ c &= (1.23A^{1/3} - 0.6) \;\; fm, \\ a, s &= 0.52, 0.9 \;\; fm, \end{aligned} \tag{3.11}$$

where r is the effective nuclear radius, $q = \sqrt{2E_{\mathrm{R}}m_{\mathrm{N}}}$ the nucleus recoil momentum, c is the typical nucleus radius and a and s, experimentally determined, are parameters describing the density decrease and the nucleus skin thickness, respectively. Using Helm parametrization, Figure 7.6 illustrates the SI form factor for xenon (black), argon (blue) and sodium (gray) the coherence loss found for certain energies after a given momentum transfer.

In the SD nuclear scattering case, the calculations need to include the contributions from all nucleons, such that the form factor is composed by different parts which can be represented as proton, neutron and interference terms or as isoscalar (p+n), isovector (p-n), and their interference terms. The representation for F_{SD} takes the form:

$$\begin{aligned} F_{\mathrm{SD}}^2 &= S(q)/S(0), \\ S(q) &= a_0^2 S_{00}(q) + a_1^2 S_{11}(q) + a_0 a_1 S_{01}(q), \end{aligned} \tag{3.12}$$

where the S_{ij} elements are computed using the shell model of the specific nucleus and the isoscalar (a_0) and isovector (a_1) coefficients are related to the WIMP-nucleon spin factors.

Using Fermi's Golden rule in the Born approximation, the energy (momentum) dependence of the scattering of dark matter off a nucleus can be factorized out and placed on the form factor F. Under

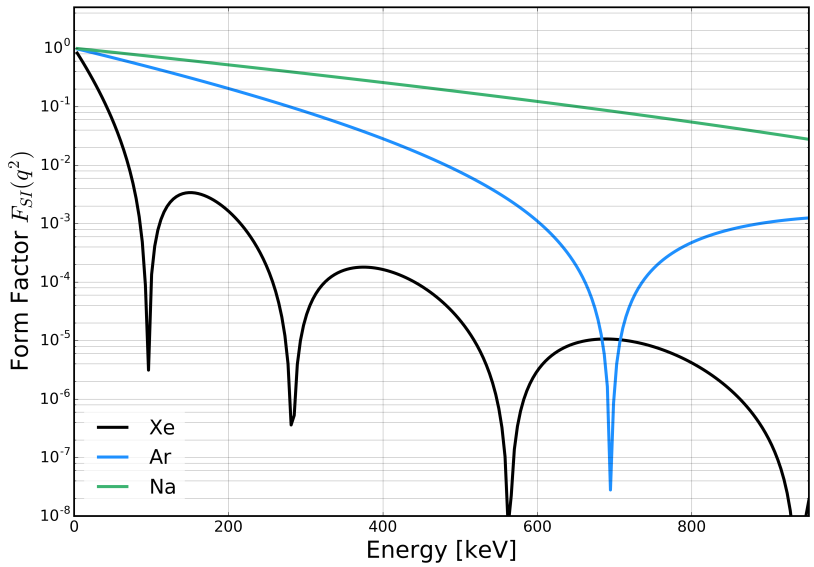

Figure 3.3. Nuclear form factor calculations, in order to take into account the spatial extent and shape of the target used, calculated by using the Helm parametrization for xenon (black), argon (blue) and sodium (gray).

this prescription, the zero momentum transfer cross sections can be expressed as:

$$\begin{aligned}\sigma_0^{\mathrm{SI}} &= \frac{\mu_{\mathrm{N}}^2}{\mu_{\mathrm{p}}^2}\left[Z+(A-Z)\frac{f^{\mathrm{n}}}{f^{\mathrm{p}}}\right]^2\sigma_{\mathrm{p}}^{\mathrm{SI}},\\ \sigma_0^{\mathrm{SD}} &= \frac{4}{3}\frac{\mu_{\mathrm{N}}^2}{\mu_{\mathrm{p}}^2}\left[\langle S^{\mathrm{p}}\rangle+\langle S^{\mathrm{n}}\rangle\frac{a_{\mathrm{n}}}{a_{\mathrm{p}}}\right]^2\left(\frac{J+1}{J}\right)\sigma_{\mathrm{p}}^{\mathrm{SD}},\end{aligned} \tag{3.13}$$

where μ_{p} is the proton-WIMP reduced mass. For the target material, Z is the atomic number, A is the mass number and J is the total nuclear spin; $\langle S^{\mathrm{p}}\rangle$ and $\langle S^{\mathrm{n}}\rangle$ are the expectation values of the total proton and neutron spin operators; f^{p}, f^{n}, a_{p} and a_{n} are the effective WIMP strength couplings to protons and neutrons (derived from couplings to quarks, supplied by an underlying theory [111]). In practice, $f^{\mathrm{p}} = f^{\mathrm{n}}$ is usually assumed such that the cross-section dependence on the number of nucleons A changes into an A^2 behavior, which can be visualized together with the effect of the form factor correction in Figure 3.4, for different target materials. Here, the event rate per keV, day and kg for SI interactions was calculated (following Equation 3.9) for different target materials when considering a WIMP mass of 100 GeV/c^2 and a cross-section of 10^{-37} cm^2. The A^2 dependence affects the shape of the energy spectrum such that heavier elements as xenon have an enhancement in their event rate at low deposited energies, while having a suppressed rate at high recoil energies due to coherence loss found in the form factor (such as observed for xenon at nuclear recoil energies close to 95 keV). In addition, the region of interest for direct dark matter detection searches is situated in the energy region below 20 keV (where for xenon the rate is the most enhanced, which reinforces the grounds to select xenon over other different target materials.

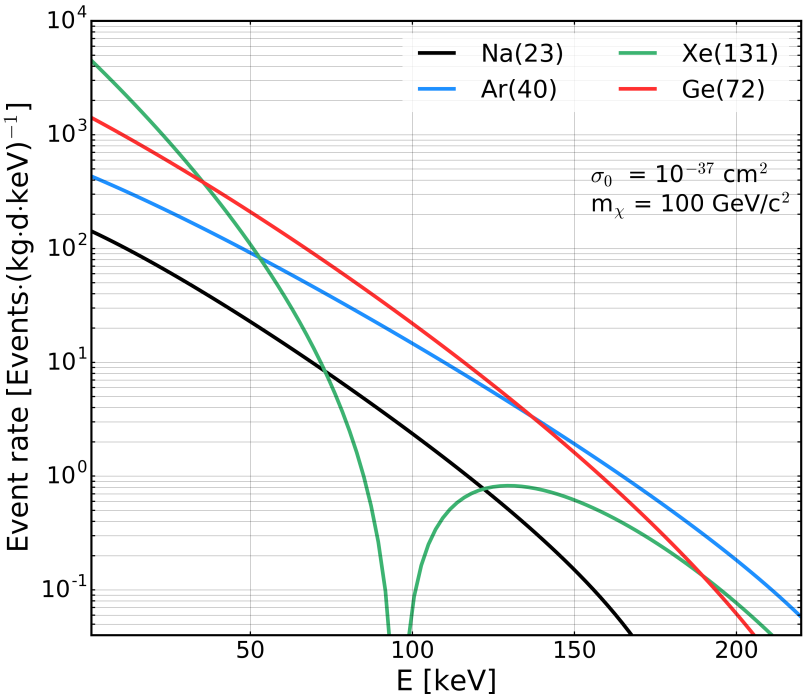

Figure 3.4. Differential event rate for SI interactions direct detection when considering a WIMP mass of m_χ = 100 GeV/c^2 and a cross-section of $\sigma_0^{SI} = 10^{-37}$ cm^2, using xenon (green), germanium (red), argon (blue) and sodium (gray) as target materials. In parenthesis, for each element, is found the mass-number of the target material.

Furthermore, the WIMP-proton cross sections $\sigma_p^{SI}, \sigma_p^{SD}$ are defined as:

$$\begin{aligned} \sigma_p^{SI} &= \frac{4}{\pi}\mu_p^2 f^{p2}, \\ \sigma_p^{SD} &= \frac{24G_f^2}{\pi}\mu_p^2 a_p^2, \end{aligned} \tag{3.14}$$

where G_f is the Fermi coupling constant and the spin of the dark matter particles is considered equal to that of the proton.

3.1.5 Generic results

Having all the elements to compute a WIMP event rate for any target, according to Equation 3.9, the expected event rate for SI interactions can be computed now in order to illustrate qualitatively the influence of varying different detector parameters in detection, as shown in Figure 3.5 for xenon as reference. Here, the changes in the rate are used to exhibit an analogue to the effects on the cross section, the desirable quantity calculated and used to define standard exclusion limits on different dark matter masses (as will be discussed in 3.1.5). Assuming a spin-independent cross section of $\sigma_0^{SI} = 10^{-37}$ cm^2 and taking $E_{Thr} = 5$ keV (which describes the typical energy threshold of a detector), in black it is shown the reference rate calculated in xenon when using a target mass m$_T$ = 0.5 tonne.

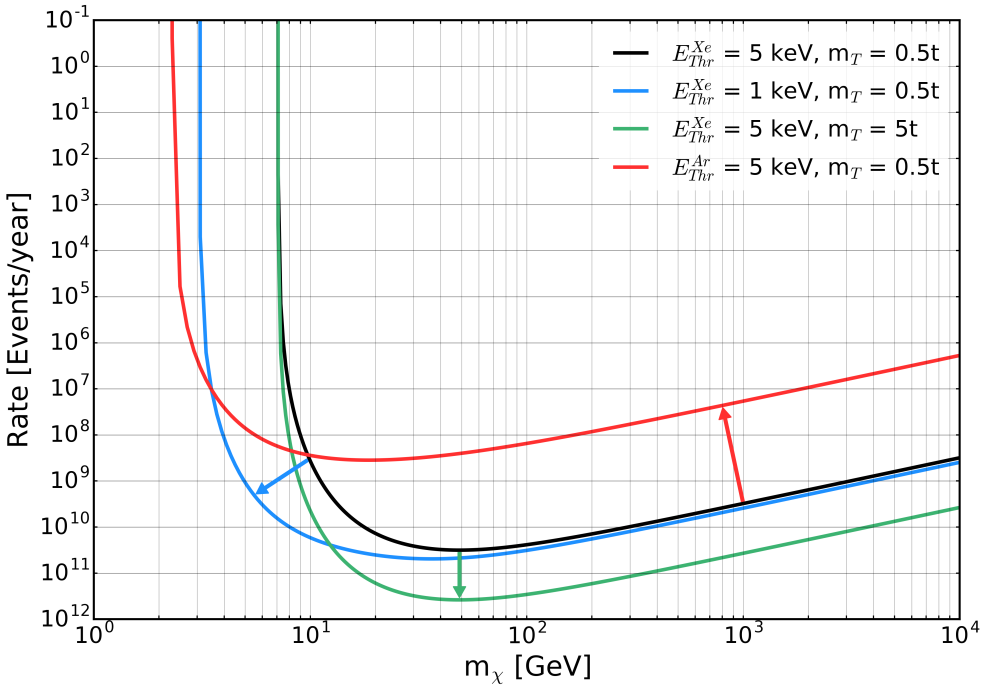

Figure 3.5. Expected event rates for SI interactions when considering $\sigma_0^{\mathrm{SI}} = 10^{-37}$ cm^2, illustrating qualitatively the influence of varying certain detector parameters. The changes in the rate are used to make an analogue to the effects on the cross section, the quantity used to define standard exclusion limits on different dark matter masses. (Black) reference Xe rate with E_{Thr}= 5 keV, m_T = 0.5 tonne. (Blue) Xe rate lowering the threshold. (Green) Xe rate increasing the target mass. (Red) Ar rate, smaller target nucleus.

The effect of using a lighter target nuclei is indicated in red. Given that $\upsilon_{\mathrm{min}} = \sqrt{m_{\mathrm{N}} E_{\mathrm{Thr}}/2\mu_{\mathrm{N}}^2}$ is reduced, along with the modification of the kinematics of the scattering, the result is a shift of the maximum sensitivity to lighter WIMP masses while the event rate, proportional to A^2, is reduce in comparison to the reference value from xenon (Argon has been used here for illustration). Next, as indicated in green, an increase in target mass will enhance the rate and in turn it will augment the ability to measure lower cross-sections. Lastly, as indicated in blue, lowering the energy threshold allows to extend the sensitivity to lighter WIMP masses, which in general will give access to smaller cross-sections since υ_{min} has been also reduced.

3.2 Signal production in liquid xenon

The understanding of the detection medium used to search for dark matter embodies the starting point needed to design a suitable strategy of detection in any experiment. Historically, liquid noble elements have been recognized as an attractive medium due to its radiation detection capabilities and background discrimination potential [112]. Among them, liquid xenon is one of the preferred mediums for different types of particles due to its high stopping power for penetration radiation (due to its high density and large atomic number), which enhances the WIMPs scattering rate. Moreover,

liquid xenon has the highest yield of scintillation photons and charge carries in response to radiation, along an ultra low electron affinity such that electrons can be efficiently drifted. Furthermore, it has only one rare radioactive isotope that ultimately does not contribute into the background of the detector[2] and from the 8 stable isotopes that xenon has, ^{129}Xe and ^{131}Xe have zero-nuclear spins, such that they can be used to probe SD interactions with dark matter, as discussed in section 3.1.3.

By measuring light and charge, as discussed in section 2.3.1, detectors using liquid xenon benefit from having highly anti-correlated and complementary signals, thus enabling a precise measurement of particle's properties interacting in the detector (such as their type, energy and position). Furthermore, background sources originally from electronic recoils **ERs** can be distinguished from nuclear recoils **NR** due to their different light and charge yields. However, due to statistical fluctuations associated to the amount of charge and light measured, ERs $\leq$ 10 keV challenge the discrimination power of particles and are the most relevant background for NRs WIMP searches (main background sources are explained in detail in Chapter 6). This section will be devoted to describe the physical processes underlying signal production in the medium of liquid xenon (section 3.2.1), the light and charge yield (section 3.2.2) and the combined energy scale that can be obtained from knowing these signals (section 3.2.3).

3.2.1 Signal formation

A particle depositing energy in liquid xenon excites atoms, creates electron-ion pairs and produces atomic motion (heat). The energy into the first two channels yields detectable signals, while the energy lost into heat is either negligible for ERs, or leads to the creation of light in the form of sub-excitation of electrons [114] or secondary NRs [115]. Overall, the energy deposition E can be described as:

$$E = N_{\mathrm{i}} E_{\mathrm{i}} + N_{\mathrm{ex}} E_{\mathrm{ex}} + N_{\mathrm{i}} \eta, \tag{3.15}$$

where N_{i} and N_{ex} are the number of electron-ion pairs and excited atoms produced, E_{i} and E_{ex} are the average expenditure ionization and excitation energies, and η is the average kinetic energy in sub-excitation electrons after their collision[3] (for NRs, an additional term considering recoil elastic scattering collisions that do not result in ionization or excitation would have to be added). By referring to the atomic ionization potential I for the ER case described by Equation 3.15, the energy of electrons in the xenon gas phase can be expressed as:

$$\frac{E}{I} = N_{\mathrm{i}} \frac{E_{\mathrm{i}}}{I} + N_{\mathrm{ex}} \frac{E_{\mathrm{ex}}}{I} + N_{\mathrm{i}} \frac{\eta}{I}, \tag{3.16}$$

where $I = 12.13$ eV for xenon. In the liquid phase, I is replaced by the band gap, $E_{\mathrm{g}} = 9.22$ eV, which is associated with the band structure of electronic states in liquid xenon. By doing this, and by

[2] Specifically ^{136}Xe, which is produced by cosmogenic activation, decaying via neutrinoless double beta decay and featuring a half-life of $T^{0\nu\beta\beta}_{1/2}\left(^{136}\mathrm{Xe}\right) > 1.8\times 10^{25}$ yr (90% C.L.) [113].

[3] These values have been estimated to be between (4.65 - 5.25) eV in liquid xenon [116].

introducing the W-value defined as $W = E/N_i$, the average energy required to produce one electron-ion pair, Equation 3.16 can be rewrite as:

$$\frac{W}{E_g} = \frac{E_i}{E_g} + \frac{E_{ex}}{E_g}\frac{N_{ex}}{N_i} + \frac{\eta}{E_g}. \tag{3.17}$$

These ratios have been both calculated and measured in xenon by several authors (e.g. by using the oscillator spectrum strength of solid xenon obtained from photo-absorption [117]). In particular, the ratio N_{ex}/N_i is estimated to be 0.06 but a value of 0.2 is more consistent with measured data. For NRs, a ratio of $N_{ex}/N_i \sim 1$ has been found to show better agreement with data. Overall, the difference found in this ration that can be measured demonstrates the underlying discrimination capabilities between different type of recoil in liquid xenon.

Primary scintillation S1

The mechanism of primary scintillation in liquid xenon starts when a particle scatters either at a xenon nucleus or an electron of the atomic shell, causing a recoil that in turn will induce secondary recoils. The excitation of the atoms from the initial impact will subsequently lead to the formation and decay of strongly bound diatomic molecules in an excited state (called excimers), leading to the emission of photons with wavelength in the vacuum ultraviolet **VUV** region:

$$\begin{aligned}
X + Xe &\longrightarrow Xe^* + X && \text{(impact excitation)} \\
Xe^* + Xe &\longrightarrow Xe_2^{*,\nu} && \text{(excimer formation)} \\
Xe_2^{*,\nu} + Xe &\longrightarrow Xe_2^* + Xe && \text{(relaxation)} \\
Xe_2^* &\longrightarrow Xe + Xe + h\nu && \text{(VUV emission)}
\end{aligned} \tag{3.18}$$

where X can be either an electron or a recoiling nucleus. The superscript ν is used to identify a state with vibrational excitation $Xe_2^{*,\nu}$ from one having only electronic excitation Xe_2^* and the emission of scintillation photons with a wavelength centered at 178 nm, corresponding to an energy of 7 eV. This emission follows from the relaxation and decay of excimers into the dissociative ground state $^1\sum_g^+$, specifically from one of the two possible lowest electronic states, a singlet $^1\sum_u^+$ or a triplet $^3\sum_u^+$. For relativistic electrons, the singlet and triplet states have a decay time of 2.2 and 27 ns respectively[4], the fast and slow components, making xenon one of the fastest scintillators [118].

An alternative process leading to scintillation light involves recombination of the ionization electrons with positive ions [118], similar to the excitation channel presented in Equation 3.18. However, the recombination process is slow in comparison to de-excitation times, which adds a non-exponential element on top of the fast and slow components [110]. This effect can be removed by applying an electric field of a few kV/cm. In general, recombination plays a big role on the total light yield and stands as a complex process that can depend on factors such as initial distribution of

[4]This characteristic is often exploited by single-phase experiments, since it provides a technique of discrimination between ER and NR, by looking at the S1 pulse shape.

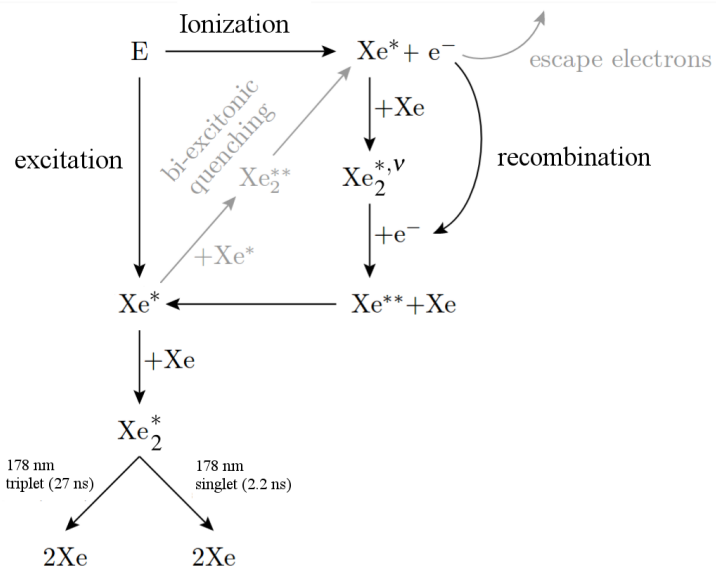

Figure 3.6. (Black) Scintillation mechanism in liquid xenon (Gray) different processes that can lead to the quenching of scintillation light. Adapted from [60].

electrons and ions after particles scatter in the medium, the speed in which sub-excitation electrons lose their energy, the distance traveled to reach thermalization inside the medium, mobility and diffusion rate for the electrons and the spatial extend of charges in the recoil track[5]. For low density tracks, it has been found that even without electric field some electrons can escape recombination. On the opposite case, when tracks have high density due to excited and ionized species, their high probability of collisions can lead to suppression of luminescence signal, which is better known as "bi-excitonic quenching". Figure 3.6 summarizes the scintillation mechanisms in liquid xenon.

Overall, observations show that for low energy ERs and NRs (bellow 100 keV), the scintillation signal S1 is proportional to:

$$S1 \propto N_{\mathrm{ph}} = N_{\mathrm{ex}} + rN_{\mathrm{i}}, \tag{3.19}$$

where r stands for the recombination fraction given a certain electric field.

Secondary scintillation S2

Typically, the number of excitations N_{ex} is smaller than the primary ionization N_{i} created in liquid for ERs, while it is comparable for NRs. In both cases, the detection of ionization is constrained to several requirements, such as that charge carriers created escape recombination, that they have a high mobility along the drift path while having low probability to form states with low mobility, and also that they find a large gain amplification mechanism. For these reasons, purification of liquefied rare gases is mandatory, given that even small traces of electronegative impurities in the medium, such as

[5]Codes such as SRIM/TRIM [119] are used to provide information about the extend of the electronic and nuclear recoils tracks, together with the stopping power, in liquid xenon.

O_2, N_2O or other molecules, can capture free electrons in their drifting path, forming negative ions with low mobility (e.g. $\mu(O_2^-) \approx 0.3 \times 10^{-3}$ cm^2/(V·s) [120]).

Despite of the difficulties to predict the number of electrons that would be detected, given to how different can many features change when considering different particles energies or the magnitude of the electric field applied, the ionization capacity of the medium can be estimated from the expected energy per electron-ion pair $W = E/N_\mathrm{i}$, where E is given by Equation 3.15. This value is not easy to measure since the total charge created by a particle can change due to factors such as recombination and electrons attachment to impurities. What is often do is to extrapolate the extracted charge measured $Q_0 = N_i e$, as function of the electric field $\mathscr{E}$. Assuming a cylinder where recombination of negative and positive ions with same mobility takes place, the parametrization to extrapolate the charge is expressed as [121]:

$$Q(\mathscr{E}) = \frac{Q_0}{1 + k/\mathscr{E}}, \tag{3.20}$$

where k characterizes the recombination strength (typical values depending on the particle type and energy can be consulted in [122, p.340]). By taking Equation 3.20, a linear fit of $1/Q$ against $1/\mathscr{E}$ lead to the intercept of $1/Q_0$, which allows to measure N_i. As result, there are several measurements for the W-value for liquid xenon [117, 123, 124], being commonly adopted the value W = 13.8 $\pm$ 0.9 eV [125].

After furthermore considering the effect of diffusion of electrons along the drift path and electrons drift velocity dependence on the electric field, together with the extraction difficulties that can be found in the procedure of extracting electrons at the liquid/gas interface (section), the observed secondary scintillation S2 signal is found to be proportional to:

$$S2 \propto N_\mathrm{e} = (1 - r)N_\mathrm{i}. \tag{3.21}$$

3.2.2 Light and Charge yield

As previously discussed, it is quite a challenge to accurately describe how a deposition of energy gets distributed into light, charge and heat. Historically, the scintillation signal was considered to be the most telling gauge of the energy of a particle in LXe, but at the same time a precise measurement of the absolute scintillation yield was found to be difficult. As explored in literature [122], a dependence of the scintillation efficiency was found in terms of the linear energy transfer **LET**. Thus, for intermediate LET values, $\sim$ (10^2 - 10^3) MeV cm^2/g, the scintillation yield was found to be close to be constant, while at lower and higher ionization densities it was found to decrease. Therefore, a common definition came into place and the evaluation of the light yield was adopted to be made relative to the scintillation yield of NRs to that of ERs produced by the 122 keV γ-ray from ^{57}Co at zero electric field [126]. Parametrized by the efficiency $\mathscr{L}_{eff}$ and W_s at zero applied electric field as:

$$\mathscr{L}_{eff} = \frac{W_\mathrm{s,e}(122\ keV)}{W_\mathrm{s,Xe}(E^\mathrm{nr})}, \tag{3.22}$$

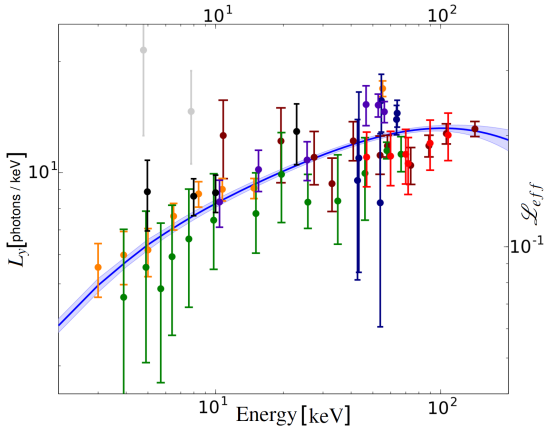

Figure 3.7. Best global fit calculated for $\mathscr{L}_{eff}$ along its statistical error band (solid blue line). Additionally different relevant literature measurements, from [127] (dark red), [128] (red), [129] (dark blue), [130] (purple), [131] (black), [132] (orange), and [133] (dark green) are shown. The two gray data points from [127] have been not included in the fit performed. Adapted from [126].

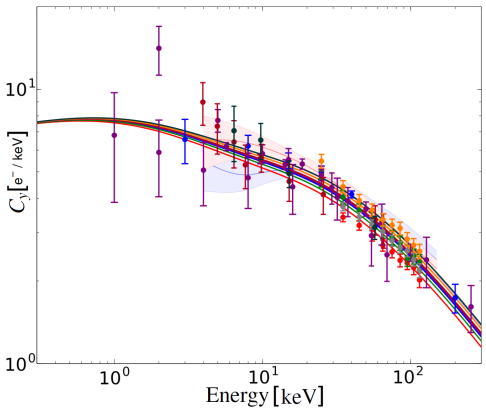

Figure 3.8. Best global fit calculated for the charge yield data collected in different applied electric fields, corresponding to data at 100 V/cm (red) [134], 270 V/cm (green) [134], 530 V/cm (blue) [135], 730 V/cm (purple) [136], 1 kV/cm (dark red) [133], 2 kV/cm (orange) [134], 2 kV/cm (gray) [134], 3.4 kV/cm (blue band) [137], 3.9 kV/cm (orange band) [137], and 4 kV/cm (dark green) [133]. Adapted from [126].

where E^{nr} represents the NR energy an the indices Xe and e correspond to xenon and ERs, respectively[6]; the number of photons produced per unit energy, or the light yield of liquid xenon when an electric field is applied is given by:

$$L_y(E,\mathscr{E}) = \frac{N_{ph}}{E_{\rm nr}} = \mathscr{L}_{eff}\frac{S_{\rm n}}{S_{\rm e}}\frac{n_{\rm ph}(^{57}Co)}{122\ keV}, \tag{3.23}$$

where $S_{\rm n}$ and $S_{\rm e}$ are the scintillation reduction factors due to applied fields for NRs and ERs, and the clear dependency on the energy transfer and the electric field applied has been made explicit.

Similarly, express as a function of the recoil energy and the applied electric field, the ionization, or charge yield, can be calculated as:

$$C_y(E,\mathscr{E}) = \frac{N_{\rm e}}{E}, \tag{3.24}$$

and it quantifies the amount of electrons produced per unit energy.

Figures 3.7 and 3.8 shows a compilation of both the energy dependent relative scintillation yield for NRs[7] and the charge yield. Along with the measurements provided by several groups, simulation packages such as NEST [139] have been developed in order to provide computational tools that try to describe and predict the excitation, ionization, and corresponding scintillation processes in liquid noble elements yield for an extensive variety of conditions.

[6] $W_{s,e}$(122 keV) is the W_s value for for 122 keV γ-ray from ^{57}Co source, defined as $W_{\rm s} = E/N_{\rm ph}$, where is the overall energy deposition.

[7] The standard method to experimentally measure the scintillation efficiency is through elastically scattering mono-energetic neutrons off a LXe target while having a fixed angle of scattering [138, 132, 131, 130], such that the transferred energy to xenon atoms can be resolved kinematically from the detected scattered neutrons.

3.2.3 Combined Energy Scale

As previously discussed, N_e and N_{ph} are of big interest since effectively $S1 \propto N_{ph}$ and $S2 \propto N_e$. Although these quantities undergo statistical fluctuations, they are fundamentally constrained by conservation of energy (the total deposition of energy in the medium). Originally proposed in [140], it was introduced to use the linear combination of S1 and S2 as their fluctuation is smaller than the one from each individual signal. The motivation is that a combined signal will lead to an improved energy reconstruction. In order to find an energy estimator independent of recombination, it was proposed to use:

$$N_i + N_{ex} = N_{ph} + N_e, \tag{3.25}$$

since this relation should hold for ERs [141]. Under the assumption that all electron-ion pairs do recombine and that all excited atoms lead to scintillation photons, the emitted photons would be given by $N_{ph} = N_{ex} + N_i$. The efficiency in which scintillation would without external electric field could be then expressed by the minimum energy needed to create a scintillation photon unaffected by quenching effects, i.e.:

$$W_s^{min} = \frac{E}{N_{ph}} = \frac{E}{N_{ex} + N_i}, \tag{3.26}$$

where W_s^{min} depends on both the type of particle and its energy. By rewriting Equation 3.26 using Equations 3.23, 3.24 and 3.25, and by expressing the result in terms of the recoil energy, this leads to:

$$E = W_s^{min}(N_{ph} + N_e) = W_s^{min}(E \cdot L_y(E,\mathscr{E}) + E \cdot C_y(E,\mathscr{E})). \tag{3.27}$$

By defying the following detector gain dependent values g_1 and g_2, whose derivation will be discussed in section 4.3.1:

$$\begin{aligned} g_1 &= \frac{S1}{E \cdot L_y(E,\mathscr{E})} \\ g_2 &= \frac{S2}{E \cdot C_y(E,\mathscr{E})}, \end{aligned} \tag{3.28}$$

Equation 3.27 can then express as:

$$E = W_s^{min}\left(\frac{S1}{g_1} + \frac{S2}{g_2}\right) = 13.8\ eV\ \left(\frac{S1}{g_1} + \frac{S2}{g_2}\right). \tag{3.29}$$

As result of these parametrization, by deriving g_1 and g_2 from calibration data, the energy deposition of a given event having a detected S1 and a S2 signal can be reconstructed.

3.3 XENON1T Experiment

From the first proposal of implementing a dual-phase noble gas Time Projection Chamber **TPC** for dark matter detection in 1989 [142], the technology used in the XENON Dark Matter Project

has been developed almost by 3 decades. XENON1T, the current detector and successor of the XENON10 prototype [143] and the XENON100 detector [144], is located underground in Hall B of the Laboratori Nazionali del Gran Sasso **LNGS**, Italy, at a depth of 3600 meter water equivalent. Due to the achievement to scale the proven detection technique from $\sim$ 100 kg to 2000 kg of target mass and to the design of implemented strategies in terms of background suppression and particles identification, XENON1T is the first WIMP dark matter detector operating with a liquid xenon target mass above the ton-scale. Up today it has not only achieved the lowest ever ER background level rate in dark matter searches, but also has set the most stringent limit on the WIMP-nucleon spin-independent elastic scattering cross-section at 4.1×10^{-47} cm^2 for a mass of 30 GeV/c^2 [62].

This section will be dedicated to the XENON1T detector and some of its features. Starting from a general overview of the instrument (section 3.3.1), a discussion about how are raw signals obtained (section 3.3.2) and lastly what is the general selection criteria defined to analyze data (section 3.3.3). More details on the XENON1T design, components, and performance can be consulted in [145].

3.3.1 Instrument overview

The core of the XENON1T Experiment is a dual-phase xenon cylindrical TPC of 97 cm length and 96 cm diameter, containing an active liquid xenon **LXe** target of 2.0 tonnes and being surrounded by 1.2 tonnes outside the TPC acting as a passive shield against external backgrounds. Figure 3.9 illustrates the working principle of the detector. There it is shown how the interaction of a particle in the target medium can scatter-off xenon nuclei or can interact with atomic electrons, depending on the nature of the interacting particle, such that the resulting moving xenon ion excites and ionizes the LXe. As discussed in section 3.2, excitation, together with recombination after ionization, prompts the emission of scintillation light **S1** that is recorded by the Photomultipliers **PMTs** installed above and below the target. Ionization is responsible of producing free electrons that are drifted from the initial interaction vertex in opposite to the direction of the applied external drifting field E_d, towards the phase boundary. Once that these electrons arrive to the grounded gate grid, a stronger anode field E_{ext} is applied to extract the electrons into the gaseous xenon **GXe**, where they are re-accelerated to high energies and recoil with the xenon atoms, which produces secondary scintillation light **S2** detected by the PMTs. Lastly the interaction position can be reconstructed in 3-dimensions by means of the S2-signal pattern observed by the top PMTs (x-y coordinates) and the time difference between S1 and S2 (depth: z-coordinate).

The TPC is enclosed by 24 interlocking and 24 fixed light-tight **PTFE** (polytetrafluoroethylene, or Teflon) panels, specifically treated such that their surfaces are optimize to the reflectivity of VUV light, and it is surrounded by 74 field shaping electrodes in order to ensure the drifting electric field homogeneity that are connected by two redundant chains of resistors to the cathode. A total of 248 3-inch diameter Hamamatsu R11410-21 PMTs are radially installed and used to record the signals inside the TPC (divided in a top and bottom array having 127 and 121 PTMs, respectively, thus

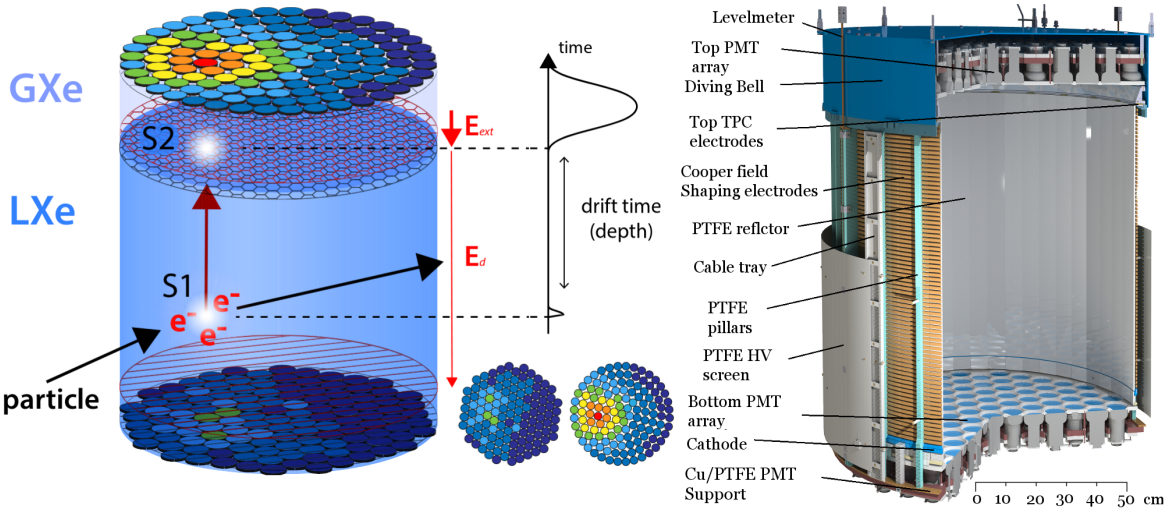

Figure 3.9. Left Working principle of a dual-phase LXe TPC: The prompt scintillation light S1 generated in the LXe is recorded by PMTs installed above and below the target. The same PMTs also measure the delayed secondary-light signal S2, which is created by proportional scintillation induced by ionization electrons (e^-) in the gas phase. The interaction position can be reconstructed in 3-dimensions by means of the S2-signal pattern observed by the top PMTs (x-y coordinates) and the time difference between S1 and S2 (depth: z-coordinate) **Right** Illustration of the XENON1T TPC and its building parts. Adopted from [146, 145].

maximizing the scintillation light collection efficiency). Moreover, a diving bell on top of the GXe is used to maintain a stable liquid-gas interface between the gate and anode electrodes.

An additional shielding from external radiation has been provided by having set up the TPC inside a double-walled, cylindrical stainless-steel cryostat specifically treated to reduce emanation of radon. At the same time, this cryostat is immersed in the center of a water Cherenkov detector of 10.2 m height and 9.6 m diameter, instrumented with 84 Hamamatsu R5912ASSY PMTs of 20.3 cm in diameter. The idea of this device is not only to limit (α,n) reactions from the surroundings of the rock cavern or the moderation of muons, but mainly to use the measured Cherenkov radiation in the water tank so that it can be correlated with events inside the TPC. Through this technique the background from muon-induced neutrons, having as source a muon flux of $(3.32 \pm 0.03) \times 10^{-8}\text{cm}^{-2}\text{s}^{-1}$ with an average energy of 270 GeV at the detector site [147], can be significantly reduced.

As shown in Figure 3.10, several auxiliary systems constitute a successful operation of the detector. These are the cryogenic system that provides the cooling power, the cryogenic distillation column removing krypton to a sub-ppt level[8] [149], a purification system for online removal of electronegative impurities, the ReStoX system for xenon storage and emergency recovery, the gas bottle rack used as a link for injection of xenon gas into the system and a gas analytics station for measuring the xenon purity before injecting it from the gas cylinders into the system. Additionally, a magnetically-coupled piston pump has been installed after the second science data measurements, specifically improving all high-purity gas applications and reducing the background levels [150].

[8] Parts per trillion, 1 ppt = 10^{-12} mol/mol.

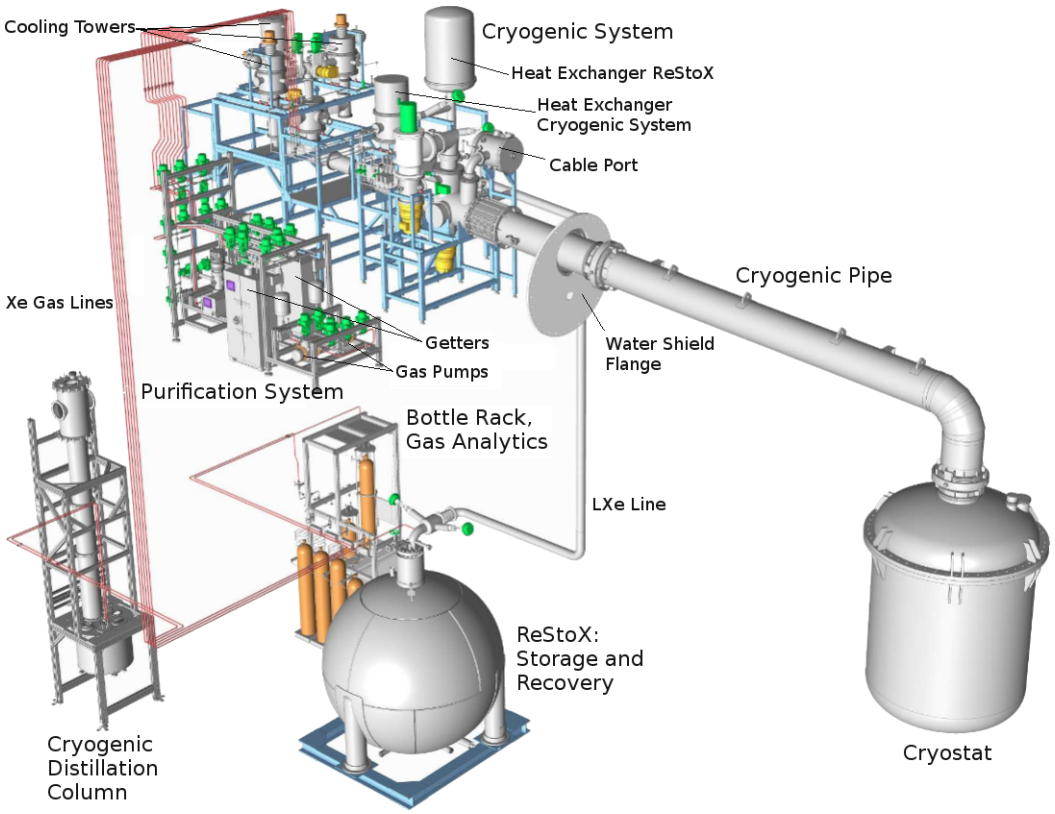

Figure 3.10. Auxiliary systems in the XENON1T Experiment, consisting of the cryogenic system, the purification system, the cryogenic distillation system, ReStoX, the gas bottle rack and a gas analytics station. Furthermore, the cryostat shown is inside the shielding water tank that accommodates the TPC. Taken from [148].

3.3.2 Data processor and signals

PAX

In order to detect and discriminate extremely low energy signals from what could be background, XENON1T uses a custom developed data processor called **PAX**, the Processor for Analyzing XENON [151]. This open source analysis tool, fully designed by using modern software engineering and based on pure python coding, takes care of performing the digital signal processing of the XENON1T raw data. Taking as input *.root* files generated by the Data acquisition **DAQ** system, PAX operates in five stages which lead to the detection of events, illustrated in Figure 3.11.

First, for every PMT channel, PAX inspects independently and asynchronously pulses (ADC waveform segments) above a ~ 0.3 photoelectron **PE** digitization threshold. By recording samples before the self-triggering peak, a local baseline and noise level are computed in order to define a dynamical high-noise rejection boundary and a signal threshold for each waveform. Pulses which exceed this boundary are considered as a **hit**, and for them a window defined by 30 *ns* to the left and 200 *ns* to the right is set to record the entire PE signal area. Second, a rough first clustering based

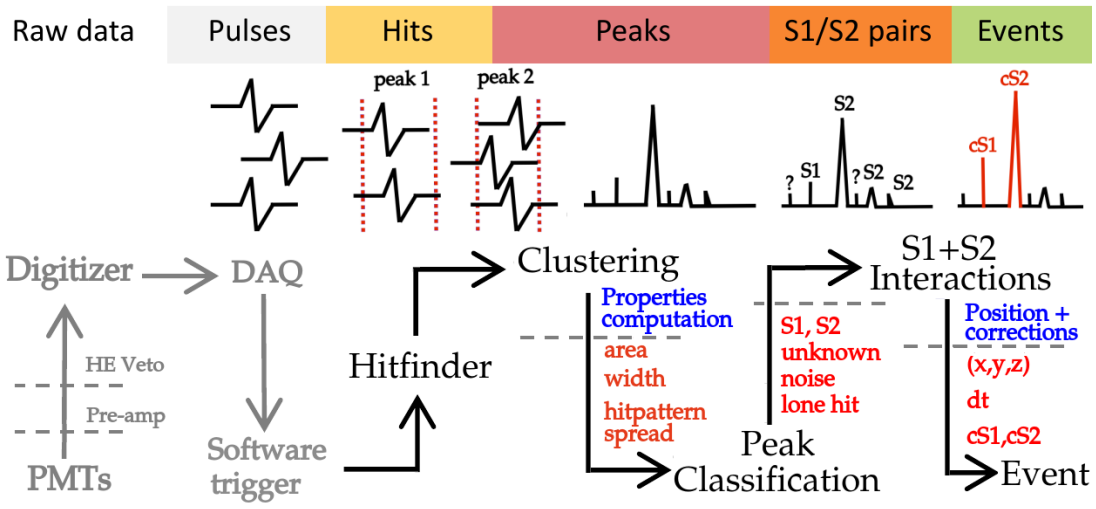

Figure 3.11. Simplified schematic processing chain of the processor for analyzing xenon PAX.

on gaps of about 2 μs between hits initially splits them into groups. Subsequently, these groups are further split based on a recursive algorithm that minimizes the clustering variance (calibrated on simulated waveforms). As results, belonging groups of hits from all channels are summed together to form **peaks**.

Third, for each peak identified several properties are calculated, such as the total area, hit-pattern spread and measures of the pulse width. Fourth, based on the rise-time[9] of the peak and the amount of PMTs contributions within 50 *ns*, each peak is classified as an S1, S2, noise, lone hit or several categories of "unknown". Specifically, a peak labelled as an S1 signal needs to have a rise-time between (70 - 100) *ns* (with at least 3 PMTs contributions), while slower rising clusters (having at least 4 PMTs contributions) are classified as an S2 signal. Lastly, given that some properties such as position and corrected energy estimators rely on knowing which S1 candidate is paired to which S2 candidate, PAX computes properties for each plausible S1/S2 pairing to give maximum analysis flexibility. For each paired S1-S2, designated as **interaction**, the corresponding 3-dimensional position will be reconstructed by using the XY-position derived from pattern of PMT hits and the time difference between the S1 and S2 peaks. Furthermore, depending on where the interaction takes place, several energy correction will be computed to obtain the corrected S1 and S2 signals.

Figure 3.12 presents an example of a XENON1T event waveform in order to illustrate how PAX works. To begin with, in the bottom panel the hits found in all different PMTs along the time window of the event are shown (step 1 and 2). Next, in the middle panel the different peaks identified after the clustering algorithm sums all hits to create individual peaks sorted by their properties are shown. A blue band defines the main S1 signal identified in the waveform, while a green one stands for the main S2 signal found. In the top panel, in the first two panels from left to right, the amplitude (PE/bin) and time window (μs) in which the main S1 and S2 signals were measured are shown. In the last two

[9]Rise time is defined as the time where the peak reaches 10% and 50% of its total area.

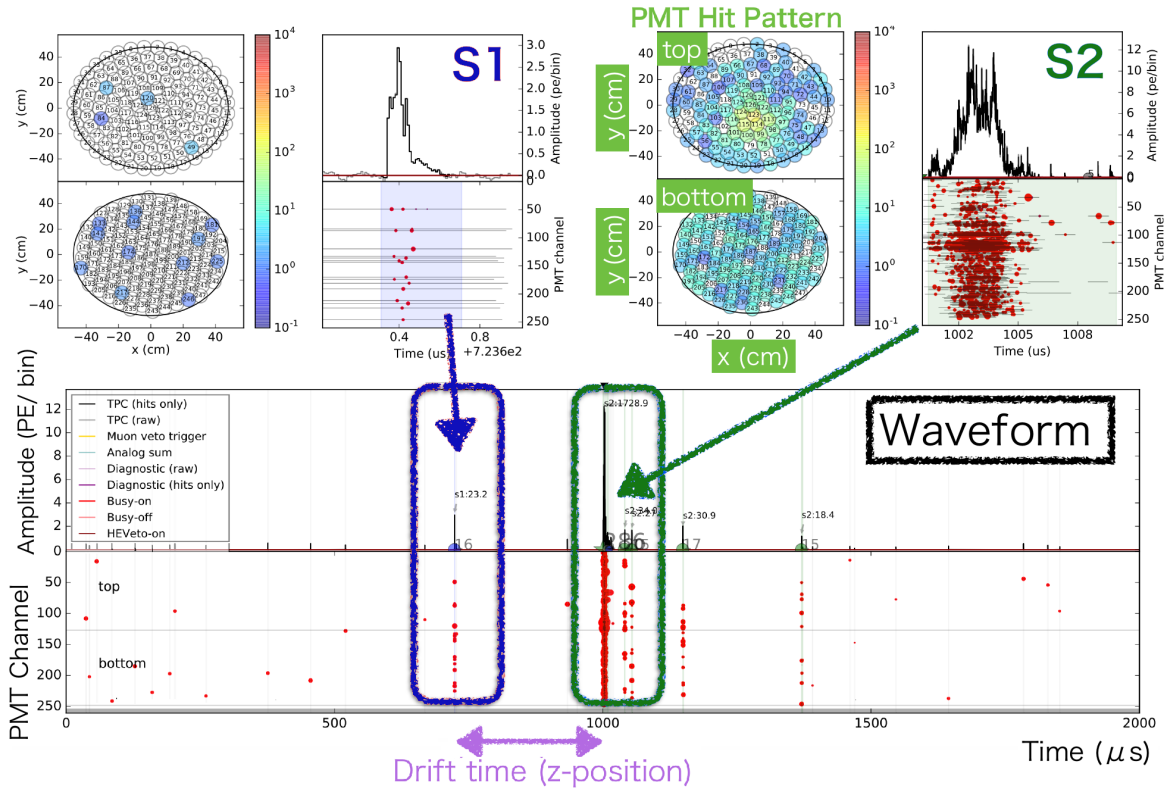

Figure 3.12. Example of a waveform for an event found in background data. As illustrated, hits from the PMT channels are clustered as peaks. Then, PAX classifies these peaks based on their properties. Subsequently, the main S1 and S2 in the waveform are paired, such that the drift time between them defines the z coordinate, while the XY PMT hit pattern defines the (x,y) coordinates of the event.

panels the PMTs hit patterns found for each one of these two signals in the corresponding XY-plane of detection are shown.

Distinct details can be indicated in the light of this example. For instance, S1 signals are typically found to be relatively sharper and smaller than an S2 signal. As it will be discussed in the next section, this is due to the prompt scintillation decay time and the fast response of the PMTs to detect this photons, about a few nanoseconds, opposite to a broader S2 signal due to electron cloud diffusion and secondary scintillation conversion. In addition, due to the internal reflection on the liquid/gas interface, the light from the S1 signal is mainly detected by the bottom array of PMTs. On the contrary, the S2 signal is mainly detected by the top array given that the extraction of electrons and secondary scintillation process occurs in the gas phase[10]. Furthermore, as the waveform indicates there can be found smaller signals identified as secondary peaks. On one hand, those signals after the main S1 normally correspond to single extracted electrons most likely created by photoionization of impurities in the LXe and of the metal component inside the TPC [152], such as the gate mesh. On the other hand, the tail of signals following the main S2 is a mixture of two effects: several single electrons

[10]To be precise, $\sim 65\%$ of the S2 signal is detected and the top PMTs array as secondary scintillation while the rest is measured as light by the bottom PTMs array.

typically of width $\sim 1\ \mu s$ (emitted over timescales $\gg 100\ \mu s$), whose origin is associated to the thermalization and trapping of un-emitted electrons just below the LXe surface [153], and single electrons caused by photoionization of a high energy S2.

Detected S1 signal

The shape of the primary scintillation S1 signal measured by PAX is characterized by several factors. For instance, as discussed in section 3.2, S1s have a time structure composed by the singlet and triplet lifetime, the recombination time and the ratio of singlet states to triplet states. Given that the decay of these components is dependent on the target medium, electric field, energy deposition per unit distance and recoil type, the shape of the final S1 signal will change depending on the effect and interplay of these parameters, whose prediction is shown in Table 3.1 by using NEST.

Table 3.1. Parameters that affect the shape of the S1 pulse in LXe detectors along the error-weighted average of world data. Values consulted from [154].

Parameters	Expected value
Singlet lifetime	3.1 ± 0.7 ns
Triplet lifetime	24 ± 1 ns
Singlet/Triplet - ER from direct excitation (γ induced)	0.17 ± 0.05
Singlet/Triplet - ER from recombination (γ induced)	0.8 ± 0.2
Singlet/Triplet - ER from both processes (α induced)	2.3 ± 0.51
Singlet/Triplet - NR (neutron induced)	7.8 ± 1.5

Moreover, several effects need to be considered, such as detector geometry (travel time spread of light inside the detector [155]), signal processing (time spread of light inside the PMTs) and electric field in-homogeneity (average local recombination of excitons and ions). For instance, while liquid xenon is mainly transparent to the scintillation photons created, there can be two processes causing photon attenuation length: on one hand there is absorption mostly due to impurities such as water vapor. For example, 1 ppm of H_2O in liquid xenon is likely to absorb almost all scintillation light under 10 cm [156]. On the other hand photons can undergo Rayleigh scatter elastically.

Lastly, the light collection efficiency is highly dependent on the reflectivity of VUV light inside the detector. Therefore, high attention is put on the PTFE reflectivity as it cover the biggest surface area in contact with LXe. Although generally can depend on the angle of incidence, PTFE has been found to reflect up to $\sim 99\%$ LXe scintillation light [126].

Detected S2 signal

The shape of the ionization signal S2 measured by PAX is determined by the interplay of several single electrons created in close proximity, drifting and diffusing in their way towards the PMTs after having escaped recombination. Having a roughly Gaussian shape, the width of these signals is

Table 3.2. Drift velocity v and diffusion constant D in XENON1T, calculated for different nominal drift fields. These values were consulted in [109].

Drift field (V/cm)	v (mm/μs)	D (cm^2/s)
155	1.482 ± 0.003	19.2 ± 0.7
134	1.456 ± 0.003	21.9 ± 0.8
124	1.440 ± 0.003	22.8 ± 0.8
93	1.371 ± 0.003	26.8 ± 0.9

composed by different features: the drift velocity and electrons diffusion through the detector, the trapping of electrons at the liquid/gas interface, their drift velocity in the electroluminescence region, the singlet and triplet state lifetimes and their mean free path to produce photons in GXe.

To begin with, the drift velocity of electrons will strongly depend on medium conditions, such as the LXe density, temperature, strength of the applied electric field, etc. By analyzing data taken, the drift velocity of the events originating from the cathode can be calculated as:

$$v = \frac{z_{\text{cathode}} - z_{\text{gate}}}{t_{\text{cathode}} - t_{\text{gate}}}, \tag{3.30}$$

where z corresponds to the depth know by construction and design of the gate and cathode and t is the drift time of these place.

While the cathode can be easily identified by looking into the maximum event rate in terms of depth close to -96.9 cm, the gate has to be determined by studying the change in S2/S1 ratio in terms of depth, as this quantity can indicate changes in recombination probability. As discussed in [109], under the nominal drift field of 124 V/cm, it follows that $t_{\text{cathode}} = (674 \pm 1)\ \mu s$ and $t_{\text{gate}} = (1.7 \pm 0.5)\ \mu s$. Taking into consideration the uncertainty of the mesh positions, the second column of Table 3.2 shows the mean drift velocity found for electrons inside XENON1T when having different nominal electric fields specified by the first column (assuming a homogeneous electric field).

Next, as shown in Figure 3.13, ionization electrons drifting through the TPC experience diffusion in three dimensions. Starting from a point source, a cloud of electrons is formed as the diffusional growth increases with time. Moving with the mean velocity of the cloud centroid, there are loss and gains of electrons along the way mainly due to attachment to atoms or molecules or to ionization of the medium. As discussed in literature [157], the time evolution of the electron density in the cloud can be described by Fick's second Equation, following the principles of Brownian motion, as:

$$\frac{\partial n}{\partial t} = D_{\text{L}} \frac{\partial^2 n}{\partial z^2} + D_{\text{T}} \left(\frac{\partial^2 n}{\partial x^2} + \frac{\partial^2 n}{\partial y^2} \right) - v \frac{\partial n}{\partial z} - \lambda v n, \tag{3.31}$$

where $n \equiv n(x,y,z,t)$ is the charge density of the cloud at any time or position; D_T and D_L are the transverse and longitudinal diffusion coefficients and λ represents the ionization coefficient minus the attachment coefficient. The solution to Equation 3.31, assuming that the drift occurs in the z direction

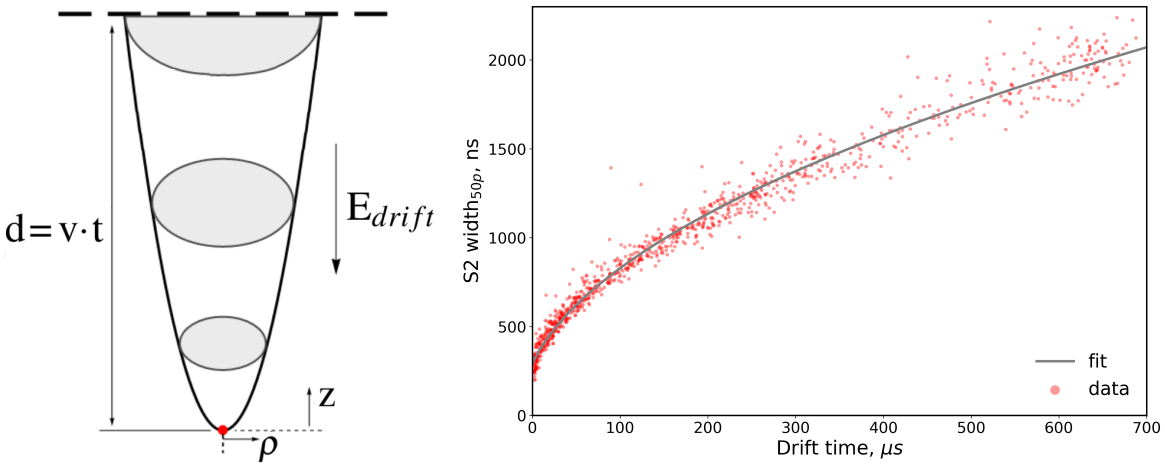

Figure 3.13. Left Illustration of electrons diffusion starting from a point source, while drifting through the medium. Adapted from [157] **Right** Background data after applying basic quality selection criteria.

when starting from a point source charge and while experiencing a constant field, is described by the function:

$$n(\rho,z,t) = \frac{n_0}{\sqrt{4\pi D_{\mathrm{L}} t}} \exp\left(-\frac{(z-vt)^2}{4D_{\mathrm{L}}t} - \lambda vt\right) \frac{1}{4\pi D_{\mathrm{T}} t} \exp\left(-\frac{\rho^2}{4D_{\mathrm{T}}t}\right), \tag{3.32}$$

where the initial distribution of n_0 electrons is treated as point like and $\rho^2 = x^2 + y^2$ is the transverse coordinate. Neglecting the transverse contribution [112] and by writing the distribution in co-moving coordinates, Equation 3.32 reduces to:

$$n = \frac{n_0}{\sqrt{4\pi D_{\mathrm{L}} t}} \exp\left(-\frac{z^2}{4D_{\mathrm{L}}t}\right), \tag{3.33}$$

which has a mean square displacement for this normal electron distribution given by:

$$\sqrt{\bar{z}^2} \equiv \sigma_t \cdot v = \sqrt{2D_{\mathrm{L}}t} = \sigma_{\mathrm{z}}. \tag{3.34}$$

As discussed in literature [158], the S2 signal shape is a convolution of the Gaussian electron distribution with an proportional scintillation distribution from a single electron. This leads to the observed S2 width defined as:

$$\sigma_{\mathrm{e}} = \sqrt{\frac{2Dt}{v^2} + \sigma_0^2}, \tag{3.35}$$

where σ_0 is a free parameter related to the single electron. In XENON1T, the measurement of the S2 width is done through the variable "range of 50% area", calculated by PAX as the time in between the 25% - 75% of the charge of the signal has arrived. Column three of Table 3.2 summarizes the diffusion coefficient D_L that can then be obtained by fitting data to Equation 3.35, once that a nominal electric field configuration is fixed.

Once that electrons reach the liquid/gas interface they have to overcome a work function barrier, for which they are assisted by a strong extraction electric field. A simplified Geant4 model built for

XENON10 [159] suggested that electrons can be modeled to be emitted from the surface following an exponential distribution depending only on the electron trapping time, found to be 140 ns. In models like NEST, the current J of these emitted electrons is modeled by the Richardson-Dushman Equation:

$$J = AT^2 \exp\Big(-\varpi/kT\Big), \tag{3.36}$$

where k is the Boltzmann constant, A is the Richardson's constant, and therefore there is a direct relation between the work function ϖ and the temperature T. Recent studies have tried to quantify the electron emission efficiency along the probability of electron emission for a single attempt or after n attempts [153]. In gaseous xenon, S2 secondary scintillation signals are generated via the direct excitation and subsequent de-excitation in the medium. These de-excitation contains both a singlet component, having this time a decay time constant of (5.88 ± 5.5) *ns*, and a triplet component with a time constant of (100.1 ± 7.9) *ns* [154]. The equivalent number of photons n_{ph} produced per ionization electron in the electroluminescence region follows a linear behavior directly dependent to the electric field E_{e} and the distance x traveled by the electron in the medium [160]:

$$\frac{n_{\text{ph}}}{x} = \left(0.140\frac{E_{\text{e}}}{\rho} \times 10^{17} - 0.474\right) \times N \times 10^{-17}, \tag{3.37}$$

where ρ is the density of the GXe.

3.3.3 Data quality and event selection

With the purpose of ensuring the quality and consistency of events found, independent of the analysis performed, specific events selection criteria, better known as "cuts", have been defined. These conditions, often motivated by technical or physical reasons, are used to reject anomalies, noise, selection artifacts or mainly to discriminate between the type or nature of an event. Summarized in Table 3.3, these cuts can be classified into three categories: basic quality cuts, consistency cuts and specific cuts for the WIMP search, outlined in green, blue and red respectively.

Basic quality cuts focus on minimal requirements on S1 and S2 signals. For instance, *Pre-PAX* conditions ensure that all events must contain a valid S1 and S2 pair, where the S1s are required to contain coincident signals from at least 3 PMTs within 100 ns. *DAQ-Veto* removes events when the data acquisition system was insensitive to trigger new events. In the same way, *Muon-Veto* removes events when the muon veto was either disabled or triggered in coincidence with the TPC. *Pre-S2 Junk* is a signal to noise condition designed to reject events that can't be analyzed due to misidentify peaks, shifted baselines or due to other effects that can cause a very large amount of signals in the waveform in addition to the S1 and S2. *S2-Tails* is a restriction on high-energy S2s, aimed to remove the tail found behind them which is composed by lots of little S2s coming from photo-ionization and

delayed electrons from extraction. Lastly, since PMT start to flash[11] frequently after too much xenon has leaked into the tube, *Flasher* removes events in a time-window before and after a flash happens.

Consistency cuts use physical models, as well as technical knowledge about the performance of the detector, in order to get rid of events with misleading topologies. For instance, the *S2 Width* cut removes several unphysical events found away from the prediction of the diffusion model discussed in Section 3.3.2. *Single electron S2* is mainly designed to suppress low-energy accidental coincidence **AC** of lone-S1s and lone-S2s events[12]: therefore, S1 candidates must not have shape properties compatible with S2 signals produced by single electrons. *S1 Max PMT* removes noisy waveforms characterized because a single PMT making most of signal, composed primarily by single electrons, after pulses, light emission, etc. *Pos-Diff* compares how different is the position reconstruction obtained for an events by using 2 different algorithms (neural network **NN** and top pattern fit **TPF** [161]). It then removes events having big differences between the positions calculated, from 2 to 5 cm, and tighter towards larger S2s where fluctuations become negligible. *S1/S2 Pattern Likelihood* are conditions used to reject events having multiple scatters or anomalous hit patterns, when compared to simulation, which would lead to a poor peak's position reconstruction quality. By making use of the ratio of area detected in the top array to the total area reconstructed, *S1/S2 Area Fraction Top* are criteria devised to identify and reject events having a bad S1 hit-pattern[13] and gas events which have a particularly high fraction of light detected by the top PMTs. Lastly, *Krypton MisIdS1* was introduced to remove ^{83m}Kr events incorrectly resolved by PAX, and possibly contaminating the ROI.

Specific dark matter search cuts are introduced so that the discrimination of the anticipated WIMP-induced single-scatter nuclear-recoil signature is enhanced. With that purpose, the *S1 Low Energy Range* and *S2 Threshold* conditions are included to allow true low energy events to be distinguished from detected artifacts or random events, while ensuring that the S1 and S2 signals are bounded to be in the ROI. Due to the low cross-section of WIMPs, only a single interaction is expected to be found inside the detector. Therefore, *S1/S2 Single scatter* cuts are introduced to allow only for a valid single interaction within a waveform. This is further constrained by *Interaction Peaks Biggest*, which checks and requires that the S1 and S2 associated with the primary interaction are also the largest S1 and S2 on the waveform. Lastly, the specification of a *Fiducial Volume* is related to the need of determining the biggest region inside the detector where its physics are well understood and data can be trusted. That means where the position/energy corrections are well defined and the anomalous background density can be reduced to the lowest, while obtaining a maximum sensitivity for WIMP masses around 50 GeV/c^2.

[11] A flash is identified by a large excess in the self-trigger rate of a single PMT in addition with a slow decrease afterwards, where the self-trigger rate stays above its mean rate before.

[12] The lone-S1 can be caused by energy deposition in below the cathode region, but mostly it has been shown to be misidentified S2s by PAX. The lone-S2s may have various sources, such as S2 after pulses, events happening too close to liquid level such that PAX is not able to distinguish a S1 from a S2, etc.

[13] In fact, for an S1 at a given interaction position, a p-value is computed based on the observed and expected top/bottom ratio and p-values < 0.001 are rejected.

Table 3.3. Overview of the selection criteria used in the dark matter search for XENON1T.

Name cut	Description
Pre-PAX	Requirements for the digitizers, trigger, and data processor (signals detection efficiencies and coincidence requirement)
DAQ Veto	It makes sure to remove events containing a dead-time trigger. It has 99% acceptance for good quality background data
Muon Veto	Removes events in coincidence with Muon veto triggers and when Muon veto is off
Pre-S2 Junk	Removes events with lot of peak area before main S2 (equivalent to removing events with noisy waveforms)
S2 Tails	Checks if an event is in a tail of a previous S2, and if so, it removes the tail to avoid lots of little S2s which are noisy in general
Flasher	Removes events within a PMT flash. In addition, an extended time-window around the flash is removed as well
S2 Width	It compares the S2 width expect from the diffusion model to the one measured. It removes several unphysical events: gas events, accidentally coincidences, after-pulses
Single electron S2	Removes mis-identified single electron S2s classified as S1s
S1MaxPMT	Defines a threshold on the maximum fractional contribution of a single PMT to an S1 signal
PosDiff	Removes events with too different patterns of position reconstruction
S1 Pattern Likelihood	Rejects accidental coincident events from lone-S1 and lone-S2
S2 Pattern Likelihood	Rejects poorly reconstructed S2s, multiple scatters or anomalous hit patterns
S1 Area Fraction Top	Removes bad S1 hit pattern removal
S2 Area Fraction Top	It is designed to remove some of the gas events which get through the S2 width cut
Krypton MisIdS1	Removes events where the 32 keV S1 of ^{83m}Kr decay is identified as an S2. These events appear above the ER band since the S1 is from the 9 keV decay, but the S2 is combined for a 41 keV event
S1 Low Energy Range	Energy selection: cS1 in (0, 200) pe
S2 Threshold	S2 energy at which the trigger is perfectly efficient: 200 pe < s2
S1 Single scatter	By checking if an alternate interaction exists between the main S2 and an S1 which is not the main S1, reduced a population to only single interactions
S2 Single scatter	Crucial for discriminating neutron background from WIMP signals (i.e. removing double scatters)
Interaction Peaks Biggest	Ensures that the main peak is larger than the other peaks
Fiducial Volume	**1 t** $-92.9 < z < -9$ cm $\mid x^2 + y^2 < 36.94^2$ cm^2 **1.3 t** Based on the spatial distribution for z vs R^2 of background rate

Chapter 4

Signal Corrections and Energy Calibration

A crucial task that dark matter particle detectors have to overcome is to find an appropriate procedure to calibrate the response of their instrument, primarily focusing on low recoil energies below 100 keV where WIMPs are expected. Since this response can vary significatively depending on the location within the detector [138], the XENON Dark Matter Project has adapted the use of the metastable short-lived isomer ^{83m}Kr, as it has been employed successfully to calibrate the time projection chamber of the ALICE detector at CERN [162], as well as large efforts such as the Large Electron-Positron Collider [163] and others. This chapter presents the usage of ^{83m}Kr as calibration source in the context of XENON1T (section 4.1), along with several applications that follow from its use, including the characterization of temporal and spatial variations in the scintillation and charge signal, position reconstruction of events and the corresponding corrections that can be derived from the observed signals variations (section 4.2). The corrections defined will thus lead to an improved discrimination of particles and energy reconstruction inside the detector (section 4.3).

4.1 Use of ^{83m}Kr as a Calibration Source

^{83m}Kr's first usage as a calibration source goes back to DELPHI [164] and ALEPH [165], followed by ALICE [166], STAR [167], and subsequently by experiments looking to measure the tritium spectrum at its endpoint, such as Troitsk [168] and the KATRIN experiment [169]. Since its initial demonstrations in LXe, ^{83m}Kr response in dual-phase detectors has also been explored in detail [170], making it a clear choice for a calibration source in XENON1T due to all the advantages discussed next. First, as illustrated in Figure 4.1, ^{83m}Kr is produced by the decay of its parent isotope ^{83}Rb via electron capture **EC**. Within picoseconds [138], any excited state into which ^{83}Rb has decayed de-excites to reach the isomeric ^{83m}Kr state. Then, ^{83m}Kr is expected to diffuse uniformly through the detector volume as it decays to a stable state with a half-life of 1.83 h. While it decays, it undergoes through two subsequent states with energies of 32.1 and 9.4 keV respectively, whose transition has a

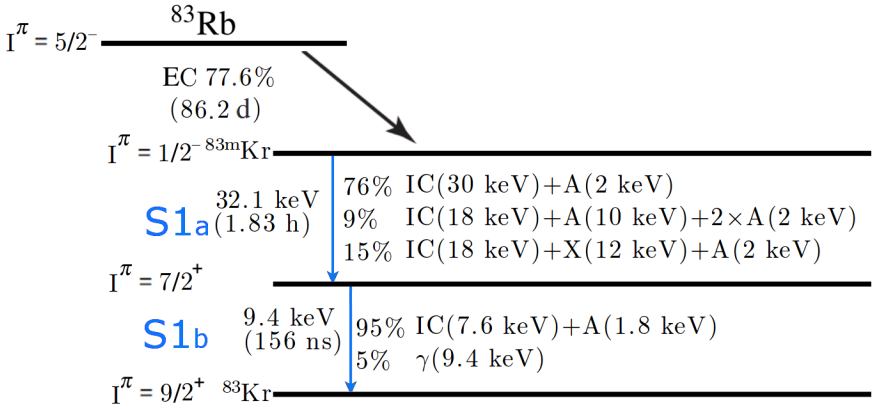

Figure 4.1. Decay scheme of ^{83}Rb and branching ratios of ^{83m}Kr. The decay proceeds in transitions of 32.1 and 9.4 keV respectively. In blue are the labels assigned to the signals identified by an specific pairing algorithm designed for ^{83m}Kr events (section 4.1.1). Adapted from [174, 138].

half-life of (156.94 $\pm$ 1.1) ns [171]. Overall, the decay modes carrying the majority of the energy are internal conversion **IC** and Auger electrons **A**, which results in a high concentration of decay energy into electron modes. In addition, with a lower probability, a small amount of the energy is also carried by γ-rays and X-rays. The low energy electrons and photons produced in the decay process will deposit their energy within $\mathcal{O}(10\ \mu m)$ with respect to their decaying vertex [172], which entails a full detection of the signals given the position resolution efficiency is in the order of 2-7 mm (z-position), while 1-2 cm (X-Y position), considering that the PMT diameter is 7.62 cm [173]. However, the signals wont be distinguishable such that only the 32.1 keV and 9.4 keV lines are measured.

The most important characteristic ^{83m}Kr is that in the context of data taking, its short half-life has as advantage a fast turnaround time following its use. This means that data to calibrate the detector can be obtained in a matter of hours and the acquisition of science data can be resumed right away without needing a special interventions to clean any contamination. Also, due to the size of the XENON1T detector and its high self-shielding efficiency, external ER sources can not reach the most inner target in the detector. Thus, ^{83m}Kr is ideal because entering as a dissolved source into the detector, it mixes very well in xenon (this is conveniently accomplished given the capabilities in XENON1T to release ^{83m}Kr doses when required). For all these reasons, in addition to the fact that ^{83}Rb source has been demonstrated not to pose any significant risk of contamination [174], ^{83m}Kr has been selected as one of the main calibration sources for the XENON Dark Matter Project.

4.1.1 Source and Flow

To release ^{83m}Kr calibration doses of a specific activity and duration, XENON1T makes use of a solution of ^{83}Rb produced at the Nuclear Physics Institute of the Academy of Sciences of the Czech Republic [175]. By employing zeolite beads, which are microporous aluminosilicate minerals well suited to trap ^{83}Rb due to their well defined pore sizes [176], a ^{83m}Kr/^{83}Rb source was prepared by absorbing part of a ^{83}Rb solution until achieving desired activity requirements, and it was later

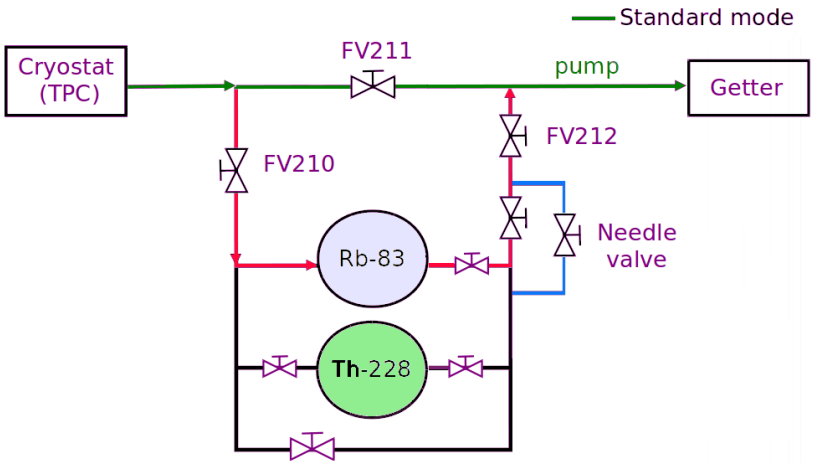

Figure 4.2. Simplified instrumentation diagram illustrating the ^{83m}Kr source (blue background) and its setting for a controlled injection through the purification system to the detector. The injection path (red) starts on the main xenon circulation path after the cryostat (green) and ends on the pump inlet. An additional line connected to a needle valve (blue) is used to further regulate the injection of the ^{220}Rn source.

installed in the gas circulation system as illustrated in Figure 4.2. This simplified diagram illustrates the basic setting in which the injection of the ^{83m}Kr source is controlled, while ensuring no release of ^{83}Rb atoms.

XENON1T started science data taking in October 2016 and continued until January 18. 2017, when a 5.7 magnitude earthquake temporarily disrupted the detector operation (named as Science Run 0 **SR0**). After a brief down time, the detector began science data again on February 2, 2017 and continued until February 24, 2018 stopped due to a power outage (named as Science Run 1 **SR1**). During the extend of both science runs, the detector often collected data in dark matter search mode, but also calibration data was taken to characterize periodically the detector response. Due to the advantages of using this source, every ∼2.5 weeks during the dark matter campaign calibrations using ^{83m}Kr were performed.

4.1.2 Characterization of ^{83m}Kr events

In order to estimate the efficiency of the S1 classification for ^{83m}Kr events, simulated data is needed. However, in order to rely on simulated data it is crucial to check if the simulated S1 signals resemble the S1s seen in the data. For this reason, XENON1T has developed a waveform simulator called **FAX**, that reproduces the response of hardware (PMT, digitizer etc.) and software (peak finding/clustering/classification/pairing algorithm etc.), to the PMT detected signals. Furthermore, it has the implementation of realistic gain, noise, PMT after pulse, photo-ionization after pulse models, and PMT hit and light collection efficiency maps [177].

Consisting of 1561 real data S1s and 3120 simulated S1s, Figure 4.3 shows a comparison of simulated and real ^{83m}Kr S1 waveforms using FAX, by presenting the average normalized sum waveforms for the 32.1 and 9.4 keV ^{83m}Kr S1s, aligned by their maximum sample (gray regions are

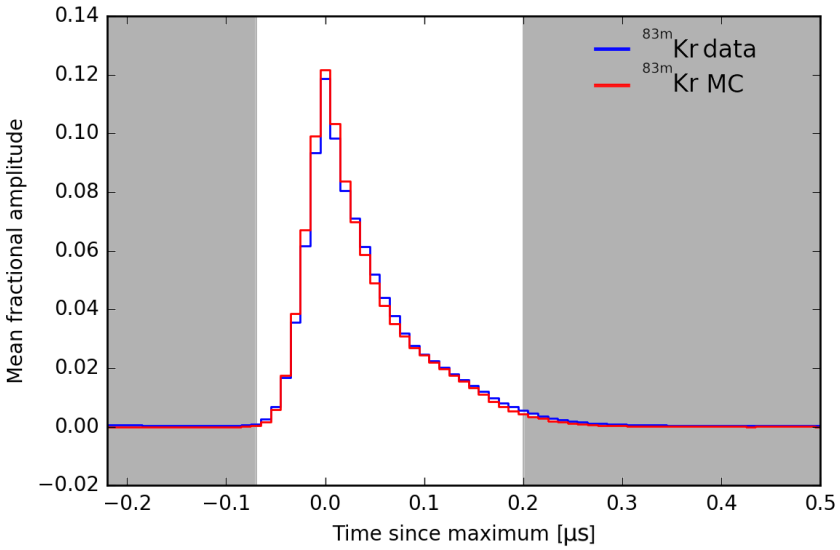

Figure 4.3. Comparison of S1 shape between simulated/real ^{83m}Kr waveforms. Adapted based on [177].

not included in the normalization integral). Although FAX is still in the transition of moving away from being an effective S1 model that does not consider the singlet/triplet of xenon response, the result show an agreement in the S1 shapes of simulation and real data. As discussed in [109], the S1 shapes do not show substantial difference at different voltages used, indicating the limitations of late-time recombination. The statistical fluctuations in the number of photons per S1 also suggest not a big influence in the shape variation[1]. Overall, the capabilities of PAX to resolve ^{83m}Kr S1 signals have been confirmed.

4.1.3 Selection ^{83m}Kr events

From the topology of the ^{83m}Kr decay, it is expected to recognize a good event PAX would need to find in a waveform a primary S1 peak briefly followed by a secondary smaller S1 peak, subsequently having one or two S2 peaks (this depends strongly on the size of the S2s and the depth in which the interaction vertex was created, given that longer drifting times lead to larger widths for S2 signals due to diffusion, translated when detection in a merged signal[2]). Since the default PAX algorithm to define interactions was optimized for WIMP-like events having only a single S1 and S2 inside their waveform, a new pairing algorithm named *DoubleScatters* was designed [178]. In the context of defining interactions and events, *DoubleScatters* approaches the tagging of ^{83m}Kr candidate events by initially time sorting physical interactions inside a waveform, demanding for a valid event to have two

[1] However, a expected difference in found when comparing the 32.1 keV and 9.4 keV peaks, as the second peak is more likely to be affected with after-pulses of the first produced peak.

[2] For instance, in SR1 a minimum distance of 4 mm is required to be resolve S2s [173]. With the typical drift velocity 1.371 ± 0.003 mm/μs discussed in section 3.3.2, two S2 signals will be only distinguishable if they fulfill the minimum time spread of 3 μs.

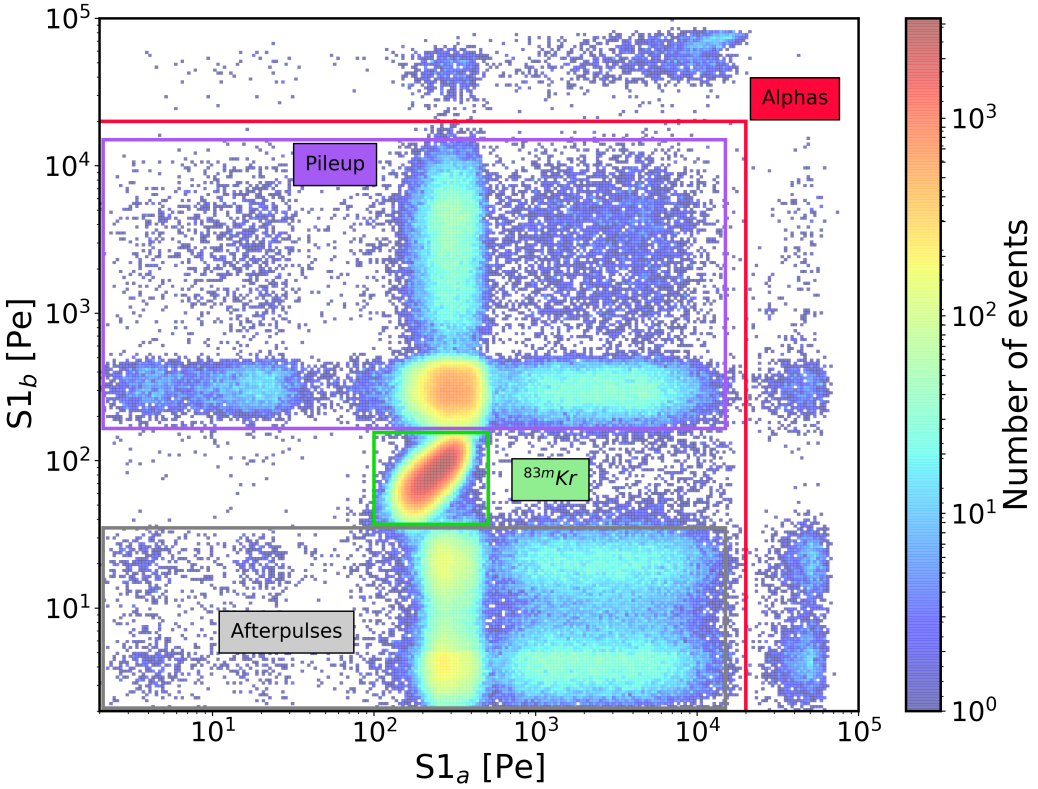

Figure 4.4. Events selection of ^{83m}Kr calibration data when employing the *DoubleScatters* pairing algorithm. The identification of different events under this approach is presented in the energy distribution parameter space for $S1_a$ and $S1_b$, associated to the expected 32.1 and 9.4 keV signals from ^{83m}Kr. The different color boxes used serve to distinguish different populations, such as afterpulses (gray), alphas (red), pileups events (purple) and most importantly ^{83m}Kr events (green).

S1s and at least one S2. Under this ordering, the first S1 peak found is labeled **S1$_a$** (meant to represent the 32.1 keV signal), while the second S1 peak is labeled **S1$_b$** (meant to represent the 9.4 keV signal).

Figure 4.4 illustrates how events are identified after using this algorithm, showing in the x-axis the energy of the $S1_a$ peak against the energy of the $S1_b$ peak in the y-axis. Several event distributions are found under this classification and therefore they have been demarcated using different colors. To begin with, events outside the red delimitation can be directly associated with alpha events (mainly recognized due to their large energy). With several populations overlaying, events inside the energy window delimited by gray are identified, from low to high energy, as: single electrons, the merged result of the two ^{83m}Kr S1s (a 41.5 keV peak), and highly energetic particles such as gammas, paired with low energy single electrons or afterpulses. Afterpulses are signal created by ionization of residual gas molecules in the PMT by accelerated photoelectrons. In principle, these positive ions drift to the photo cathode and proceed to release electrons and create an afterpulse[3]. Furthermore, as different studies shown [179], afterpulses can be classified in different categories:

[3]Experimental measurements compared to the calculated and simulated ion drift times indicate that the afterpulses found mainly in the medium correspond to: CH_4, Ne, N_2, Ar/CO_2, X^{++} and Xe.

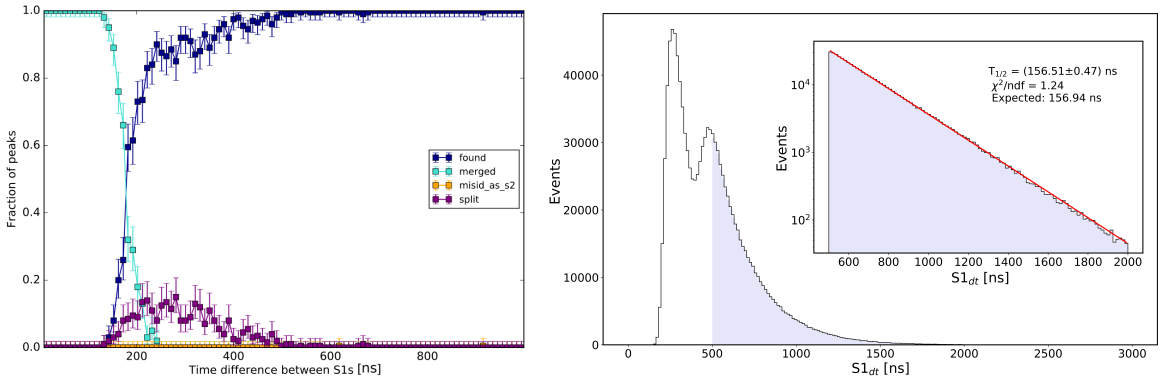

Figure 4.5. Left Performance test on the close pair of S1s produced by the 32.1 and 9.4 keV decays of ^{83m}Kr. This test assumes a light yield of 5 pe/keV and a photon detection efficiency of 0.12 [180], such that the number of photons to simulate were drawn from a binomial at 32.1 keV (or 9.4 keV)×(5 pe/keV/0.12) **Right** Determination of the half-life for ^{83m}Kr events selected.

1. Pulses with a very short time delay ($\sim$ ns) and amplitudes around 1 Pe, generated by elastic scattering electrons on the first dynode
2. Pulses with a time delay of up to several μs and amplitudes around 1 Pe
3. Afterpulses produced by photoelectrons from the trigger pulse in the volume of the PMT (mostly near the focusing grid).

Inside the region delimited by purple, going from low to high energy, there are mainly pileup events: betas, ^{83m}Kr S1s and gammas paired with delayed electrons and other gammas. Lastly, the region delimited in green contains the expected population of ^{83m}Kr events. In order to isolate these events from any background, specific selection cuts are introduced. For instance, a cut on the number of PMTs contributing to $S1_b$ distinct from the PMTs that contributed to the $S1_a$ has been imposed as it has showed to remove a significant amount of afterpulses. Next, as shown in Figure4.5 *left*, due to the performance efficiency of PAX in terms of clustering, distinguishing and splitting peaks happening extremely close in time, a time delay cut on the occurrence between the $S1_a$ and $S1_b$ signals has been found to be optimal in the range of 500 - 2000 ns, since this ensures 100% efficiency of selection. This window of time corresponds as well as to the fitting region used to cross-check the half-life of the selected events. In addition to a fiducial volume cut, events fulfilling these conditions lead to a half-life of 156.51 $\pm$ 0.47 ns, as presented in Figure4.5 *right*.

With this selection, it can be seen that ^{83m}Kr distributes uniformly inside the detector after several minutes from its injection, as shown in Figure 4.6. After the distribution is observed to remain unchanged, the activity has been assumed to be spatially homogeneous. Lastly, to further illustrate the population of detected events, Figure 4.7 presents the waveform of a typical event falling in the selection presented. From bottom to the top, the bottom panels present a zoom in of the resolved main S1 and S2 peaks from the full waveform presented in the top panel. On one hand, the event presented has two consecutive decays identified as individual S1 signals. As it was expected, this topology in

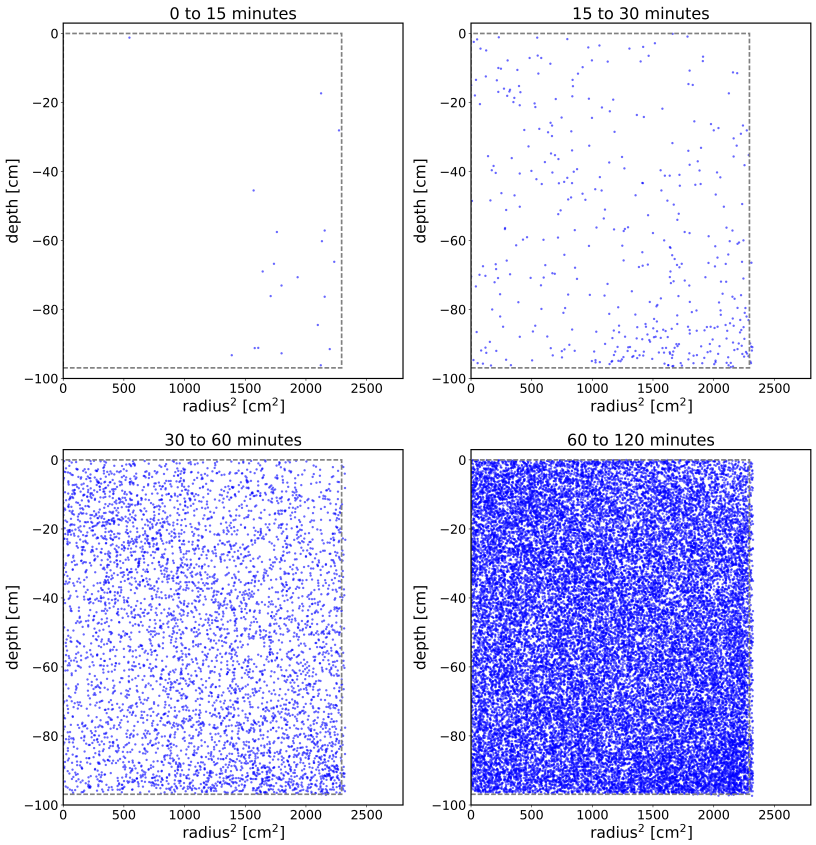

Figure 4.6. Reconstructed ^{83m}Kr events from the mono-energetic 41.5 keV energy peak at four different times after a ^{83m}Kr injection in November of 2016 took place.

the context of ^{83m}Kr corresponds to $\mathbf{S1_a}$ (32.1 keV) and $\mathbf{S1_b}$ (9.4 keV). On the other hand, because of the broadening of the electron cloud created at the interaction site due to diffusion, the two contiguous S2 signals created can not be distinguished separately, such that they result in a equivalent merged single S2 peak for most of the identified ^{83m}Kr events.

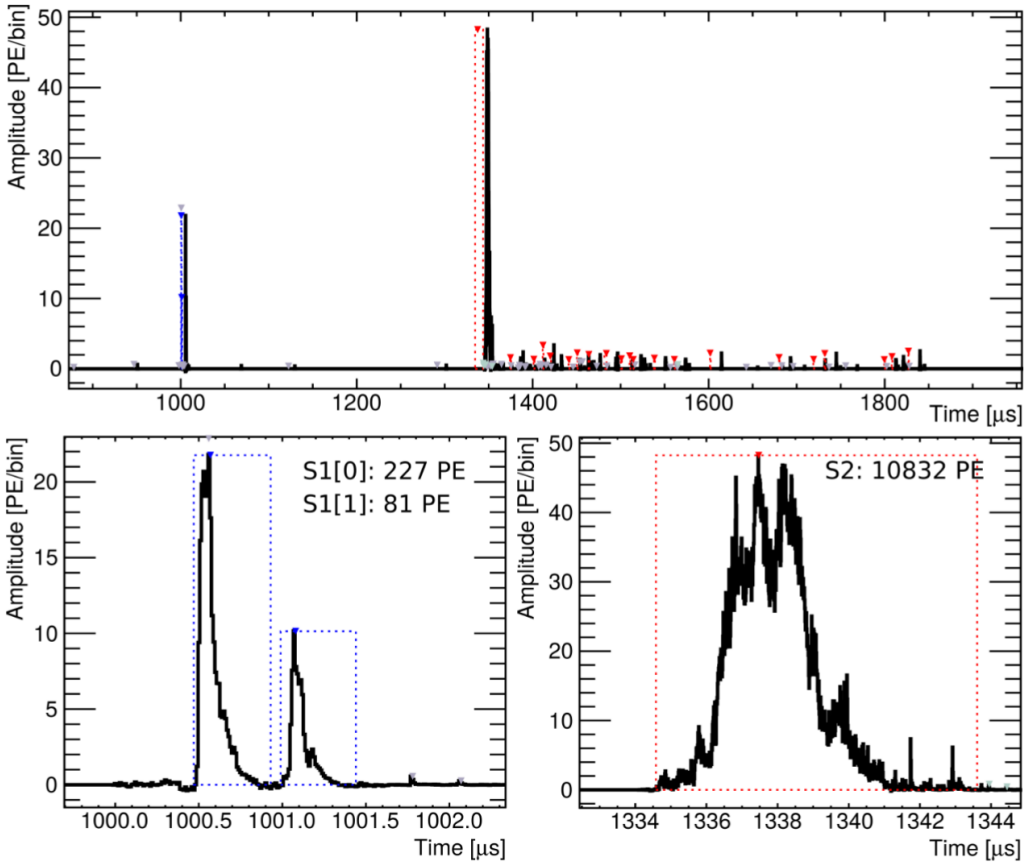

Figure 4.7. Example of the waveform of a selected ^{83m}Kr event. The waveform illustrates the detection of the 32.1 and 9.4 keV S1s signals, together resulting in a mono-energetic 41.5 keV energy peak due to the merging of the two S2 signals. Taken from [173].

4.2 Signal Corrections

The two signals detected in the XENON1T Experiment are the prompt scintillation light S1 and the delayed secondary scintillation signal S2. Since the efficiency with which both signals are measured, together with their stability and variation, determines the search energy threshold and allows a proper energy reconstruction of events, pertinent signal corrections addressing underlying effects altering their detection need to be implemented. This section describes the procedures implemented to quantify and apply position dependent corrections for the S1 and S2 signals, as they results in increased energy resolution of the S1 and S2 signal spectra.

4.2.1 S1 corrections

As discussed in section 3.3.2, not all scintillation photons originally emitted after the energy deposition of a particle end up contributing to the observed S1 signal. On one hand there are effects of attenuation associated to photons being repeatedly reflected at the PTFE panels surrounding the active volume,

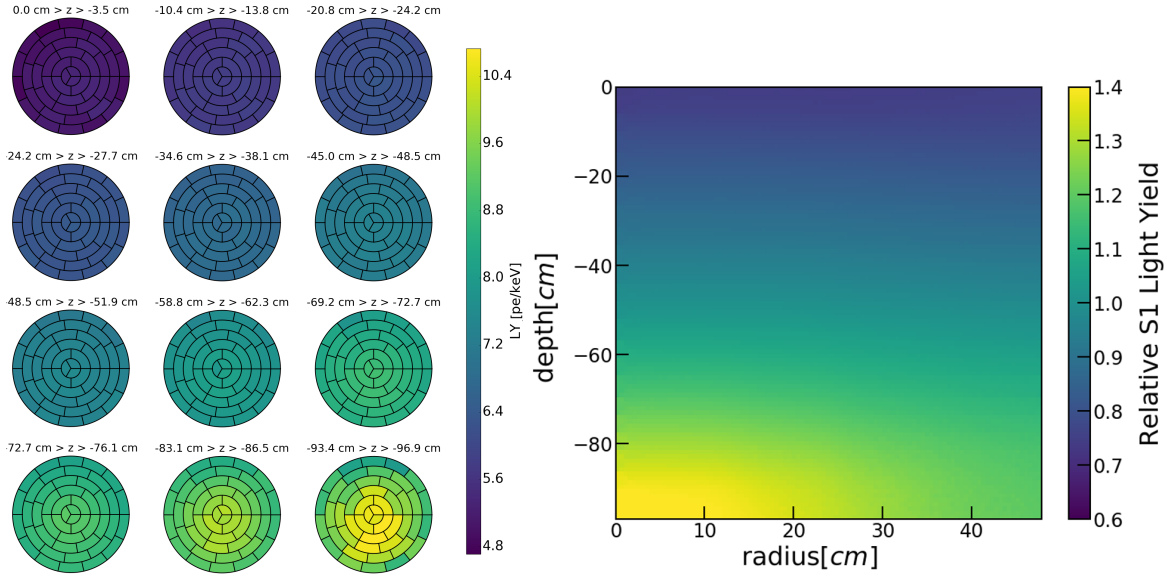

Figure 4.8. Left Several slides of light yield map from the 32.1 keV peak from the ^{83m}Kr calibration source **Right** Azimuthally averaged position dependent LCE correction derived from the 32.1 keV peak from the ^{83m}Kr calibration source. Taken from [181].

the liquid/gaseous interface or attenuation in the form of light quenching as consequence of traces of impurities in the medium. On the other hand there is a finite probability of converting all incoming photons into photoelectrons, mainly associated to the solid-angle coverage of the PMTs. The later contribution is called quantum efficiency **QE**. Although this efficiency changes from PMT to PMT, the average QE measured for XENON1T PMTs is ∼30% for wavelengths between 300 - 600 nm [145] (PMTs found with the highest efficiency are thus placed in the bottom array since the high refraction index of LXe entails that most of the light will stay inside the LXe phase).

Given that the detection of the S1 signal is limited by its collection, rather that its production, the combination of the mentioned effects is referred to as "geometrical effects". Corrections for these effects are derived from the 32.1 keV peak from the ^{83m}Kr calibration source. They are obtained by calculating the mean light yield from a Gaussian fit to the S1 distribution across the active volume, for different slices of z in discrete (r,φ)-regions, as shown in Figure 4.8 (*left*). After having calculated the light yield of each 3D cylindrical bin[4], its content is normalized by the average light yield found inside the whole TPC. This position dependent fraction of detected light is referred to as light collection efficiency **LCE**, and is used as a multiplicative correction that is applied to all S1s, depending on their position. For visualization, the azimuthally averaged projection of the LCE is shown in Figure 4.8 (*right*).

Due to the more compact PMT coverage in the bottom array of PMTs, the light collection is found to be the largest towards the central bottom PMTs and it starts decreasing in the direction of

[4]To ensure complete coverage of the active volume, the number of bins is optimized in each dimension described by limiting its maximum variation to be less than 2.5% between adjacent bins.

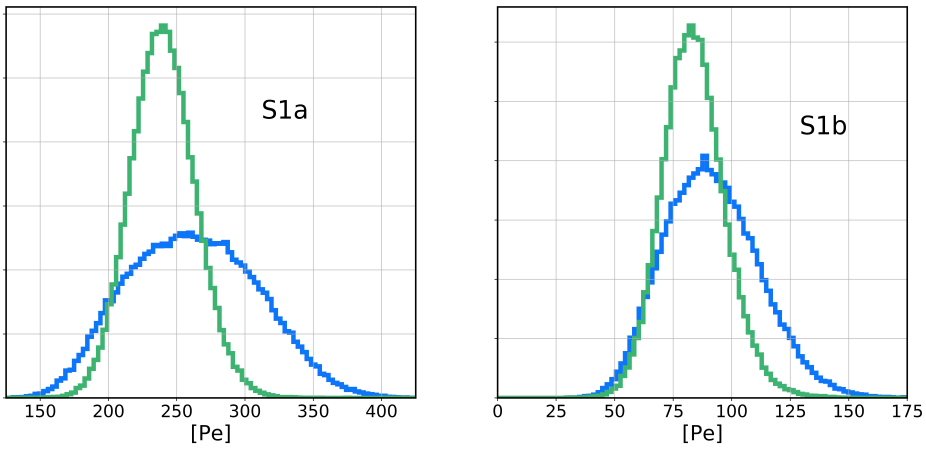

Figure 4.9. Illustration on the effect of the use of the light collection efficiency map in the two expected ^{83m}Kr signals. For both $S1_a$ and $S1_b$, each plots shows the uncorrected (blue) and corrected (green) signals obtained after the selection of events described.

larger radii and with rising z positions; i.e., the variation in light collection in the detector is mainly caused by solid-angle effects and light reflection. Additionally, the LCE performance was found to be in agreement when comparing it to results obtained from the 40 keV and 164 keV γ signals from ^{131m}Xe and ^{129}Xe, respectively, produced by inelastic neutron scattering [181]. Their homogeneous distribution in the active volume, associated to the large penetration length of neutrons, served as a convenient comparison calibration sample.

The signal S1 after the discussed corrections is referred to as **cS1**.

4.2.2 S2 corrections

Electron lifetime

Similar to scintillation photons, not all free electrons escaping recombination and traveling from the interaction site to the liquid surface end up contributing to the observed S2 signal. As these charges drift along the electrical field lines, several electrons are captured by electronegative impurities in liquid xenon such that the observed S2 signal is inevitably attenuated. As discussed in literature [112], the decrease of electrons given certain elapsed time can be described by an exponential function:

$$S2(t_d) = S2_0 \cdot \exp\left(-t_\mathrm{d}/\tau_\mathrm{e}\right), \tag{4.1}$$

where $S2_0$ is the initial S2 that would be found after measuring all the charge signal created at the interaction site. This signal exponentially decreases after electrons drift the time t_d, until reaching the liquid-gas interface. The constant $\tau_\mathrm{e} \equiv 1/k_\mathrm{s}S$, called electron lifetime, contains the information about the attachment rate k_s and the impurity concentration S.

Given that xenon is continuously purified in order to remove impurities, the parameter τ_e changes over time and it has to be evaluated periodically. Figure 4.10 *left* shows how the S2 signal decreases

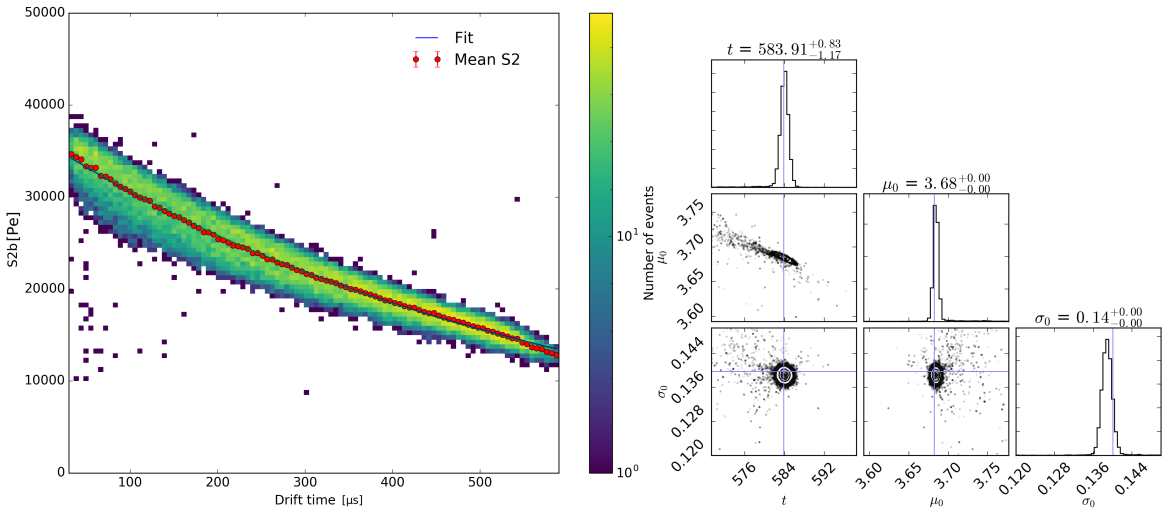

Figure 4.10. Left Visualization of the loss of electrons as function of drift time, associated to the attachment of charges to electronegative impurities as they drift towards the liquid/gas interface. The data illustrating the calculation of τ_e is the 41.5 keV peak from the combined S2 signals of ^{83m}Kr **Right** Best fit model obtained by maximizing the standard unbinned maximum likelihood using a Markov chain Monte Carlo [182].

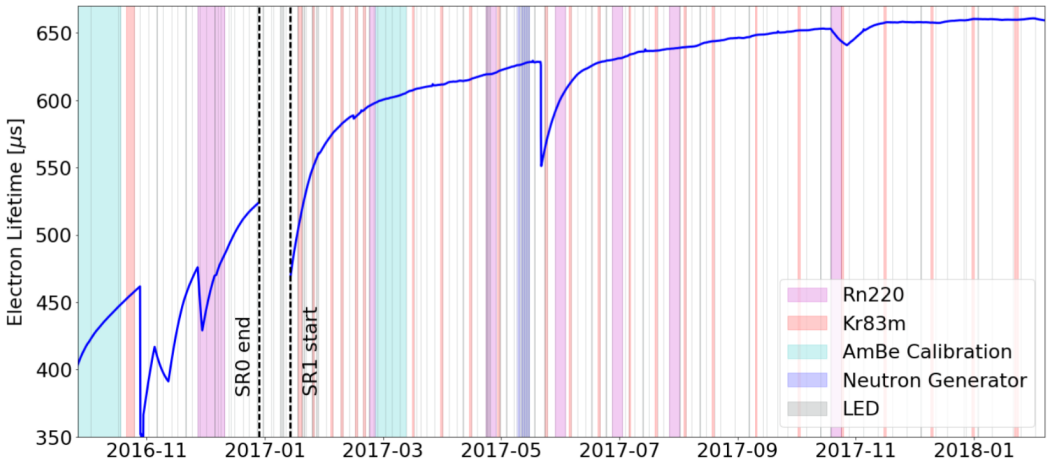

Figure 4.11. Electron lifetime evolution fit using ^{83m}Kr calibration data, and verified by alpha-decays. The drop in purity in late November 2016 was due to a power disruption. The drop in early June 2017 is from washing the gate. Some of the decreases observed around SR0 and October 2017 ^{220}Rn calibrations are associated to interventions in the system. Electron lifetime plateau occurs at ~650 μs. Taken from [183].

as function of drift time[5]. A standard approach to calculate the electron lifetime is to make several drift time slices and then compute the mean S2 area for each slice, fitting an exponential function to data while having as free parameters $S2_0$ and τ_e. A different method that avoids slicing the data, consist of evaluating the likelihood for the entire data at once, such that the electron lifetime can be find at the point of maximum likelihood. Assuming that the 41.5 keV photopeak found from the

[5]The data shown correspond to calibration data taken at the end of February 2017. The selection of events was obtained after implementing a 1 tonne cylindrical fiducial volume, demanding R <36.94 cm, -92.9 cm <Z < -9 cm.

merged ^{83m}Kr signals is a Lorentzian, the best fit model can be obtained by maximizing the standard unbinned maximum likelihood:

$$L(\tau;\mu_0,\sigma_0) = \sum^{\text{events}} \text{Lorentzian}(\text{loc} = \mu_0 \cdot S2(t), \text{scale} = \sigma_0 \cdot S2(t)) \tag{4.2}$$

where μ_0 and σ_0 are the photopeak mean size and width at zero drift time, while t is the drift time. Finding the maximum likelihood is equivalent to minimizing the negative log-likelihood. The results of the fit are shown in Figure 4.10 (*right*), in a corner plot illustrating the marginalized likelihood in every 1- and 2- dimensional subspace of the parameter space.

By following the procedure discussed to calculate the electron lifetime, its evolution throughout SR0 and SR1 is presented in Figure 4.11. Here the points in black indicate the measured τ_e at every ^{83m}Kr calibration, while the green band shows the uncertainty of the best fit of a model created to estimate the evolution of impurity concentrations by considering several detector operational parameters [183]. The trend of the electron lifetime is modeled with the help of mono-energetic decays from the ^{222}Rn decay chain, which are observed in background data. In contrast to ^{83m}Kr, these decays provide sufficient statistics such that a value can be calculated for monitoring the trend on a daily basis. Then, the absolute values obtained from the ^{222}Rn decay chain are scaled to the electron lifetime derived from ^{83m}Kr. In terms of the trend found for the evolution of the electron lifetime, decreases can be associated to releases of impurities into the system due to changes in operational parameters or conditions, such as the variations of the thickness of the electron amplification region, changes of the xenon cooling power or in the flow of the purification system. Furthermore, the electron life time was found to reach a plateau at the end of SR1, around $\tau_e \sim 650\ \mu s$, which corresponds to an oxygen equivalent impurity concentration of ~ 0.5 ppb. At this point, improvements are limited by the flow in the purification circuit and outgassing of the materials in contact with the active volume.

S2 amplification and (x,y) correction map

There is a known dependence of the S2 signal size associated to two different effects. On one hand, at small scales, there are fluctuations induced by the PMT array solid angle coverage, tight closely to individual PMTs malfunctioning. On the other hand, at large scales, the S2 size has been found to change as function of the X-Y position where the signal is created. This is associated to the mesh-warping of the anode, where the anode and the gate mesh pull themselves closer together at the center due to the electrostatic and gravitational force[6], and a tilt of the TPC, such that there are changes on the ratio of gas gap/liquid level and sagging of the anode [185].

The correction to these effects is derived from the merged 41.5 keV peak from ^{83m}Kr signals, by fitting a 2D quadratic scaling function to the X-Y distribution of the S2 sizes, and by by fitting the electron lifetime corrected S2 distribution in bins of R and φ. Results from these fits suggest that the center for S2 signals registered by the bottom array is displaced 1.5 cm to negative x and y values

[6] This inevitably leads to reduced S2 width values in the center of the X-Y plane, given that the electrons drifting have a shorter way from the liquid/gas interface to the anode [184].

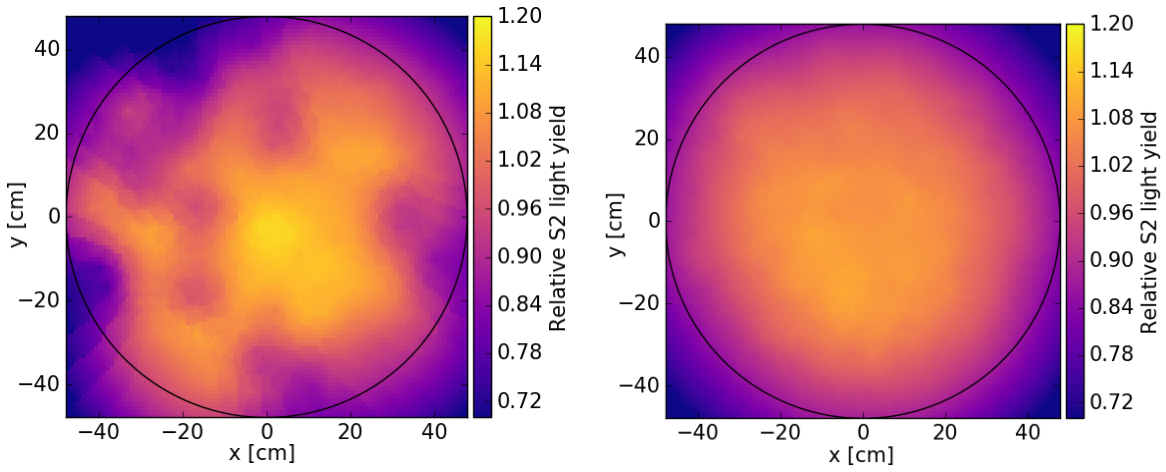

Figure 4.12. Relative S2 correction maps taking into consideration the non-uniform charge response at the **Left** top PMT arrays, and at the **Right** bottom PMT arrays. Taken from [186].

from the origin [173], confirming a slight anode sagging that reduces the electron extraction efficiency up to 20% close to the edges of the detector. The multiplicative correction map that is applied to all S2s, depending on their observed position, is shown in Figure 4.12. Through the derivation of such results, the top array of PMTs was found to have local variations at the level of 10 - 15 % level. Since the response of the bottom PMT array was found to be rather locally homogeneous, the S2 signal from bottom was used throughout SR0 and SR1 [145].

The signal S2 after the discussed corrections is referred to as **cS2**. Given that the better coverage of the bottom array of PMTs translates in a more uniform signal, the bottom component will be used throughout most of the analyses, $\mathbf{cS2}_{\mathrm{b}}$.

4.2.3 Position reconstruction

Due to the electrostatic transparency of the gate grids and cathode, the expected uniform electric field in the z-direction has an additional small radial field component whose effect increases close to the boundaries of the active volume, at high radii. These contributions have been shown to be most relevant in two parts of the TPC: below the gate grid where a region of increased field is created due to the downward leakage of the higher above-gate field, and above the cathode grid where a region of decreased field is created by the upward leakage of the reverse-field region below the cathode, just like experienced by LUX [172]. As consequence, events originally created close to the PTFE walls can be slightly pushed inwards and therefore reconstructed at smaller radii, as shown in Figure 4.13 (*left*). Due to a longer drift time, events created at deeper z will travel further radially, which explains the distribution of events measured[7].

[7] As it will be discussed in more detail in section 5.1, a non-uniform distribution of events in the X-Y plane is found as well, specially at high radii, close to the PTFE wall, accompanied with slight traces of position smearing due to PMTs turned off.

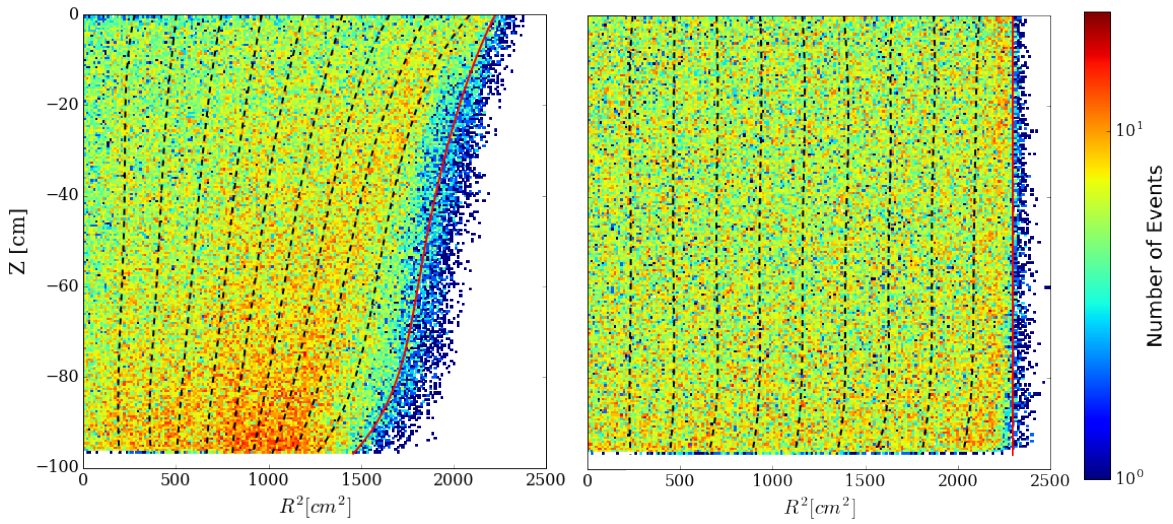

Figure 4.13. Illustration of how the radial position from observed positions using NN is mapped by using the 3D data-driven approach described, in order to define the corrected positions used **Left** The different dashed lines plot represent the distribution of 10%, 20%...90% of events in the r^2 direction, while the line in red represent the 98% equivalent detector boundary **Right** Similar distribution of events once that the position corrections are applied. Taken from [187].

In order to correct this bias, a data-driven field distortion correction method based on ^{83m}Kr data has been implemented in XENON1T. Taking as principles that the 41.5 keV ^{83m}Kr signature is radially uniform and that the field distortion affects the distribution of events only in the radial direction, data is first divided into several slices, in the three dimensions (r,z,ϕ). Given that from construction uniformity has to fulfill, the detector is segmented into 180 bins in ϕ 40 bins in z. Then, observed positions from each small slice are shifted into corrected positions such that an even spacing in R^2 is ensured. The results obtained are shown in Figure 4.13 (*right*), and just as for the LCE map, the performance was found to be in agreement when comparing it to Monte Carlo simulations and to uniformly distributed ^{131m}Xe data. In a way, this method homogenizes the observed (x,y,z) event distribution to an expected distribution (x',y',z')[8]. Lastly, as it will be discussed in more details in Chapter 5, this approach had also to be updated to consider the found time-dependent inwards position reconstruction seemingly associated to charge building up at the PTFE panels.

4.3 Energy Calibration

The corrections derived in the previous section allow to have a better estimate of the light and charge created in the TPC, which in turn opens the opportunity to reconstruct the energy of several known calibration sources in order to calibrate and understand the detector response. Furthermore,

[8]From this approach is inevitable to disentangle field distortion effects and reconstruction bias from (x,y) position reconstruction due to, for example, turned-off PMTs or different systematics, which means that they are corrected as well. However, the procedure was still used since field effects are found to be more dominant.

the characterization of the microphysics involved through these calibrations can be used to better interpret the energy spectra of the WIMP mode science data. The following sections explore the parametrization used to define a combined energy scale for both SR0 and SR1 data, along the results of its usage in terms of energy spectra reconstruction.

4.3.1 g_1, g_2 and Combined energy scale

As discussed in section 3.2.3, the gain dependent value g_1 contains information about the photon detection efficiency, while the value g_2 accounts for the combined effect of the efficiency at which electrons are extracted at the liquid/gas interface, along the number of photoelectrons detected per extracted electron. Together, these values can be used to define an energy deposition estimator independent of recombination:

$$E = W_{\mathrm{s}}^{\mathrm{min}}(E \cdot L_y + E \cdot C_y) = W\left(\frac{cS1}{g_1} + \frac{cS2_{\mathrm{b}}}{g_2}\right), \tag{4.3}$$

where $W_{\mathrm{s}}^{\mathrm{min}}$ = 13.8 eV. In the context of XENON1T, combining the response of different signatures from γ-rays in the detector allows an accurate determination of the g_1 and g_2 values by using a linear fit to the light and charge yields (this approach is known as obtaining the "Doke plot" [125]). Given that light and charge are anti-correlated, the energy deposition of mono-energetic sources appears in the energy parameter space of $cS1$ and $cS2_{\mathrm{b}}$ as tilted ellipses, as shown in Figure 4.14. Table 4.1 summarizes in green the sources selected to make the fit for g_1, g_2, along the background isotopes that can play a role on causing a slight energy offset, broadening the γ peaks and as consequence to reduced the resolution of selection due to their partial overlap to desired γ-lines.

After basic sanity of background data, the desired ellipses can be fitted with a rotated 2D Gaussian by using the following function:

$$\begin{aligned} f(cS1, cS2_{\mathrm{b}}) = A \cdot exp\Bigg(&- \frac{[(cS1 - \mu_{cS1})\cos\theta - (cS2_{\mathrm{b}} - \mu_{cS2_b})\sin\theta]^2}{2a^2} \\ &- \frac{[(cS1 - \mu_{cS1})\sin\theta + (cS2_{\mathrm{b}} - \mu_{cS2_b})\cos\theta]^2}{2b^2}\Bigg) + C, \end{aligned} \tag{4.4}$$

where the coefficient A is the amplitude, μ_{cS1}, $\mu_{cS2_{\mathrm{b}}}$ are the centers, a ans b are shape parameters quantifying the spread, and θ is the rotation angle (anti-clockwise) of the ellipse, while C is a constant associated to the background. By normalizing these two variables by the energy associated with the identified peak, the results is to have the light yield L_y and charge yield C_y. Equation 4.3 can be rearranged so that there is a linear function where g_1 and g_2 are the equation coefficients to obtain from the fit, i.e.:

$$C_y = \frac{g_2}{g_1} \cdot L_y + \frac{g_2}{W}. \tag{4.5}$$

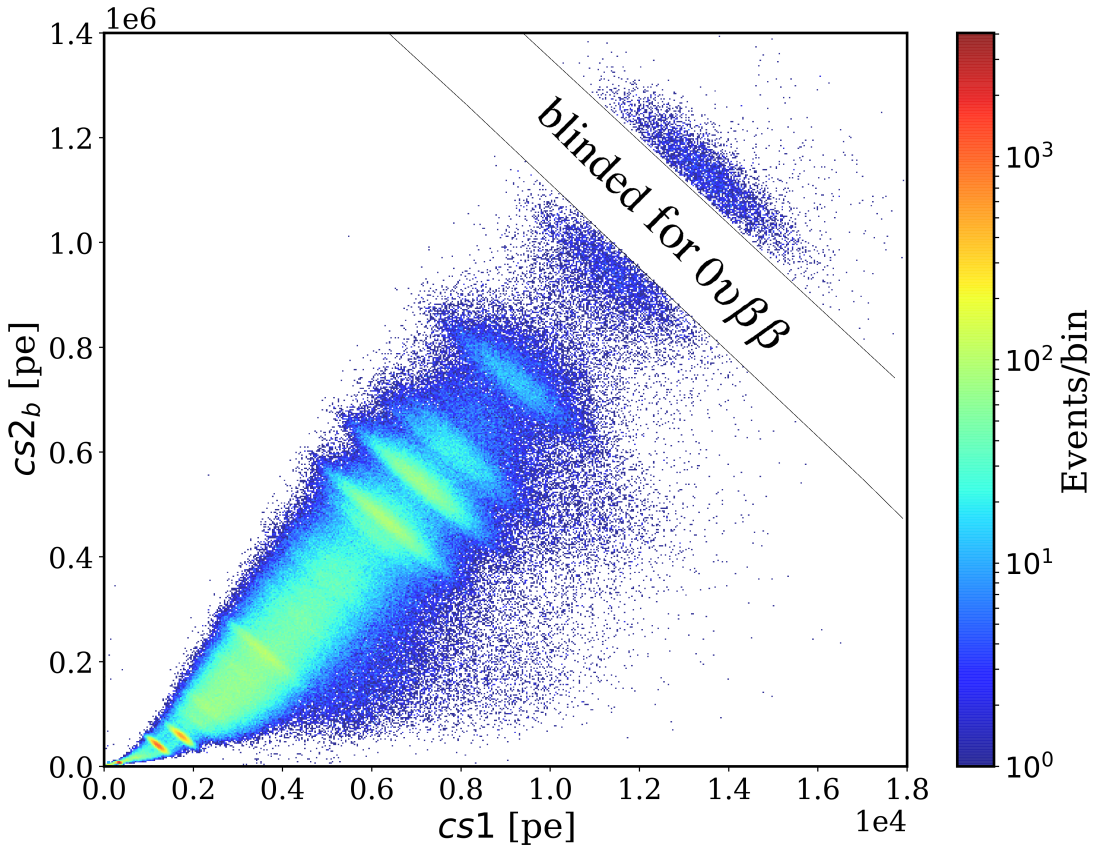

Figure 4.14. Background spectrum projected in the $cS1$ vs $cS2_b$ space. The spectrum is mainly composed by the response of different signatures from γ-rays and product of ^{238}U decay chain. Table 4.1 summarizes most of the relevant isotopes found and expected, sorted by energy. In addition, it is important to mention that not all transitions have been included, such that the sum of some intensities may be lower than 100%.

Depending on the energy, particle type and electric field applied, the light and charge yields are known to change. However, since the total number of quanta is fixed due to the anti-correlation of the signals, changes in these conditions would only move the values of the yields along a constant line in the L_y (cS1) vs C_y (cS2) space, which makes these detector efficiency parameters so useful. The result of a χ^2 fit for SR1 data is presented in Figure 4.15. From it it follows that:

$$\begin{aligned} g_1 &= (0.1426 \pm 0.0001_{\text{stat}} \pm 0.0017_{\text{syst}}) \text{ pe/ph}, \\ g_2 &= (11.55 \pm 0.01_{\text{stat}} \pm 0.24_{\text{syst}}) \text{ pe/e}, \end{aligned} \tag{4.6}$$

For this fit, only sources below 1.5 MeV were used since at higher energies the possibility of effects such as saturation can play a role in reconstruction the deposit energy after an interaction. Although an additional likelihood fit was performed, which would incorporate an extra term under the assumption that data could be systematically underestimated, both results were found to be compatible within errors. Furthermore, the systematic uncertainties of both parameters include the use of different selection cuts, mono-energetic lines for the fit and fiducial volumes. These results demonstrate that

Source	Energy [keV]	Half-life	Intensity [%]	Comments
^{83m}Kr	41.5	1.83 h	100	IC signal compound from 32.1 keV and 9.4 keV decays
^{131m}Xe	163.9	11.8 d	100	Produced by inelastic neutron scattering
^{125}Xe	221.6	16.8 h	25.4 (γ) & 88.2 (K-shell X-ray)	Signal compound from 188.4 and 33.2 keV decays
^{129m}Xe	236.2	8.9 d	100	Produced by inelastic neutron scattering
^{214}Pb	242.0	26.8 m	7.4	Product of ^{238}U decay chain
^{125}Xe	276.6	16.8 h	66.6 (γ) & 88.2 (K-shell X-ray)	Signal compound from 243.4 + 33.2 keV decays
^{214}Pb	295.2	26.8 m	19.3	Product of ^{238}U decay chain
^{228}Ac	338.3	6.15 h	11.3	Product of ^{232}U decay chain
^{214}Pb	351.9	26.8 m	37.6	Product of ^{238}U decay chain
^{208}Tl	510.8	3.053 m	22.6	Product of ^{232}U decay chain
^{208}Tl	583.2	3.053 m	84.5	Product of ^{232}U decay chain
^{214}Bi	609.3	19.9 m	46.1	Product of ^{232}U decay chain
^{208}Tl	860.6	3.053 m	12.4	Product of ^{232}U decay chain
^{228}Ac	911.2	6.15 h	25.8	Product of ^{232}U decay chain
^{228}Ac	968.0	6.15 h	15.8 + 5.0	Overlapping decays at 969.0 (15.8%) and 964.8 (5%) keV
^{214}Bi	1120.3	19.9 m	15.1	Product of ^{232}U decay chain
^{60}Co	1173.2	5.271 y	> 99.9	
^{60}Co	1332.5	5.271 y	> 99.9	
^{40}K	1460.8	1.251×10^{9} y	11	
^{214}Bi	1764.5	19.9 m	15.4	Product of ^{232}U decay chain
^{214}Bi	2204.1	19.9 m	5.1	Product of ^{232}U decay chain
^{60}Co	2505	5.271 y	< 0.1	
^{208}Tl	2614.5	3.053 m	99	Product of ^{232}U decay chain

Table 4.1. Information about isotopes used for g_1, g_2 fits, along possible backgrounds and identified energy signatures in the energy spectrum when using the CES [188].

XENON1T has a linear energy scale from keV to MeV signals. Moreover, deriving g_1 and g_2 from calibration data allows to reconstruct the energy deposition of a given event having a detected S1 and a S2 signal.

4.3.2 Energy Spectra and Resolution

Figure 4.16 shows the overall energy spectra of all energy depositions when looking in background data, inside 1 ton fiducial volume with 1 keV bins. The energy in keV corresponding to each measured

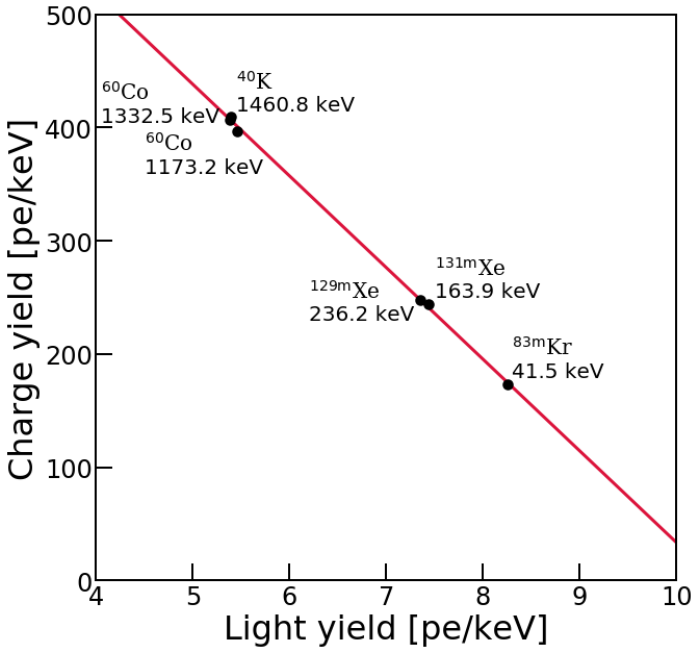

Figure 4.15. Light and charge yield from different mono-energetic peaks, corrected from position dependent effects. The fit allows to obtain the photon detection efficiency detection efficiency factor g_1 and along the efficiency factor g_2 at which photoelectrons are detected per extracted electron. Adapted from [188].

event has been reconstructed by using the CES derived from the calculated values g_1 and g_2. To calculate the rate shown, each bin has been divided by the live-time and mass of the detector volume. The spectrum showed can be split in terms of the different regions of interest where the potential to discover new physics exists. Going from low to high energies, starting at the first keV bins of energy up to $\sim$ 50 keV, this domain corresponds to the dark matter search region for the standard WIMP. Next, shown in gray, there is a blinded region restricted for analysis in order to search for the rare double electron capture signature from ^{124}Xe, expected to be found around 65 keV. Roughly inside the energy window of 90 - 2300 keV, multiple mono-energetic γ peaks from several radioactive isotopes contained in xenon or forming part from the detector material can be found. These peaks are not found completely sharp because either γ-rays deposit only part of their total energy due to Compton scattering inside, because the continuous energy contribution of β decays, or the possible continuous contribution of two neutrino double β-decay from ^{136}Xe. Due to this later rare decay, an additional blinded region has been established around 2458 keV. In blue, in Table 4.1, all isotope signatures in this energy spectrum has been listed.

Lastly, in order to quantify the discrimination of signals from background, the energy resolution of the experiment can be calculated by estimating how efficiently different sources can be distinguished. Based on the constructed energy deposition spectrum shown in Figure 4.16, the resolution can be obtained by performing a Gaussian fit to all the different mono-energetic peaks found in the cS1 vs cS2 space. Thus, dividing each of the Gaussian mean deposited energy μ obtained by each peak standard deviation σ, σ/μ, the XENON1T energy resolutions is presented in Figure 4.17. Linear or

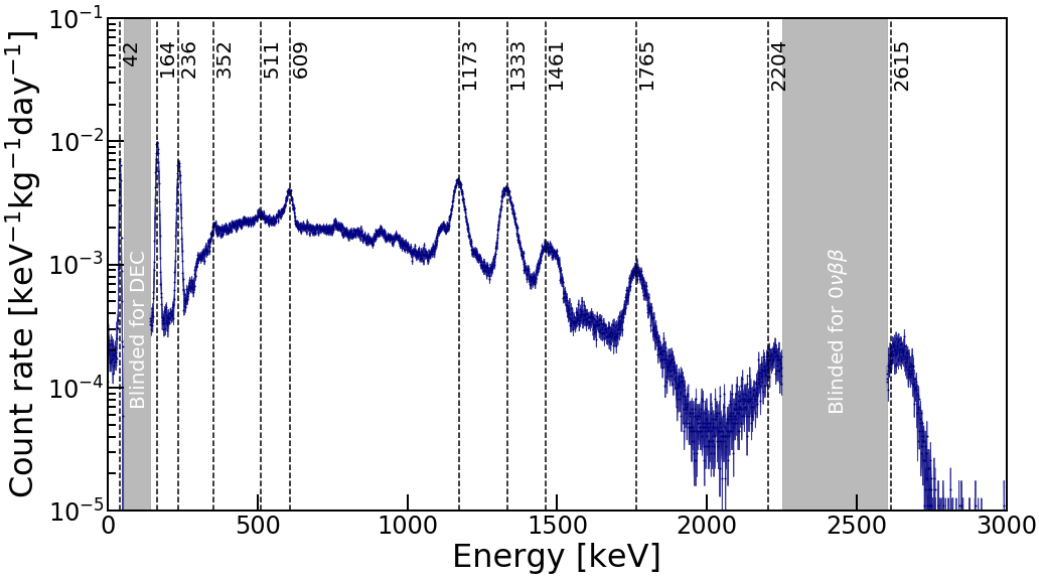

Figure 4.16. Full energy spectrum of the background data reconstructed by using the CES, defined by determining g_1 and g_2 efficiency coefficients. The gray regions correspond to the blinded locations where the signatures of the double electron capture from ^{124}Xe and the possible continuous contribution of two neutrino double β-decay ($0\upsilon\beta\beta$) from ^{136}Xe are investigated. Taken from [188].

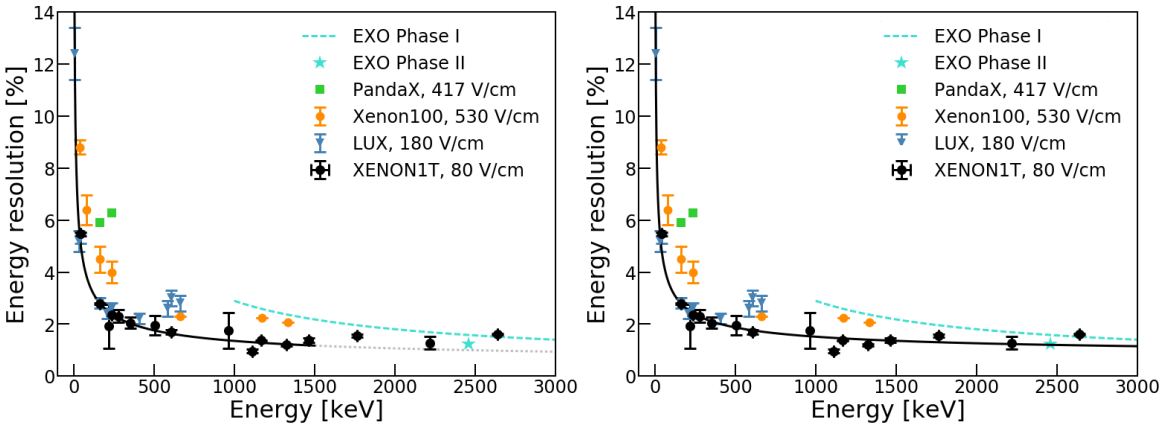

Figure 4.17. Energy resolution of the peaks found in Figure 4.16 versus deposited energy. An empirical formula is fit to the data, resulting in an improved energy resolution at higher energies deposition. **Left** Fit to 1500 keV only, gray dotted projection to higher energies **Right** Fit up to 2615 keV .Taken from [188].

exponential functions are often used to try to model the underlying background components that are included in addition to each of these peaks. Nevertheless, the fit presented up to 1500 keV is next fit by using the empirical function:

$$\frac{\sigma}{E} = \frac{a}{\sqrt{E}} + b, \tag{4.7}$$

where a = 30.98 $\pm$ 0.43 and b = 0.37 $\pm$ 0.03, excluding data points above 1.5 MeV and a = 27.30 $\pm$ 0.37 and b = 0.65 $\pm$ 0.03 including high energy data points. Furthermore, Figure 4.17 compares

the resolution at various energies for different xenon detectors. The results obtained in the context of XENON1T show a big improvement in terms of resolution at high energy depositions, mainly because as more quanta is being made in the liquid xenon, the statistical fluctuations become less prominent.

Chapter 5

Charge Accumulation

In Chapter 4 it has been explained how ^{83m}Kr calibration data is used to produce different correction for the light and charge signals as result of several detection inefficiencies. These inefficiencies arise due to different reasons. On one hand because of the solid-angle coverage of the PMTs and their quantum efficiency, the mesh-warping of the anode and tilt of the detector. On the other hand, and most importantly, as result of light quenching together with charge losses, as consequence of traces of impurities in the medium. Overall, these effects introduce a three-dimensional **3D** spatial dependency in the measured peaks area refer to as *detector inefficiencies*. During the analysis of the SR1 data, hints of under-densities at large radii in the XY plane were found to coincide with the location of the sliding PTFE panels in the TPC (a 24-fold pattern). Simultaneously, a time-dependent inwards reconstruction effect was found even after the 3D field distortion position corrections described in section 4.2.3 were applied. Furthermore, hints of electric field non-uniformity were found when inspecting the local and temporal evolution of the light and charge yield in ^{83m}Kr.

The same effects were found by the LUX experiment [189], associated with charge accumulation at the PTFE walls. There, the charge density was was found to increase from -3.6 to -5.5 μC/m^2 over the course of two years.Thus similar studies and simulations in the context of XENON1T were performed in order to confirm the hypothesis of charge presumably accumulating on the PTFEs panels. Since this phenomenon has consequences not only on important studies such as position and energy reconstruction, but also in signals corrections and therefore in discrimination of particles, this chapter is dedicated to provide a full description of all the evidence found supporting the notion of charge building up (section 5.1). This is followed by different efforts made to quantify and correct these effects for the SR1 dark matter search (section 5.2). Subsequently, different methods to estimate the time-dependent electric field are discussed (section 5.3). Lastly, a summary on the overview of the topic and the consequences from these findings is presented (section 5.4).

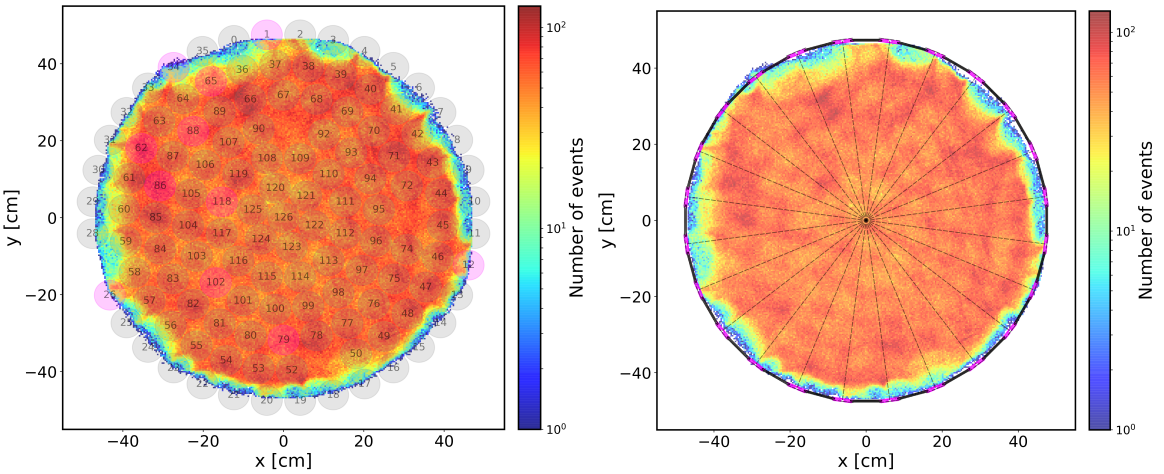

Figure 5.1. Observed XY distribution of ^{83m}Kr events reconstructed by the neural network algorithm. As described in the text, the so called bite structure appearing at large radii seems to coincide with the 24-fold PTFE array of sliding panels. **Left** Overlay of the top array of functioning (gray) and turned-off (red) PMTs **Right** Overlay of the CAD drawings, showing the locations the sliding (black) and fixed (purple) PTFE panels.

5.1 Description of non-uniform Electric Field

5.1.1 Collection of Evidence

The first indications from unexpected features related to charge accumulation followed discussions about the performance of different position reconstruction algorithms, specifically when looking into the observed XY distribution of ^{83m}Kr events, as presented in Figure 5.1 (*left*). The distribution of events found seemed to indicate periodically repeated under-densities at large radii, similar to what would correspond to partial "bites" in the data. This pattern will be refer from now on as the "bite structure". The first idea to explain this effect was to consider the influence that non-functioning PMTs could have in the position reconstruction algorithms used. In principle, XENON1T makes use of both the neural network **NN** [190] and top pattern fit **TPF** [62] algorithms in order to derive the (x, y) coordinates from events by looking into the hit pattern of the S2 signal on the top PMT array. While the NN algorithm is based on the Fast Artificial Neural Network Library [191], and it is trained by optical simulations, the TPF algorithm matches the measured S2 hit-pattern to the expected one from simulations, depending on the light collection efficiency of each PMT and based on the maximum likelihood of each specific event.

This is achieved by using training data generated with optical Monte Carlo simulations [180] which implement the known detector geometry and optical parameters via the GEANT4 toolkit [192]. Since results strongly rely on the training simulated data, it was expected that including the full information about all turned-off PMTs would explain the bite structure. However, only a few PMTs were actually inactive and not included in the simulations to produce training data. Once this information was updated, the events distribution found was not able to explain the features observed.

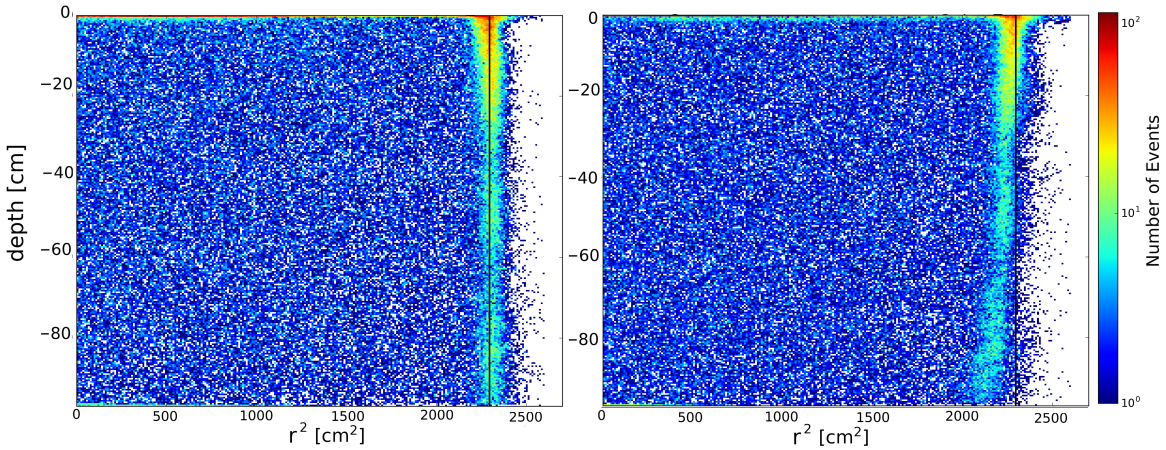

Figure 5.2. Time variation of the boundaries of the detector found in background data *after* position reconstruction corrections have been applied. In particularly, the selection of data includes ^{210}Po events whose origin is the location of the PTFE walls (see section section 6.3). This selection allows to highlight the boundaries of the TPC (solid black). The data shown was taken at the beginning of SR1, in February 2017 **Left**, and August 2017 **Right**. A time-dependent inwards reconstruction effect on the events at the wall can be recognized.

An important indication was discovered after the observed XY distribution of events was overlaid with the computer-aided design **CAD** drawings of different parts of the TPC, as illustrated in Figure 5.1 (*right*). Here fixed PTFE panels are indicated in purple, while sliding PTFE panels are highlight in black. The comparison reveals that the bite structure observed coincides with the 24-fold PTFE array of sliding panels. Thus, most of the charge in front of these specific panels seems to be either not detected or missing, opposite to what was expected from ^{83m}Kr events.

This triggered several checks on position reconstruction. As discussed in section 6.3, a complementary approach to check the boundaries of the detector is to make use of background data. Given that ^{210}Pb ions can plated-out on the surface of materials of the detector, specially in the surfaces of the PTFE walls, after decaying there is an expected alpha signature from its daughter ^{210}Po. These events can be identified exclusively at the wall and therefore can be used to trace its boundary (this approach has already been used in the past [190]). This idea is presented in Figure 5.2, for background data showing highlighting the location of ^{210}Po events after the 3D field distortion corrections were implemented. The performance of these corrections at the beginning of SR1 fulfilled all the requirements needed, as seemed for February 2017 data (*left*). However, data taken 6 month later features an inwards position reconstruction at the wall under the same field distortion corrections, as indicated by the location of ^{210}Po events in Figure 5.2 (*right*).

In order to investigate if this was caused due to an artifact of the 3D field distortion corrections, an estimation of the inward time-dependency as function of the depth was performed. To start, the distribution of events was projected along the radius squared in 10 cm slices in the z-direction, going from 0 to -100 cm. For each slice, the increase in the distribution of events due to ^{210}Po at high radii was fitted with a Gaussian function, as illustrated in Figure 5.3, for data taken on February 2017 (*left*) and August 2017 (*right*).

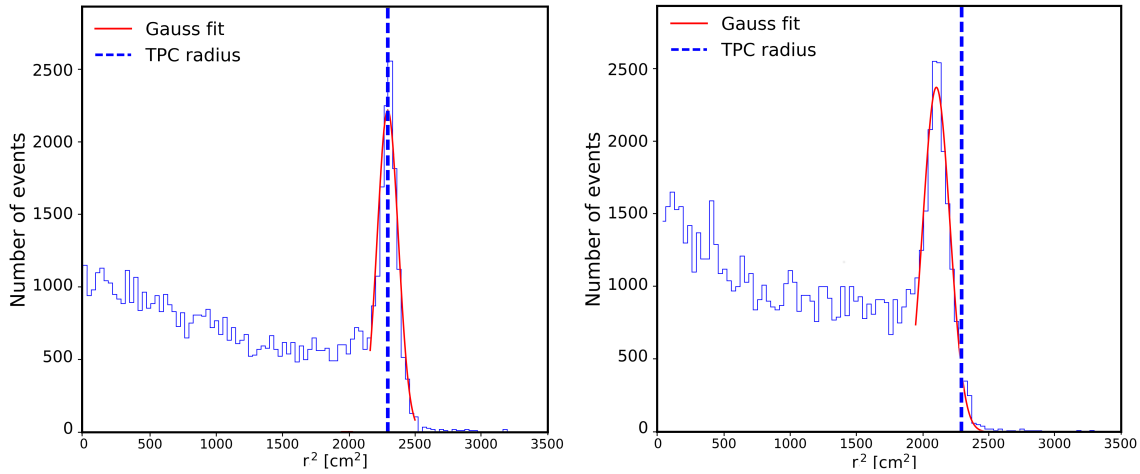

Figure 5.3. Distribution of background events as function of the radius square and depth, in order to investigate any inwards position reconstruction effect in time. Shown are two slices in the range of -50 $< z <$ -40 cm, for data taken in February 2017 **Left** and August 2017 **Right**. The fit to the distribution of events confirms a time-dependent inwards reconstruction effect on the events at the wall.

For both periods of time, the corresponding mean values from each fit and their uncertainties are showed in Figure 5.4, which covering in that way the full depth of the TPC. These results reveal that at different depths in the detector an inwards bias developing in time can clearly be found. Furthermore, at the start of SR1 the boundaries found correspond to the expected detector wall in average, as showed by the solid *red* line. However, as time progressed, the effects seen in terms of the depth are found to be different. One argument to explain this z-dependency may be related to the fact that events reconstructed deeper in the TPC had to diffused longer time.

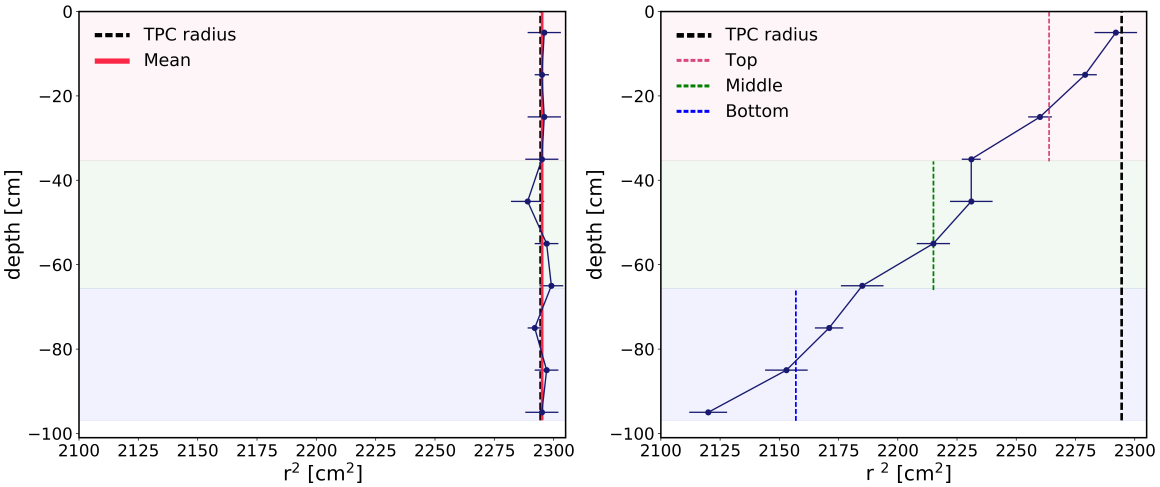

Figure 5.4. Mean radial boundaries of the detector calculated for **Left** all depth of the TPC at the same time **Right** independently in three different subsections showed in red (top), green (middle) and blue (bottom).

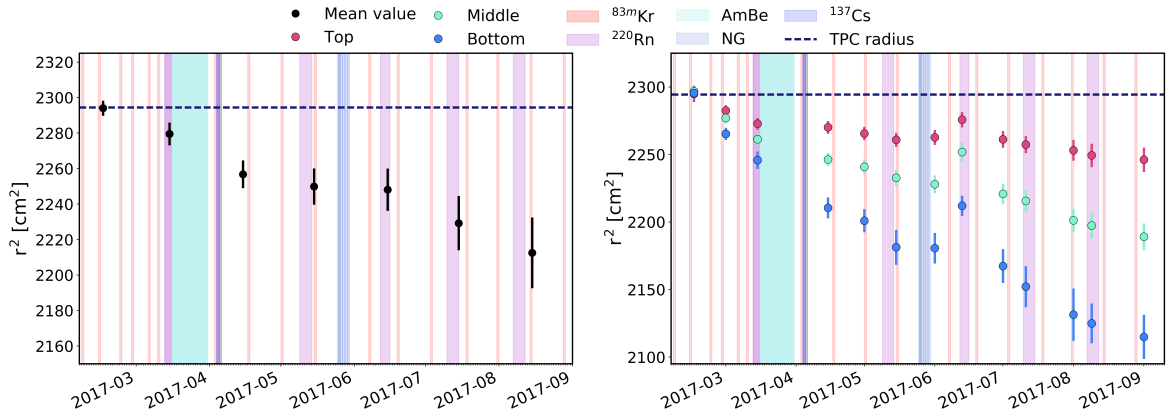

Figure 5.5. Evolution of the mean radial boundaries of the detector found for the *corrected* coordinates, calculated using the 95th percentile of distribution of the data in radius squared, along with the calibration sources used during SR1. Mean value for all depths **Left** Mean value for 3 different subsections defined at different depths **Right**.

Given that the overall bias may not be homogeneous in the z-direction, the height of the detector was divided in three different subsections to study the locality of the strength of the effect, as presented in Figure 5.3 (*right*). Here, the color dashed lines related to the *top* (red), *middle* (green) and *bottom* (blue), illustrate the mean value found in each subsections. The result indicates a bigger inwards bias at the bottom subsection, relative to what was found between the *middle* and *top* subsections. With the purpose of understanding if each subsection followed an independent evolution trend in time from the others, and furthermore in order to explore if a z-dependency can be correlated with the different uses of calibration sources, the described procedure was applied on all the available background data. The average for each month of data, from February to September 2017, is summarized in Figure 5.5. Here, the evolution of the average boundaries of the detector are presented, measured in the different subsections selected through ^{210}Po events. The evolution for the mean values of the full depth (*left*), and for each particular subsection (*right*), are shown along with the calibration sources used.

At first view, the changes do not seem to be strongly correlated with calibrations. For instance, even when there are not major interventions due to source calibrations (e.g. middle of February or April), a decrease in the trend seems to be present. This partially suggest that calibration sources don't seem to play the main role to explain the mechanism of inward bias, although this is still not straightforward to conclude as one would need to consider the energy of the interactions, the rates and the position of the calibration sources. The different subsections used for comparison show a different magnitude in the behavior of their variations. For instance, the top and middle subsections change slightly among themselves while the bottom subsection shows a stronger average change. In addition, there is an intriguing decrease in the enlargement of the average trend, found in the three different subsections around the middle of June. This will be discussed in the next section.

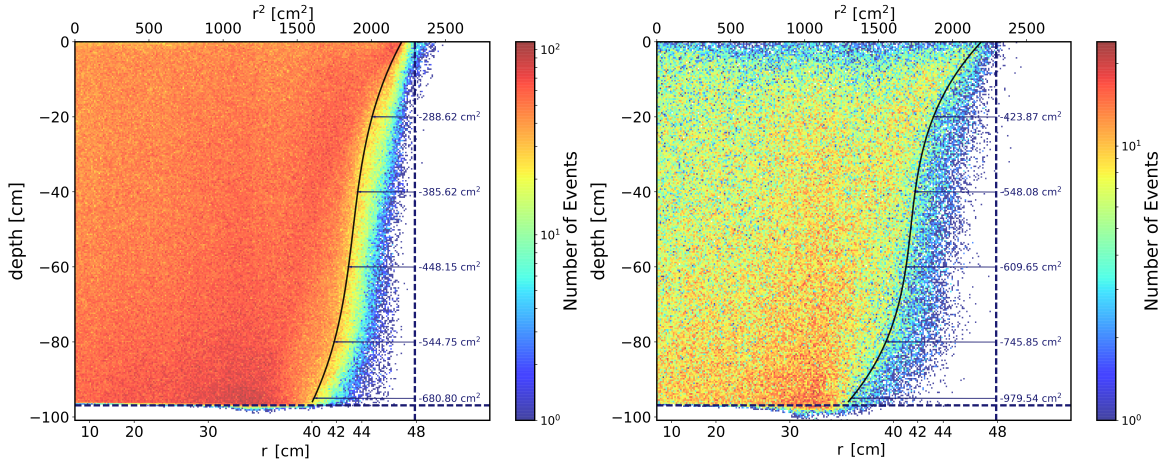

Figure 5.6. Time evolution of boundaries for NN observed coordinates. Interpolated limits from 95th percentile of events for z slices (solid black), along the TPC boundaries (dashed blue) and R^2_{95th} - R^2_{TPC} (solid blue). Several reference depths for comparison were selected: (-20,-40,-60,-80,-95) cm. Data taken in February 2017 **Left** and January 2018 **Right**.

5.1.2 Observed Coordinates

The previous studies on changes of event's positions were done after having implemented corresponding 3D field distortion corrections. Although the outlined procedure to obtain these corrections was seemly correctly done, as evidenced in the distribution of the events on February data, due to an unknown reason a time dependent effect modified the detector boundaries calculated from data. In order to trace down more fundamentally the features measured, next the attention turned into investigating the event's *observed coordinates*, which do not have corrections due to the original field of the detector. The idea was to use the observed position of ^{83m}Kr events to investigate if there were time-dependent changes resembling the results previously found, which would indicate that it was not an artifact from the position corrections proposed. Thus, as shown in Figure 5.6, events were projected in depth vs radius square and from several sliced in z, the 95th percentile of the ^{83m}Kr events was calculated (starting from -96.9 to 0 cm, in steps of 2 cm). After using a third order polynomial interpolating function to cover the full depth extend of the detector, the calculated boundaries were traced (solid black line) along with the distribution of events, the detector physical limits (dashed blue line) and the distance between the boundaries and physical limits R^2_{95th} - R^2_{TPC} (solid blue line).

In order to track down different changes in depth as previously done, several reference depths for comparison were chosen: (- 20,- 40,- 60,- 80,- 95) cm. Moreover, for a direct comparison, data from February 2017 (*left*) and January 2018 (*right*) is presented alongside. The results from the two periods compared confirmed the same features found in the events after the 3D field distortion corrections, i.e., an evident time-dependent inwards reconstruction of the detector boundaries from events at all depths. In addition to this effect, an increasing fraction of events below the cathode can be also identified. However, hints from the area fraction top of these events, an indirect indication that can be related to some event's original depth, suggests that they may be mis-reconstructed as probably the initial field

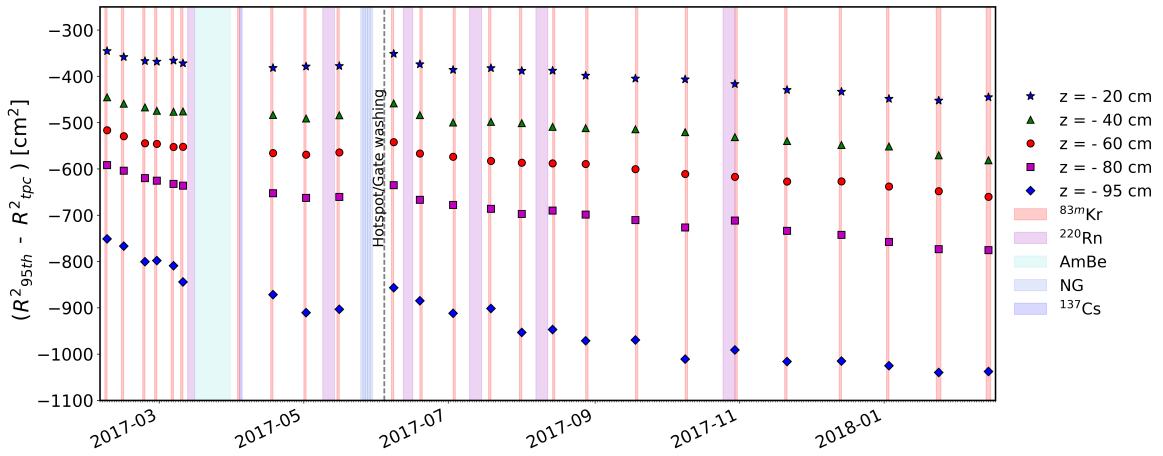

Figure 5.7. Evolution of the radial boundaries of the detector found for the *observed* coordinates at different depths, calculated using the 95th percentile of distribution of the data in radius squared, along with the calibration sources used during SR1.

surrounding the interaction vertex happened to push some electrons downwards such that a fraction of them would have a longer drift time in average until they would reach the extraction plane.

For completeness, by applying the same procedure to all the ^{83m}Kr calibrations taken during SR1, the time evolution history of the boundaries of the detector obtained from *observed* coordinates is presented in Figure 5.7. Results support the fact that the distance from the TPC wall to the 95th percentile where data lies increases progressively. Manifesting at all depths, the trend is of significant importance as it even reaches a maximum differential change of positions of 286.37 cm^2 ($\sim$17 cm) at -95 cm depth, when comparing February 2017 and January 2018 data (whereby this poses as $\sim$ -35% inward reconstruction). Two other interesting features can be recognized as well. The first one is the indication that an intervention to the detector seemingly countered the inwards reconstruction bias trend, improving momentarily the boundaries found. This can be seen for the values related to the ^{83m}Kr calibration at the beginning of June. In short, as explained in more details in the next section, background data measurements in the first days of June reveled the appearance of a *hotspot*[1] around the PMT 119, located on the top array. In order to reset to normality the rate around this PMT, a procedure called *gate washing* took place. As recognized, this is the only ^{83m}Kr calibration in which boundaries at all depths reduced the distance from the TPC wall to the 95th percentile simultaneously and significantly. The second one, in the context of section 5.1.4, is that the trend found for the inwards bias in the boundaries seems to have a close resemblance to the evolution of density charge at the walls found by LUX, as presented in Figure 5.12.

Lastly, for an illustrative way to understand more fundamentally how do these boundaries have changed, the overall XY distribution of events can be decomposed as presented in Figure 5.8. Comparing three different reference depths, corresponding to the representative distribution of the

[1] In this context, a hotspot refers to the physical location on the signal read-out (top array of PMTs), where there is a distinctive rate increase in a single or several PMTs from electrons emitted from the grids.

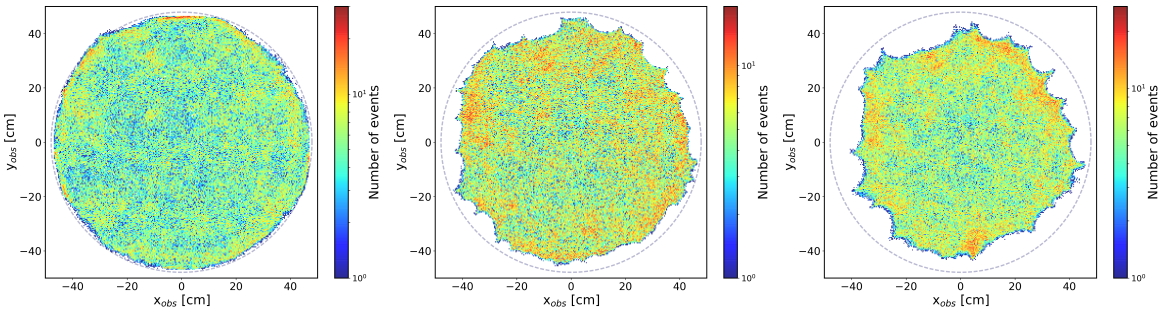

Figure 5.8. Developing of bite structure found when looking into the XY observed NN coordinates at different depths for data taken in August 2017. The reference depths to study the data are: **Left** from 0.0 to -10 cm **Center** from -45 to -53 cm **Right** from -86.9 to -96.9 cm.

(top) 0.0 to -10 cm (middle) -45 to -53 cm and (bottom) -86.9 to -96.9 cm of the detector, results suggest that the effect alters the distribution of events not-symmetrically, such that the overall change found is just the average of the center of the bites. There is no a clear explanation to this observations as the most and less smeared out reconstructed sections do not follow any pattern or periodicity, nor they coincide with the location of turned-off PMTs or to the location of external elements to the TPC, such as the position of the Neutron Generator, the source box or the inlets for the calibrations sources.

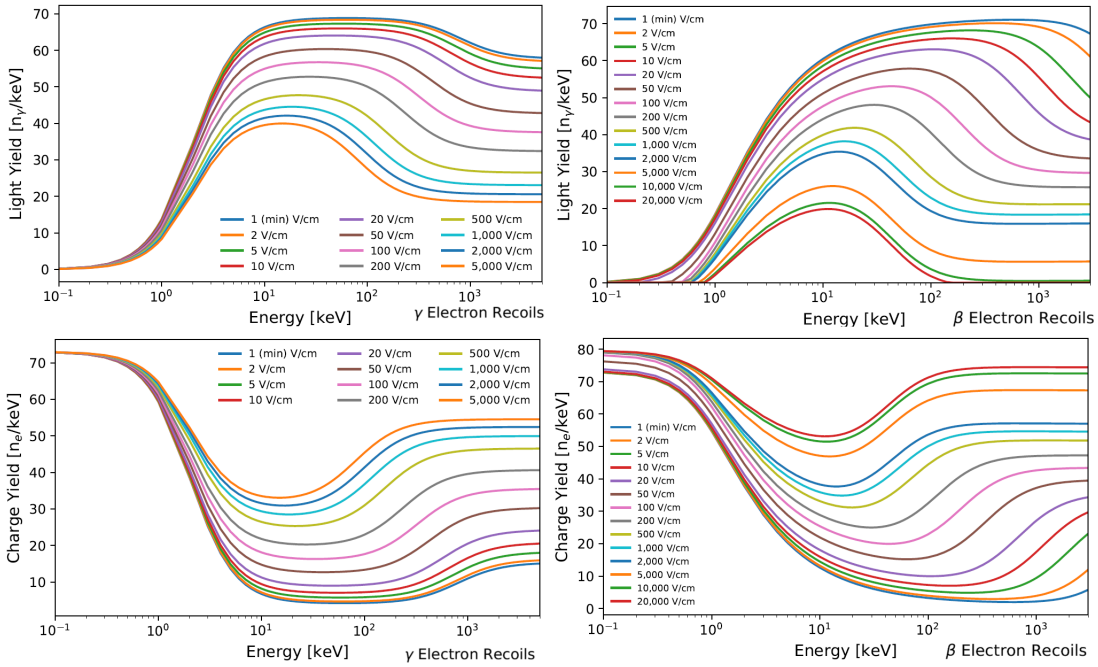

Figure 5.9. Set of benchmark plots for light and charge yields in LXe for γ and β interactions (up to date as of NEST v2.0.0). Modified from [193].

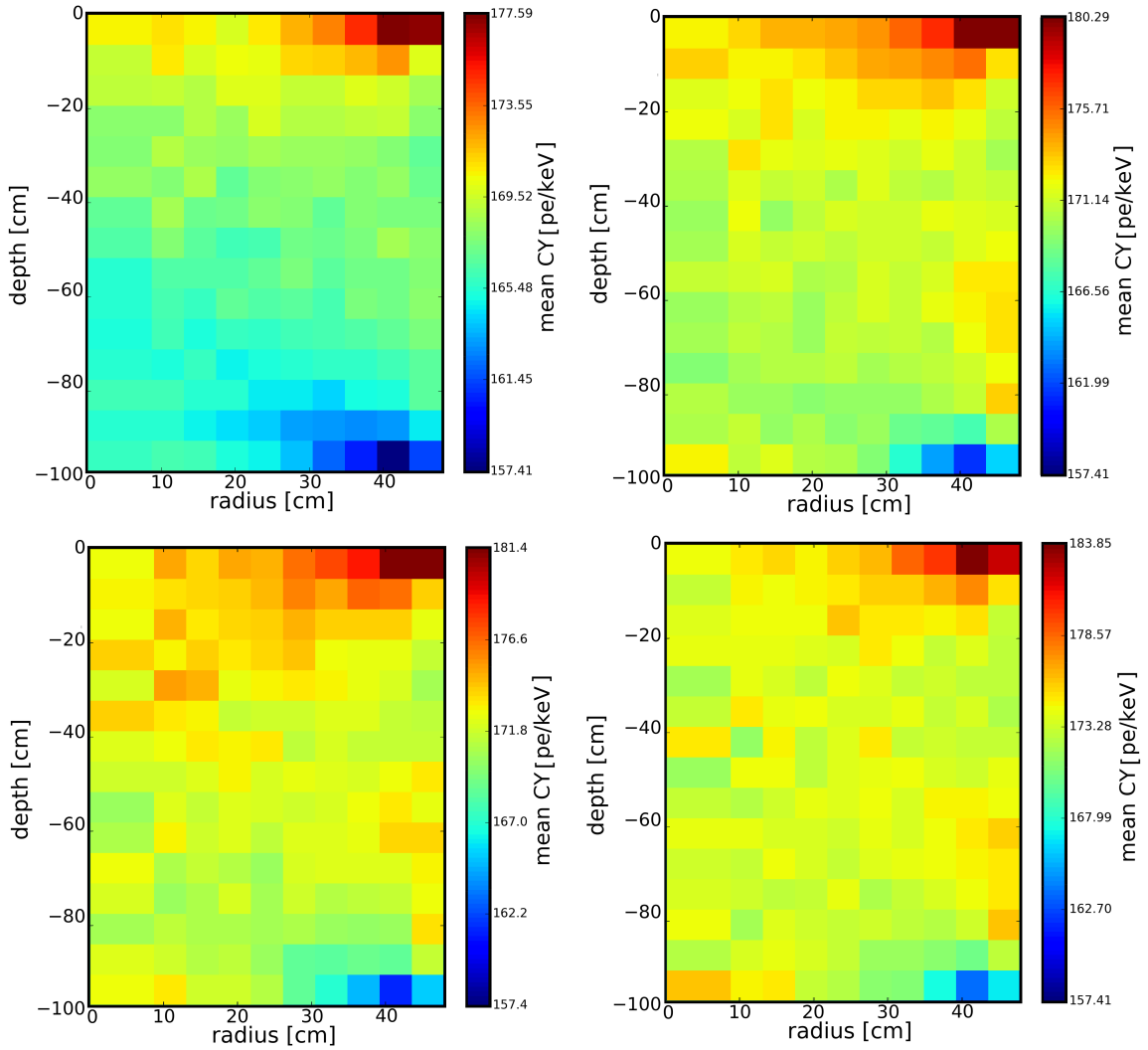

Figure 5.10. Monitoring of time-dependent changes and uniformity of the light and charge yield across the detector. This inspection was done for four different sets of ^{83m}Kr calibration data, taken at spaced times during SR1. An absolute increase in the CY changes up to $\sim 4\%$ is found, while for the LY this increments is about $\sim 2\%$.

5.1.3 Light and Charge yield time-dependency

As previously mentioned, minor electric field inhomogeneities inside the TPC are expected to arise from the design of the TPC itself, for instance, due to the electrostatic transparency of the grids. Since the electric field determines the amount of recombination, which ultimately drives the light and charge production, local yield inhomogeneities of signals can be trace down to direct changes on the field (this also depends on the energy and type of an interaction involved [139]). NEST benchmark plots presented in Figure 5.9 illustrate the interplay between the field and the light yield (expressed in terms of photons per keV), as well as the charge yield (expressed in terms of electrons per keV), both for γ and β interactions. From these relations it follows that changes in the yields are closely related to field

changes, slight in magnitude at low energies while quite significant at higher energies. Nevertheless, and most importantly, these field variations from the design of the detector are not expected to be time-dependent as the detector's integrity is not significantly modified during science data acquisition.

With this guiding principle in mind, studies related to monitoring time-dependent changes and uniformity of the light and charge yield across the detector were done. By using a grid of (12×15) bins in radius vs depth, chosen to ensure having enough event per bin while considering the position reconstruction resolution, the outcome revealed in addition to the inward bias for positions clear local average yield variations, as presented in Figure 5.10. Here 4 different sets of calibration data taken at spaced times during SR1 were analyzed. Results indicate that the magnitude of the average charge yield found slightly raised with time, reaching in six months an increment of $\sim 4\%$ (while in the case of the light yield, the increment is close to $\sim 2\%$). Furthermore, it was found that the expected uniformity of these yields does not hold as time passes but rather presents average local variations around 0.9 - 1.7%, while finding even a maximum of 6.1% close to the corners of the TPC for the charge yield and a local maximum of 1.8% for light yield.

5.1.4 LUX Experiment

All together, the preliminary hints from a bite structure in the XY plane, the time-dependent inward bias on the reconstruction of data and local changes in light and charge yield suggested a possible mechanism altering the collection and detection of events. Contemporary to these founding, LUX published a paper [189] where it was discussed that, from January to March 2014, LUX followed a conditioning campaign for the detector grids in order to improve the voltages at which the used electrodes could be biased[2]. After this campaign, evident effects on the detected distribution of ^{83m}Kr calibration data were found. As shown in Figure 5.11, a strong time-dependent bias in z and the azimuthal angle could be noticed when projecting the reconstructed radius of the detector along with the drift time (equivalent to the z coordinate). The changes found in data were attributed to modifications of the electron's drift trajectories, whose origin is related to the electric field inside the detector. As conclusion, the found time evolution of the electric field was related to the building up of electrons and holes in the PTFE panels.

LUX hypothesis is that during conditioning, VUV photons from discharges in GXe were created. Given that these photons have typically greater energies than the PTFE's band gap [195–198], the procedure lead to the creation of electron-hole pairs, localized within 1 - 2 μm of the panels [199]. Since PTFE is known to be one of the materials in the "triboelectric series" that most develops a negative charge after contact or frictional electrification [200], being able to maintain at least charge densities of 0.1 mC/m^2 [201]. And because measured energy levels of electrons (0.85 - 1.0 eV) and hole traps (0.80 - 0.90 eV) have shown a bigger energy trap in the case of electrons [199], after a standard electric field is applied to these panels in operational mode, more electrons would be expected

[2]Through this procedure LUX reported to have increased the strength of the applied anode voltage, which in turn increased the electron extraction efficiency from 49 $\pm$ 3 %, from April 21 to August 8, 2013; to 73 $\pm$ 4 %, from September 11, 2014 until May 2, 2016 [194].

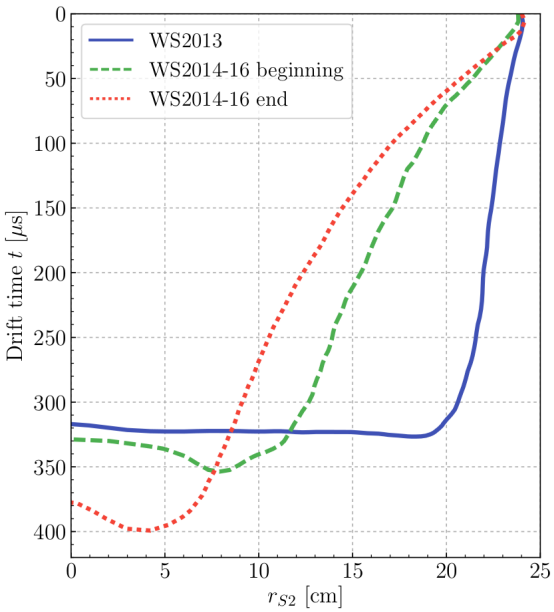

Figure 5.11. Boundaries of the LUX detector reconstructed from ^{83m}Kr calibration data. Data before conditioning is from 2013-05-10 (solid blue), while after conditioning corresponds to data from 2014-09-03 (dashed green) and 2016-05-03 (dotted red). A clear time-dependent inward bias can be identified in the detector limits derived from observed events after the conditioning campaign. Adopted from [189].

to be found due to a faster removal of holes. Figure 5.12 illustrates the charge density obtained when following this hypothesis, once that position and field changes on data are related to simulations, which in turn results on an estimation of the averaged charge over the PTFE panel surfaces inside the TPC (this will be discussed in more details in the next sections).

Overall, the effect of negative charges accumulating in the PTFE panels are expected to introduce an additional radial field component along with a z gradient, which not only would worsen the position reconstruction of events, as shown, but would also introduce time-dependent systematic effects, such as direct changes in recombination that could produce in turn an spatially-dependent S1 and S2 signals [154] and a spatially-dependent electron lifetime (due to an electric field dependency on the capture rate of electrons [202]). Features of those expected effects can be right away related to the founding presented in the previous subsections, therefore, establishing a case for the underlying effect affecting SR1 data as the result of charge building up at the PTFE panels. However, before concluding that such a similar phenomenon was being experienced in XENON1T, simulations were developed to test this hypothesis in more detail.

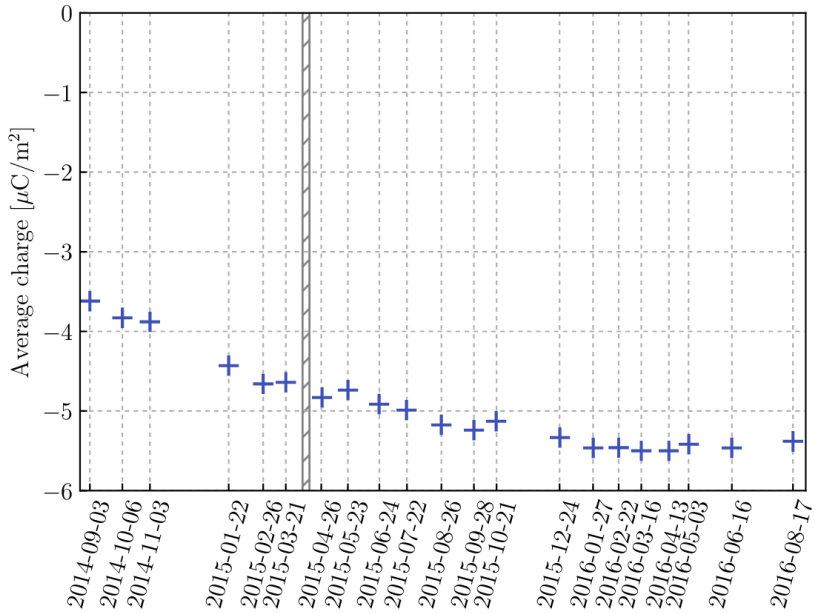

Figure 5.12. Increase of the charge density, averaged over the entire PTFE panel surfaces from WS2014-16, obtained from studying ^{83m}Kr data. Modified from [189].

5.1.5 Early indications from Simulations

Under the hypothesis proposed by LUX, that presumably charges build up at the PTFEs panels in the TPC, several observations already described in the context of XENON1T could be better understood (despite not knowing the underlying principle causing such an effect). In order to correctly react to the possibility that this hypothesis is true, in the sense that efforts on correction for data and to the underway design for the upgrade of XENON1T would have to take place, initially this hypothesis was explored based on indications of simulations. Specifically, through 2D and 3D finite element method simulation created by using COMSOL Multiphysics v5.2® [203]. The basic idea was to explore the consequences of locating charges on the PTFE panels, initially in terms of effects on the position reconstruction.

Details 2D Axisymmetric Model

The geometry implemented is based on the final XENON1T TPC CAD drawings. Given the detector's geometrical complexity and that initially a quick scan tool should not be complicated, several model simplifications were adopted while ensuring that they would produce negligible effects to the resulting drift field. For instance, details of boundaries within the PTFE volumes are omitted, as well as the cathode cable and the heat exchanger. The inner cryostat shape has been simplified while the cathode and gate grids were accurately modeled as parallel wires of appropriate spacing, thus capturing details about the electrostatic transparency of the detector. In terms of specific details of the parameters used in simulation, a 1.5% teflon shrinkage at the LXe temperature is assumed. For the dielectric constants,

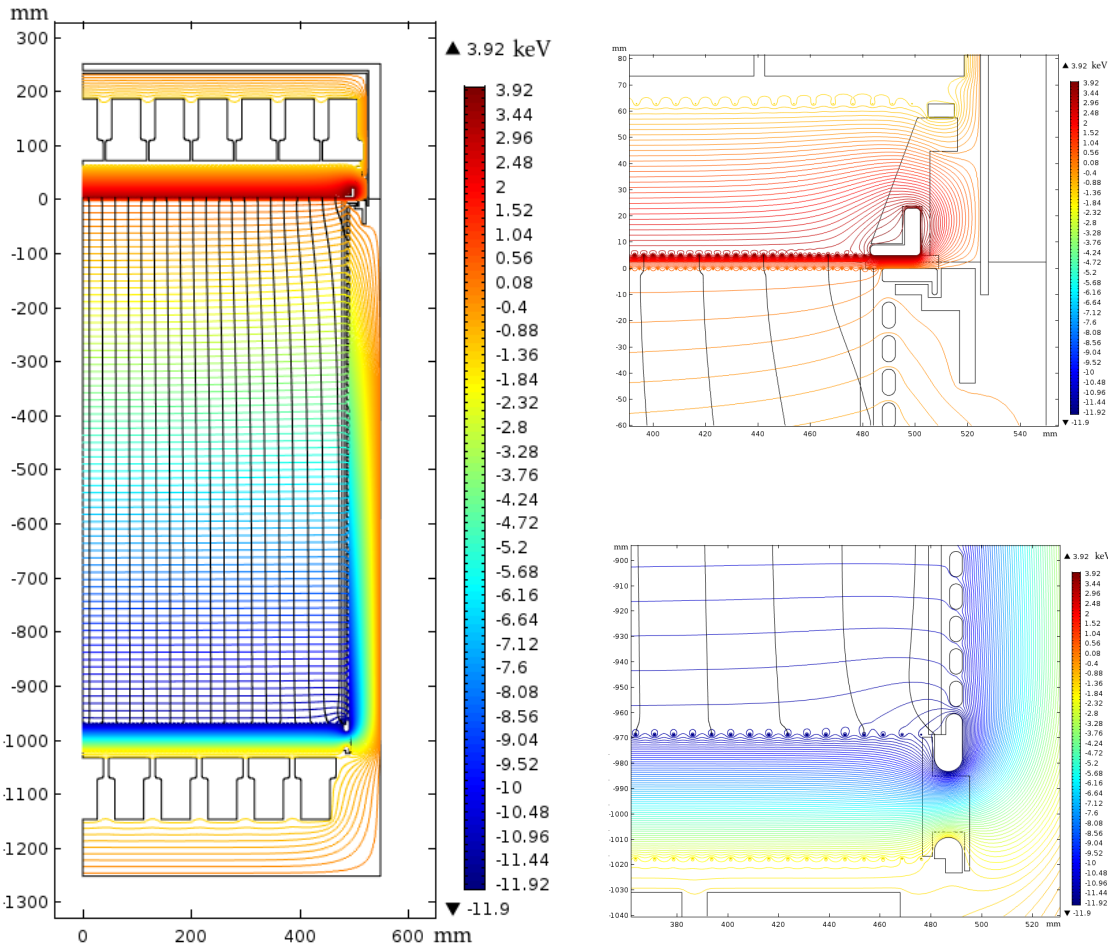

Figure 5.13. Electric potential contour and streamlines of 2D axisymmetric model used to initially investigate charge building up.

the following values are chosen: GXe = 1.00, LXe = 1.96, PTFE = 2.10. The voltages of each element used follow the description specified in each of the science run searches [145, 62][3].

Figure 5.13 illustrates the electric potential contours in kV, together with the streamlines of the field (black) obtained from the simulation created. As expected, some field distortion is visible near top and bottom corners from the design of the detector, while these effect becomes smaller towards center. The electric field simulated is then exported on a 1500×3000 grid and interpolated using regular grid interpolation functions from scipy [205], in order to have its full description in the TPC. The information derived was used next to build a framework to simulate electron-like particles, drifting along with the streamlines of the electric field found. As described in section 3.3.2, drift velocity measurements in terms of the electric field can be used to parametrize and include the field-dependence of the drift velocity of the simulated particles, as illustrated in Figure 5.14.

[3]For example, in terms of operation conditions during SR0: *Top screening* = -1.55 kV, *anode* = +4 kV, *cathode* = -12 kV, *bottom screening* = -1.55 kV, *PMT* = -1.45 kV, while grounding the gate, top ring, cryostat and the bell.

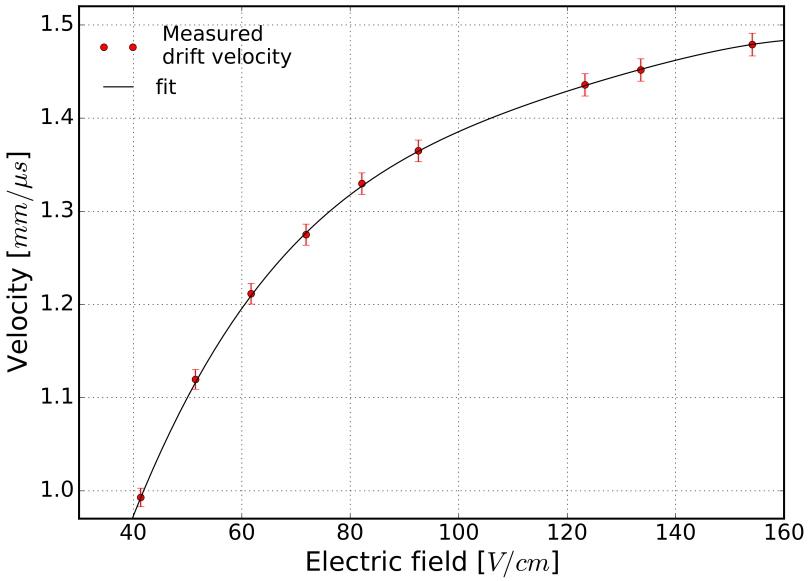

Figure 5.14. Drift velocity for electrons in XENON1T in function of the electric field. Data adapted from [204].

By using a fourth degree polynomial function, the drift velocity of electrons given a field $v_{drift}(\vec{E})$ was determined and used to iteratively define the position of simulated events, subject to follow the relation:

$$\vec{x}_{i+1} = \vec{x}_i + \frac{\vec{E}(\vec{x}_i)}{|\vec{E}(\vec{x}_i)|} \cdot v_{drift}(\vec{E}(\vec{x}_i)) \cdot dt, \tag{5.1}$$

where $\vec{x}_i$ is the position of the particle simulated at a position i, $\vec{E}(\vec{x}_i))$ is the drift electric field at the position $\vec{x}_i$ and dt is the time step used to propagate the particle, chosen to be 1 μs. The parametrization presented for the drift velocity is valid up $\vec{E} < 165$ V/cm, where a constant value of 1.50 $mm/\mu s$ would need to be assumed. Contributions from the acceleration of the charged particles are neglected in the simulation, as similar results obtained while using a Runge-Kutta 4 method for propagating particles to the one proposed through equation 5.1 showed no significant difference [206].

Once the 2D axisymmetric model was tested, the limitations of having a two dimensional model in terms of radius and depth, while pretending to reproduce features as the bite structure in XY coordinates became evident. As this simulation model can not precisely describe hexagonal meshes (anode/gate) nor straight wires (cathode/bottom screening), the wire openings of top (anode and gate) and bottom (cathode and bottom screening) were tuned to resemble and match the distribution of edge ^{83m}Kr events, as it was done in XENON100 [207]. These features will be explored in a 3D model in the next section. Nevertheless, in this 2D model the effect of the placement of charge at the PTFE wall can provide plenty of insight in terms of exploring the effect in the electric field and consequently on position distribution of events, and if can be traced an association between charges and the inward bias effects found in data. In COMSOL, either the full element simulated or a partial segment of it can have related a density charge. In order to prevent simulation errors due to an unphysical behavior where two PTFE segments meet, a smoothing linearly falling charge density approach was used, i.e.,

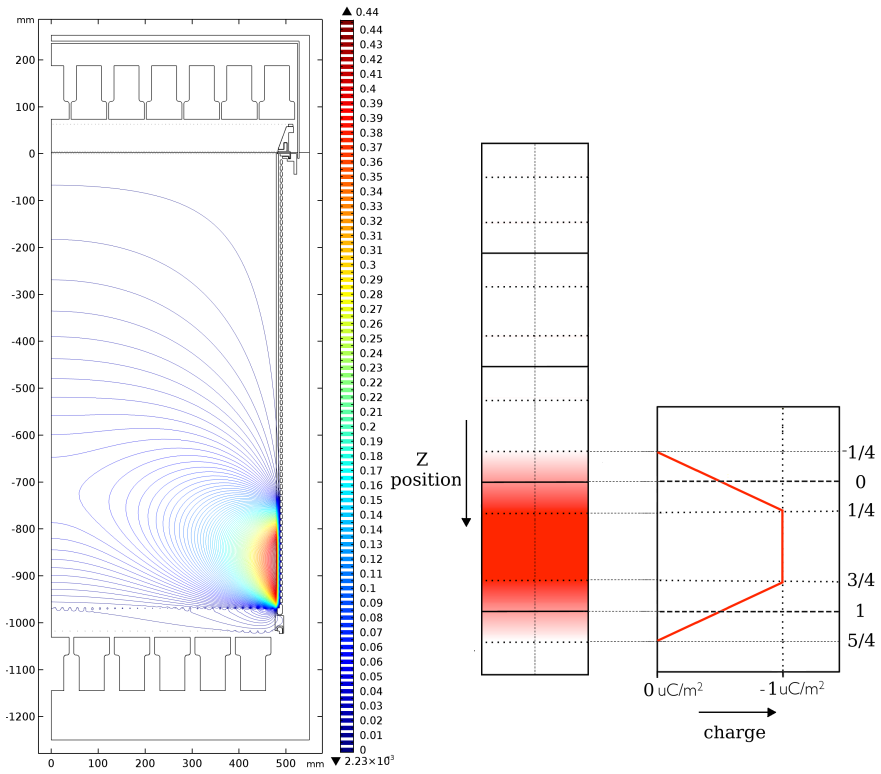

Figure 5.15. Electric potential contours inside the TPC when placing a charge distribution on the lower fifth of the TPC PTFE panels, while the voltages of the rest of the elements are set to zero. Illustrated is the smoothing linearly falling charge density approach developed to place charges at segments of the PTFE panels.

each segment only has its maximum charge density applied from 1/4 to 3/4 of its length, with a linear drop to zero extending 1/4 into the length of the neighboring segments, as illustrated in Figure 5.15. This translates in a continuous distribution of charge density, shared with the adjacent segments.

Next, in order to explore up to what extend density charges at the wall could affect the event edge distribution of simulated events, the TPC wall was divided into 5 segments (Figure 5.15 illustrates in fact the placement of -1 $\mu C/m^2$ in the last segment). Under this set up, 4 different configuration of charges are explore and their events boundary are reconstructed. The results presented in Figure 5.16 correspond to the placement of charge in (*top left*) bottom segments: 4, 5 (*top right*) bottom/middle segments: 3, 4 (*bottom left*) middle/top segments: 2, 3 (*bottom right*) top segments: 1, 2. Several particles are simulated and drifted by using information about the design electric field in addition to the contribution derived from the placed segments charged. For this purpose, a thin layer of particles was initially placed at the TPC boundary. Since not all propagated particles reach the liquid-gas interface, multiple layers with some distance from the wall were used.

The resulting features observed seem to support the notion that an inward position reconstruction bias can be directly related to place negative charges in the PTFE panels. The findings suggest as well that the magnitude of the altering of the reconstruction position depends strongly on the magnitude and depth where charges are located. From the time changing trend of boundaries related to observed

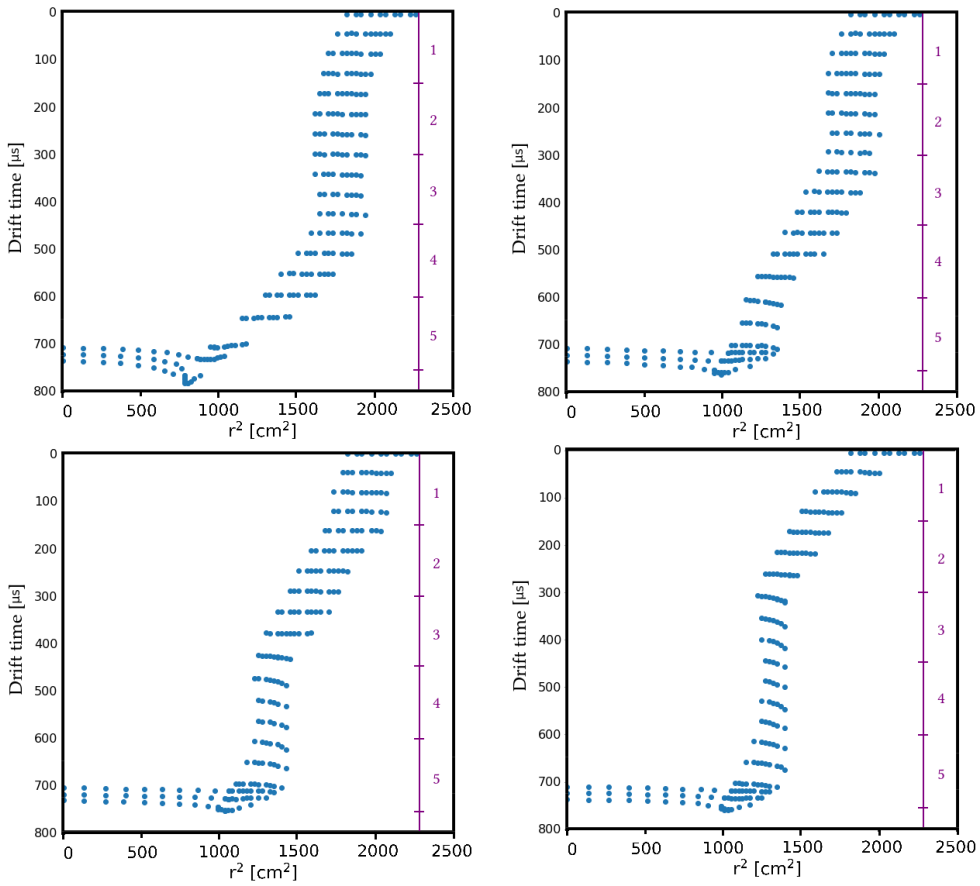

Figure 5.16. Reconstruction of event after 4 different configuration of charged segments have been introduce to modify the electric drift field inside the TPC. The cases show correspond to the placement of -1 $\mu C/m^2$ charge in the (*top left*) bottom segments: 4, 5 (*top right*) bottom/middle segments: 3, 4 (*bottom left*) middle/top segments: 2, 3 (*bottom right*) top segments: 1, 2.

events, it can be state that its description can not be achieved by a uniform distribution of density charge in PTFE panels along with the z direction. Rather, there may be an interplay of segments charged with slight changes in comparison to their surroundings. This observation is additionally supported by the asymmetric features found in the 24-fold bite structure. Given the limitations of the 2D axisymmetric, that basically it can not account for phi-dependent effects, a simplified 3D model will be introduce next to continue testing if the hypothesis about charge building up in the detector can be used to reproduce the bite structure.

Details 3D Model

The work presented in the next section, concerning different results from a COMSOL 3D model, was developed in collaboration with Michael Wigard during his Master studies. A complementary description to several details presented here can be found in his master thesis [206]. To begin with, this model builds up from the 2D axisymmetric framework previously presented. For its extension,

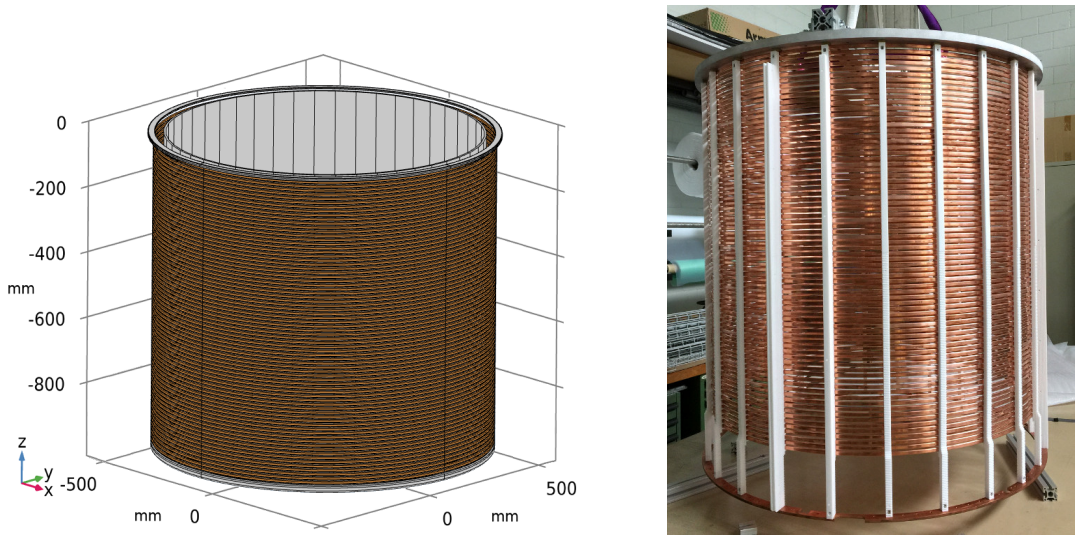

Figure 5.17. Left Geometry of the 3D COMSOL model developed for investigating charge accumulation in XENON1T. Showed are the field shaping rings surrounding the detector, together with PTFE panels defining the TPC. The gate and the cathode planes have been hidden. **Right** XENON1T cage field, illustrating the field shaping rings surrounding and elements of interest for the simulation.

given that an extra dimension scales the complexity related to discretizing and modeling all different elements that make up such a large analysis volume, different model simplifications are implemented. Most importantly, PMTs, screening meshes and the anode were left out while attention was placed on modeling the gate, the cathode, the reflectors and the shaping rings. Since the extension and distances inside the bulk, where the electric field is of most interest, are much larger than then typical sub-millimeter wire spacing for the electrodes, the gate mesh and the cathode wires are effectively modeled as planes[4]. The potentials for the planes defined were derived from a robust 3D simulation with a boundary element method **BEM** framework called xenon simulation and analysis package **XSLAP**. This framework is based on KEMField [209], which includes all elements and part specified in the CAD drawings design of the XENON1T TPC. The geometry implemented in the final model is illustrated in Figure 5.17 (*left*) along with the original cage field of the detector (*right*).

Once that the detector geometry, electrical properties and materials information are specified inside COMSOL, the boundary and electrostatic conditions of the model are defined. Then COMSOL generates a mesh based on the discretization of the space in tetrahedra such that in each of these elements the field can be calculated. Due to the size of the XENON1T detector, the calculation of a configuration of elements given certain conditions is computationally expensive. A resourceful procedure to avoid recalculating the electric field for every different combination of conditions that may be worth exploring (e.g. adding different charge densities), is to exploit the superposition principle. This consists in computing the electric field of the designed TPC $\vec{E}_{\mathrm{TPC}}$ only once. Then, for

[4] As demonstrated in the context of the KATRIN experiment, where the field from a plane determined by an effective potential made out from the potentials of individual elements approximates to the field created by a set of wire electrodes [208].

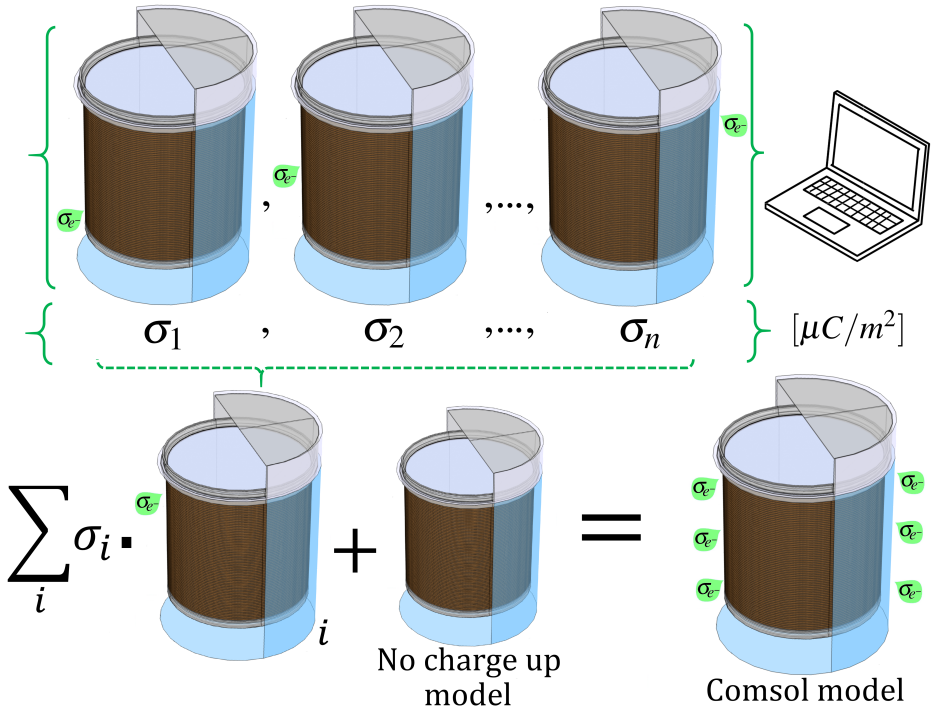

Figure 5.18. Illustration of the superposition principle when simulating a charge configuration with COMSOL. The final model contains information of the design of the TPC, having no extra charge, together with several segments containing σ_{e^-} charge densities that can be independently computed to speed up the simulation time.

any additional feature included, all voltages are set to zero and the new field can be independently simulated. Thus these fields serve as basis vectors that can be added up to obtain the field for arbitrary charge configurations.

In the context of simulating charges at the TPC wall, the panels are divided into segments carrying certain charge density $\sigma_{e^-,\mathrm{i}}$, such that the field of each segment $\vec{E}_{\mathrm{i}}$ can be precomputed, as illustrated in Figure 5.18 The resulting electric field from a total arbitrary charge Q placed at the wall can be defined as the superposition of the fields for the individual sections:

$$\vec{E}_{\mathrm{Q}} = \vec{E}_{\mathrm{TPC}} + \sum_i \vec{E}_{\sigma_{e^-,i}}, \tag{5.2}$$

where $\vec{E}_{\mathrm{TPC}}$ does not include any extra charge, and the total electric field for a configuration of charges investigated $\vec{E}_{\mathrm{Q}}$ can be exported in a regular grid of $200 \times 200 \times 300$ with a resolution in the (x,y)-directions of 4.8 mm and 3.2 mm in the z-direction.

As showed in Figure 5.19, where the top view of the CAD drawing of the TPC presents the interlocking system of PTFE sliding and fixed panels, there is one crucial difference between these two elements. Opposite to the sliding panels, the fixed panels are embedded on the pillars, which are directly in contact with the shaping rings, as illustrated in the lateral zoom-in slice also presented. An hypothesis proposed was that this design may work as a way to *ground* the panel. Thus the direct

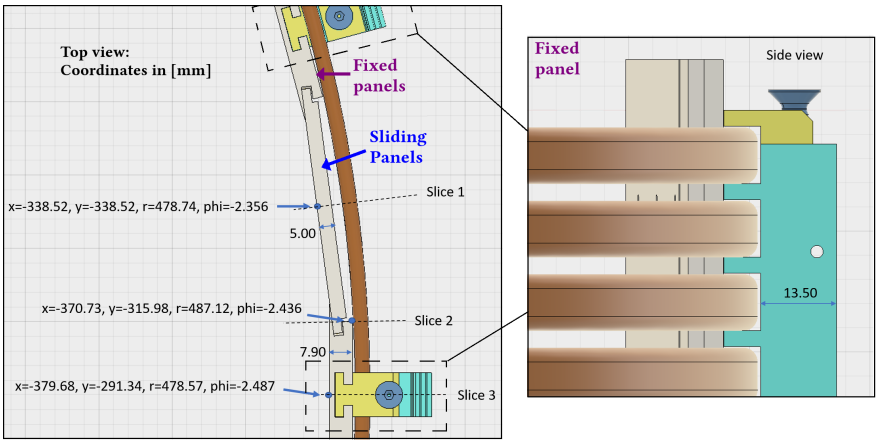

Figure 5.19. CAD drawing of the TPC illustrating the interlocking system of PTFE sliding and fixed panels.

contact with the shaping rings translates on preventing charges to build up on it. In terms of the observations found in data, this would be compatible with the fact that events in front of fixed panels are not affected in terms of inwards position reconstruction. At the same time this would suggest that since sliding Panels are not *grounded*, due to the empty spacing between them and the shaping rings, they do not have a path to get rid of any excess of charges. Hence they could end up accumulating over time.

In order to investigate this hypothesis, fundamentally based on location of the under-densities and the difference of the two type of panels, two initial charges placing settings were explored in order to find hints on condition reproducing the effects found in data. As showed in Figure 5.20, the first setting consisted on placing a uniform amount of charge in the sliding panels while no charge was added on fixed ones, specifically a charge density of -0.1 $\mu C/m^2$ along z[5]. Once that the electric field of this configuration was calculated, simulated particles were created and drifted using the field-dependent velocities parametrized, using equation 5.1. Figure 5.21 presents the observed XY distribution of events (*left*) along with the simulated distribution that resulted from this hypothesis (*right*). It follows that the features of a bite structure are for the most recovered, presenting a clear 24-fold symmetry that due to the same magnitude of charge placed, reproduces identical under-densities in contrast with smeared out bites found in data. On the contrary, in a different setting of charges where there is equal amount of charges accumulating in both fixed and sliding panels, no bite structure is found. This suggest that as proposed, charges preferably may accumulate where there is no draining path, i.e., where there is no contact with the shaping rings. Furthermore, the resulting distribution of event in terms of their distribution in depth and radius can be as well inspected. Figure 5.22 presents the observed r^2 vs z distribution of events for data at the beginning of SR1 (*left*), together with the simulated distribution corresponding to a uniform charge densities of -0.1 $\mu C/m^2$ placed only on sliding panels (*right*). Both distributions are found to be alike. However, as time passes by, the inward

[5]Here, the distribution of density charge with respect to the adjacent panels follows the same principles introduced in the 2D axisymmetric model.

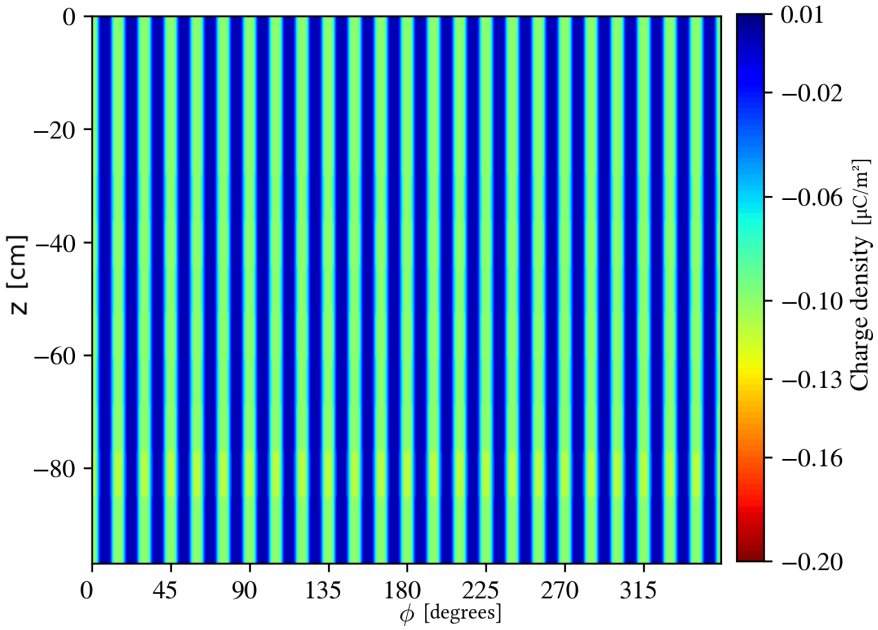

Figure 5.20. First setting simulation for the 3D COMSOL model motivated by the location of the under-densities and the difference between fixed and sliding panels. For this simulation, the placing of a charge density of -0.1 $\mu C/m^2$ along z in all sliding panels takes place, while no charge was added on fixed panels.

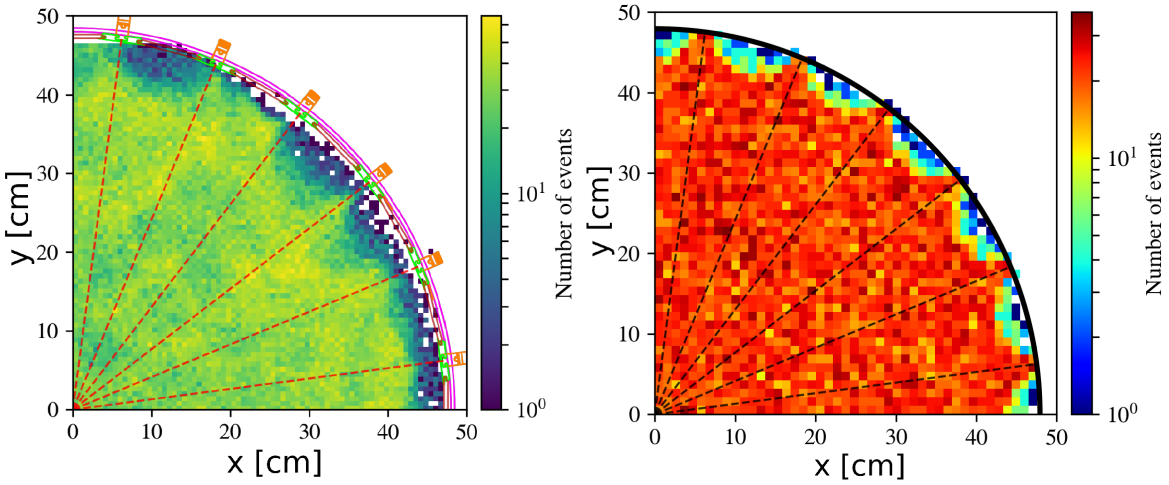

Figure 5.21. Comparison on the event distribution in the XY-plane between **Left** ^{83m}Kr calibration data and **Right** simulated events having a uniform charge density of -0.1 $\mu C/m^2$ along z in all sliding panels.

bias in position reconstruction is found not to change uniformly along z but rather it manifested strongly at different depths. This seems to confirm that there is a z dependency on the charge building up process. These observations are being considered in the XENON Dark Matter Project for future generation designs of LXe TPCs, particularly within the context of XENONnT (see section 5.4.2). Furthermore, with a partial confirmation about charges accumulating at the walls as the responsible

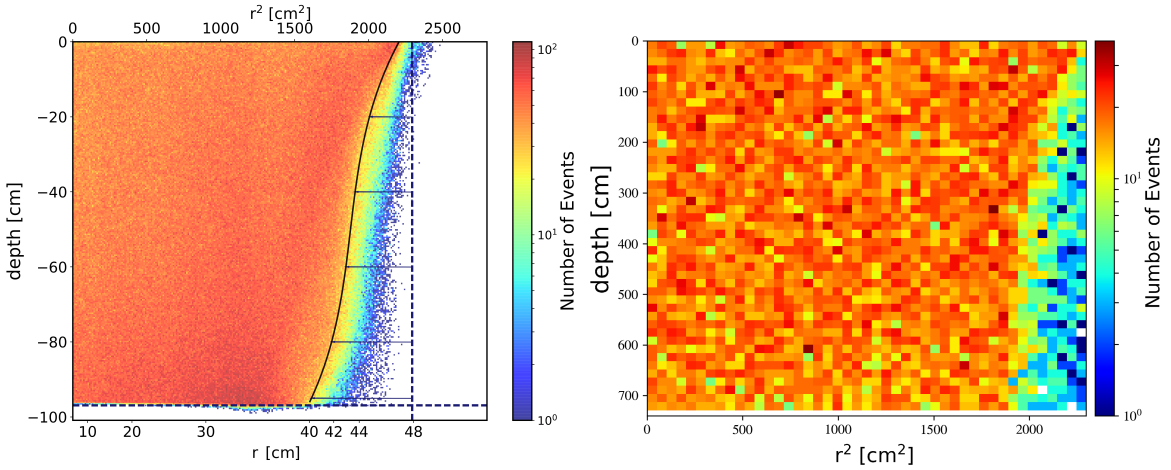

Figure 5.22. Comparison on the event distribution in the radius squared versus z-position between **Left** ^{83m}Kr calibration data and **Right** simulated events having a uniform charge density of -0.1 $\mu C/m^2$ along z in all sliding panels.

mechanism producing the inwards bias, a dedicated study quantifying the evolution charge density inside XENON1T during SR1 is explored in section 5.3.

5.1.6 Alternative Explanations for the Field Distortion

Other than charge building up in the surface of the PTFE panels, the possibility of changes in the field-shaping ring resistor chain was explored. As illustrated in Figure 5.23 (*left*), the design and configuration of the field when going from the cathode, passing through different stages of shaping rings, up to the gate, comprise a 197.5 GΩ total resistance. If one connection would happen to break, an increase in the resistance would be expected along with the creation of a dead, field-less region within the detector which in turn could produce small and localized field deformities. However, the resistance of the chain got evaluated between April and May 2016 and nothing like this was found. Nevertheless, the results suggested a lower total resistance was found[6]. Most importantly, since this effect would not evolve through SR1, it is incompatible with the field distortion observed inside the detector and therefore ruled out as a explanation.

From the measurements made, ignoring for a moment the high systematic effect, another hypothesis could be that the cathode is on the same potential as the first field shaping ring, as shown in Figure 5.23 (*right*). This in turn would generate a stronger field distortion at the bottom of the TPC. Under this assumption, COMSOL simulations were created to compare the resulting contour of the electric potential and the streamlines of the electric field. Both cases are presented in Figure 5.24, the one where there is no problem on the resistive chain (*left*), while also the case of considering a short circuit between cathode and the first shaping ring (*right*).

[6]The measurements from May indicated a total resistive chain estimation of $\sim$ 188 GΩ $\pm$ 3 %, although high systematic effect were reported to limit the information to be more precise.

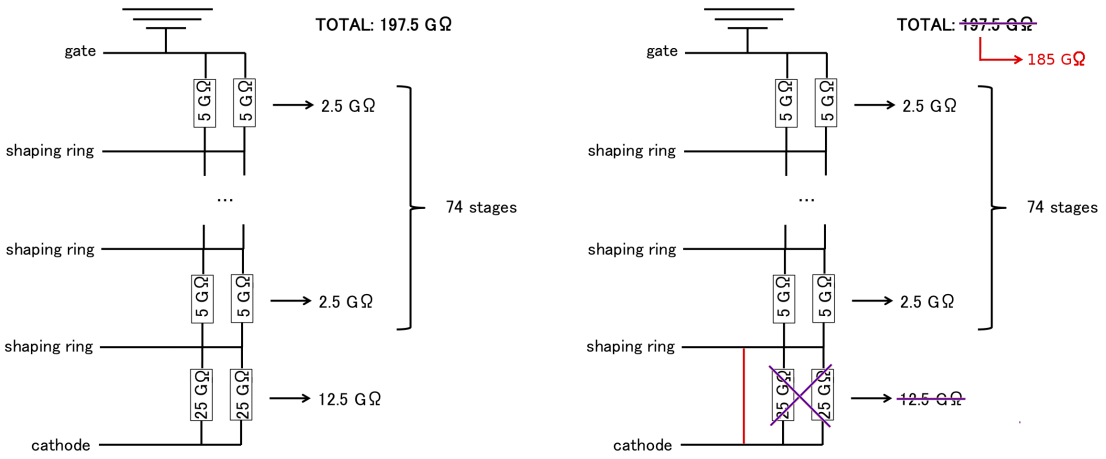

Figure 5.23. Left Two parallel resistor chain configuration from design, expected to provide a 197.5 GΩ total resistance for the electric field inside the detector **Right** Tuning for the field distortion correction to test the hypothesis that the cathode is on the same potential as the first field shaping ring. Adapted from [210].

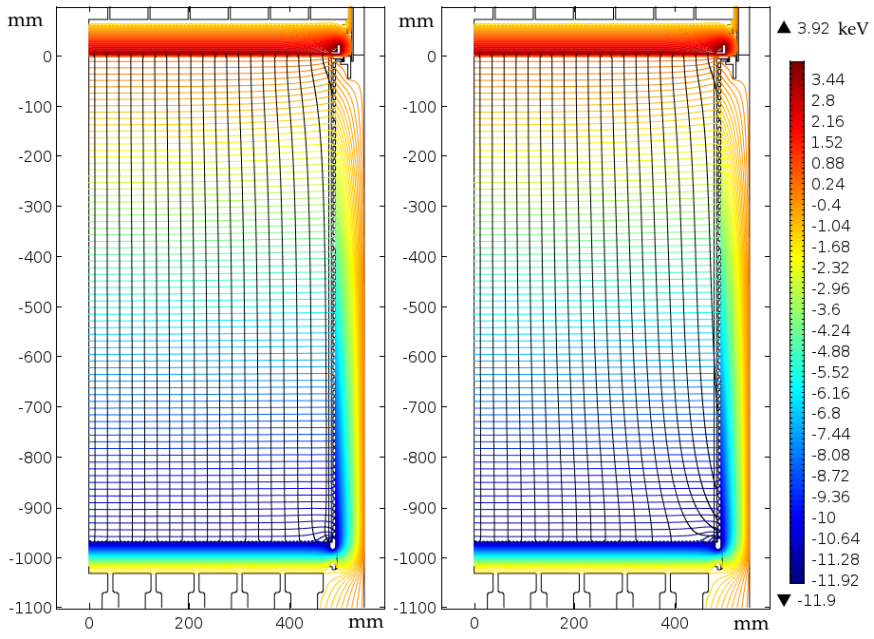

Figure 5.24. Simulations illustrating the contour of the electric potential and the streamlines of the electric field, produced to explore alternative explanations for the field distortion found in data **Left** for designed resistive chain **Right** hypothesis that the cathode is on the same potential as the first field shaping ring. The difference between both simulations can be observed at bottom corner, where the effect of the cathode being at the same potential as the first field shaping ring produces a strong deformation on the field, and as consequence in the reconstruction of the events.

As result a tuned field distortion correction map for data was created under this approach and the effects were compared to the boundaries obtained by the distribution ^{83m}Kr events. The distortion on the field streamlines translates into an improvement when matching the position of data at the beginning of SR1 to simulated particles than drift following the equivalent electric field. However, the

possible reason to explain having the short circuit, such as that a broken cathode wire touches to the shaping ring or that there is a wavy copper wire touching to both cathode and the shaping ring do not seem to be likely, in the first case there is a teflon reflector that separates the volume with wire and outside and in the second case there is insulator around copper. Nevertheless, even if this assumption could partially coincide with data at the beginning of SR1, the full time-dependence of the inwards bias found in the measured boundaries can not be explained, ruling out this hypothesis.

5.2 Data Driven Correction for SR1

5.2.1 Time-dependent Corrected Coordinates

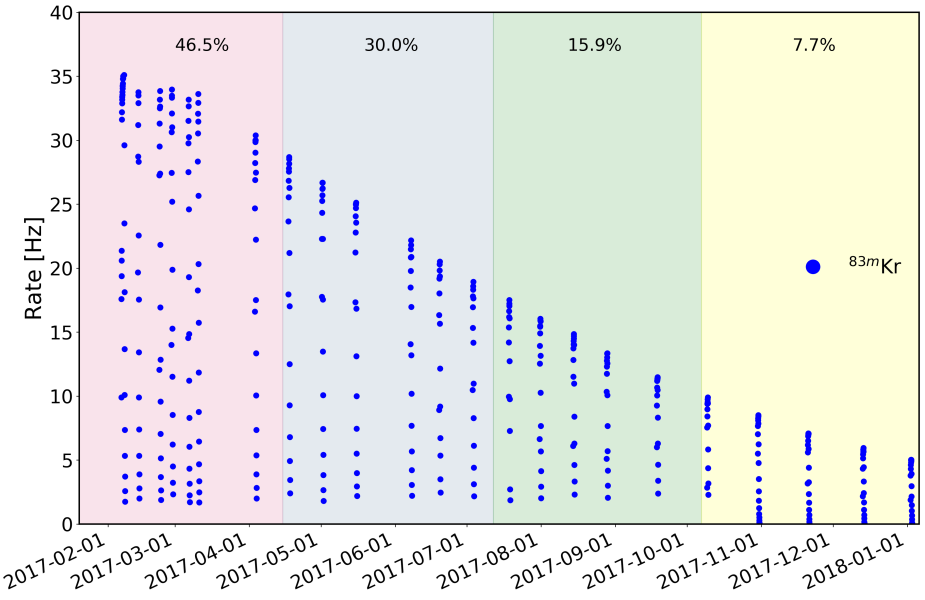

Figure 5.25. Trigger rate of ^{83m}Kr data during SR1 along with the four different periods defined to reproduce the time-dependent 3D field distortion corrections implemented. The percentage presented indicate the ratio of ^{83m}Kr data in this period over the total ^{83m}Kr data taken during SR1.

In order to correct for the time-dependency found, an update on the approach to generate the correction was made by Jingqiang Ye. The ^{83m}Kr calibrations data previously use all at once was divided in four equally time-spaced periods to generate continuous corrections during SR1. The time range and divisions used are illustrated in Figure 5.25. The details about these periods and the final data effectively used for the corrections is specified in Table 5.1. The procedure follows the same idea already introduced when discussing *position reconstruction* corrections in section 4.2.3. As result, not only the bite structure and the inward bias are gone, but the procedure also ensures the capability to use bigger fiducial volumes for different studies, including the search of dark matter. Without this correction, conclusions involving different aspects of the detector happening near the TPC wall could not be trusted and the understanding of the full capacity of the detector would be limited.

Table 5.1. Information about the four equally time-spaced periods of time during SR1 where ^{83m}Kr data was used to generate the continuous field distortion correction for position reconstruction.

Period	Time interval	Statistics	ϕ-slices	z-slices	Statistics slice
1	01/18/2017 - 04/15/2017	7513747	180	40	1043
2	04/15/2017 - 07/12/2017	4561936	180	40	633
3	07/12/2017 - 10/07/2017	3616848	180	40	502
4	10/07/2017 - 01/18/2018	1972731	120	30	547

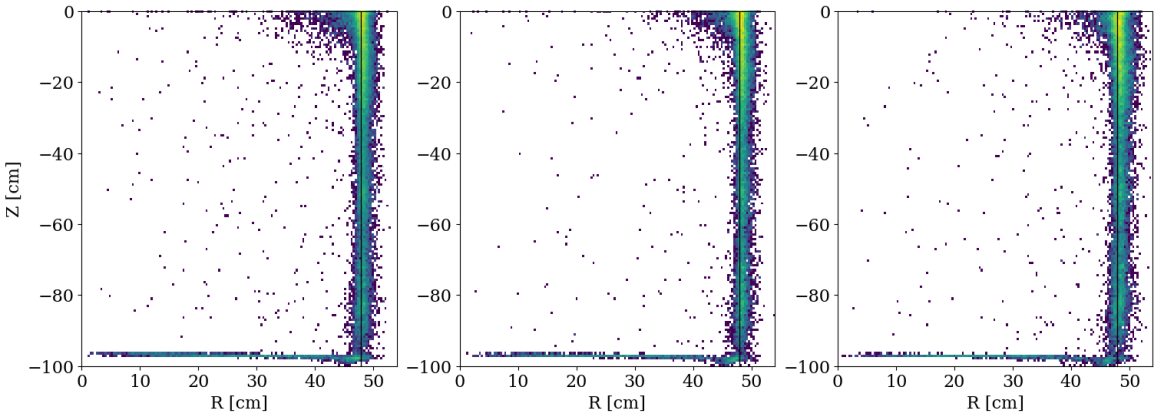

Figure 5.26. Reconstruction of ^{210}Po which generate at the wall in order to check the performance in time of the time dependent position reconstruction approach developed. The data shown corresponds to April (*left*) August (*center*) and December (*right*) of 2017. Modified from [187].

The performance of the position reconstruction for data taken in different periods of time is illustrated in Figure 5.26. Here background data has been selected and after isolating the population of ^{210}Po, which originate at the inner surfaces of the detector, it is found that for the 3 different periods of time compared, April (*left*) August (*center*) and December (*right*), that the location of these events follow the expectation and furthermore do not present anymore an inward bias.

5.2.2 True Light Collection Efficiency Map

Given that the detection of the S1 signal is limited by its collection, the combination of solid-angle coverage of the PMTs and light attenuation due to reflection and impurities in the medium are referred to as geometrical effects. Corrections for these effects are derived from the 32.1 keV signal in ^{83m}Kr calibration data in terms of a light collection efficiency **LCE** map that normalizes the mean of the S1 distribution when looking into discrete (R,φ)-regions in slices of z, to the S1 average across the TPC. However, in presence of a not homogeneous time-dependent drift field in the detector due to charge accumulation, in addition to the expected geometrical effects there are introduced field effects dependent on the particle type and energy deposition, which as consequence influence the final energy reconstruction. Different studies indicate that the impact on the light yield of NR is below 1% in the

ROI when looking for WIMP signals [62]. For ER, induced by the 32.1 keV line of ^{83m}Kr, the impact is in the order of $\sim 4\%$ for the average field variations and is becomes even larger for events located in the outer detector regions. The main problem under the evidence found is that the LCE map directly derived from the krypton mono-energetic line will contain a combination of both, geometrical and time-varying field related effects. This can result in a bias for reconstructing and identifying events, specially low energetic NR.

Since it is not desirable that corrections are dependent on time, position, energy and recoil type, a data driven approach to disentangle the two effects was developed. The main goal was to obtain a *true* LCE map expected to account only for geometrical effects, such that corrections are not subject to the particle type from using ^{83m}Kr, and therefore any time-dependency in the map is removed. In order to disentangle these effects, the guiding principle that the total combined change on electrons and protons should remain insensitive to recombination variations arising from a non-uniform electric field is used. These changes are quantified from local changes encountered in time for the S2 signal of the 41.5 keV line from ^{83m}Kr, as krypton is the main source to generate correction, it has enough statistics to make robust analyses and since several studies demonstrated that the observed spatial-dependent variations on the charge yield for this data are not related to detector conditions changing in time and thus altering the charge production.

As discussed in the context of the LUX experiment [211], considerations about an additional bias introduced in the electron lifetime calculation for the cS2 signal have to be considered, i.e., the non-uniformity of the drift field in the detector induces a higher recombination of ^{83m}Kr events at bottom detector regions. This translates in an attenuation of the S2 signal directly related to the drift time of the events. This feature mimics the expected attenuation introduced to the S2 signal by impurities in the medium that capture electrons as they drift. Therefore, if field effects are overlooked, corrections for the S2 signal become bias and the electron lifetime get overestimated, which in turn translates into over correcting all S2 signals. In order to try to decouple the bias introduced in the charge yield already monitored from the 41.5 keV signal of ^{83m}Kr, since this quantity has been corrected by the electron lifetime also obtain from ^{83m}Kr data, the following methodology is applied [173]:

Prelude

- Consider the light yield **LY** measured in the detector as the number of detected photoelectrons per deposited energy, resulting from the interplay of the generation of photons given an incident energy (i.e. the photon yield **PY**) and the light collection efficiency ε_L (i.e. number of photons reaching the PMTs given the number of photons created after the original deposition of energy in the interaction site). It follows that:

$$LY(R,z,\varphi,E_r,E_f) = \frac{S1}{E_r} = \varepsilon_L(R,z,\varphi)\cdot PY(E_r,E_f), \tag{5.3}$$

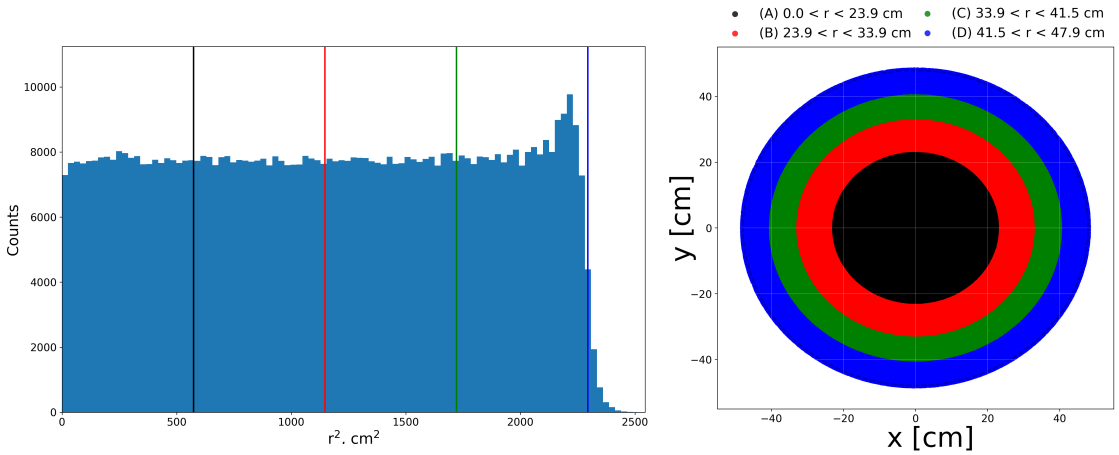

Figure 5.27. Left Analyzed volumes for ^{83m}Kr events selection, defined such that an equal amount of events are located inside of them **Right** visualization of this selection in the XY plane.

where E_r is the recoil energy, $E_f \equiv E_f(R,z,\varphi,t)$ is the drifting field featuring time variations across the TPC (specially close to the PTFE panels) due to charge accumulation and t is the time when the data is analyzed.

- In order to correct for the spatial dependencies found in the S1 signal, first the mean of the S1 distribution is calculated in different z segments for discrete (R,φ)-regions. Then each value is normalized to the average S1 evaluated across the detector, such that there is scaling map *LCE* correcting all S1 signals inside the TPC:

$$\frac{S1}{<S1>} = LCE(R,z,\varphi,E_r,E_f,t) = \frac{\varepsilon_L(R,z,\varphi)\cdot PY(E_r,E_f(R,z,\varphi,t))}{<\varepsilon_L \cdot PY>}. \tag{5.4}$$

- Even though the *LCE* map should only account for geometrical effects, due to the field changing in time given charge accumulation, this map carries a bias since it was calculated using a specific particle type, ^{83m}Kr. Therefore it is not longer correct to use this scaling map to correct all events, having different energies and interaction types.

- To decouple these effects, the corrected cS2 signal from the 41.5 keV line of ^{83m}Kr is used.

Stage 1

- For this signal measure the mean of the cS2 distribution in bins of (R,z,φ) for a fix time in SR1. For each of these bins, the amount of electrons found differing from the expected number of electrons related to the 41.5 KeV line are quantified (this expected number is derived from the average cS2 signal in the full TPC, convert into electrons by using the gain g_2 factor).

- Due to electron-ion recombination, the total combined change on electrons and photons has to remain insensitive to the average recombination variations arising from a non-uniform electric

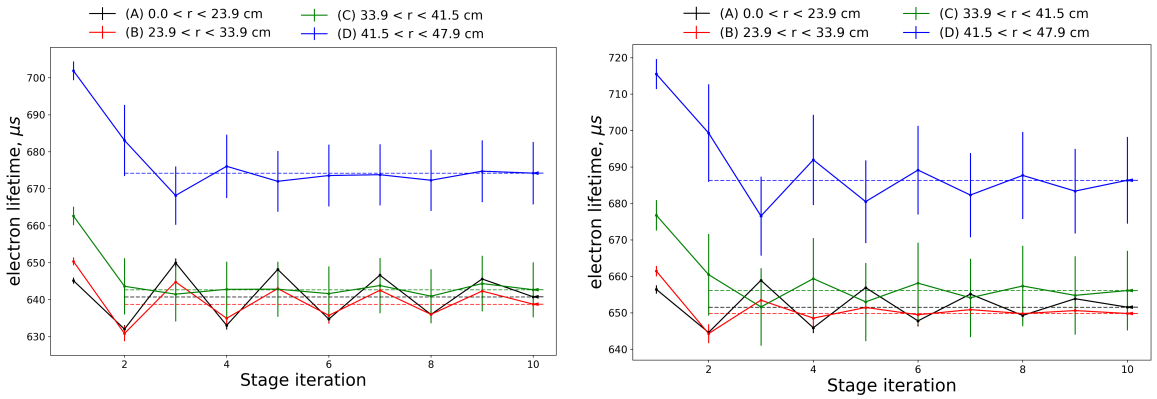

Figure 5.28. Iterative electron lifetime evolution for different stages. The illustrating trends correspond to measurements from ^{83m}Kr calibration data taken in July **Left** and September **Right** during SR1.

field, such that: $\Delta_e + \Delta_{ph} = 0$, where $\Delta = N_{expected} - N_{detected}$. Written in terms of the detected and averaged signals it follows:

$$\begin{aligned} M_e &= (N_e - \Delta_e)/N_e = \frac{cS2}{< cS2 >} \\ M_{ph} &= (N_{ph} + \Delta_{ph})/N_{ph} = \frac{< cS1 >}{cS1} \end{aligned} \tag{5.5}$$

where $M \equiv (R, z, \varphi, t, E_r, E_f)$ are the maps quantifying variations in charge and light. Therefore, they satisfy the relation $M_e \cdot M_{ph} = 1$ due to anti-correlation of both signals.

- A valid scaling map $LCE_{true} \equiv LCE_{true}(R, z, \varphi)$ only dependent on spatiality, rather than the drift field changing in time and the particle type, is obtained then from calculating:

$$\begin{aligned} LCE_{true} &= \frac{LCE(R, z, \varphi, E_r, E_f, t)}{M_{ph}(R, z, \varphi, t, E_r, E_f)} \\ &= LCE(R, z, \varphi, E_r, E_f, t) \times M_e(R, z, \varphi, t, E_r, E_f). \end{aligned} \tag{5.6}$$

Stage n+1

- In order to account for the electron lifetime bias introduced in the available cS2 signal, the map M_e is calculated iteratively to remove the cS2 signal bias from the field dependency on the capture rate of electrons [202]. This is achieved by re-calculating the electron lifetime[7] in each iteration and evaluating the correction M_e

- This means that at first order, one generates the correction maps $M_{e,1}$ and $M_{ph,1}$ (Stage 1). Next these maps are use to correct the S2 signal. This is done by following the relation:

[7] The methodology to calculate this quantity is the same explained in 4.2.2, which describe the decrease in charges in terms of the lapsed drift time by using an exponential function, and the best fit is obtained by maximizing the standard unbinned maximum likelihood using a Markov chain Monte Carlo.

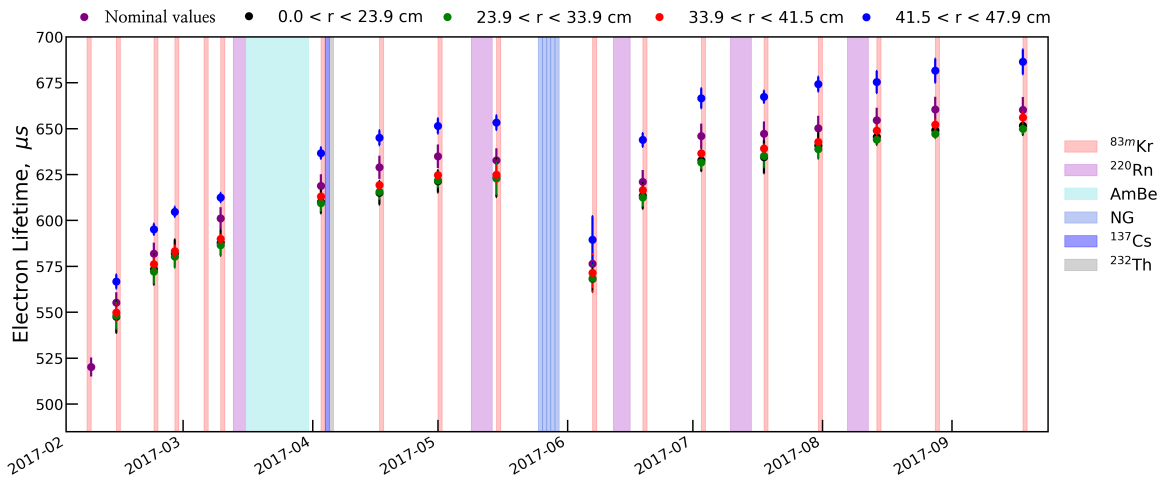

Figure 5.29. Comparison of the electron lifetime evolution calculated (*black*, *red*, *green*) when decoupling field effects for different active volumes(*purple*) with the nominal values obtained when ignoring field effects.

$$S2 \times M_{ph,n-1} = S2 \cdot \exp -t/\tau. \tag{5.7}$$

- This is done defining four different fiducial volumes that ensure to have an equal amount of events inside of them, as shown in Figure 5.27. In each of these sub-volumes the electron lifetime is fit in the range of 100 - 700 μs. The nominal values inside each volume are used then to understand and investigate if there is a field dependency in terms of the radius of the events.

- Finally it is expected that the bias on the field introduced by external mechanisms is overcome once that the convergence of the electron lifetime is reached (i.e. when the relative change from Stage n-1 to Stage n is less that the uncertainty in the electron lifetime model).

Figure 5.28 illustrates the convergence of this method for the calculated electron lifetime measurements from ^{83m}Kr calibration data taken in July (*left*) and September (*right*). On one hand, as it was expected, the electron lifetime derived for the inner volume of the TPC is significatively less affected through different iterations that regions at high radii (in terms on how much does the initial value changes in comparison to the convergence value). This seems to confirm that field bias in the already calculated corrections due to charge accumulation are bigger for events detected close to the PTFE panels. On the oder hand, as illustrated in Figure 5.29 when this methodology has been implemented to all calibration data available, it can be seen that the nominal value used for the standard correction before to this approach (*purple*), exceeds the average values obtained in the inner active volumes after the decoupling (*black, red, green*). In other words, the overestimated values previously used were introducing a bias in the correction to all S2 signals.

From these results, the convergence value for the electron lifetime and therefore the stage at which the correction map is fully generated corresponds to the iteration stage number 10. At this point the maps M_e and M_{ph} contain all history of needed steps to generate through equation 5.6 a rightful light

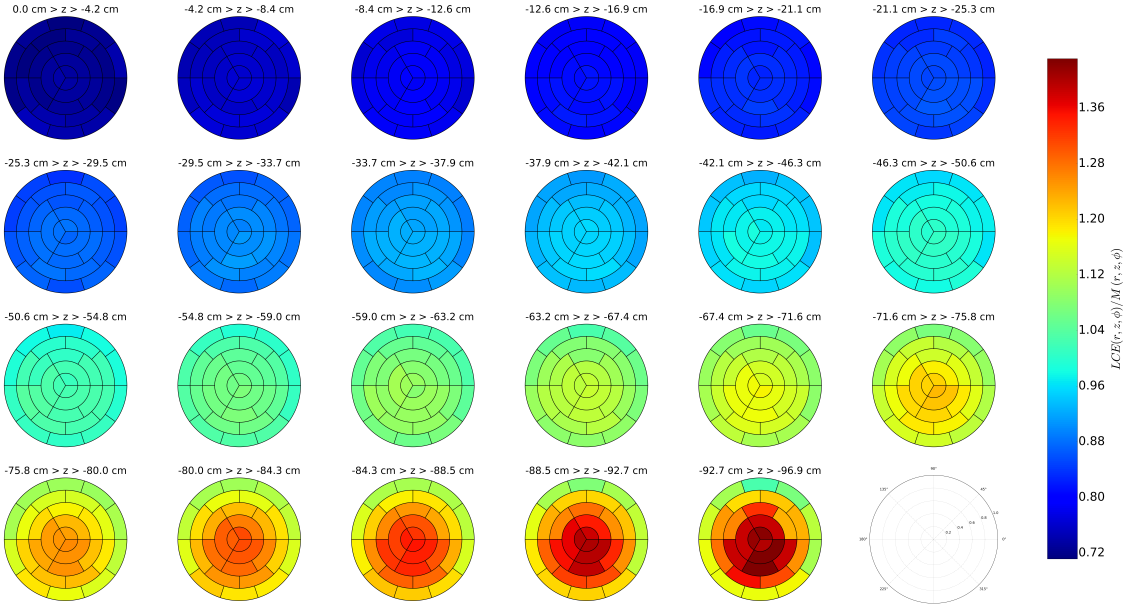

Figure 5.30. Resulting light collection efficiency map LCE_{true}, decouple from field effects from charge building up, applied to all S1s depending on their corrected position in order to correct for the solid angle coverage on S1 light subtended by PMTs, attenuation of light within the detector medium and the quantum efficiency of the PMTs.

collection efficiency LCE_{true} design to correct only geometrical effects, rather than time-dependent field features. The resulting map is presented in Figure 5.31. Given that at the beginning of SR1 at February the rate of the ^{83m}Kr is bigger, the final map used for SR1 was generated from data taken this month. The binning used was optimized by considering the maximum variation in each dimension and by scaling the number of bins in each dimension to the maximum variation. This translated in a the maximum variation between adjacent bins of 2.5%. The visualization of the variations of each dimension used for the light collection efficiency LCE_{true} are presented in Figure 5.31. These results show the changes of the LCE_{true} in terms of the (*top left*) depth z (*top right*) radius r and (*bottom*) angular φ. Along with z it is found that given the coverage from the bottom PMTs array and due to their solid angle, less number of reflection of photons before reaching the PMTs happen such that the LCE is maximum, opposite to further location on the detector where attenuation and reflection decrease the S1 signal. Along with φ it is found that small variations of the light yield are found in terms of different positions at larger radii mainly because turned-off PMTs around this region.

On one hand, Figure 5.32 (*left*) indicates that the error of the LCE_{true} map is less than 1% before the map is implemented in to PAX. Once the map is generated, for spatial continuity purposes a routine of interpolation is applied. The uncertainty introduced by the interpolation itself is negligible. On the other hand, Figure 5.32 (*right*) compares the shape of the resulting measured S1 signals for ^{83m}Kr data, corresponding to the two peaks correspond to the 9.4 and 32.1 keV lines (*green*) without

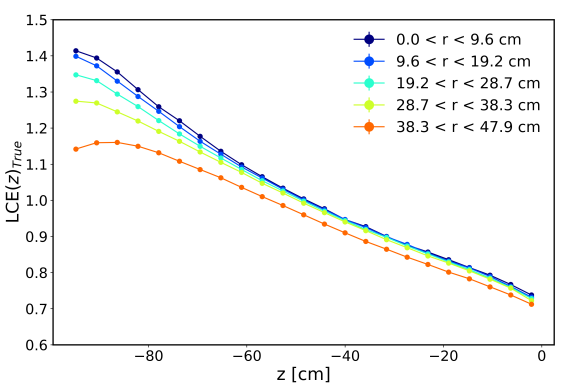

(a) LCE_{true} variations in terms of depth z.

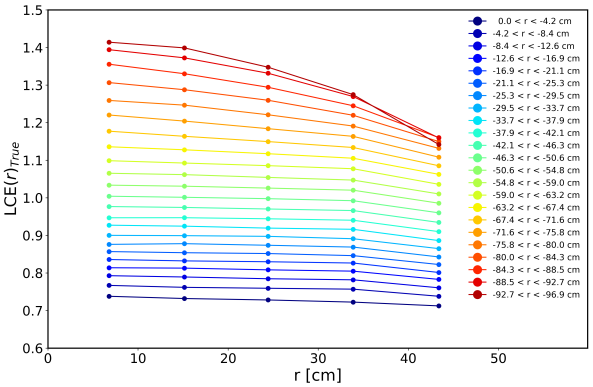

(b) LCE_{true} variations in terms of radius r .

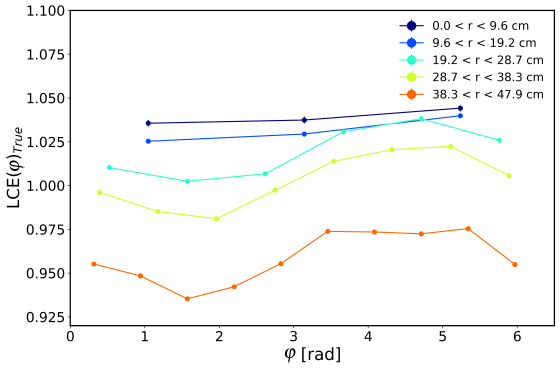

(c) LCE_{true} variations in terms of the angle φ.

Figure 5.31. Effective variations of light collection efficiency map LCE_{true} in terms of the (*top left*) depth z (*top right*) radius r and (*bottom*) the angle φ.

using the LCE. Additionally it is compared the effect of the correction (*blue*) produced by the LCE_{true} map versus (*red*) the bias correction in PAX produced by the $LCE(R,z,\varphi,E_r,E_f,t)$ map.

Furthermore, when comparing the LCE_{true} map produced by using ^{83m}Kr calibration taken on February with respect to the map produced from October data, it can be confirmed the expected stability of this map throughout time. As shown in Figure 5.33, the average change per bins corresponds to 0.4%, while the maximum difference found does not overcome a change of 1.2%. This is a great improvement from the map previously used $LCE(R,z,\varphi,E_r,E_f,t)$ given that this map would vary in time up to $\sim 7\%$. Most importantly, not bias in included in this map.

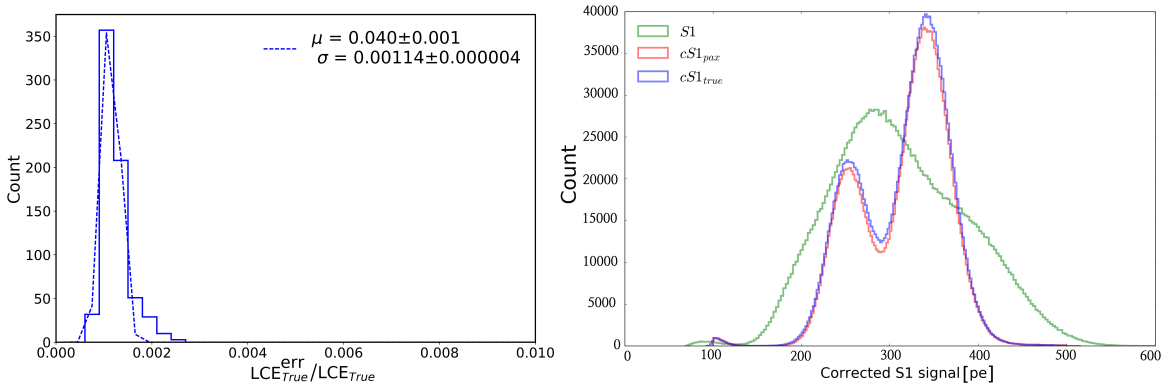

Figure 5.32. *Left Right* Resulting measured S1 signals for ^{83m}Kr data when (*green*) not using a *LCE* (*blue*) produced by the LCE_{true} map and (*red*) produced by the bias $LCE(R,z,\varphi,E_r,E_f,t)$ map.

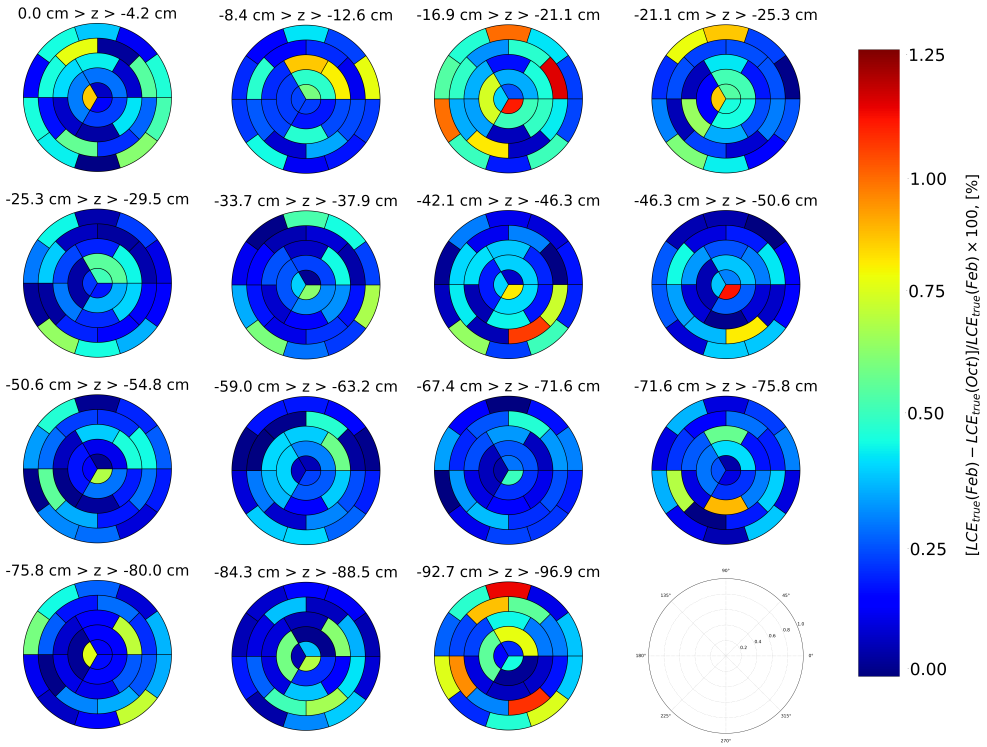

Figure 5.33. Percentage changes in time of the LCE_{true} map in order to check it's stability. Here maps obtained from February and October data are compared, revealing an average change per bins of 0.4%, while a maximum of 1.2%.

5.3 Methods to Obtain Electric Field

5.3.1 COMSOL simulations

The developed 3D COMSOL framework was used to estimate the average charge density evolution on the PTFE wall during SR1. As illustrated in Figure 5.34, the principle used is the one of comparing

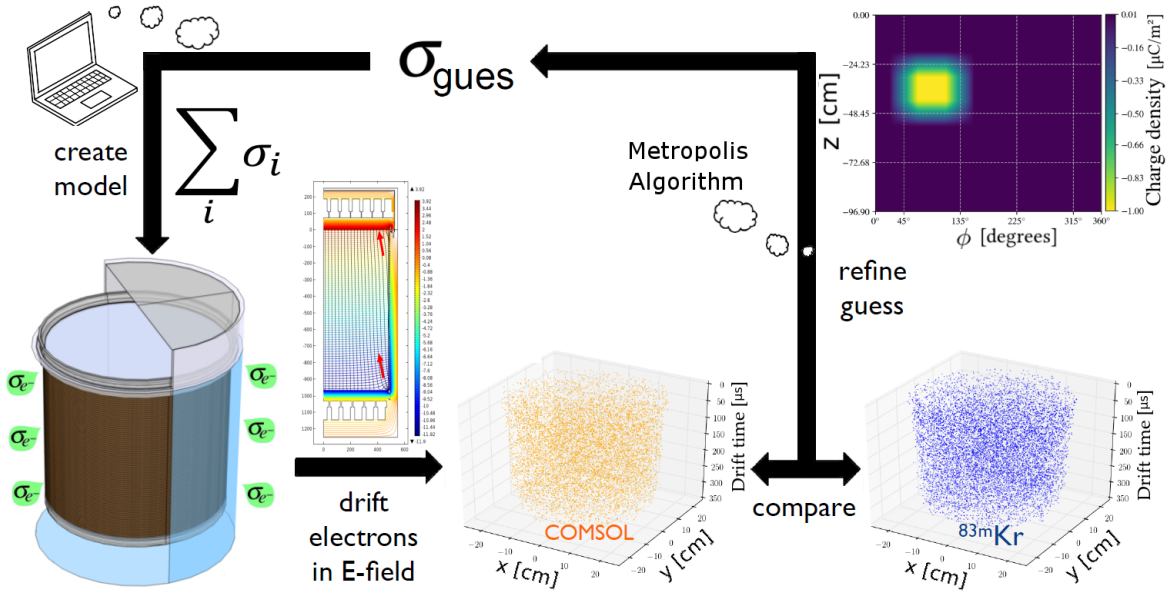

Figure 5.34. Illustration of the iterative algorithm used to estimate the charge accumulation distribution at the walls of the TPC, such that the distribution of simulated events coincides with the position distribution of ^{83m}Kr events in data.

the position distribution of ^{83m}Kr in data to the position obtained from simulated particles that are found affected by a specific charge distribution. Starting by an initial charge distribution guess, a Metropolis algorithm designed for sampling from a multi-dimensional distributions of charges was used to iteratively redefine the initial guess used until an agreement in observed and simulated positions is found. In practice, the matching algorithm described in [206] needs to iterate about 700 to 1300 times for a given position distribution of ^{83m}Kr calibration data. Only until reaching stability and if possible convergence in the likelihood, the algorithm continues sampling different charges. In order to explore the consistency of the procedure, the algorithm was run under two different initial conditions referred to as **IC 1** and **IC 2**. For the former, no actual charge density is placed on any of the PTFE panels. For the latter, a charge density of -0.2 μC/m^2 is initially placed on each sliding panel.

As illustrated in Figure 5.35, the increasing trend of the average PTFE charge density found on the PTFE panels during SR1 supports the fundamental understanding of charge accumulating over time (this happens for both initial conditions). The trends resembles the result previously published by LUX, see Figure 5.12, changing in the maximal case from -0.04 to -0.16 $\mu C/m^2$. Furthermore, the distribution of charges obtained after the iterative process indicated an average change distribution pattern with a higher concentration of charges near the anode of the TPC. These observations are as well consistent with what was found by LUX, which uses a very similar TPC design as XENON1T.

Although the result is encouraging, it is important to mention that a discrepancy between the values in the trends for the two initial conditions was found. To explore the underlying difference of th results, the edge boundaries from ^{83m}Kr data from 13.12.2017 are used, together with the

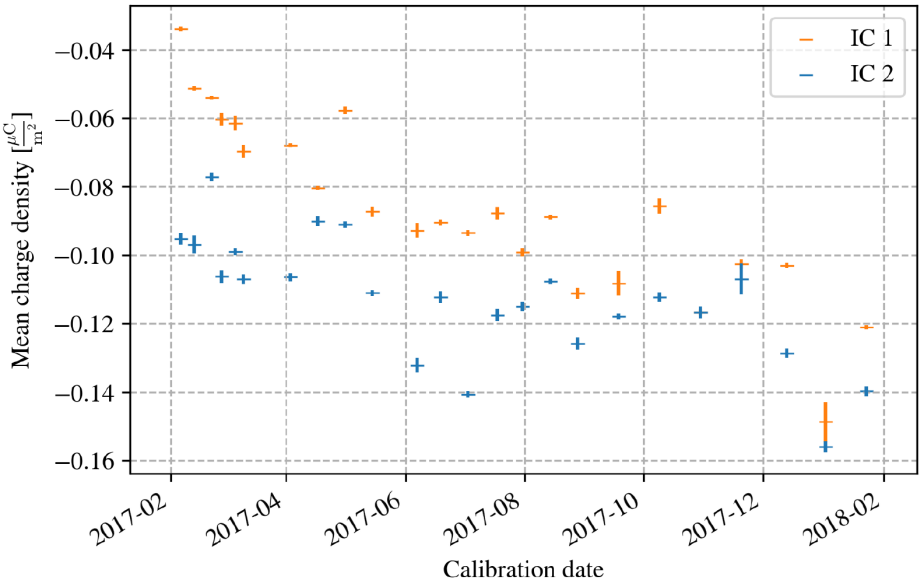

Figure 5.35. Mean charge density evolution monitoring on the PTFE panels inside the detector. The values were obtained by comparing the position distribution of ^{83m}Kr in data to the position obtained from simulated particles that are found affected by a specific charge distribution. Over the course of SR1 it is found an increase on the charge density from -0.04 to -0.16 μC/m^2, consistent with the increased effect of the inward position reconstruction effect on observed coordinates.

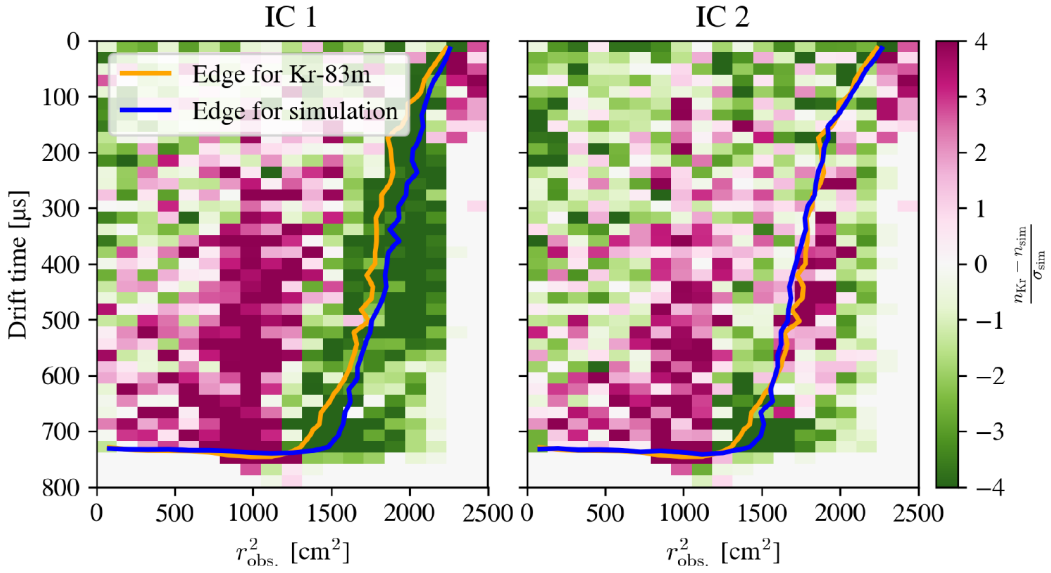

Figure 5.36. Comparisons of event distributions for simulated particles based on the charge distribution obtained when running the matching algorithm for ^{83m}Kr data from 13.12.2017. In terms of radius squared and drift time (z-position), the edge boundaries for ^{83m}Kr (orange) and the one obtained from the matching algorithm for simulated events (blue) are presented, both for the *IC 1* **Right** and *IC 2* **Left**.

reconstructed boundaries obtained in simulation data due to the derived charge distribution found through the matching algorithm for this exact date. First, to define the edge boundaries for ^{83m}Kr

data and simulations, the data was binned in radius and drift time and the median number of events in the nonempty bins was calculated. The edge is then defined to be where the number of events in a bin drops below half the median. Figure 5.36 illustrates the boundaries found for ^{83m}Kr (orange) and simulated data (blue), for both used initial conditions in the matching algorithm: *IC 1* (*left*) and *IC 2* (*right*). To compare two distributions, a normalized histogram $n = N_{\text{bins}}/N_{\text{tot}}$ is computed for each distribution, having a deviation $\Delta = \frac{n_1 - n_2}{\sigma_2}$, where N_{bins} is the number of events in a bin, N_{tot} is the total number of events in the histogram and $\sigma = \sqrt{N_{\text{bins}}}/\text{tot}$. In terms of density of events, the results for both initial conditions indicate that in the case of the *IC 1*, the reconstructed simulated distribution has too many events at large radii, while the *IC 2* simulation has fewer than expected. On one hand, in terms of the calculated boundaries, this translated as underestimating the amount of negative charge for the *IC 1*, such that the edge ends up lying towards higher radii in comparison to the boundaries calculated in the data. On the other hand, for the *IC 2*, the results suggest that the charge calculated was marginally overestimated. Therefore, the boundaries can appear towards smaller radii in comparison to those from data. These observations hold true for most of the simulations. Further results suggest that results from the *IC 2* describe the data best. However, further investigations to obtain agreement between both conditions needs to done, given that in principle a robust algorithm should result in same charge configurations.

5.3.2 Using field distortion correction

An alternative data-driven method to estimate the time-dependent electric field inside the TPC follows from using the information contained in the 3D field distortion correction **FDC**, as done by Jingqiang Ye for SR0 and SR1 data [187]. The procedure is summarized in the next steps:

1. Define the electric field streamlines from the calculated FDC
2. Draw equipotential lines to these lines
3. Assume that the wall position has voltage given by the shaping divider
4. Calculate $\vec{E} = -\nabla V$
5. Interpolate electric field map

Under the assumption that the electric field lines can be approximated at first order to be straight, for the most they would overlap the true electric field streamlines and their construction would circumnavigate technical issues for calculating curved equipotential lines. Thus, as illustrated in Figure 5.37 (left), they connect the observed and interaction position for events happening close the cathode. Following the next steps and using the same four divisions in time used in the 3D time-dependent field distortion corrections (see section 5.2.1), the average electric field in each period can be calculated, as summarized in Table 5.2 and illustrated in Figure 5.37 (*right*).

Table 5.2. Electric field calculated using an alternative data-driven method based on the the information contained in the 3D field distortion correction. The average field has been calculated for four equally time-spaced periods of time during SR1 where ^{83m}Kr data was used to generate the continuous field distortion correction for position reconstruction.

Period	**Time interval**	**Average E inside 1.3T FV** $[V/cm]$
1	01/18/2017 - 04/15/2017	80.4 ± 2.3
2	04/15/2017 - 07/12/2017	80.5 ± 1.3
3	07/12/2017 - 10/07/2017	80.6 ± 1.6
4	10/07/2017 - 01/18/2018	80.9 ± 4.0

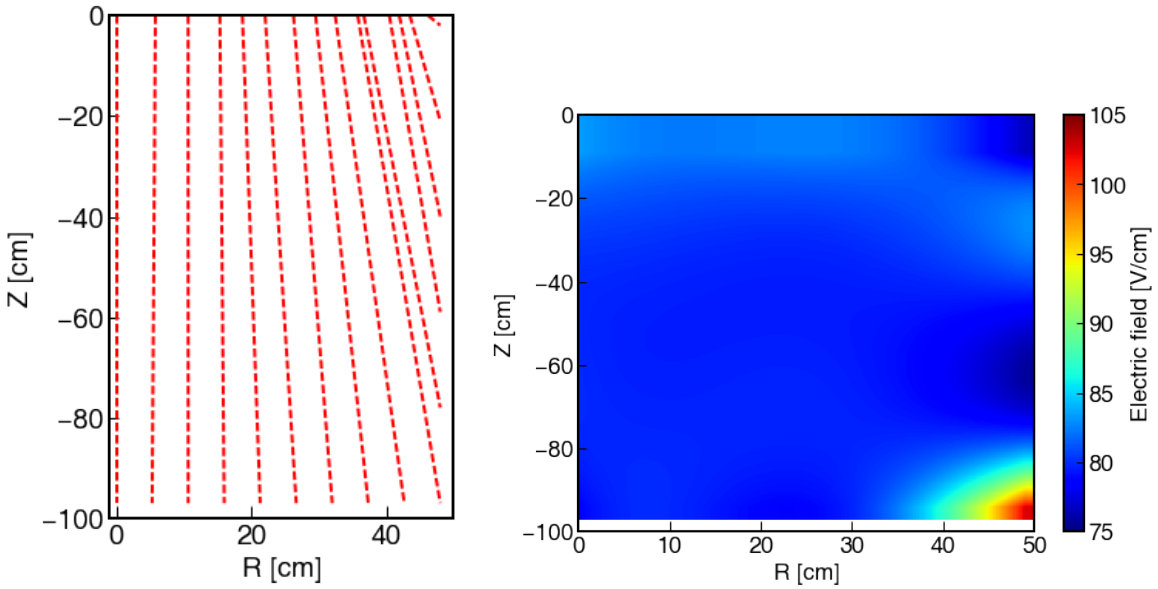

Figure 5.37. Left Illustration on the assumption of the electric field lines **Right** resulting electric field inside the detector for SR1 data, calculated from interpolating the electric field obtained after evaluating the field $\vec{E} = -\nabla V$ in terms of the field distortion correction and voltage from the wall position.

5.4 Summary and Applications

The features introduced by the non-uniform drift field during SR1, which seems to be changing due to charges building up in the PTFE panels, have been found to introduce several systematic effects altering the quality of the data. On one hand, as the charge density increases in time on the surfaces of the PTFE panels, there is a field gradient that produces a radial inward bias in the reconstruction of events. This is found to constraint the fiducial volume that can be used in any potential physics search in the detector, which in turn constrains significantly the exposure, since surface background events at the wall are pushed inwards in the detector. On the other hand, a field changing in space and time introduces variations in the process of recombination, which translates on producing corrections that

are function of time, energy, space and recoil time. A bias in the corrections for the signals leads to problems in terms of discrimination of background over potential dark matter signal candidates.

Through several studies it was first identified that there was a time-dependent problem with the event's positions resulting after implementing field distortion corrections. These effects went unnoticed for some time, but eventually were confirmed by monitoring the position reconstruction evolution of observed coordinates, which are independent of position corrections. At the same time, spatial and time dependent variations of the signals yield suggested a bias introduced in the energy correction. In order to understand if the underlying principle was related to what was observed by the LUX experiment, the hypothesis of charges accumulating at the PTFE panels, 2D and 3D COMSOL simulations were develop. By placing under scrutiny several aspects of ^{83m}Kr calibration data in comparison to simulations, several indications about this hypothesis seemed to be confirmed. For instance, that negative density charges placed in the PTFE panels, specially on the sliding ones, allows to reproduce the 24-fold under-densities features at high radii found in the XY plane, in addition to generate the observed radial inward bias affecting in the reconstructed events. As consequence, first and foremost, the procedure to correctly generate position reconstruction corrections was updated. Moreover, in order to decouple geometrical effects from field effects that were propagated for the signals energy corrections, a new procedure to calculate the electron lifetime and correct the S2 signals was introduce, through which a field-independent light collection efficiency map for the S1 signals was derived, LCE_{true}. In terms of further considerations for the update of XENON1T, all these studies have triggered different discussions and effective approaches to mitigate similar effects in the future (see section 5.4.2).

Lastly, with the help of a master student, the 3D COMSOL framework developed was used with the implementation of a Markov chain Monte Carlo routine in order to try to describe the needed distribution of charges in the detector such that they would reproduce the features observed in data. Through this work a preliminary estimation of the mean charge evolution in time was achieved.

5.4.1 Outlook

The different methods explored so far to accurately describe the drift field inside the detector at a given time, both through simulations and data, are important for several reasons. On one hand, knowledge about how the field changes in time could be used to explore a different technique to deal with the position reconstruction of events. As described, this approach would have a different underlying principle and it would be complementary to the current data driven method used. On the other hand, as the field dictates recombination, which in principle drives the production of light and charge, the continuous knowledge about how these yields are affected could be used to decouple and corrected the energy corrections at different energy scales. This would be translated not only at low energies, where it has been done so far as it is the region of interest when looking for dark matter. This could be down by incorporating tools such as NEST or by implementing a model based on measurements from XENON1T [212]and LUX [213, 214].

Given the encouraging results achieved through the COMSOL 3D model, to reproduce several features found in data and to estimate an approximate value of the charge density distribution in time during SR1, further efforts could be placed on reducing the simplifications of the model. At the expense of computational time, the 90 degrees symmetry assumption used could be drop in order to capture to a full extend distortion caused by the asymmetric distribution of charges. Instead of modeling the wires and mesh electrodes as planes having an effective potential, these elements could be described more accurately and be tuned in by using the reference from the robust KEMField simulation framework. This is important given that at the moment, the field streamlines near the top and lower corners of the TPC inherit a bias which can differ up to 3 degrees with respect to KEMField simulations, increasing the uncertainty of the position of simulated events. Furthermore, aspects such as multi-parallel computing, grid resolution and constraint on the matching algorithm used could be investigated in more detail in order to increase the extension of relevant elements included in the simulation while balancing the computational time required. As discussed in this work [206], the implementation of packages such as Cython [215], which allows the compilation of Python language into statically-typed C code, could speedup the 3D interpolation routines used almost by a factor of 7, which is one of the most time consuming procedures found in the matching algorithm. Lastly, the partial progress of the COMSOL model has draw more efforts into extending the KEMField framework in order that it can deal as well with charges accumulating at the PTFE panels. The computed charge density distributions found in COMSOL could serve as a starting point for the KEMField simulations to scan different parameter spaces to achieve more accurate results.

5.4.2 Design Feedback XENONnT

From the observations on data and simulations, it seems to be that charge accumulation happens as a consequence of the design of the interlocking system of PTFE panels. Due to the lack of contact to the field shaping rings **FSRs** or paths for the charges to be drained for the sliding panels, charges accumulating can manifest on these surfaces. In order to assure in XENONnT that there is mechanical contact of the FSRs with the PTFE panels in order to avoid this problem, it is proposed a set of 5 notches (each 10 mm in length) per panel per FSR. Then a preliminary idea is to install a small (0.5 mm diameter) hole centered in each notch. These holes are intended to facilitate a path for charges that might accumulated on the inside of the PTFE to leave the panel faster, as they would be collected on the FSRs and then be removed. Figure 5.38 (*left*) shows the respective technical drawing produced for the the mechanical sample of the PTFE panels. As discussed in [216], this idea follows the assumption that surface conductivity of PTFE is significantly higher than the respective bulk conductivity. As result of approaching this hypothesis in the way presented, the notches would be set up to correctly guide and align the FSRs and assure the expected mechanical contact even without tensioning of the FSR wires (however, possible increased levels of light leaking as consequence in the detector have to be studied).

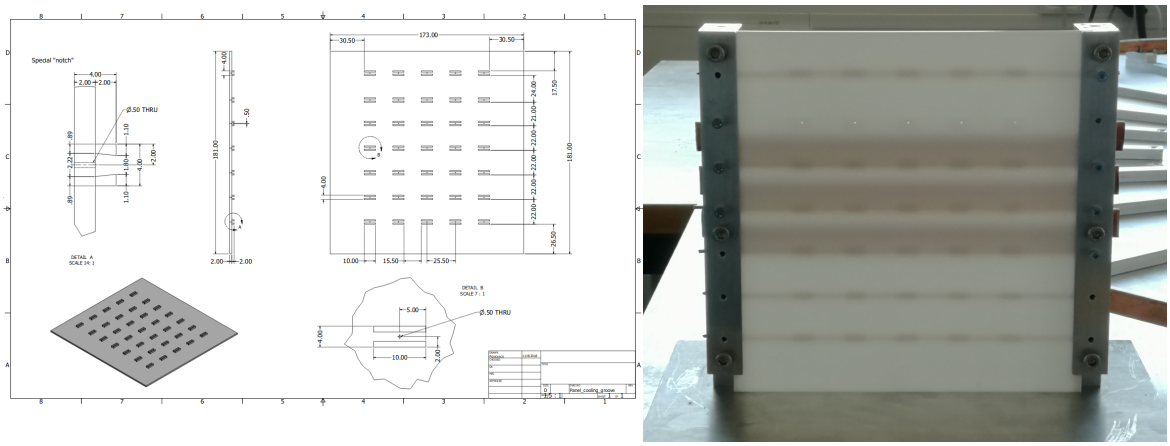

Figure 5.38. Mechanical sample of PTFE reflector including notches and holes **Left** technical drawing of sample **Right** assembled mock-up PTFE sample illuminated from the back.

Figure 5.38 (*right*) presents an assembled mock-up PTFE sample consisting of two pillars, having 15×5 mm rounded copper guards and 2 mm copper wires (FSRs). The decision on the amount and position of the holes follows the idea of optimizing the geometry, number and positions of the notches (where the FSR wires are clipped in) in the laboratory mainly on practical considerations. That is, the realization focused on having straight copper wires, that touch the PTFE but allow the panels to shrink with respect to the wires when cooled down. The holes for charge collection have to be close to the wires and should not significantly contribute to the level of light leaking inside the TPC. Hence, holes have to be placed along with the notches just in front of the FSRs. The diameter of the hole was chosen such that machining is easy but their (S2-insensitive) volume is small (effectively there are 5 rows × 24 panels × 70 FSRs = 8400 holes).

Chapter 6

Low Energy Background and Annual Modulation Studies

For any rare event search it is essential to extensively understand all different possible sources of background inside the detector. If the background rate is too high, it becomes impossible to convincingly claim a dark matter signal. Moreover, if the background is small but poorly quantified, any statistical significance can not be immediately attributed to any excess that is observed over expectation. In the context of XENON1T, background interactions lead to nuclear recoils **NR** when scattering off the Xe nuclei or electronic recoil **ER** when scattering off the atomic electrons. Up to the current generation of direct search dark matter experiments, ERs constitute the main source of background. In like manner, a new source of background has been identified as ^{222}Rn progeny can plate-out on the inner surface of the PTFE panels. The decays from ^{210}Pb and its daughters occurring directly on those surfaces exhibit charge-loss related to electrons of the S2 signal being trapped on the surface, consequently producing an S2/S1 ratio compatible with a NR.

This chapter provides an overview of the background of XENON1T, focusing on the characterization of ER background such as ^{85}Kr and Rn (section 6.1) and the understanding of the population known as "wall events", happening at the surfaces of the detector (section 6.2). Studies about these topics are followed by a summary of all relevant background, their contributions and impact (section 6.3). Additionally, one alternative model that could describe dark matter interactions with matter is based on the potential interaction with the atomic electrons of xenon. A signal would manifest itself in an annual modulation of the total electronic recoil rate. Thus, the key parameters for such analysis are described (section 6.5). Here the data selection criteria and their efficiencies were investigated, which allowed to determine the electronic recoil rate during SR1. These studies will serve as input of the subsequent statistical analysis.

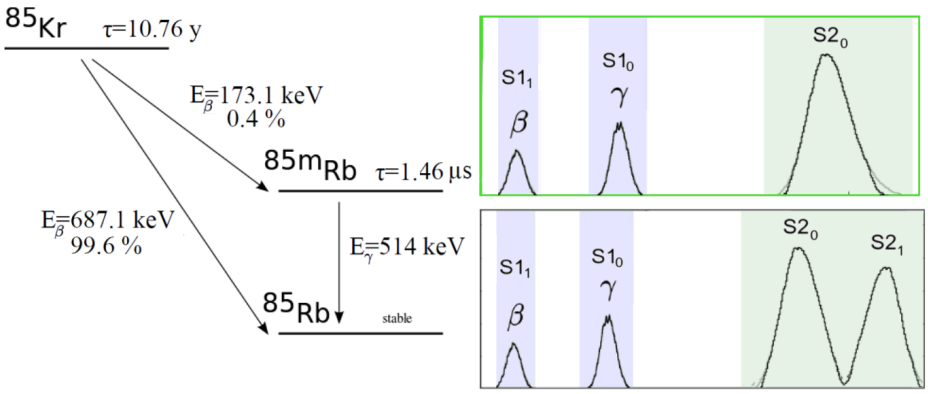

Figure 6.1. Decay scheme of ^{85}Kr. With a branching ratio of 0.4 % of the cases, it decays into its second excited level with end point energy of 173 keV and a subsequent 514 keV γ, delayed by 1.46 μs and therefore used for a delayed coincidence analysis. Different topologies accompanying the $S1_\beta$ and $S1_\gamma$ inside of a waveform can be found in XENON1T, mainly 2S1s having a merged S2, or depending on the depth of the interaction, 2S1s with their corresponding 2S2s.

6.1 Electronic Recoil backgrounds

The main origin of ER is related to sources which can be *extrinsic*, such as radioactive contamination from the materials surrounding the active volume or solar neutrinos scattering off electrons, as well as *intrinsic* due to radioactive isotopes in the LXe medium, such as ^{85}Kr, ^{222}Rn and its daughters and ^{136}Xe double-beta decays. In principle, ERs can be distinguished from NRs based on their light and charge yields. However, statistical fluctuations in terms of the produced and detected amount of light and charge translates in an imperfect distinction. These sources and their contribution are briefly reviewed in this section.

6.1.1 ^{85}Kr

Commercially produced by extraction from the atmosphere, xenon contains natural krypton at the parts-per-billion **ppb** level, which contains traces of the radioactive isotope ^{85}Kr. Almost a pure beta emitter and having a relatively long half-life of 10.76, ^{85}Kr is produced by nuclear fission and released to the air by nuclear-fuel reprocessing plants and nuclear weapons [217]. ^{85}Kr is a serious internal background because it distributes homogeneously throughout the LXe medium and when dacaying, induces low energy events that can potentially leak into the region of interest. Thus, the ^{nat}Kr/Xe has to be reduced at least to the parts-per-trillion **ppt** level by cryogenic distillation [149] in order to mitigate its contamination. One approach to identify ^{85}Kr decays in data consists on doing a delayed coincidence analysis. The estimates from this approach can serve to quantify the krypton concentration and can be compared to direct measurements obtained by the extraction of gas samples into pipettes that are measured offsite by using a rare gas mass spectrometer **RGMS** [218]. The results from these two methods are presented next.

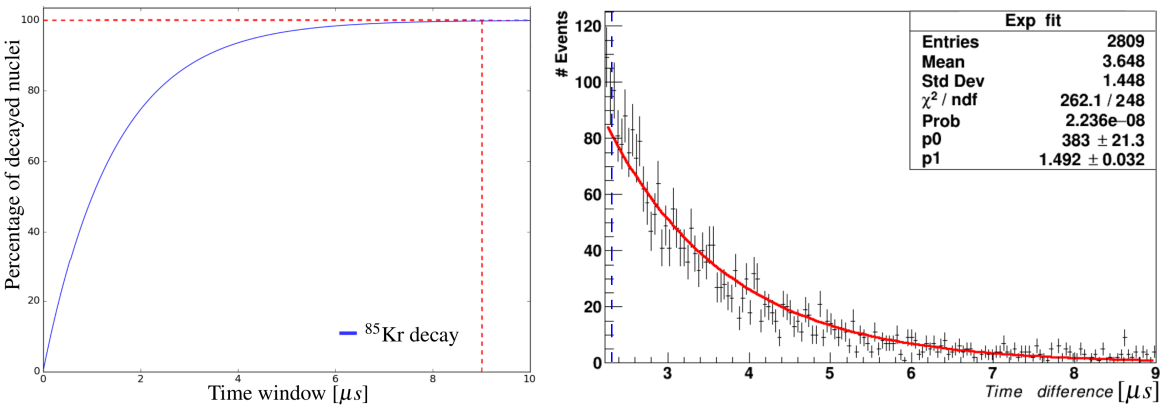

Figure 6.2. Left Exploration of the optimal coincidence time window in terms of the percentage of decayed nuclei **Right** Measured decay signature of ^{85}Kr S1s: $\tau_m = 1.492 \pm 0.032$ μs.

^{85}Kr Delayed coincidence analysis

In 99.6% of all decays, ^{85}Kr disintegrates via β-emission into the ground state ^{85}Rb with an endpoint energy of 687 keV and a half-life of 10.76 yr. In the rest of the cases, as illustrated in Figure 6.1 (*left*), it decays into its second excited level with end point energy of 173.4 keV and a subsequent 514 keV γ, delayed by 1.46 μs. Despite the small branching ratio and therefore low statistics, this signature provides a unique feature to identify ^{85}Kr.

Basic selection criteria and considerations

The selection criteria is mainly based on the time delay condition found for the two S1s detected, related chronologically to β and γ, as well as in the size of the signals measured for these corresponding S1s. At the same time, two different topologies of valid events can be found as illustrated in Figure 6.1 (*right*). On one hand, a waveform may contain only one large S2 signal peak created as an overlap of the two expected S2 signals from $S1_\beta$ and $S1_\gamma$. This is due to the fact that the 514 keV γ is emitted at approximately the same position as the β interaction vertex, and it has a mean free path of $\sim$3 cm in LXe [218]. Thus, it is possible that the difference in z-position of the two interactions is not large enough be resolved in PAX as two S2 singular peaks. In order to ensure the selection of ^{85}Kr candidates, the following criteria is used:

- **Pre-selection:** Event inside 1 t FV: $-92.9 < z < -9$ cm $\mid x^2 + y^2 < 36.94^2$ cm^2
- **Data quality cuts:** Conservatively, the *S2 width* of each signals measured has to be < 4.5 μs. Based on waveforms watching, this removes events away from the diffusion model
- **Signals range condition:** 330 keV $\leq S1_\gamma \leq$ 698 keV, while the maximal accepted energy for $S1_\beta$ is 219 keV
- **Delay coincidence condition**: Initially, the center of time of $S1_\beta$ and $S1_\gamma$ is set to a time window from 2.5 to 9 μs in which two S1 signals have to be registered. The lower threshold is

chosen such that possible background from ^{220}Rn is minimized by keeping a highest possible acceptance, while having into account the loss of acceptance probably due to leaked gas events. The upper threshold ensures that the probability of having measured the decay is close to 100%, as showed in Figure 6.2 (*left*)

After having implemented the selection criteria discussed, the half-life of those surviving events can be calculated. The fit of one collection of background data sets is used to illustrate the result obtained, as showed in in Figure 6.2 (*right*). With a measured half-life $\tau_m = 1.492 \pm 0.032\ \mu s$, the approach seems to be in agreement with the expected half-life $\tau = 1.46\ \mu s$. Therefore, this approach can be used to calculate the ^{85}Kr/ ^{nat}Kr concentration inside the detector. By assuming as true the combined acceptance extracted from a Monte Carlo simulation on the cuts used, the averaged krypton concentration is calculated by using the expression:

$$\frac{^{nat}Kr}{Xe}\left[\frac{mol}{mol}\right] = \frac{\#\text{ selected events} \cdot M_{\text{Xe}}}{N_{\text{a}} \cdot (^{85}Kr/^{nat}Kr) \cdot t \cdot \lambda \cdot a_{\text{comb}} \cdot BR \cdot m_{\text{Xe}}}, \tag{6.1}$$

where N_{a} the Avogadro number, ^{85}Kr/ ^{nat}Kr the measured isotope abundance at LNGS, t is the lifetime of the runs used, λ is the decay probability (taken as 0.000176 decays/day), a_{comb} is the combined selection cut acceptance, BR is the branching ratio of the delayed coincidence decay mode, m_{Xe} the xenon mass considered for the analysis and M_{Xe} the molar mass of xenon. Due to the low

Table 6.1. RGMS measurements. Absolute krypton in xenon extracted from LXe within the bulk of XENON1T during the different online krypton distillation periods, SR0 and SR1. These values, taken during commissioning and SR0, are showed in Figure 6.3.

Date	$^{nat}Kr/Xe$[ppt]	**Comments**
17.07.2016	530 ± 90	After liquid + gas
22.08.2016	1000 ± 200	After liquid + gas
05.09.2016	330 ± 50	After gas only
14.10.2016	190 ± 30	During upgraded gas only
08.11.2016	31 ± 6	During upgraded gas only, SR0
21.11.2016	2.6 ± 0.5	During upgraded gas only, SR0
01.12.2016	1.3 ± 0.3	During upgraded gas only, SR0
21.12.2016	0.62 ± 0.13	During SR0
16.02.2017	0.36 ± 0.06	During SR1
09.03.2017	< 0.62	During SR1
13.04.2017	0.47 ± 0.07	During SR1
25.05.2017	1.99 ± 0.31	Liquid + gas mixture, during SR1
01.06.2017	0.57 ± 0.09	During SR1
26.07.2017	0.68 ± 0.11	During SR1
29.09.2017	0.63 ± 0.10	During SR1
10.11.2017	1.09 ± 0.20	During SR1
26.01.2018	0.87 ± 0.16	During SR1

Table 6.2. Summary of the ^{85}Kr/ ^{nat}Kr concentration calculated by using the delayed coincidence analysis presented. Here each column specifies details about the conditions of the data used to derive the concentration. From left to right are presented the details about: the data taking mode used, the settings of the anode and cathode, the range in time of the data used, the exposure related to this data, the events found inside a 1.0 t FV used and finally the concentration obtained from Equation 6.1.

Mode	**Anode, Chatode [KV]**	**Date**	**Exposure [hr]**	**Events in FV**	$\frac{^{nat}Kr}{Xe}\left[\frac{mol}{mol}\right]$ 90%C.L.
Background	A,C = 4,-15	(23-28.07)	89.1	19	$696.59^{+164.98}_{-146.65}$
DST Liquid + Gas	A,C = 4,-15	(12-22.08)	183.1	66	$1177.36^{+285.42}_{-231.90}$
DST Gas	A,C = 4,-13	(25.08-02.09)	141.6	12	$276.80^{+121.10}_{-103.80}$
Only circulation	A,C = 4,-15	(03-08.09)	104.0	11	$345.47^{+109.92}_{-94.22}$
Background	A,C = 4,-13	(16-23.09)	76.0	4	$171.91^{+219.21}_{-128.93}$
Background	A, C = 4,-12	(23-28.09)	98.9	4	$132.16^{+176.21}_{-99.12}$
Background	A,C = 4,-12	(04-08.10)	127.9	8	$204.30^{+153.23}_{-127.69}$
^{220}Rn source closed	A,C = 4,-12	(14-20.10)	93.3	4	$140.09^{+185.07}_{-70.05}$
Start AmBe	A,C = 4,-12	(23.10-28.10)	119.0	9	$247.12^{+164.75}_{-82.37}$
Start DST, Bulk (AmBe)	A,C = 4,-12	(28.10-02.11)	90.5	6	$216.51^{+180.43}_{-90.21}$
AmBe	A,C = 4,-12	(02.11-11.11)	188.7	5	$86.56^{+69.25}_{-34.63}$

rate found after this selection, the probability function for the number of measured events follows a Poisson distribution. Thus, to estimate the errors the confidence regions have been computed with the graphical maximum likelihood method [219]. This is done by selecting the values at which the log-likelihood function *logL(N)* decreases by 2.71/2 for 90%, and by 3.84/2 for 95% C.L., from its maximum value *log(L)max*.

Results commissioning phase and SR0

With the intention of testing if the distillation column developed for XENON1T and XENONnT [149] could effectively remove ^{85}Kr, the xenon used from the start of the operation of the detector (in the commission phase) was not distilled. Instead, the performance of the distillation pump was tested during this phase. The results from the RGMS summarized in Table 6.1, whose satisfactory performance was already established [220], proved the reduction of the krypton concentration in LXe from a maximum of (1.0 $\pm$ 0.2) ppb , down to a sub-ppt level concentration with (0.36 $\pm$ 0.06) ppt. These measurements provided a comparison reference for the calculated concentration with the delayed coincidence method described, summarized in Table 6.2.

The concentrations obtained from the RGMS (red) and the delayed coincidence method (blue) are compared in Figure 6.3. Despite the systematic uncertainties altering the ^{85}Kr/Xe concentration, related to the acceptances, the ^{85}Kr/^{nat}Kr ratio, to the decay constant and modeling of the beta spectrum in order to define the selection range, before distillation (when krypton was the most dominant background), both methods seem to be in agreement. However, as distillation makes ^{85}Kr sub-dominant, the number of events that can be found are too low such that the uncertainties dominate the result and this method is not longer handy. As result, it was decided that for SR1 only RGMS measurements would be used to have an indication about the ^{85}Kr/Xe concentration.

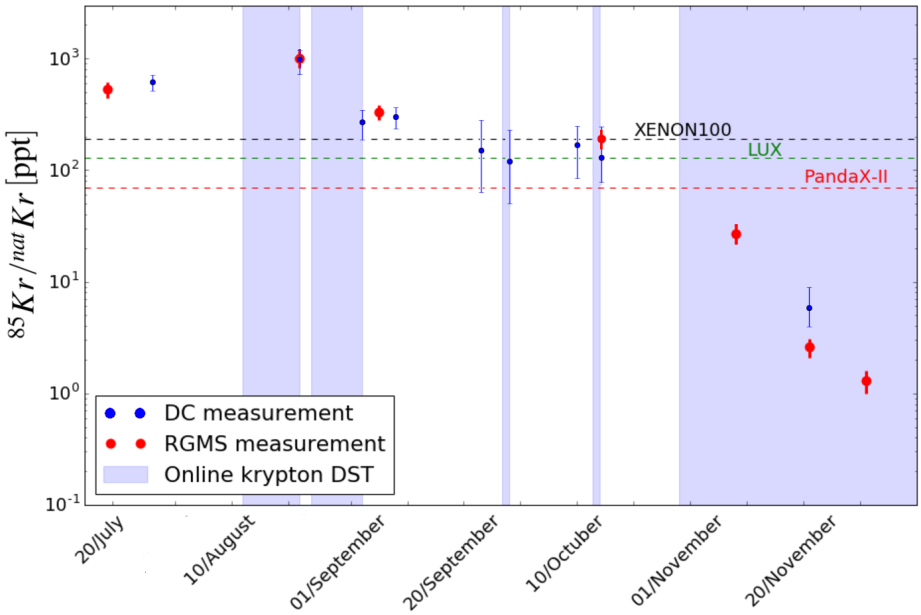

Figure 6.3. Average krypton concentration evolution obtained from a delayed coincidence analysis (blue) and from RGMS measurements (red) during commissioning and SR0. Online distillation campaigns (blue shaded area), while the achieved backgrounds of XENON100 [185] (black), LUX [194] (green) and PandaX-II [221] (reed) are visualized for comparison.

Results in SR1

For SR1, assuming the trend as given by the data (without fitting an assumed evolution model), the average value was weighted by the time-period each measurement spanned. Since it was regularly taken (approximately equally time-spaced), a simple mean values was used. The result corresponds to ^{85}Kr/Xe = (0.66 $\pm$ 0.11) ppt, where the uncertainty is dominated by the 17% systematic error on the absolute concentration of the reference sample in the RGMS measurement [218]. A conversion factor from ^{85}Kr/Xe concentration to ^{85}Kr event rate, ζ, was derived from simulation in the MC paper assuming a ^{85}Kr/^{nat}Kr ratio of 2×10^{-11} mol/mol and ^{85}Kr/Xe = 0.2 ppt, resulting in ζ = 38.5 μdru/ppt.

Before the last few online distillation campaigns when the ^{222}Rn was sub-dominant ($\sim$ 0.2 mdru[1]), ER rate measurements gave (31.86 $\pm$ 0.64) mdru with a corresponding RGMS ^{85}Kr/Xe concentration of 1000 ppt, such that:

$$\zeta' = \frac{(31.86 \pm 0.64\ mdru)}{(1000 \pm 200\ ppt)} = (31.86 \pm 6.4)\mu dru/ppt, \tag{6.2}$$

Then, the ^{85}Kr/Xe concentration can be converted to ^{85}Kr event rate as:

$$\begin{aligned} \text{Rate} &= (^{nat}Kr/Xe) \times \zeta' \\ &= (0.66 \pm 0.11)ppt \times (31.86\mu dru/ppt) \times (1000\ \text{kg} \times 365.25\ \text{day}) \\ &= (7.7 \pm 1.3)ytu \end{aligned} \tag{6.3}$$

where the uncertainty on ζ' ignored because it is dominated by the RGMS systematic in the denominator and thus should mostly cancels out the correlated systematic on the ^{85}Kr/Xe factor in the numerator.

6.1.2 ^{136}Xe

Naturally occurring xenon consists of seven stable and two long half-lives radioactive isotopes, ^{124}Xe and ^{136}Xe. Natural xenon consists on 0.095% of ^{124}Xe and 8.9% of ^{136}Xe, from which the latter is a two-neutrino double-beta emitter with a Q-value of 2458 keV (and from those two isotopes is the only one relevant in XENON1T). Having a half-life of 2.17×10^{21} years, at low energies the expected average background rate in the energy region (1 - 12) keV is (0.84 $\pm$ 0.13) Events/(t$\times$yr$\times$keV) [180].

6.1.3 Radon

Being part of the ^{238}U and ^{232}Th chain, ^{222}Rn and ^{220}Rn progeny can pose as intrinsic background sources for low energy rare rare event searches (particularly ^{222}Rn). Trace amounts of these radioisotopes can be found to different degrees in every material or substance on Earth. Once formed, these gaseous isotopes can emanate out of the material they were produced or diffuse into the active search volume, thus distributing themselves homogeneously. Therefore, low energy background experiment such as XENON1T use only radiopure materials in order to minimize the number of background events. Figure 6.4 illustrates the ^{222}Rn decay scheme together with the information of each isotope most likely decay channel. The greatest threat from the ^{222}Rn progeny lies in the decays from ^{214}Pb and ^{214}Bi, as they may undergo into a naked or semi-naked β-decay. The former refers to a decay without emitting a γ-ray, thus it is impossible to veto. In the latter, a γ-ray is emitted but it has such high energy that it is most likely to escape the active region, such that it is as well difficult to veto and identify. Moreover, ^{214}Pb and its daughters may adhere to material surfaces (plate-out), leading to (α, n) reactions inside the active volume.

[1] To simplify the notation, dru = Events/(kg$\times$day$\times$keV) while ytu = Events/(t$\times$yr$\times$keV$_{ee}$).

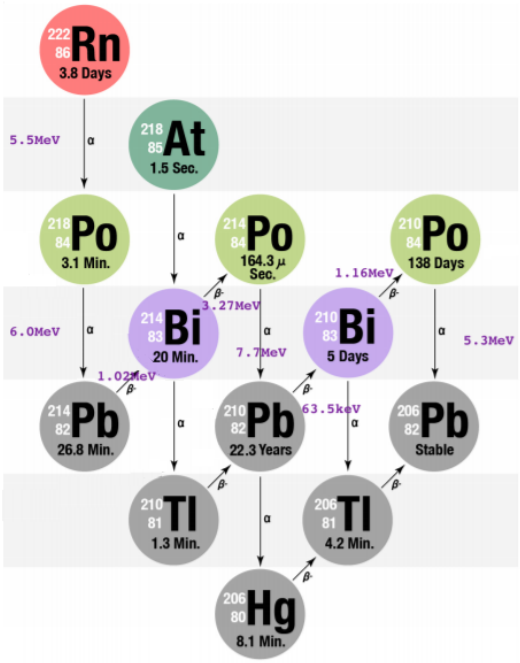

Figure 6.4. ^{222}Rn decay chain. With a half-life of 3.8 day, ^{222}Rn can disperse homogeneously inside the active volume. Inside its chain, the subsequent β-decays from ^{214}Pb and ^{214}Bi represent a direct contaminant to the low energy background since they may undergo into a naked or semi-naked β-decay, or after having out-plated in the surfaces of the detector, they may lead to (α, n) reactions that can mimic a NR. Taken from [187].

In XENON1T, the main goal is to calculate the concentration of ^{214}Pb. One approach to do this consists on measuring the concentration of ^{222}Rn, ^{218}Po and ^{214}Bi/^{214}Po inside the active volume. On one hand, α-decays are very energetic events (even compared to γ-rays). Thus ^{222}Rn and ^{218}Po can be identified quite straightforward. On the other hand, given that the half-life of ^{214}Po is short (164 μs), the β-decay of the mother nuclei ^{214}Bi is promptly followed by the α of the ^{214}Po decay. Since its half-life is within the typical time-window of recorded events, their unique topology allows for their event identification (referred to as BiPo coincidence). As ^{214}Pb decay happens between ^{218}Po and ^{214}BiPo, both measurements act as upper and lower limit respectively, given that not all isotopes can be identified as some can stick to the cathode and not reenter the FV. The second approach consists on fitting the MC spectrum of ^{214}Po to the data.

Each α peak found in data can be fitted using a Gaussian, having as mean value the Q-value of the decay. This is true for all alphas but ^{210}Po. As it is deposited on the walls, this is fitted by a a Crystal Ball [222]function (consisting of a power law tail stitched to a Gaussian core function, created specifically to describe energy loss processes). A full summary of the result is presented in Figure 6.5. Here the rate of the three targeted daughters discussed has been monitored during SR0 and SR1. The evolution of the rate is stable over (without considering a period of ^{222}Rn distillation). After radon distillation, the rates went back to the nominal value just before distillation had started. The maximum and minimum decay rate of ^{214}Pb was determined to be (12.6 $\pm$ 0.8) and (5.1 $\pm$ 0.5)

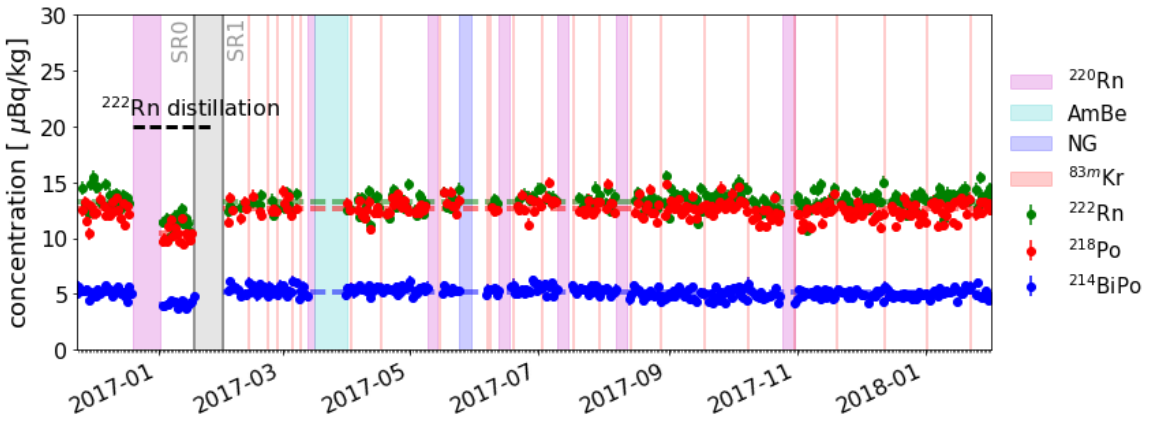

Figure 6.5. Radon monitoring of the rates from ^{222}Rn (green), ^{218}Po (red) and ^{214}BiPo (blue) in order to constraint the rate of ^{214}Pb, the most dominant background for dark matter search due to its β-decay nature. Adapted from [223].

μBq/kg, estimated from the first approach described, by measuring the concentrations of the ^{218}Po α-decays and time-coincident ^{214}BiPos, respectively. This corresponds to an event rates in the dark matter region of interest of (71 $\pm$ 8) and (29 $\pm$ 4) Events/(t$\times$yr$\times$keV$_{ee}$).

6.2 Surface backgrounds

The next generation of low background dark matter detectors operating deep underground aim for unprecedented low levels of radioactive backgrounds. Despite the background reduction success achieved so far by the online krypton and radon removal distillation program used in XENON1T [149, 224, 150], together with an intensive material screening program [148], the deposition and presence of radon progeny on the detector's surfaces presents itself as one of the next generation challenges. Widely observed by others experiment [225, 226], this background not only constrains enlarging the fiducial radius of analysis and making use of much more exposure, but it also introduces a harmful background source that can mimic a nuclear recoil. In this section, the possible physical source of these events is explored with the hypothesis that those events are due to ^{210}Pb beta decays from the surfaces of the detector. As control populations to understand events at the wall, ^{83m}Kr, ^{210}Po and background data will be used to understand in detail this population.

6.2.1 ^{210}Pb beta decays as the origin of surface events

Surface contamination created during phases such as machining, assembling or storing of different detector components, can be in general mitigated or removed via mechanical or chemical surface treatments [227]. However, it has been observed that it is almost impossible to avoid the exposure of the detector parts to ambient air during these phases. Thus, with a half-life of 3.8 days, large amounts of decay daughters from atmospheric ^{222}Rn can plate out on the detector surfaces. Subsequently, the

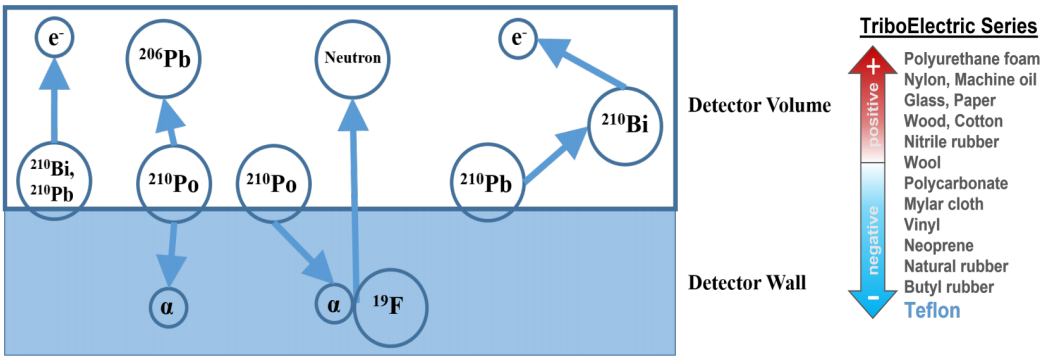

Figure 6.6. Decay reactions from radon daughter plate-out on the surface of a detector wall and triboelectric series, illustrating that since PTFE is one of the most negative in the spectrum, it is a material that tends to attract negative charges. Taken from [229].

decay of long-lived ^{222}Rn daughters, such as ^{210}Pb can lead to wall background events during the operation of the detector. In comparison, the concentration of constantly emanating ^{222}Rn from the detector components during operation is significantly smaller than the ones measured in ambient air. Therefore, the described plate out effect is minor from internal ^{222}Rn that can be traced to the emanation and diffusion of gaseous components such as ^{222}Rn (in the context of XENON1T, the CRY system is a major emanation source, especially the cryo-pipe and the porcupine along with cables. Likewise, the PUR system, mainly due to the QDrives, the PMTS, bases, PTFE and the getter [228]).

Once ^{222}Rn is inside the detector, regardless of the way it got in, it decays into ^{210}Pb in a short time ($\sim$ 1 hour) emitting four alphas, it was showed in Figure 6.4. With a 22.3 yr half-life, ^{210}Pb is found to be deposited on the walls and cathode of the detector, where it decays at a constant rate within the lifetime of the XENON1T experiment. Illustrated in Figure 6.7, the following are the possible reactions from radon plating-out:

- ^{210}Pb on the surface may generate low energetic betas and X-rays (see Figure 6.7), while ^{210}Bi, as a pure beta emitter having a characteristic decay with and endpoint of $\sim$ 1.2 MeV, may as well. In both of these cases, an electron is release into the detector volume that can generate an ER signal
- When ^{210}Po decays, it emits an energetic alpha together with a ^{206}Pb nucleus having 103 keV energy into the detector volume (this can result in a continuum of NR signals)
- Likewise, the α-particle resulting from ^{210}Po may interact with fluorine atoms. As result, this would cause neutron emission in the detector volume via (α,n) reaction
- Lastly, the β-decay of ^{210}Pb on the surface may release a ^{210}Bi nucleus into the detector volume, where it can subsequently decay as a naked β-decay

All these different reactions can threaten the dark matter search, and therefore, understanding these backgrounds produced at the PTFE is crucial. This resonates further in XENON1T because the

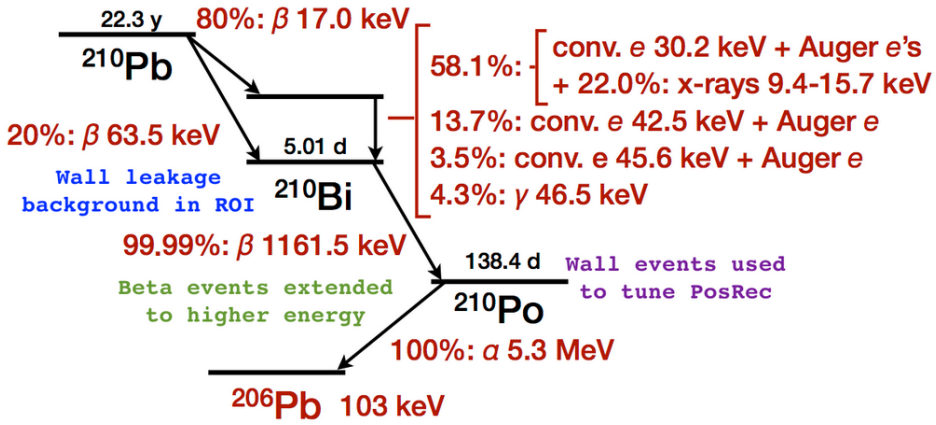

Figure 6.7. Detailed ^{210}Pb decay scheme. Originally this isotope can be used to tune the position reconstruction with ^{210}Po sited at the wall (purple) and it can produce background to the region of interest ROI in terms of wall leakage via low energetic β-decays (blue) or betas extended at high energy (green). Adapted from [230].

total surface area of PTFE in contact with LXe is ~ 3 m^2. Since PTFE has the strongest tendencies in the triboelectric series to acquire negative charges upon contact [200], and radon progeny tend to be positively charged (about 88% of the time), thus more radon daughters are expected to plate-out onto PTFE than onto other materials. Overall, given that these daughters physically originate from the walls, they can be used to characterize the events happening at the walls.

Method

When dealing with the ^{222}Rn decay chain, it is assumed that after a fixed period of time, secular equilibrium takes place and all the elements have the same activities, such that the activity of ^{210}Pb, and ^{210}Bi beta decay, is the same as ^{210}Po alpha decays (see Figure 6.7). Given that it's relative easy to identify ^{210}Po alpha events inside the XENON1T detector, the first step to understand these background was to identify and select ^{210}Po alpha events. If possible, they could help to determine the activity of the ^{210}Pb decay chain, together with provide information for a charge-loss model on the PTFE surfaces.

Data and basic selection criteria

For this analysis SR1 background data processed under PAX version 6.6.5 and 6.8.0.

- **Pre-selection:** z-cut: $-92.9 < z < -9$ cm
- **Data quality cuts:** *S2 width* and *S2 area fraction top*, both used to prevent gas events, accidentally coincidences, events with unphysical drift time
- **^{210}Po energy selection:** cS1 > 0 PE, cS2 > 0 PE, cS1 < 1×10^4 PE, $cs2_b < 1\times10^6$ PE

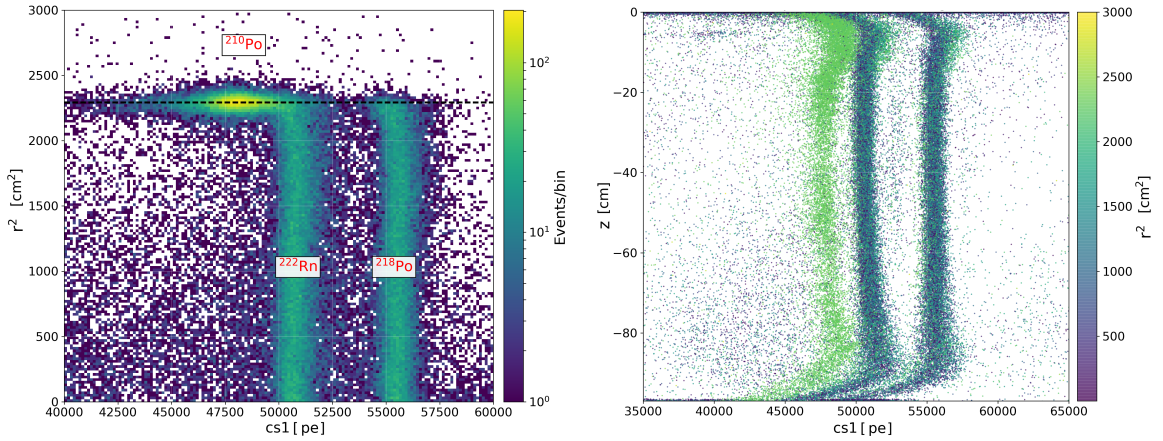

Figure 6.8. Distribution of alpha daughters from ^{222}Rn decay. The three populations showed from left to right correspond to ^{210}Po, ^{222}Rn and ^{218}Po. **Left** cS1 vs radius squared distribution used to identify ^{210}Po, produced at the wall from its decay related to ^{210}Pb **Right** Distribution of the three alphas across the entire depth. For the three alphas detected, traces of saturation can be still observed close to the anode or to the cathode, where the response to correctly reconstruct these signals is smeared and bended.

^{210}Po events identification

The first step consisted on introducing a *saturation map* in order to mitigate and correct the PMTs response for energies. Thus, the cS1 for alphas is not fully saturated and distorted [231]. As showed in Figure 6.8 (*left*) when plotting the distribution of events in cS1 vs radius squared, three alpha populations can be identified up to 6×10^4 PE. These three signatures correspond to ^{210}Po, ^{222}Rn and ^{218}Po events. While ^{222}Rn and ^{218}Po are distributed across the entire radius, as well as across the entire depth of the detector as illustrated in Figure 6.8 (*right*), ^{210}Po can be identified as the only one produced at the wall. Those events, identified as surface background events, are studied next.

As discussed in Chapter 4, the shape of the deposition of energy of a mono-energetic signal in the cS1 vs cS2 parameter space should be ellipse-like due to the anti-correlation between light and charge. In the context of these alphas, the energy spectrum is visualized in Figure 6.9 (*a*). The first feature that can be recognized for the ^{210}Po distribution is that it is significantly smeared out from lower to higher S2 signal values, opposite to what is observed for ^{222}Rn and ^{218}Po daughters, where their energy deposition is relatively well localized. This seems to suggest that events having a S1 related to an α from ^{210}Po are either paired with uncorrelated peaks with different S2s values, or that the S2 found for these events has suffer the lost of charge during its drift or while being produced. The former explanation fails to explain that as expected, the ^{210}Po events identified are distributed correctly in the depth and radius. The latter explanation hints towards charge being effectively lost (this effect will be referred to as charge-loss). In order to differentiate between the expected and found location of the alpha distributions, the condition of cS2 $> 7.8\times10^4$ PE has been used such that events above this values, where the energy reconstruction of an α is expected to be, are plotted with a transparent mask.

As presented in Figure 6.9 (*b*), more information can be extracted when analyzing these events in the discrimination space as function of the radius. As illustrated for the two differentiated populations,

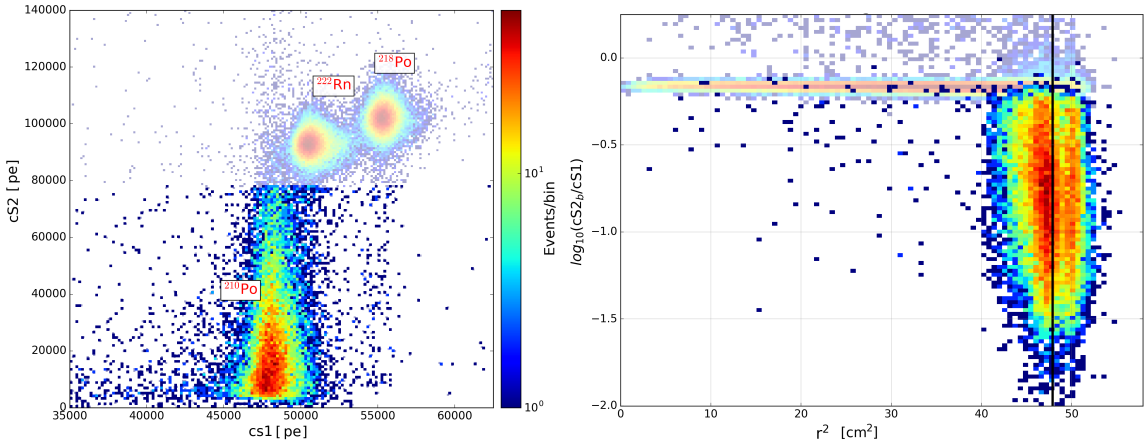

(a) Energy distribution deposition for α's from ^{222}Rn **(b)** Charge-loss pattern for ^{210}Po

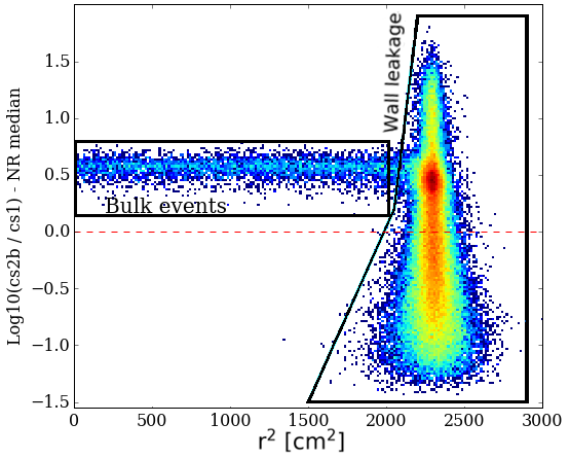

(c) Charge-loss pattern for background data

Figure 6.9. Distribution of ^{210}Po, ^{222}Rn and ^{218}Po alpha events in (**a**) cS1 vs cS2 energy parameter space, where a diminished trend for the S2 of the ^{210}Po distribution is found (**b**) Discrimination space, where the denominated surface events show their potential to leak into having charge-loss (**c**) Distribution of ^{210}Po alpha events located at the wall along with in the discrimination space, as well as background data for 200 $\leq$ cS1 $\leq$ 300 PE, using standard quality cuts and a z-cut given by: - 92.9 $<$ z$<$ -9 cm. Two clear populations can be identified, events at the bulk consisting on Kr leaked event (contamination from ^{83}Rb) while wall events are related to alphas.

the well behaved ^{222}Rn and ^{218}Po alpha distributions feature a constant ratio for their charge and light across the whole radius. In fact, this happens generally for other data, as showed in Figure 6.9 (*c*), or in mono-energetic depositions of energy as also encountered for ^{83m}Kr in Figure6.14 (*c*). However, as complete opposite, events suffering charge-loss are characterized because they are spread in a long tail across the whole ratio axis of charge and light. Although it is true that the majority of them lie near the TPC radius, their leakage can reach several cm inwards. Thus, these events represent a threat for the dark matter region of interest given that they have the potential to leak/be found almost anywhere in the discrimination space. Furthermore, it is also important to consider that if charge accumulation is not treated correctly, as it was proposed in section 5.2.1, the inward bias produced

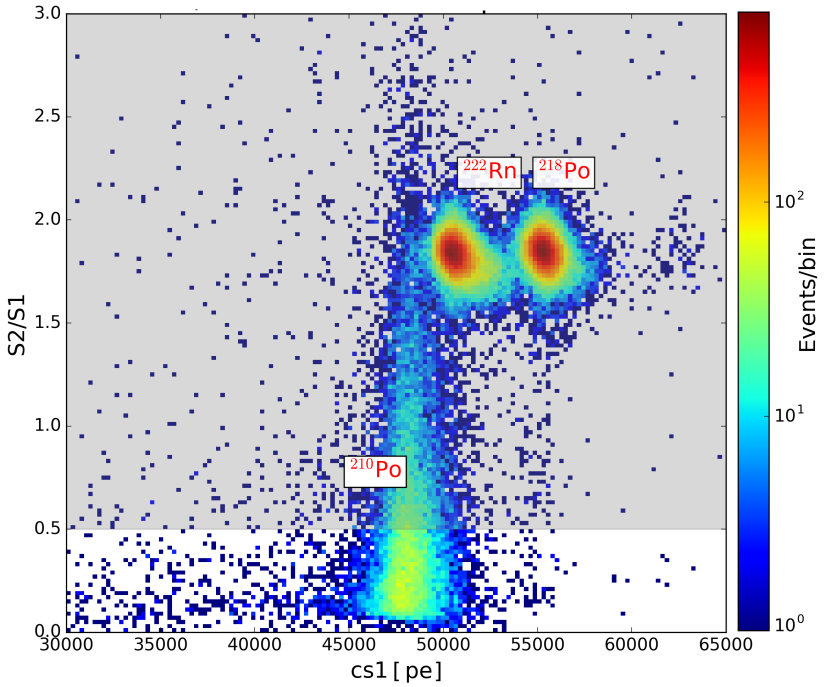

Figure 6.10. Charge to light ratio S2/S1 for the alpha population found at high energies. Here are identified ^{222}Rn, ^{218}Po and the partially degraded population of ^{210}Po. In this space, alphas should be normalized to the same ratio.

by the distortion of the field lines as charges accumulate can as well affect severely any search by reconstructing these wall events away from the wall. This effect is enhanced by a limited position reconstruction resolution.

Charge Loss Function CLF

As explored working together with Fei Gao, an interesting quantity regarding the wall leakage events is the charge loss function **CLF**. Since a full understanding of the underlying mechanism of charge-loss has not been achieved yet and a detailed simulation to estimate this CLF is out of the scope of this work, a data-driven approach was explored to reconstruct it. The biggest constraint to calculate CLF is that a reliable emission model for alpha events is not available, therefore it can not be estimated by dividing the detected electrons with emitted electrons. Nevertheless, the relative CLF can be estimated from considering the S2/S1 ratio from the previously selected alpha population, as illustrated in Figure 6.10. Here two distinctive features can be recognize:

1. For ^{222}Rn and ^{218}Po events, the S2/S1 value seems to align well close to ~ 1.8
2. For ^{210}Po, however, the S2/S1 value extends to much lower values. However, the S1s signals seem to be rather constant despite that the ratio S2/S1 changes. This is supported by the fact that when projecting the energy distribution in terms of cS1, and using a Crystal ball function in addition to two Gaussians [231], the light yield of the α daughters can be determined. The

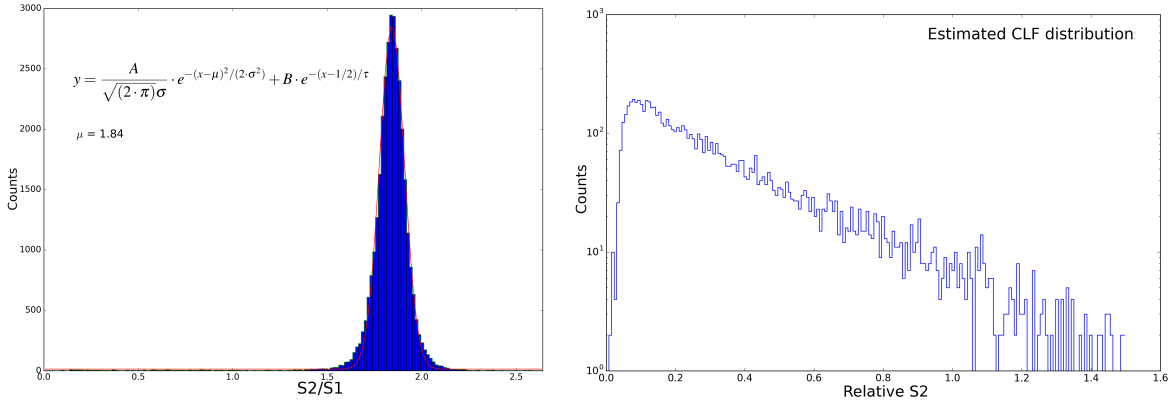

Figure 6.11. Estimation of the charge loss function derived by using the population from ^{222}Rn and ^{218}Po. **Left** The function explored is obtain by fitting the spectrum together with a energy smearing **Right** The estimated predicted normalization from the CLF derived.

results demonstrates that $LY_{^{222}Rn}$ = (9.05 $\pm$ 0.01) PE/KeV, $LY_{^{218}Po}$ = (9.06 $\pm$ 0.01) PE/KeV and $LY_{^{210}Po}$ = (8.89 $\pm$ 0.02) PE/KeV. Thus, the difference in yield between ^{222}Rn and ^{210}Po is less that 2%.

Under these observations, the following could be hypothesized and explored for the charge loss process:

- The edge effect does not affect the recombination greatly (as pointed out by the $\lesssim 2\%$ change of the ^{210}Po with respect to ^{222}Rn). This is because even if an electron or ion is attached on the wall during the recombination stage, it can still absorb other electrons/ions to recombine. Hence, the reason why the S1 signal is not affected
- After recombination, many electrons and ions are still on the wall and can hardly be extracted by the small electric field applied in the detector[2]. Thus the collection efficiency is not unity at the edges

Hence, the CLF is derived by normalizing the S2/S1 values to the one from ^{222}Rn and ^{218}Po, as shown in Figure 6.11 (*left*). Since S1 is no affected for alpha events, the relative S2/S1 values can be used to estimate the distribution of CLF. The CLF distribution derived by this method is shown in Figure 6.11 (*right*). Due to energy smearing, the CLF values can be larger than unity. The true CLF values may be calculated using unfolding techniques [232]. In this approach, a convoluted energy resolution to the observed spectrum is fitted. The functional form for this expression is:

$$y = \frac{A}{\sqrt{(2\cdot\pi)}\sigma} \cdot e^{-(x-\mu)^2/(2\cdot\sigma^2)} + B \cdot e^{-(x-1/2)/\tau}. \tag{6.4}$$

The CLF parametrization found can be used to predict the S2 vs S1 distribution for all events happening on the wall. One particular interest are the β-decay events from ^{210}Pb on the surface since

[2]Unfortunately, XENON1T did not reach the -100 kV design goal on the cathode, but -12 kV (-8 kV) for SR0 (SR1).

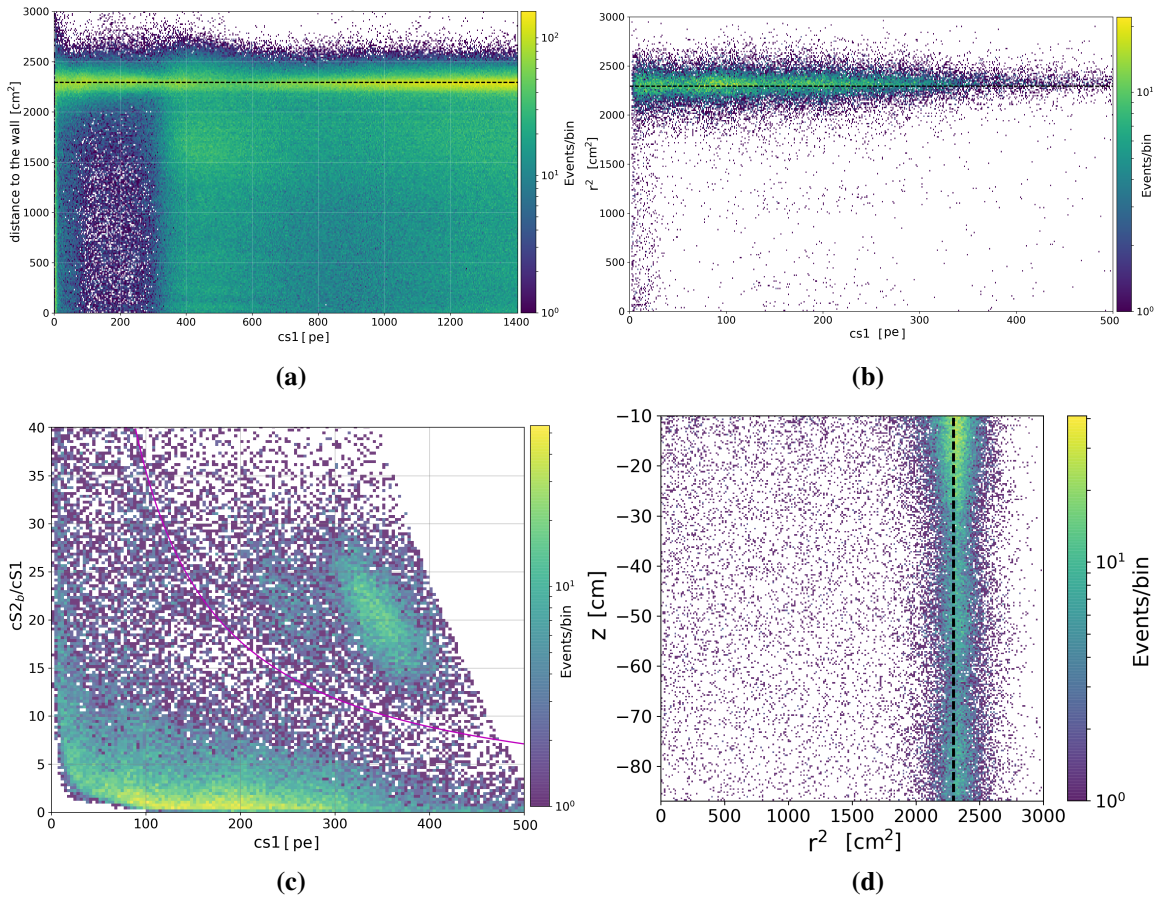

Figure 6.12. Selection procedure to isolate β-decays from the ^{210}Pb chain. (**a**) Initial distribution of events at low energy deposition in terms of the distance to the wall. A clear population is always found at high radii, most likely related to betas and gammas (**b**) Isolated β-decays after ad hoc selection (**c**) Discrimination space as function of energy cS1 in order to discriminate between ER-like events and wall events (**d**) Distribution of selected β wall events.

they may release a ^{210}Bi nucleus into the detector volume, where it can subsequently decay as a naked β-decay, becoming a threatening background for the dark matter search region of interest. Before trying to build a full background model for wall beta events along the CLF, it can be investigated first whether the observed events in the detector are consistent with the β-decays from the ^{210}Pb chain. This is explored in the following section by using SR0 background data.

To begin with, a similar selection to the specified for ^{210}Po events is used. Although the energy region that will be explored next is not specifically the region of interest for dark matter search, it is low enough to perform the β-decay searches, with a maximum range of $\sim$ 400 keV. Figure 6.12 (*a*) shows the corrected S1 signal as function of the radius squared. From the color scale, it can be recognized that a larger event distribution is always seen at the edge of the detector. It can be argued that this edge population is due to the contribution from γ's Compton scattering, however, these events the β-decays pursued). Now, the specific distribution of events to inspect after the selection is done in

the discrimination space. Without a FV cut, no clear indication of the guidance of an ER band can be identified (as expected). However, a large population of *surface leakage events* (also called wall events) can be identified since they have abnormally small S2/S1 values (specifically, the population delimited in cS1 from 75 to 300 PE between S2/S1 values in 0 to 5). A rough cut on S2/S1 (purple) is used to separate those leakage events from mono-energetic depositions of energy (this definition was originally motivated in the context of ^{83m}Kr, as showed in Figure 6.14 (*c*), where ^{83m}Kr events undergoing charge-loss are located below this line).The distribution of events above this line is mainly made of the energy deposition from ^{83m}Kr and energetic gamma peaks, activated xenon lines, etc, observed throughout the whole detector.

The position distribution of the events selected after introducing this ad hoc cut is presented in Figure 6.12 (*d*). This confirms that the majority of events selected are indeed located at the wall. To provide further evidence that they are most likely induced by β-decays, Figure 6.12 (*b*) illustrates the energy distribution of these events as function of the radius squared once more. Two arguments can be mode from these observations:

- The population selected, spread up to 300 PE and located specifically at the wall, is consistent with Q-value of different ^{210}Pb decays. A more detailed check on the S1 energy spectrum will follows below. The S1 spectrum for events near ER band is relatively flat.
- When in turn the events above the ad hoc cuts investigated such as it was done in Figure 6.12 (*a*), in terms of their energy cS1 as function of radius squared, it is found that at larger S1 regions, these normal ER events can extend to much inner radii than the wall leakage events just characterized. This is because the wall events are dominated by betas on the wall while the ER events are dominated by gamma Compton scatters that can penetrate several cm in liquid xenon. If the wall events are also induced by the same gamma events, it would be expected for those events to extent further in radius as their S2 is much smaller than events closer to the ER band

In order to confront these arguments, next it is checked how consistent the S1 spectrum in comparison to the expected spectrum from the ^{210}Pb beta decay chain. If this distribution is verified, This model could be used to describe the wall leakage events with a solid underlying physics background. This check has to start having a closer look into the ^{210}Pb decay chain. If the decay happens inside the active volume, the expected spectrum should be determined from a pure β-decay with a Q-value of 63.5 keV (BR $\sim$ 20%) and the β-decay with Q-value of 17 keV accompanied by 46.5 keV energy depositions (BR $\sim$ 80%). However, the energy spectrum becomes more complicated when the ^{210}Pb decays on the surface of PTFE. This only matters for the 17 keV recoils decay modes. For each of the particles: β electron, X-rays, internal conversion electrons, auger electrons. They can propagate either to the inner side of the detector (or vice versa). The combination of those gives a full energy spectrum inside the liquid xenon detector.

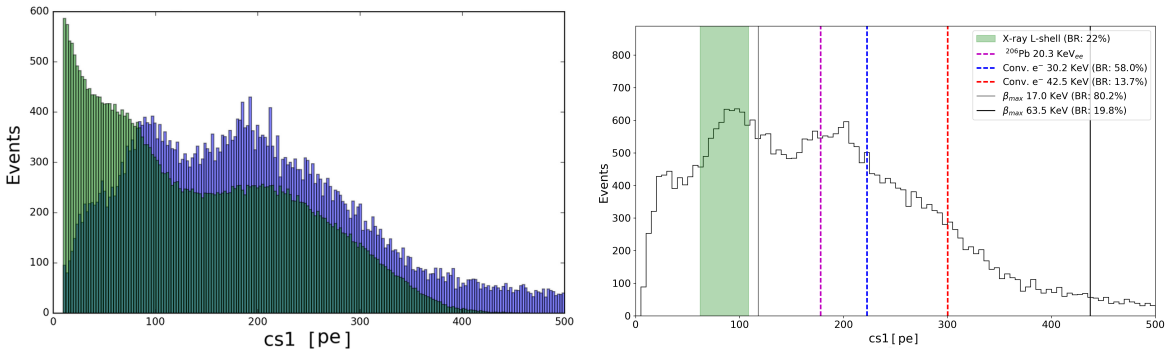

Figure 6.13. Left Expected ^{210}Pb beta spectrum from simulation **Right** Scan on the resulting energy spectrum in terms of the expected features measured in cS1, after the deposition of energy was converted using NEST (following Table 6.3).

Table 6.3. Decay products of ^{210}Pb with their energy and probability. Values taken from [222]. The highly energetic values from α events have not been calculated as they are not included in the analysis window.

	Decay	Main	Secondary	Energy [keV]	cS1 [PE]	Prob [%]
^{210}Pb						
	β			17.0	118.12	80.2
		γ		46.53	-	4.252
		conv. e		42.54 - 43.95	297.56 - 307.18	13.65
		conv. e		45.60 - 46.38	318.27 - 323.53	3.50
		L-shell IC		30.15 - 33.12	212.26 - 232.95	58.0
			Auger L-shell	8.15	52.50	28.0
			X-ray L-shell	9.421 - 15.708	61.98 - 108.64	22.0
	β			63.5	437.27	19.8
^{210}Bi						
	β			1161.2	6772.39	99.99
	α			4650	-	8.4×10^{-5}
	α			4687	-	5×10^{-5}
^{210}Bi						
	α			5304.33	-	99,99
	α			4516.70	-	1.2×10^{-3}
^{206}Pb	NR			20.3 (97.9 keV$_{nr}$)		

Thus the expected energy spectrum was calculated by a combinations of the decay particles in a fast toy MC (following the Fermi theory of beta decay). The resulted spectrum (green histogram) is presented along the observed spectrum (blue histogram) in Figure 6.13 (*left*). Unfortunately, the assumptions explored concerning the wall events having as main source the ^{210}Pb decay chain was not confirmed. Although a more detailed simulation, for instance Geant4, could provide a spectrum

that would agree much better to the one from the isolated population explored, fundamentally it seems that without a deeper understanding of the complicated decay structures and unknown underlying mechanism of charge-loss it is not possible to postulate a physics background-based model. Therefore, in section 6.2.3, the details of a data-driven approach are reviewed.

Furthermore, In order to understand better the control sample procedure discussed for future studies, a scan on the resulting energy spectrum in terms of the expected features measured in cS1 (after the deposition of energy was converted using NEST), can be performed. Figure 6.13 (*right*) presents the spectrum derived with the previous selection presented, together with demarcations where signals from the ^{210}Pb beta decay chain would be expected. Specified in detail in Table 6.3, the expected signals were included in the spectrum measure: X-ray L-shell (green band), the signature from the ^{206}Po nucleus after it has recoiled back from the decay of ^{210}Po (dashed purple), the maximum of the 17 keV (gray line) and 63.5 keV β (black line) betas, and from the 39.2 keV (dashed blue) and 42.5 keV (dashed red) conversion of electrons. The result suggest that the low energy X-ray from the L-shell and perhaps the ^{216}Po recoil are partially observed, while the rest of the features of the decay chain are difficult to identify. Thus, once more, a data-driven approach may be better suited to describe this background until further knowledge is found.

6.2.2 Characterization for charge loss with ^{83m}Kr

Complementary to the studies presented in the context of ^{210}Po and ^{210}Pb in order to further understand more about charge-loss, ^{83m}Kr calibration data was used as well for this characterization given that it distributes uniformly through the TPC and thus it does as well close to the walls. The main intention was to obtain more hints that could be used in the data-driven description of this background. Using the same data selection outlined in Chapter 4, 34.8 live hours of ^{83m}Kr (corresponding after pre-selection to 491825 events) taken on April were used to characterize further hints of charge-loss.

As illustrated in Figure 6.14 (*a*), to begin with, the ^{83m}Kr events selected were projected in the discrimination space as function of the distance to the wall. By introducing a further z-selection defined for events to be inside -90 $\leq z \leq$ -5 cm (in order to ensure capturing only features of the from the wall), the mean and standard deviation for the mono-energetic distribution across the radius (of the "good events") was found to be 1.44 $\pm$ 0.08. These distribution is characterized because it located between 1.22 and 1.75 in the $\log_{10}$(cS2$_b$/cS1) axis. However, at large radii next to the wall, a population of events unlike the one from the mono-energetic peak is found. This population isolated in the selection box spread down to -0.5 in the charge to light ratio axis, located within several cm inside/outside the TPC[3]. Although this population is was cross-checked to be made out of ^{83m}Kr events given that they follow its expected unique decay time, they are clearly affected in terms of the charge. In fact, the selection box specifies that for the data studied around 1279 events (0.47 % of the

[3]The inwards or outwards reconstruction of their positions may be blurred due to the position reconstruction uncertainties.

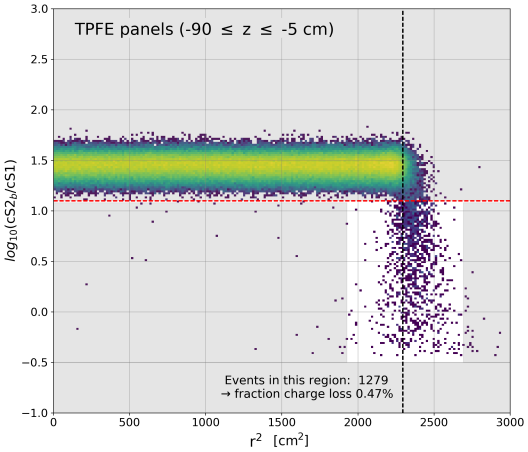

(a) Discrimination space vs r^2

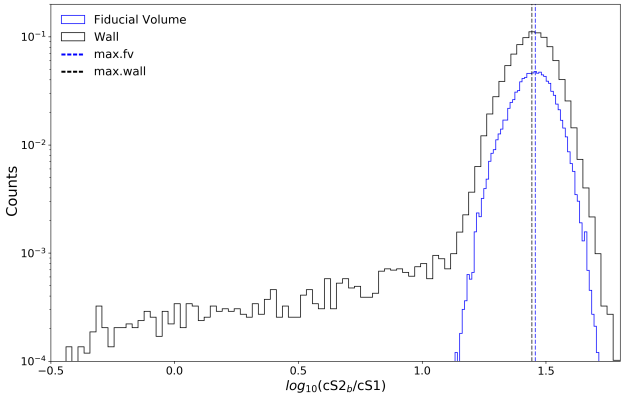

(b) Wall vs Inner FV distribution of events

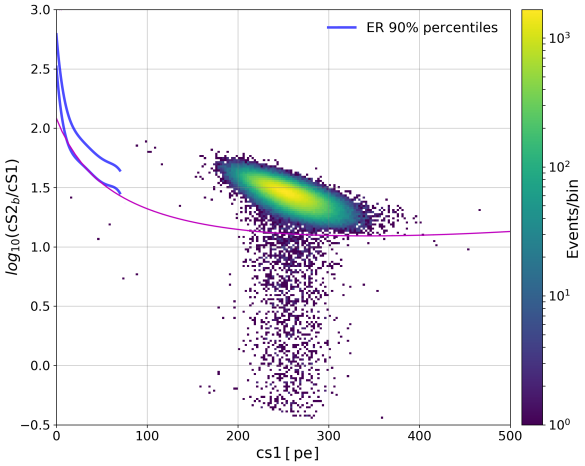

(c) Discrimination space vs cS1

Figure 6.14. (**a**) Hints of charge-loss through the characterization of ^{83m}Kr in the discrimination space as function of the radius squared (**b**) Comparison: Wall vs Inner FV events (**c**) Further hints of charge-loss in terms of the distribution of energy for ^{83m}Kr in the discrimination space as function of the corrected S1. A clear tail can be observed for the expected ellipse energy deposition given the light-charge anti-correlation along the 90% percentile from the ER band (blue).

total events) happen to suffer charge-loss. This means that event with a small fraction, the effect of charge-loss can affect different sources than ^{210}Pb or ^{210}Po.

As presented in Figure 6.14 (*b*), this features can be visualized by projecting the charge to light ratio for events at the wall (black box) in comparison to events selected inside a 1 t FV (blue). The tail found exclusively for events at large radii provides strong evidence about charge-loss. Another complementary way to understand how charge-loss can be identified can be done by looking the discrimination space as function of the energy cS1, as illustrated in Figure 6.14 (*c*). In this parameter space, the expected energy deposition from ^{83m}Kr is in the form of an ellipse. However, when charge-loss is encountered this deposition is diminished and the ellipse is accompanied by a tail. For

exploration purposed, an ad hoc selection (purple) was introduced to discriminate between ^{83m}Kr events suffering or not from charge-loss (this definition was used in the ^{210}Pb characterization).

6.2.3 Surface background model

Despite of the extensive efforts to characterize the population of events happening close to the PTFE wall, the incomplete knowledge about the detector and LXe responses in presence of charge accumulation, as well as the complicated decay structures and unknown underlying mechanism of charge-loss, prevented the development of a full model including all relevant physics processes observed. Thus, a data driven approach had to be developed in order to model and predict the distribution of this background. Motivated by all the studies presented in the previous sections and based on the observation that due to significant charge losses at the PTFE panels the surface background population can overlap significantly with the NR region of interest (as illustrated in Figure 6.20 (*gray*)), a data-driven approach was proposed by Jingqiang Ye and Alexey Elykov. The procedure consisted on modeling the probability density function of surface background events in cS1, S2, cS2$_b$, R, and z spaces.

This modeling is done by creating the distribution f_{surf}(cS1, S2, cS2$_b$, R, z) that uses an S2 dependent radial distribution of surface background inside the TPC in combination with an energy prediction from unblinded data outside the TPC to obtain a 5D prediction of the surface background distribution in both:

$$f_{\text{surf}}(cS1, S2, cS2b, R, z) = f(R|S2) \times KDE_{4\text{D}}(cS1, cS2_b, R, z), \tag{6.5}$$

where the $KDE_{4\text{D}}$ function is obtained from a fixed kernel-density-estimation **KDE** model of unblinded events outside the detector, as it was done in LUX [233] (see Figure 6.15, *right*). To construct the distribution of surface background in R and S2 space, events originating at the PTFE surface are selected as control sample with an S1 size out of the region of interest, including the ^{210}Po α-decays [212]. Then this sample was divided into multiple S2 slices, and in each S2 slice the radial distribution was fitted by using a skew Gaussian function and Skew-t function. The latter was found to be the most sensitive to outliers in the data while it also quantifies the uncertainty from the unknown shape of radial distribution better. Thus, showed in Figure 6.15 (*right*), it is the one considered the most.

The characterization of this background became particularly important for the combined SR0+SR1 dark matter search analysis because of the introduction of a radial component in the profile likelihood. Thus, with the inclusion of R in statistical inference, the final active volume could be increased by a 30% in SR1 comparison SR0.

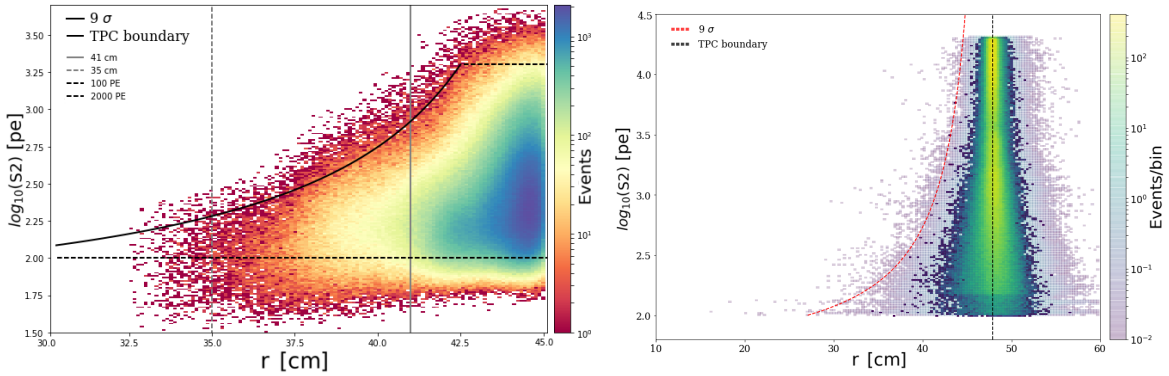

Figure 6.15. Left Illustration of a toy MC prediction generated from ND AKDE after simulating 2 million events **Right** Radial distribution component of the surface background model. Here is showed the Skew-t fitting function and a 9σ reference line (red) that illustrates the relation between S2 and position resolution σ.

6.3 Summary of ER background contributions

6.3.1 Accidental coincidence background

In XENON1T, uncorrelated S1s and S2s signals (referred to as lone-S1 and lone-S2, respectively) can originate from energy depositions in different non-active regions of the detector where light or charge are not detectable. For example, an energy deposition below the cathode where the is no electric field to drift electrons leads to lone-S1s without a related charge signal. In the case of energy depositions very close to the gate, the scintillation signal may be blocked by the mesh such that only lone-S2s can be detected. Lone-S1 and lone-S2 events normally do not threaten the dark matter search analysis. However, if their rate is high enough, they can be appear close enough to mimic a real interaction with one S1 and one S2 signal. Accidental coincidence **AC** events are those caused by the combination of the lone-S1 and lone-S2 events.

The estimated lone-S1 rate ranges from 0.7 to 1.1 Hz, depending on the requirement of noise rate in the search window. The observed lone-S2 rate is determined to be 2.6 mHz. In order to consider this background, an accidental coincidence background model has been implemented in the dark matter search of SR0 and SR1 data combined, as described in more details in [212]. This model is illustrated in Figure 6.20 (green), and it has a rate prediction of (0.47 - 0.74) Events/(t $\times$ yr) in the ROI.

6.3.2 ER results

The expected background rate related to the different relevant ER components inside the TPC have been calculated from MC [180] simulations for a 1 t FV. At the same time, the measured ER rate is extracted from the different studies on data presented, or directly from the ER modeling fit to dark matter search data, corrected for efficiencies of detection. The shape of the ER component comes from the bbf (see section 7.2) fitted of ^{222}Rn calibration data and the systematic uncertainty on energy

Table 6.4. Comparison of the expected ER rate inside the detector, calculated from MC [180], and the measured rate from all known components relevant to the rate in the (1 - 12) keV energy range.

Component	**Expected background (1t)** [Events/(t×yr×keV$_{ee}$)]	**Measured background (1.3 t)** [Events/(t×yr×keV$_{ee}$)]
^{222}Rn	$(1.54 \pm 0.15)\times10^{-4}$	$(1.29 \pm 0.22)\times10^{-4}$
^{85}Kr	$(7.7 \pm 1.5)\times10^{-6}$	$(2.1 \pm 0.5)\times10^{-5}$
Materials	$(7.3 \pm 0.7)\times10^{-6}$	$(3.1 \pm 1.0)\times10^{-5}$
Solar υ	$(8.9 \pm 0.2)\times10^{-6}$	$(6.8 \pm 0.9)\times10^{-6}$
^{136}Xe $2\upsilon\beta\beta$	$(2.3 \pm 0.3)\times10^{-6}$	$(2.3 \pm 0.4)\times10^{-6}$
Total:	$(1.80 \pm 0.15)\times10^{-4}$	$(1.90 \pm 0.24)\times10^{-4}$

scales (the values are presented in Table 6.4). Despite of the abundance of background particles that induce ERs, where the most threatening are the ^{222}Rn progeny (particularity ^{214}Pb) happening at energies below 10 keV, as result of the 99.7% ER discrimination power of XENON1T 50% nuclear recoil acceptance, only $\sim$ 2 Events/(t $\times$ yr) are expected in the region of interest. Hence, the result confirms that both expected and measured[4] rates are in agreement within their errors. Furthermore, from the ER rate measured in a 1.3 t FV:

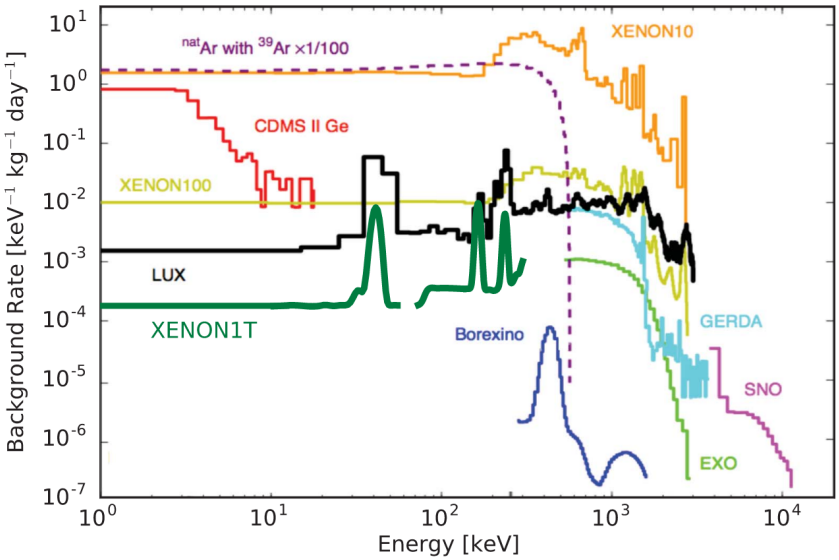

Figure 6.16. Summary of background rates for several rare events experiments. The spectrum from XENON1T (green) is found to be the experiment having the lowest ER background at low energies < 200 keV. XENON100 (orange), CDMS (red), XENON100 (yellow) and LUX (black) search for dark matter. Borexino (blue) and SNO (pink) are neutrino observatories, while EXO (light green) and GERDA (turquoise) look for $0\upsilon\beta\beta$ decay. The reference line for the rate of depleted argon is included as well (purple).Adapted from [231].

[4]This refers so far to the rate from the ER modeling. As discussed in section 6.5.7, the rate measured from low energy monitoring studies agrees as well with the MC prediction and ER modeled rates.

$$(82^{+5}_{-3}(\text{sys}) \pm 3(\text{stat}))\ \text{Events}/(t \times yr \times \text{keV}_{\text{ee}}),$$

it can be recognized that XENON1T has the world leading lowest ER background level ever achieved in a dark matter detector (using 1.3 t FV). The summary of background rates for several rare events experiments is illustrated in Figure 6.16.

6.4 XENON1T results

After the commission phase, the first science run from XENON1T **SR0** consisted on 34.1 live days [190]. This was followed by a major science run **SR1** consisting of 246.7 live days. Until writing, the latest dark matter search result from XENON1T consist on the combined analysis of these two science runs. This section will present the results to find direct evidence for WIMPs from this combined analysis, which relied greatly on the data corrections from charge accumulation studies, the guiding characterization of surface backgrounds to motivate their modeling, the background monitoring studies and several other data analysis efforts presented in this thesis.

The latest result from the dark matter science campaign consists on 34.1 live days of data acquired from November 22, 2016 to January 18, 2017 and 246.7 live days of data acquired between February 2, 2017 to February 8, 2018, briefly interrupted because of an earthquake. Thus, 278.8 days of data including corrections for DAQ dead-time, intervention, muon veto triggers or down-time, photomultiplier malfunctions, or brief periods of increased detector activity following high energy background events. Both science runs had different cathode voltage settings during their operation, -12 kV (SR0) and -8 kV (SR1). Hence, their drift field were 120 V/cm and 81 V/cm, respectively. Additional to background data-taking, as illustrated in Figure 6.17, regular internal and external calibration measurements were performed. As discussed in Chapter 4, ^{83m}Kr (red) were collected every 2.5 weeks. The ER band, and their response at low energies, was calibrated by using the intrinsic source ^{220}Rn (magenta) for 17 days split in 7 periods throughout both science runs. For low energy NRs, the external sources ^{241}AmBe (green) was used for 30.0 days, while a D-D neutron generator (blue) source 1.9 days [234]. PMT were calibrated by illumination with blue LED light through a plastic fiber (gray).

As overview in Chapter 4, the S2 signal is corrected (cS2) for the mesh-warping of the anode, the tilt of the detector and the loss of electrons due to electronegative impurities in the medium. Since the S2 reconstruction is more homogeneous in the bottom PMT array, this component is used in analysis ($cS2_b$). On the other hand, as discussed in Chapter 5, the S1 signal is corrected (cS1) for position-dependent light collection efficiency after having decouple electric field effects from charge accumulation LCE_{true}, thus only due to geometrical effects in terms of light collection. In order to avoid events selection bias, data in the expected dark matter search region was blinded in the region above the S2 threshold of 200 PE and below the ER-2σ quantile in cS1, $cS2_b$ spaces [62]. Therefore

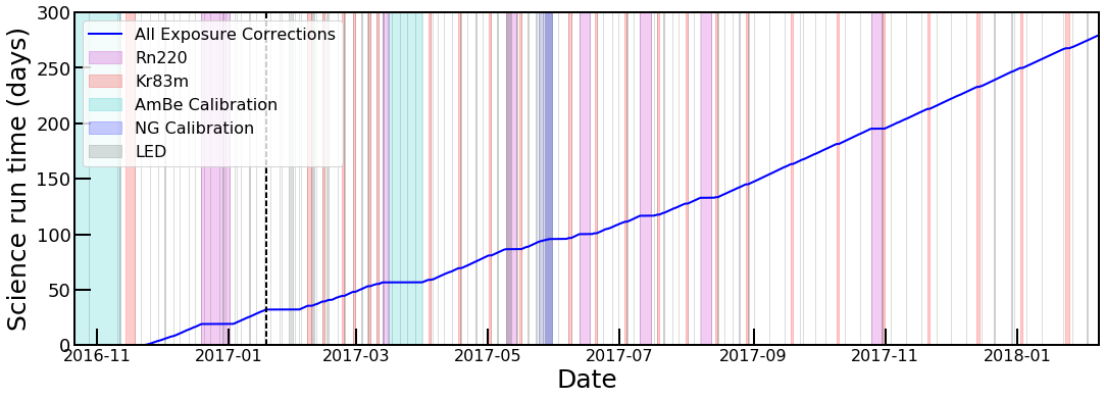

Figure 6.17. Exposure of the dark matter science campaign consisting on 278.8 live days of data taken. Composed by two different science runs, SR0 and SR1, in colors are illustrated the different internal and external calibration measurements performed: ^{83m}Kr (red), ^{220}Rn (magenta), ^{241}AmBe (green), D-D neutron generator (blue) and PMT calibration using LED light (gray).

all cuts, signal and background models were not tuned to this data. The WIMP region of interest was defined to be between (3 - 70) PE in cS1, corresponding to an average (1.4 - 10.6) keV$_{ee}$.

The efficiency of S1 detection (green) and that of S1 detection and selection using all cuts introduced in section 3.3.3 Table 3.3 (blue) is illustrated in Figure 6.18. these efficiencies were estimated using a combination of simulations and calibration control samples. The final NR efficiencies (black) for SR0 (dashed) and SR1 (solid) are showed as well with uncertainties (gray band), together with the NR energy spectrum shape of two reference WIMPs (purple) of masses 50 GeV/c^2 (dotted) and 200 GeV/c^2 (dashed).

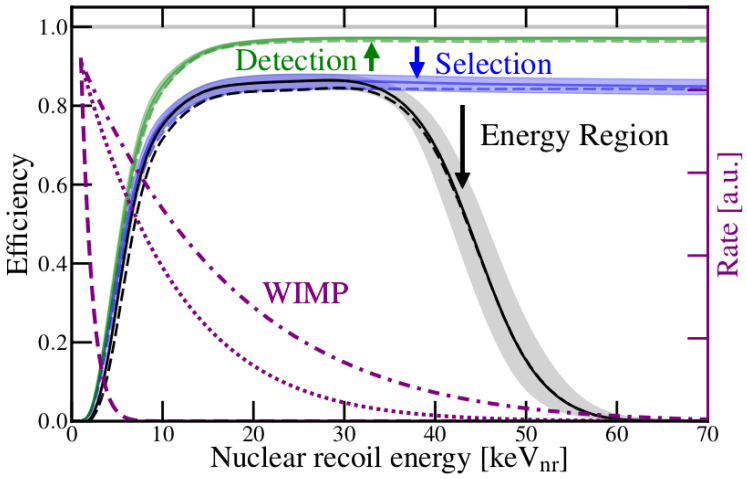

Figure 6.18. S1 detection efficiency (green) and selection efficiency (blue), both for SR0 (dashed black) and SR1 (solid black) as a function of the NR energy. Two WIMP reference spectra (purple) for the masses 50 GeV/c^2 (dotted) and 200 GeV/c^2 (dashed) are also illustrated. Taken from [62].

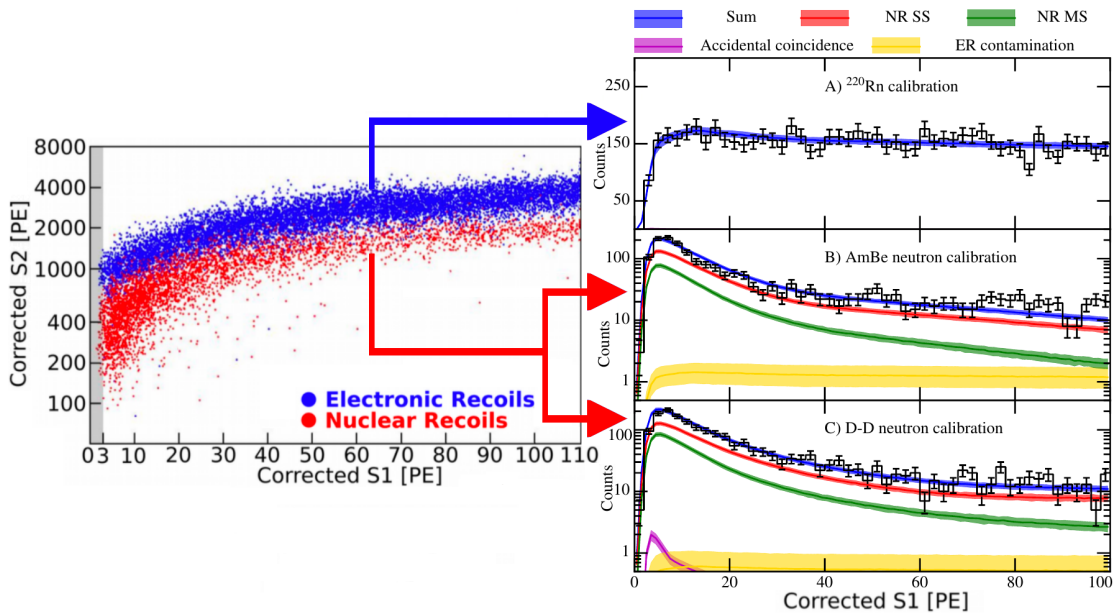

Figure 6.19. MC-data from combined fit of ^{220}Rn, ^{241}AmBe, and D-D neutron generator data. Projected in cS1 are showed the SR1 data (black bars) and the total sum of the signal response from the models (blue). Additionally, for each fit are specified the different components: accidental coincidence (magenta), ER contamination (yellow), single NR scatter (NR SS, red) and multiple NR scatter (NR MS, green).

Therefore, to model the distributions of electronic and nuclear recoil signals, the parameters of a detailed MC simulation with all detector processes, operational conditions and known microphysics in xenon, were fitted and constrained to multiple calibration sources [212]. As showed in Figure 6.19, the matching between the calibration SR1 data (black bars) and the total sum of the signal response (blue) is in good agreement. This was confirmed by calculating the goodness of fit p-values between in different (cS1,cS2$_b$) ranges for ^{220}Rn (ER response), ^{241}AmBe and D-D neutron generator (NR response) calibration data. This successful result is critical both to know the shape of a WIMP signal and to model the backgrounds well, as the fit provides information about all different components: accidental coincidence (magenta), ER contamination (yellow), single NR scatter (NR SS, red) and multiple NR scatter (NR MS, green). Furthermore, the fit is used to predict the ER and NR distributions in the analysis space of the dark matter search data, achieving a 99.7% ER discrimination in the signal reference region.

For the statistical inference procedure, the analysis space is cS1, cS2$_b$, R and z. Hence, all background discussed in Chapter 6 were modeled as a probability density function of these 4 dimensions. In terms of their derivation, the surface background and accidental coincidences were estimated by using sidebands or other data samples, while a radiogenic expectations was estimated by using simulations. In addition, for the WIMP signal model its signal is assumed to be uniformly distributed inside the FV used. The signal energy spectrum is computed as discussed in section 3.1.3 and specified in [62]. Figure 6.20 illustrates the modeled probability density function of each background component in the discrimination space.

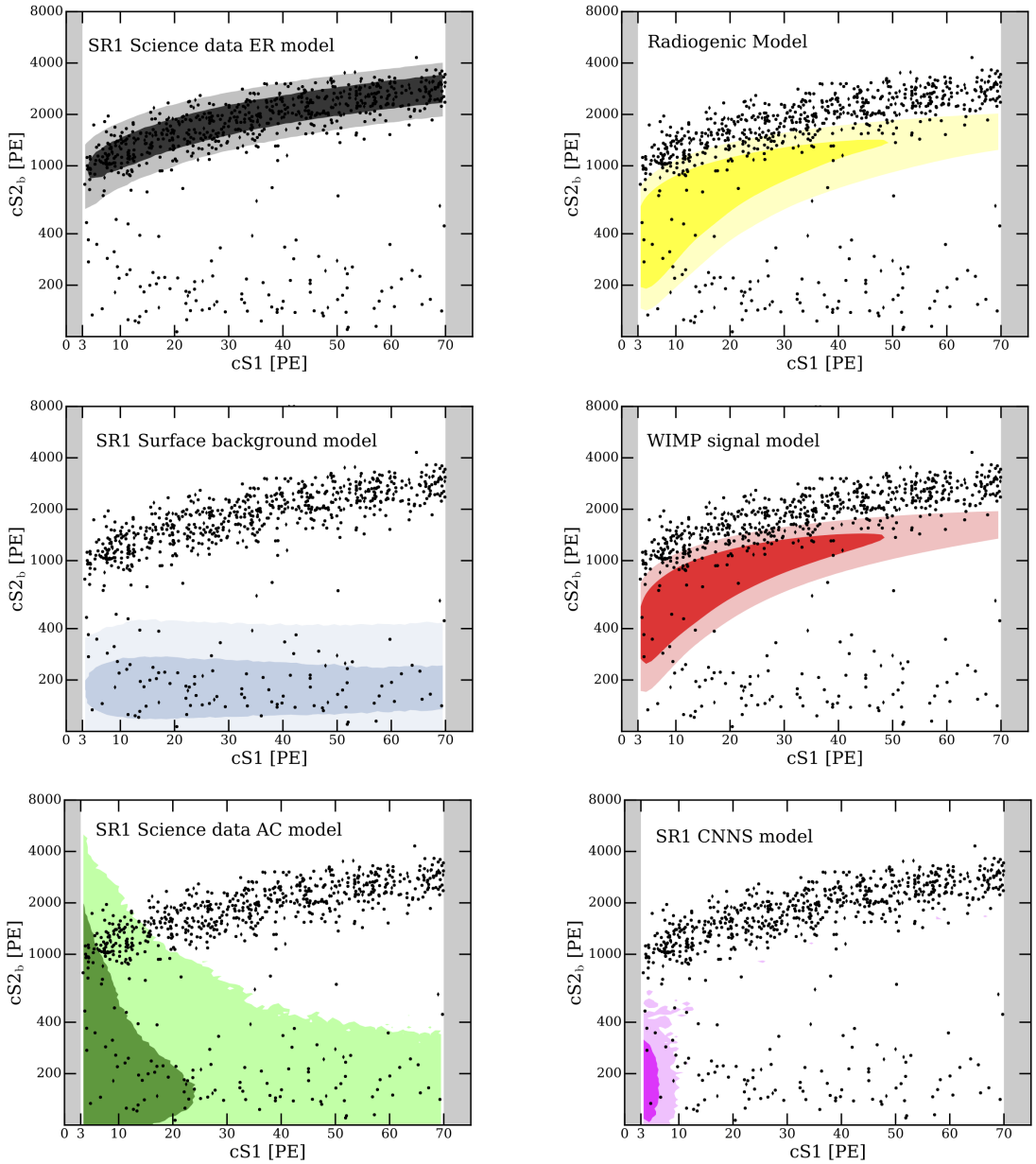

Figure 6.20. Models of each background component and the expected WIMP signal in the discrimination space. The models showed correspond to accidental coincidence (green), surface backgrounds (gray), to ER (black), the WIMP signal (red) and two sources of NRs: radiogenics (yellow) and coherent neutrino-nucleus scattering **CNNS** (purple).

Characterizing and subsequently modeling the surface background resulted in the addition of the R dimension in the inference procedure in comparison to SR0 dark matter search analysis [190]. As presented in Figure 6.21 (*left*), the surface background model allowed to maximize the selection of the largest radius (42.8 cm) while constraining the rate to remain flat and to guarantee for the ER contribution not to be sub-dominant (explicitly it was demanded for this maximal value to predict less than 100 surface-like events). As illustrated in Figure 6.21 (*right*), the limit for the FV close to

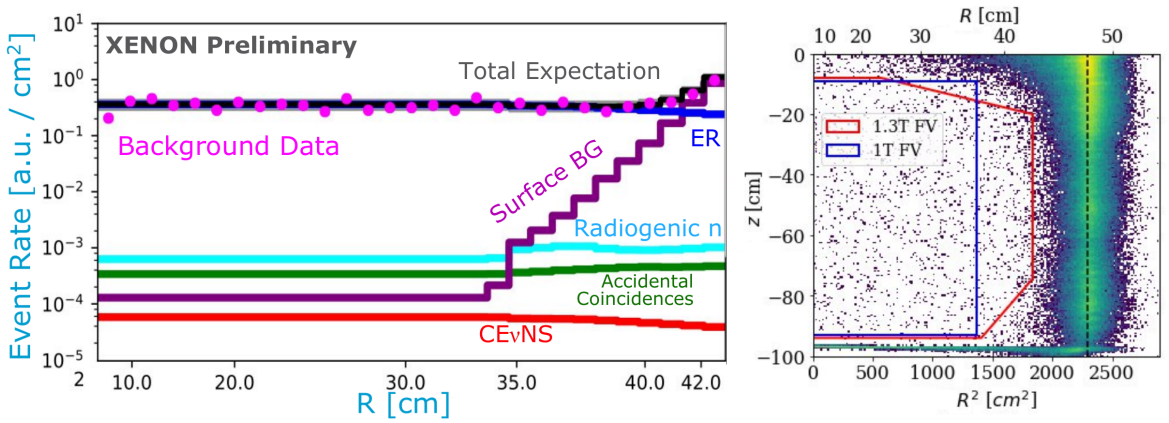

Figure 6.21. Left: Optimization of the radial definition of the FV for SR0 + SR1 data analysis based on the flatness of the total rate and the contribution of each background component **Right**: New defined FV for SR0 and SR1 combined, in comparison to SR0. The addition of modeling the surface background

the anode is chosen in to be 8.0 cm below the liquid level to prevent artifact or mis-reconstructed interactions from the GXe. On the other end of the detector, the FV is chosen to be 2.9 cm above the cathode in order to avoid events undergoing non-uniform and particularly strong electric fields. The corners were optimized using the radiogenic models, such that the rate was flat to < 10% in z across slices of R [173]. As result, with an almost $\sim$ 30% increment in the FV used in SR0 (blue) in comparison to SR1 (from 1 t to 1.3 t), it was achieved an increase in 10% sensitivity gain for the dark matter search.

Figure 6.22 presents the unblinding result the discrimination (*top*) and positions distribution (*bottom*) parameter spaces, the four dimensions included in the modeling of signal and backgrounds: (S1, S2, R, Z). The remaining events observed have passed all cuts defined and are located within the 1.3 t FV. The best-fit model then predicts in the form of pie chart the percentage of events that at those coordinates are WIMP or background-like (it determines the relative probability of each component). The size of the pie chart is related to the WIMP probability. The difference of this result with the previous analysis is that, with the information in a multi-dimensional space of parameters, XENON1T is not longer only a counting experiment. Tracing back the interaction site of the candidate events provides further constraints when understanding the likelihood that a signal observed is in reality a WIMP. For instance, 6.22 (*bottom*) indicates that those candidates with larger pie chart (larger WIMP probability) can be traced originally to be close to the walls.

Furthermore, before unblinding, the median projected sensitivity was found to have seven times better sensitivity compared to other experiments (LUX [194], PANDAX-II [221]) at WIMP masses > 50 GeV/c^2. The 2σ band around the median was found to span almost one order of magnitude due to random variation of the limit based on background fluctuations. Once unblinded, the data in the defined 1.3 t was interpreted using an unbinned extended likelihood with profiling over nuisance parameters [235, 50]. All model uncertainties were included in the likelihood as nuisance parameters, with addition of a mis-modeling safeguard [236]. Together with the background measurements, signal,

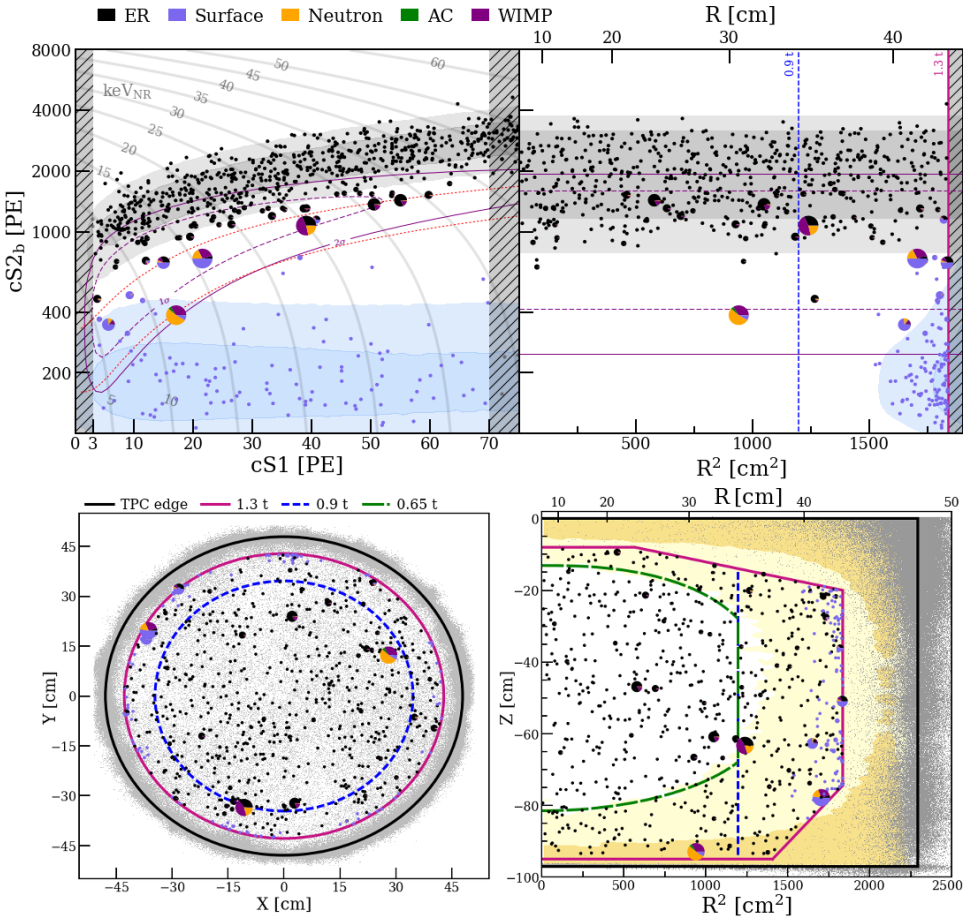

Figure 6.22. Distributions of events after unblinding. **Top**: Discrimination space and radial information of the events. The shaded regions show the surface (blue) and ER (gray) background components for SR1. The 1σ (purple dashed) and 2σ (purple solid) percentiles of a WIMP with mass of 200 GeV/c^2 has been overlaid for reference. The gray lines show iso-energy contours in NR energy. **Bottom**: Spatial distributions of the events, along the 1 t FV (blue), 1.3 t FV (magenta) and a inner core segmentation (green) used to further discriminate background in the corners of the FV from potential radiogenics.

background models and results post-unblinding, the profile likelihood analysis indicated no significant excesses in the 1.3 t FV at any WIMP mass. Thus, as illustrated in Figure 6.23, an upper limit on spin-independent WIMP interactions was set. Specifically, XENON1T set the most stringent limit to date for direct detection of dark matter in the context of WIMP-nucleon SI elastic scattering with a cross-section σ_{SI} at 4.1×10^{-47} cm^2 for a mass of 30 GeV/c^2 and 90% C.L.. The result excludes new parameter space never reached before, particularly for WIMP masses above 6 GeV/c^2.

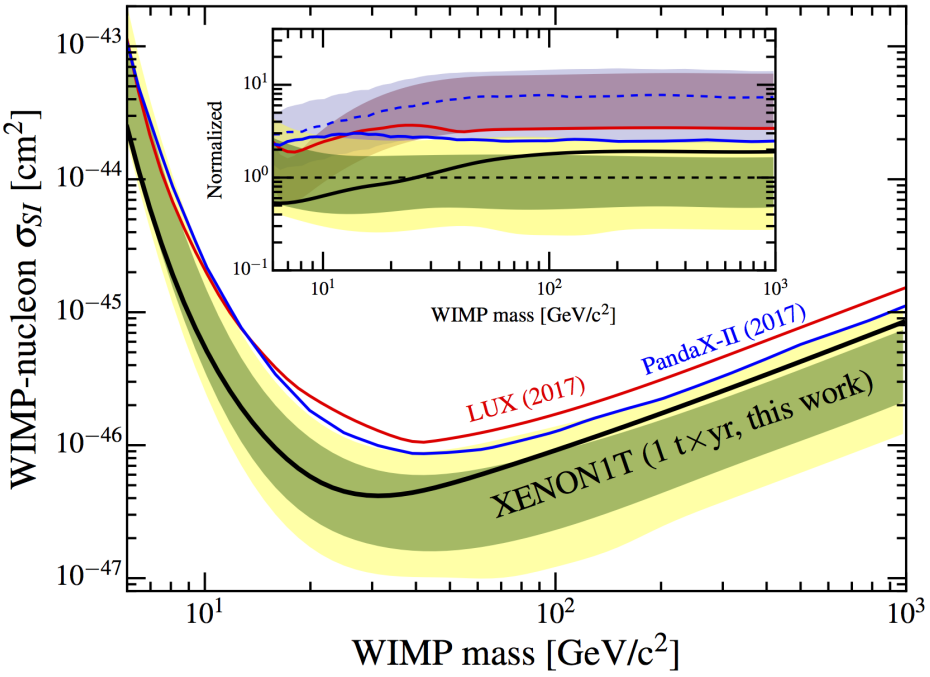

Figure 6.23. 90% C.L. upper limit on σ_{SI} from 1 yr×t exposure (thick black line), together with the 1σ (green) and 2σ (yellow) sensitivity quantiles. The results from LUX [194] and PANDAX-II [221] are over-laid. The inset illustrates for these limits the median sensitivities and their corresponding $\pm$ 1σ quantiles normalized to the XENON1T median sensitivity result. Taken from [62].

6.5 Annual Modulation studies

Since the mid 1980s, from the development of the first ultra-pure germanium detectors [237], direct detection searches of dark matter have explored several innovative approaches in order to take advantage of every piece of evidence collected at several scales in the Universe. It was not longer after these first detectors demonstrated their range of capabilities that a complementary idea came into play when looking for WIMPS. The conception that locally speaking, if dark matter exists as a roughly spherical and non-rotating halo where Earth is contained, given that Earth is moving with respect to the center of the galaxy in a disc rotating at around $\sim$ 220 km/s, the rotation of the Earth around the Sun would translate in a time-dependent WIMP's interactions count rate [238]. Specifically, an annual sinusoidal rate dependency would be expected, having its maximal around 1st of June (when the Earth travels against the relative direction of the WIMPs) while its minimal around 1st of December (when the Earth travels away from it), as illustrated in Figure 6.24.

The key of this feature is that it can provide an additional background discrimination, one of the biggest challenges of any direct detection experiment, given that most of background components found in measurements are not expected to exhibit a time dependency[5]. Thus, this section will

[5]However, as explained in more detail next in section 6.5.2, this is not true for backgrounds varying due to environment conditions changing at the different locations where the experiments are located (such as the temperature dependent muon

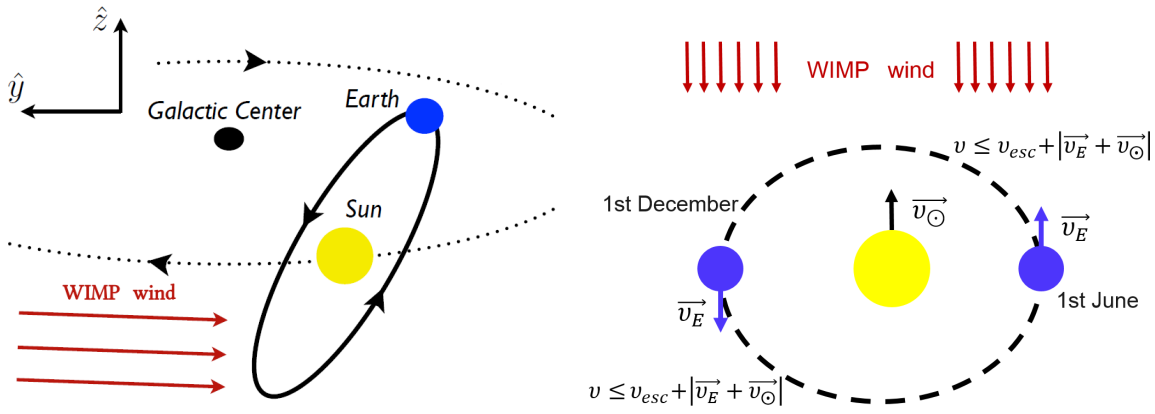

Figure 6.24. Left Right

introduce the characteristics of the event rate modulation (section 6.5.1), the current experimental status of this field (section 6.5.2) and the outline, together with preliminary results, of studies done in the context of XENON1T (section 6.5.3).

6.5.1 Rate modulation

As discussed in section 3.1.4, direct detection experiments expect to observe the nuclear recoil produced after the scattering of a WIMP in their set up. The differential recoil rate for this happening is expressed as:

$$\frac{dR}{dE}(E,t) = \frac{N_A}{A}\frac{\rho_\chi}{m_\chi} \cdot \int_{\upsilon_{min}}^{\upsilon_{max}} d^3\mathbf{v} f(\mathbf{v},t) \cdot |\mathbf{v}| \cdot \frac{d\sigma}{dE}(E,\mathbf{v}), \tag{6.6}$$

where specifically $f(\mathbf{v},t)$ is the time-dependent WIMPs velocity distribution of dark matter in the Galactic halo. Given that in the local neighborhood this halo is presumably smooth [30], for its description it is often assumed an isothermal sphere having an isotropic Maxwell velocity distribution. By smoothing the transition of this distribution near the escape velocity, such that it doesn't have an unphysical sharp cut-off, the distribution can be expressed as:

$$\widetilde{f}(\mathbf{v}) = \begin{cases} \frac{1}{N_{esc}}\left(\frac{3}{2\pi\sigma_\upsilon^2}\right)^{3/2}\left[e^{-3\mathbf{v}^2/2\sigma_\upsilon^2} - e^{-3\upsilon_{esc}^2/2\sigma_\upsilon^2}\right], & \text{for } |\mathbf{v}| < \upsilon_{esc} \\ 0, & \text{otherwise} \end{cases} \tag{6.7}$$

having N_{esc} as a normalization factor[6]. Now, in terms of the Earth's reference frame, $f(\mathbf{v},t)$ will vary around the year given the time dependent motion of an observed on Earth. Considering $\widetilde{f}(\mathbf{v})$ as the velocity distribution of dark matter in the rest frame, by using a Galilean boost, this distribution can

flux rate), or for background having as origin solar neutrons (due to flux variations found from changes in the Earth-Sun distance).

[6]This factors is defined as $N_{esc} = \text{erf}\left(\frac{\upsilon_{esc}}{\upsilon_0}\right) - \frac{2}{\sqrt{\pi}}\left(\frac{\upsilon_{esc}}{\upsilon_0}\right)\left[1 + \frac{2}{3}\left(\frac{\upsilon_{esc}}{\upsilon_0}\right)^2\right]e^{-\left(\upsilon_{esc}/\upsilon_0\right)^2}$.

be expressed in the laboratory frame as:

$$f(\mathbf{v},t) = \widetilde{f}(\mathbf{v}_{\odot} + \mathbf{v}_{\oplus}(t) + \mathbf{v}), \tag{6.8}$$

where $\mathbf{v}_{\oplus}(t)$ is the velocity of the Earth relative to the Sun and $\mathbf{v}_{\odot}$ is the velocity of the Sun relative to the dark matter rest frame. As often parametrized in literature [239], on one hand, the SHM smooth non-rotating halo is expressed as:

$$\mathbf{v}_{\odot} = \mathbf{v}_{\mathrm{LSR}} + \mathbf{v}_{\odot,\mathrm{pec}}, \tag{6.9}$$

having $\mathbf{v}_{\mathrm{LSR}} = (0, \upsilon_{rot}, 0)$ as the Local standard of rest **LSR**, the point in space that has a velocity equal to the average velocity of stars in the solar neighborhood, and $\mathbf{v}_{\odot,\mathrm{pec}} = (11, 12, 7)$ km/s as the Sun's peculiar velocity, related to the Sun's motion with respect to the LSR. On the other hand, the $\mathbf{v}_{\oplus}(t)$ term contains changes on the Earth's velocity as it changes it's position through the orbit that it has with respect to the Sun. This term is expressed as:

$$\mathbf{v}_{\oplus}(t) = |\mathbf{v}_{\oplus}|[\hat{\varepsilon}_1 \cos\omega(t-t_1) + \hat{\varepsilon}_2 \sin\omega(t-t_1)], \tag{6.10}$$

where the Earth's speed around the Sun is $|\mathbf{v}_{\oplus}| = 9.8$ km/s and $\omega = 2\pi/year$. At the same time, by aligning the coordinates such that the directions $\hat{x}, \hat{y}$ and $\hat{z}$ point in towards to the Galactic center, the local disk rotation and orthogonal to the plane of the disk, respectively, $\hat{\varepsilon}_1$ corresponds to the direction of the Earth's motion at the Spring equinox (March 20 or t_1), while $\hat{\varepsilon}_2$ corresponds to the direction at the Summer solstice (June 21)[7]. Because of the modulation in the velocity distribution introduced by the time dependent terms discussed in equation 6.8, an annual modulation in the differential rate specified by equation 6.6 is expected. In fact, by defying t_0 as the time of the year where the Earth moves fastest with respect to the rest frame of the dark matter and given that the modulation in the rate is expected to have a fixed period of 1 year, thus the differential rate can be expanded as Fourier series:

$$\frac{dR}{dE}(\upsilon_{\mathrm{min}}, t) = A_0 + \sum_{\mathrm{n}=1}^{\infty} A_{\mathrm{n}} \cos n\omega(t-t_0) + \sum_{\mathrm{n}=1}^{\infty} B_{\mathrm{n}} \sin n\omega(t-t_0), \tag{6.11}$$

such that A_{n} and B_{n} are Fourier coefficients defined as function of υ_{min} (see equation 7.11, section 3.1.1). Under the isotropic velocity distribution introduced in the SHM assumption, $B_{\mathrm{n}} = 0$. Thus, the modulating recoil rate through the year can be approximated to:

$$\frac{dR}{dE}(E,t) \sim S_0(E) + S_{\mathrm{m}}(E) \cos\omega(t-t_0), \tag{6.12}$$

where the coefficients S are related to the Fourier expansion of the coefficients A in equation 6.11, S_0 is the averaged rate in time, S_{m} stands as the modulation amplitude, t_0 represents the phase of the modulation and $|S_{\mathrm{m}}| \ll S_0$.

[7] In these coordinates, $\hat{\varepsilon}_1 = (0.9931, 0.1170, -0.01032)$ and $\hat{\varepsilon}_2 = (-0.0670, 0.4927, -0.8676)$.

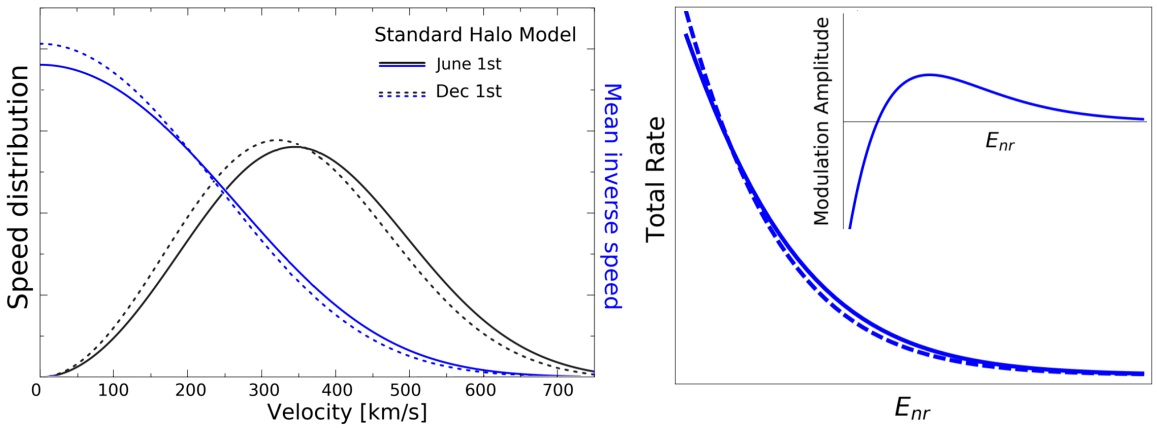

Figure 6.25. Left A velocity modulation in the dark matter rest frame would correspond to about 7% of the total orbital velocity of the Earth. **Right**

On one hand, as showed in Figure 6.25 (*left*), the time dependent variation of the Earth can be explored both for the SHM velocity distribution (black) and the inverse mean speed (blue), at the times in the year where these are expected to be maximal (solid line, June 1) and minimal (dashed line, December 1). On the other hand, as showed in 6.25 (*right*), the corresponding variations from these velocity distribution end up having a noticeable impact on the recoil spectra when comparing at the same previous two extreme times of the year. Furthermore, from the amplitude of the modulation, illustrated in the inset of this figure and computed as:

$$A_1(E) \approx \frac{1}{2}\left[\frac{dR}{dE}(E,\text{June 1}) - \frac{dR}{dE}(E,\text{Dec 1})\right], \tag{6.13}$$

several observations from this approach can be asserted. First, the expected modulation should have a sinusoidal shape approximately following equation 6.13. This suggests that it's amplitude will be relatively small in comparison to the average of the rate[8]. Second, there is change on the sign of the modulation amplitude that happens at υ_{min} (low recoil energies). This phase reversal would be the most telling feature of dark matter, since it could be used to exactly bound it's mass [239]. Third, the amplitude of the modulation is dependent on the energy window selected and its proximity to the threshold energy of the detector. Lastly, if in reality there is a halo substructure or a multi-component halo, the previous observations discussed would not longer be true and much more complicated features would need to be derived from the characteristics of the assumptions used, as described in literature [30].

6.5.2 Experimental status of Annual Modulation studies

Historically, experimental searches such as DAMA [240], CoGeNT [241] and CRESST [71] have reported to see an annual modulation that would be consistent with a change in the event rate due to

[8]This observation does not hold, however, for $\upsilon_{\text{min}} \gtrapprox 500$ km/s since scatters come only from WIMPs in the tail of the Maxwellian velocity distribution, where experiments are generally not sensitive.

dark matter. The long standing results from the DAMA experiment, together with counterpart efforts meant to confirm their claims, are presented next to cover the current status of the field.

Originally proposed in 1990, the DAMA/NaI set-up was one of the pioneer efforts aiming to detect WIMPs in the galactic halo by measuring an annual modulation signature. Consisting in nine 9.7 kg of highly intrinsic radiopure sodium iodide crystals NaI(Tl), this project obtained over 7 annual cycles of measurements and postulated as result the WIMPs presence through a dark matter model independent annual modulation study at 6.3σ C.L. [242]. DAMA/LIBRA (Large sodium Iodide Bulk for RAre processes) was the predecessor of this set up, comprising this time 25 ultra-radiopure NaI(Tl) detectors, 9.7 kg each one. With a total exposure of 1.04 ton$\times$yr collected from 2003 to 2013, DAMA/LIBRA-phase1 claimed at 7.5σ C.L. the discovery of dark matter through an annual modulation signature (which by including the first generation DAMA/NaI exposure corresponding in total to 14 annual cycles, resulted in a 9.3σ C.L. discovery [243]). Following several improvements in the configuration, which has allowed DAMA to lower the software energy threshold, DAMA/LIBRA-phase2 has presented a claim of dark matter annual modulation at 9.5σ C.L. in the energy region between 1 and 6 keV. Furthermore, when putting together the data taken originally by DAMA/NaI and DAMA/LIBRA-phase1 in the region between 2 and 6 keV, a total exposure of 2.46 ton$\times$yr is achieved, leading to an annual modulation discovery claim at 12.9σ C.L. [77] (results are summarized in Table 6.5). Figure 6.26 shows the low energy residual rate from the events measured by DAMA/LIBRA-phase2 as function of time, in the energy intervals of (1-3), (1-6) keV, as well as the residual rate measured by DAMA/LIBRA-phase1 and DAMA/LIBRA-phase2 in the (2-6) keV. The curve superimposed to the data measured corresponds to the function $A\cos\omega(t-t_0)$, where the modulation amplitude A is derived from the best fit on the data following a Maximum Likelihood analysis, while taking the period T = 1 yr and the phase $t_0 = 152.5$ days.

Despite such a strong, these results have triggered several debates as to whether they represent a real first measurement of dark matter via direct detection methods or if this modulation corresponds to some other process or artifact being measured. Although the expected phase of dark matter is very close to that of DAMA data, the amplitude of the modulation requires a cross section that is tension several results in the field. In fact, under the same hypothesis made by DAMA of looking for nuclear recoils produced by dark matter, their claim has been repeatedly ruled out by limits set by experiments such as EDELWEISS-III [244], SuperCDMS [245], LUX [194], PandaX-II [221], XENON10 [246], XENON100 [185], XENON1T [62], etc. Broadly speaking, there are only three approaches in order to justify the results found:

1. Modify the current dark matter model to evade XENON, SuperCDMS, etc., by altering the rate, i.e., establish the notion that dark matter interacts preferentially with NaI.

2. Establish that dark matter is not a good model for DAMA, which would demand the need to find another source causing the annual modulation found, having such a period and phase.

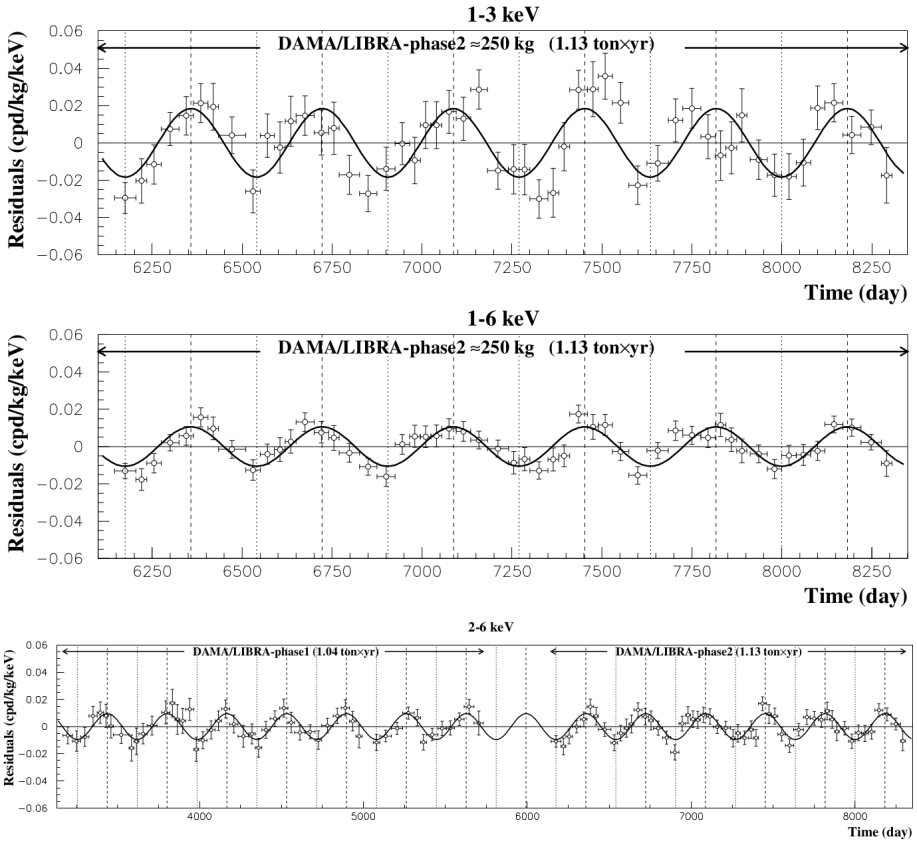

Figure 6.26. Low energy residual rate from DAMA/LIBRA-phase1 and DAMA/LIBRA-phase2 as function of time. Dashed vertical lines correspond to the maximum expected for the dark matter signal (June 1st), while the dotted vertical lines correspond to the minimum. The curve superimposed to the data measured corresponds to the function $A\cos\omega(t-t_0)$, where the modulation amplitude A is derived from data, the period T = 1 yr and the phase $t_0 = 152.5$ days. Taken from [77].

3. Consider that the signal being detected comes in reality from WIMP-electron scattering and it is found by DAMA given the it can not separate nuclear from electronic recoils.

To the first option, given that all the other experiments excluding DAMA results are based on different detection techniques compared to DAMA (e.g. XENON uses a dual-phase LXe detector, SuperCDMS uses cryogenic germanium, etc.), in order to reconcile the idea that for some reason nature would had decided for dark matter to preferentially interact with NaI, independent experiment using sodium iodide as the target medium should obtain similar results. This motivated the design and construction of NaI(Tl) experiments such as ANAIS [247], SABRE [248] and COSINE-100 [249]. The latest and most important result related to this task comes from the COSINE-100 experiment, where after 59.5 days of data taken and assuming the standard dark matter halo model, their limits show that the annual modulation in the signal observed by DAMA is inconsistent with spin-independent interactions between WIMPs and sodium or iodine [250] (see Figure 6.27). To further rule out this

	A (cpd/kg/kg/keV)	$T = 2\pi/\omega$ (yr)	t_0 (days)	C.L.
DAMA/LIBRA-phase2:				
1-3 keV	(0.0184±0.0023)	1.0	152.5	8.0 σ
1-6 keV	(0.0105±0.0011)	1.0	152.5	9.5 σ
2-6 keV	(0.0095±0.0011)	1.0	152.5	8.6 σ
1-3 keV	(0.0184±0.0023)	(.0000±0.001)	153±7	8.0 σ
1-6 keV	(0.0106±0.0011)	(0.9993±0.0008)	148±6	9.6 σ
2-6 keV	(0.0096±0.0011)	(0.9989±0.0010)	145±7	8.7 σ
DAMA/LIBRA-phase1+phase2:				
2-6 keV	(0.0095±0.0008)	1.0	152.5	11.9 σ
2-6 keV	(0.0096±0.0008)	(0.9987±0.0008)	145±5	12.0 σ
DAMA/NaI+DAMA/LIBRA-phase1+phase2:				
2-6 keV	(0.0102±0.0008)	1.0	152.5	12.8 σ
2-6 keV	(0.0103±0.0008)	(0.9987±0.0008)	145±5	12.9 σ

Table 6.5. Summary of results achieved by the legacy of DAMA. Here A stands for the modulation amplitude, obtained when fitting data to the formula: $A\cos\omega(t-t_0)$. The period T = $2\pi/\omega$ and the phase t_0 were kept fixed at 1 year and at 152.5 days, respectively. Results are found to be compatible with the hypothesis of a signal from annual modulation of dark matter [77].

claim at a higher confidence level and through the same analysis, COSINE-100 is expected to collect data for two more years, followed by an upgrade to start COSINE-200 expected to start at 2020.

Table 6.6. Compatibility of three different models with DAMA data, where AIC $= \chi^2 + 2k$ is the Akaike information criterion, an estimator of the relative quality between statistical models given a set of data. The smaller the AIC value is, the more compatible the model tested with he data is. BIC $= \chi^2 + k\ln n$, with k stands for the number of parameters and $n = 80$ is the amount of data points. Values consulted from [251].

	χ^2	AIC	BIC
Muons and Neutrinos	66.74	70.74	75.50
Dark matter	69.76	71.76	74.14
Muons-only	90.39	92.39	94.77

For the second option, it would have to be considered that dark matter is not the only source generating a modulation in a direct detection experiment. On one hand, a promising candidate for the DAMA modulation is neutrons stimulated by muon spallation, generated after having interacted with the surroundings of the detector. As studied by Borexino [252], the muon's flux at Gran Sasso is correlated with the temperature of the atmosphere such that more Pion and Kaon decays occur in Summer than in Winter. Although the period found for them is consistent with DAMA data, $T_\mu = 366 \pm 3$ days, the muon flux peaks around 30 days too late, having $\phi_\mu = 179 \pm 6$ days, such that

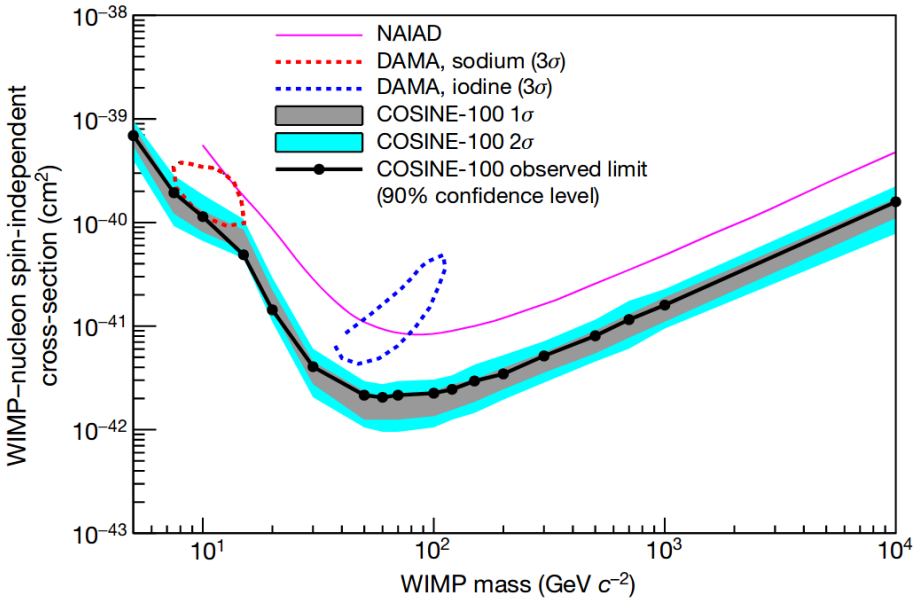

Figure 6.27. Exclusion limits at 90% C.L. on the WIMP-nucleon SI cross-section from the first 59.5 days of the COSINE-100 experiment, together with their 68% (grey shading) and 95% (blue shading) probability bands. These limits are directly compared to the 3σ allowed regions of the WIMP mass and the cross-section associated to the DAMA/LIBRA signal for the WIMP-sodium (red dotted contour) and the WIMP-iodine (blue dotted contour) scattering hypothesis. Taken from [250].

a muon-induced only-signal is incompatible with DAMA at 5.2σ C.L. [253]. On the other hand, there is another source of annually modulating neutrons generated by ^8B solar neutrinos interacting with the rock of the mountain or the shielding surrounding of the DAMA detector. In fact, as measured by Borexino [254] and Super-Kamiokande [255], solar neutrinos have a consistent annual modulation with the Earth-Sun distance variation, having a period of $T_\nu = 1.01 \pm 0.07$ years and a phase of $\phi_\nu = 11.0 \pm 4.0$ days. Considering the combination of solar neutrinos and atmospheric muons, a signal model taking the form:

$$A_{\mu+\nu} = A_\nu \cos\omega(t-\phi_\nu) + A_\mu \cos\omega(t-\phi_\mu)$$

can be used to try to fit the amplitudes to the DAMA data while keeping the phases held fixed [251]. As illustrated in Figure 6.28 and summarized in Table 6.6, by making the comparison of the dark matter model fit with the muons and neutrinos model (and muons-only model), it is found that the smaller contribution from neutrino-induced neutrons manifests as a forward phase shift, relative to the moun-induced neutrons, such that the combination of both components produces a signal model that fits the DAMA data as well as dark matter hypothesis[9].

[9] In terms of the requirements needed from muons and neutrinos to produce enough neutrons in order to have a similar rate to the one measured by DAMA, it has been discussed that provided a scattering volume of $\sim 1000\ m^3$ surrounding the detector, similar rates would be achieved [251].

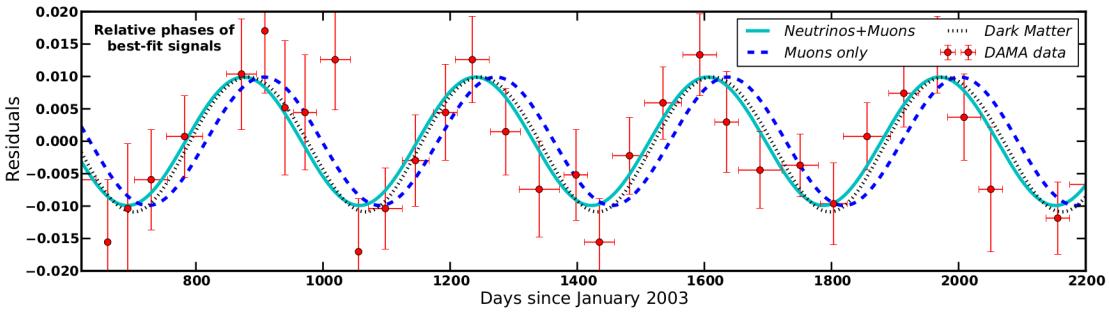

Figure 6.28. Comparison of different signal models presenting a modulation to DAMA data. The fit combining the contributions of solar neutrino to that from atmospheric muons (solid cyan line) shows to describe the data as well as the dark matter model (black dashed points) and better than the muons-only model (blue dashed lines). Taken from [251].

Now, within the same category of finding an alternative modulating source explaining the data, there have been suggestions concerning questioning DAMA's assumption about having completely excluded from measurement all sources of variable backgrounds. A recently discussed option has to do with helium migration through photomultiplier tubes **PMTs**, causing an inflated amount of dark noise waveforms that can potentially mimic scintillation events at a rate of $\approx$ 1 cpd/kg/keV [256], which in principle, consistent with the rate observed in the data. Under this explanation, a detected seasonal variations of the He partial pressure in the local environment would explain DAMA results, rather that the apparent dark matter interaction claim. The possibility of having overlooked this background has not been confirmed yet.

Lastly, in terms of the third option, there have been proposed efforts such as the one done by XENON100 [257], where it was considered the possibility that the annual modulation measured by DAMA would be due to dark matter electron interactions (since DAMA does not have electron and nuclear recoil discrimination). However, the absence of a statistically significant modulation signature after analyzing data accumulated over a period of 4 years, in the low energy region of (2.0-5.8) keV, allowed to exclude this hypothesis with a 5.7 σ C.L.. Furthermore, complementary and dedicated annual modulation searches done by experiments such as LUX [258] and XMASS-I [259] have as well not produced a result compatible with the DAMA hypothesis to the date. Thus, despite all efforts to corroborate their founding, results from similar and different technologies suggest that their measurements are likely to be interpreted as some form of modulating background not properly understood. Until is proven contrary, the consensus within the dark matter community on DAMA's claim is that their results are not consistent with a dark matter signal.

6.5.3 Annual Modulation in XENON1T

Within it's lifetime, during the extension of three science campaigns, the XENON1T detector has collected dark matter search data during the course of more than one year. Thus, following the efforts started by XENON100 [257] although this time having a lower background, more sophisticated

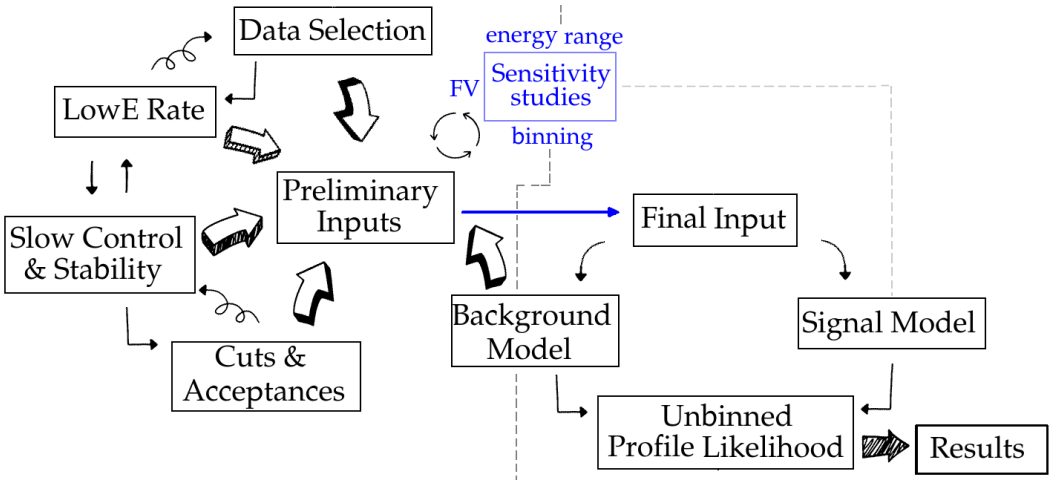

Figure 6.29. Simplified strategic plan of analysis for the annual modulation studies.

analysis tools and a bigger exposure, XENON1T is currently working on performing a search for annual modulation. This section details the procedure followed to test the hypothesis of an annual modulation of dark matter through electronic recoils using XENON1T data. Furthermore, since the XENON1T experiment is located underground in the same laboratory as the DAMA experiment, any statement from these results will provide strong insight about DAMA results.

As illustrated in Figure 6.29, the procedure to perform an annual modulation analysis depends on the examination of several interconnected aspects of the detector. To simplify the extensive complexity of the analysis one can divide the efforts in two categories: obtaining preliminary inputs and testing these inputs. For the first category, fundamentally, efforts start by demonstrating the detector *stability* by examining all different *slow control parameters* (e.g. temperature, pressure, liquid level, etc), together with the PMT gains and electronic noise evolution. The impact of any significant condition variation on data acquisition has to be considered in order to restrict the process of *data selection*, as any artificial correlation between the rate that would be obtained triggered by a change of conditions should be avoid. Next, in terms of working towards obtaining a trustworthy rate, the stability of the different *selection criteria* used to select the specific data needed has to be cross checked, as well as the acceptance's evolution these criteria. In parallel to calibrate and understand the detector response and it's operational stability, different analyses studying the backgrounds behavior have to take place, both to further restrict the data used and complementary to account for any correlation on the rate measured. The characterization of all previous aspects, as function of a fiducial volume, time binning and energy range constitute a preliminary estimation of the rate evolution inside the detector.

For the second category, once that all preliminary inputs are ready to be tested, several sensitivity studies have to be performed in order to explore the optimal conditions for which a discovery potential is maximized, i.e., given a signal model, different fiducial volumes, time binnings for the correlated backgrounds and energy ranges have to be tested. Any correlation between the rate obtained and background/slow control parameters has to be checked before proceeding. Lastly, the constituted

final input is study by performing an unbinned likelihood analysis, preferred among other methods because this statistical test is binning independent and consequently yields more precise results and interpretations. Thus, once that all inputs are in place for a fixed signal model, a characterization of any variation present (e.g. period, phase, amplitude) is done while quantifying the significance/rejection of the annual modulation hypothesis.

6.5.4 Slow Control and Detector Stability

In order to ensure that quality of the event rate measured inside the detector, its thermodynamic stability has to be monitored over time. In XENON1T, the different subsystems and instruments used are controlled, operated and monitored by a slow control **SC** system based on an industry standard process control hardware and software from General Electric **GE**. Specifically, for hardware are used programmable automation controllers **PACs** while for software it is used a supervisory control and data acquisition **SCADA** architecture system [145]. With the values of approximately 2500 parameters are stored in a GE proficy historian database, the raw SC data from relevant detector parameters can be consequently extracted from the database, with a time resolution of minutes, to inspect if there are datasets which are affected at any time during operation.

The main detector parameters studied for annual modulations during data was taken are summarized in Table 6.7, along their mean and standard deviation values. For illustration, Figure 6.30 presents the time evolution monitoring of some of these performance parameters: pressure (PT101), temperature (TE101) and liquid level (SLM1), where the blue points represent extracted data. The results found based on a 3σ deviation from the median indicate that there is not relevant behavior or outliers affecting the data. For the parameters showed, as well as for the rest mentioned, it is found a stable behavior during operation. In addition, it is also presented the PMT stability for randomly selected channels[10]. In summary, the detector was found to be thermodynamically stable during the data acquisition through SR0 and SR1. Generally speaking, the variations stay within a 3σ level from the mean value of each parameter and data from major interventions has not been included. Overall, some of the different changes observed can be attributed for the most part to the perturbation of the system through the use of external calibration sources, such as the neutron generator. Nevertheless, correlation studies have shown that these changes have not relevant impact on the rate at low energies.

6.5.5 Data Selection

In order to achieve a greater measuring sensitivity for the amplitude of a possible periodic rate variation at a given period, it is paramount to make use of all available and well understood data. At the same time, lowering as much as possible and correctly describing the background rate also helps to constraints the size of random fluctuations, hence improving the signal-to-noise ration of a signal.

[10] In the case presented, gains differ such that several channels can be shown without overlapping.

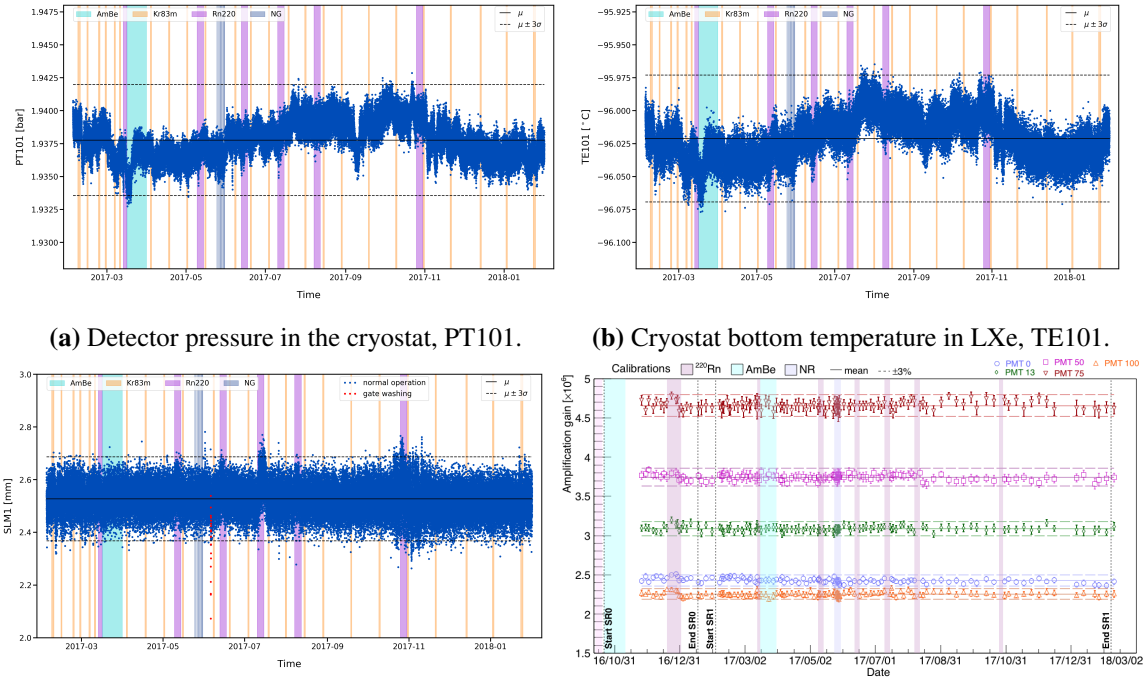

(a) Detector pressure in the cryostat, PT101.

(b) Cryostat bottom temperature in LXe, TE101.

(c) Short level meter 1 reading, SLM1.

(d) Example of the PMT gain evolution.

Figure 6.30. Pressure, temperature, level and PMT gain stability monitoring from SC database. Taken from [260].

Thus, for the first attempt of searching for an annual modulation signature in XENON1T, the already understood data used for the spin-independent NRs search from WIMPs has been used[11].

As described in section 4.1.1, data from two dark matter searches corresponding to ∼443 live days (including background and calibration data), has been considered for this analysis. On one hand, SR0 data consist of 32.33 (37.18) days with(without) corrections concerning deadtime, PMTs flashes, etc, while SR1 consist of 247.69 (264.91) days before any data run has been excluded. This translates roughly into 280.02 (302.09) days of total available data taken over the course of more than one year. Given that both campaigns have slightly different experimental conditions, the combination of both exposures needs to consider in detail checking carefully changes in background levels (as well as their uncertainty), together with detection efficiencies, changes in selection criteria and signal processing. For this reason, the version of the minitrees containing all variables for analysis were hold fixed to the PAX version 6.8.0, while the HAX version also was kept as 2.5.0.

In terms of inspection of the quality of the data, two background runs were removed because the neutron generator was tested during this data acquisition but those runs did not include the tag concerning its use (taken the 2 and 8 of May, 2017). Next, two addition runs were also removed while doing this analysis due to their incompatible event time. These correspond to the manually introduced salted events used in the dark matter search [62]. Lastly, around 31 additional runs are preventively

[11] However, at the time of writing this thesis, efforts have been placed to start analyzing and understanding the data taken from the beginning of February of 2018 to the end of December of 2018, officially referred as *SR2 data*.

Table 6.7. Key detector parameters description for SR1. The parameters represent here contain information about the thermodynamics performance of the detector, for instance, temperatures in LXe and GXe, pressure in detector, pressure in insulation vacuum, GXe flow in different loops, etc. Mean and standard deviations calculated for data from 2/2/2017 to 2/7/2018. Values consulted from [260].

Parameter name	Unit	Description	Mean	Standard Deviation
PT101	bar	Detector pressure (cryostat)	1.937×10^{0}	1.397×10^{-3}
PT102	bar	Detector pressure (porcupine)	1.935×10^{0}	1.220×10^{-3}
PT103	bar	Detector pressure (cryogenic system)	1.934×10^{0}	1.240×10^{-3}
PT104	bar	Detector pressure, relative (cryogenic system)	1.031×10^{0}	5.790×10^{-3}
TE101	°C	Cryostat bottom temperature (LXe)	-9.602×10^{1}	1.597×10^{-2}
TE102	°C	Cryostat bottom PMT array temperature (LXe)	-9.616×10^{1}	1.587×10^{-2}
TE103	°C	Cryostat middle temperature (LXe)	-9.624×10^{1}	1.576×10^{-2}
TE104	°C	Cryostat below bell temperature (LXe)	-9.591×10^{1}	1.580×10^{-2}
TE105	°C	Reservoir temperature (LXe)	-9.589×10^{1}	1.851×10^{-2}
TE106	°C	Inside bell temperature (GXe)	-9.603×10^{1}	1.839×10^{-2}
TE107	°C	Cryostat top temperature (GXe)	-8.854×10^{1}	2.587×10^{-2}
FC201	SLPM	GXe mass flow through QDrive 201	3.000×10^{1}	4.864×10^{-1}
FC202	SLPM	GXe mass flow through QDrive 202	1.788×10^{1}	1.861×10^{-2}
SLM1	mm	Short level meter 1 reading	2.527×10^{0}	5.298×10^{-2}
SLM2	mm	Short level meter 2 reading	2.375×10^{0}	4.890×10^{-2}
SLM3	mm	Short level meter 3 reading	2.717×10^{0}	5.428×10^{-2}
SLM4	mm	Short level meter 4 reading	2.444×10^{0}	5.667×10^{-2}
LLM2	mm	Long level meter 2 reading	3.453×10^{1}	4.764×10^{0}
R121	W	PTR-102 tower heater power	7.024×10^{1}	8.870×10^{0}
Vanode	V	Anode voltage	4.000×10^{3}	8.982×10^{-1}
Vcathode	kV	Cathode voltage (negative)	7.993×10^{0}	1.361×10^{-3}
TILTMA	rad	Tilt meter A reading	4.389×10^{-3}	8.920×10^{-6}
TILTMB	rad	Tilt meter B reading	3.697×10^{-3}	2.471×10^{-5}

excluded given that after the different uses of the ^{220}Rn calibration source, a decreasing contamination tagged through the analysis of the ^{212}BiPo is observed following the next 4 runs after the source is closed. Figure 6.31 shows the monitoring of the ^{212}BiPo rate (black dots) in terms of the run number (related to the date of acquisition). The threshold (dashed red line) indicates which events are more likely induced by a ^{220}Rn contamination than from background events (with the exception of few events that clearly should not be affected by the use of the ^{220}Rn calibration source, as it happens for several runs after the last use of the source). Thus, the removed events (and their associated runs) correspond to those events located after the use of the source while the rate exceeds the threshold, which corresponds to reducing the total livetime $\sim$1.3 days [223].

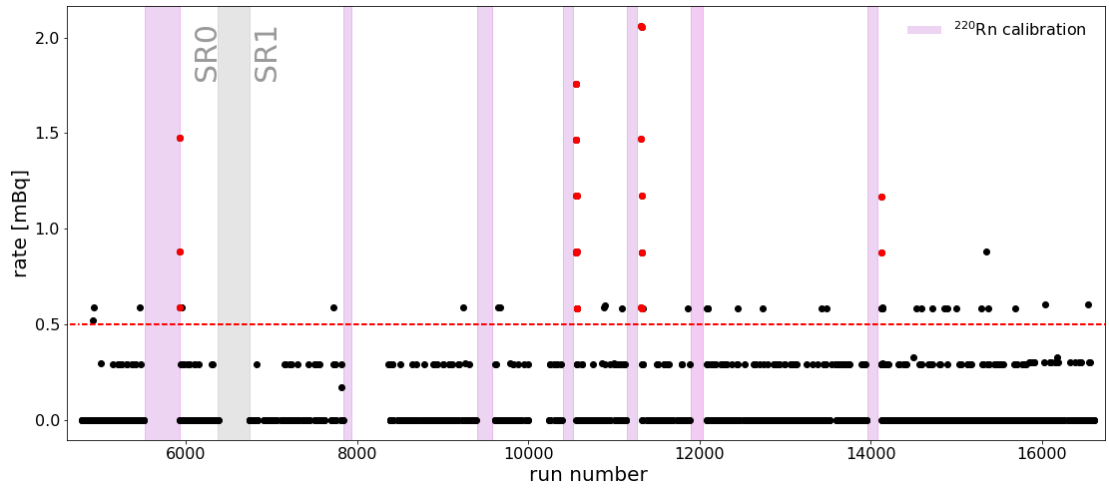

Figure 6.31. Monitoring of the ^{220}Rn contamination on background runs due to ^{212}BiPo events. Adapted from [223].

6.5.6 Cuts and Acceptances

Determination of Cuts

As discussed in section 3.3.3, in order to analyze the SR0 and SR1 dark matter search data, 20 different selection cuts were developed to ensure the quality and consistency of the events found. However, since this analysis focuses on ERs, opposite to the standard SI dark matter WIMP search where the attention is mainly on NRs, not all these cuts may be actually needed or some may even need to be adapted. A final selection of cuts resulted from a study exploring the minimal set of cuts that being physically motivated, would achieve a good ERs events selection while guarantying the removal of events having poor quality (e.g. events recorded under changing conditions, excessive noise) or an anomalous nature (e.g. events from regions where the signal reconstruction is not fully reliable yet[12]).

As presented in Table 6.8, from the original 20 set of cuts developed (see Table 3.3, section 3.3.3), there are 9 whose definition suggests that they may not be fundamental. On one hand, the cuts *S2 Threshold* and *S1 Low Energy Range* can be omitted because in terms of energy selection, a specific search energy range is expected to be defined through the combined energy scale CES. On the other hand, cuts such as *Muon Veto*, *S1 Pattern Likelihood*, *S1 Max PMT* and *Single electron S2* are likely not to be needed since they were designed for a good selection of NRs, while cuts such as *PosDiff*, *S1 Area Fraction Top* and *Pre-S2 Junk* need to be investigated in order to determine their impact in the data selection.

The procedure to define which of these seven cuts, if any, has a case to be used is the following:

[12]For example close to the cathode while in the most outer radius possible, near the PTFE walls, where there are strong local variations of the electric field or charge loss.

[13]For simplicity in the notation in this table, *S1 Pattern likelihood* was referred as *S1 PL* while *S1 Area Fraction Top* was referred as S1 AFT.

Table 6.8. Overview of cuts available cuts that need to be investigated in order to decide if they are fundamental to the selection of events[13]

Name cut	Description	Comment
Pre-S2 Junk	Removes events with lot of peak area before main S2, equivalent to exclude events with noisy waveforms	Has to be investigated
PosDiff	Removes events with too different patterns of position reconstruction	Has to be investigated
Single electron S2	Removes mis-identified single electron S2s classified as S1s (lone-S1s), which could potentially leak into the NR band	Relevant for AC background, should not be relevant in AM ROI
S1 PL	Aims at reduce the anomalous leakage from the ER recoil band into the NR band (e.g. AC from lone-S1s and lone-S2s)	Has to be investigated
S1MaxPMT	Defines a threshold on the maximum fractional contribution of a single PMT to an S1 signal (which reduces anomalous leakages from the ER recoil band into the NR band)	Relevant for AC background, should not be relevant in AM ROI
S1 AFT	Removes bad S1 hit pattern removal	Has to be investigated
Muon Veto	Removes events in coincidence with Muon veto triggers and when Muon veto is off, which are tried to be avoid since mimic a NR event	Not relevant since it removes NRs
S1 LowE Range	Energy selection: cS1 in (0, 200) pe	Omitted due to CES selection
S2 Threshold	S2 energy at which the trigger is perfectly efficient: 200 pe < s2	Omitted due to CES selection

1. Load all background data using the 20 available cuts (all but *S2 Threshold* and *S1 Low Energy Range*) for a relatively broad energy interval, i.e. 0-20 keV[14]. Then, by including a $\pm 3\sigma$ ER band selection (see next in text) and a 1T FV, quantify and characterize the events that are removed by the seven cuts under investigation in several parameter spaces.

2. In a next step, those events only removed by these seven cuts can be further investigated by exploring if there is a correlation between these cuts removing them. This could suggest that maybe some of these cuts are redundant, while it could be hinted that there is one well cut removing most of these events.

[14]This energy range covers the possibility of exploring the signal regions of experiments such as DAMA/LIBRA [77] (1-6 and 2-6 keV), LUX [258] (2-6 keV) and XMASS-I [259] (1-6 keV), while offering two possible control regions which are away from any calibration source contamination: 6-10 and 10-20 keV.

3. Based on the results, inspect waveforms and propose a final set of cuts to be used.

To begin with, in order to obtain a full selection of ERs events, the $\pm\mathbf{3}\sigma$ quantile limits from the modeled ER band are derived to further discriminate between events selected. As illustrated in Figure 6.32, this definition follows from the ER model constructed for the discrimination between NRs and ERs in the latest dark matter search of XENON1T [62, 212]. The referred ER model is based on a fit constrained to ^{220}Rn calibration data while it makes use of all the understanding of the detector response, i.e., it includes the simulated and measured intrinsic response of particles in LXe together, containing information such as position reconstruction uncertainties, PMT efficiencies, signal reconstruction efficiency, detection bias and signal fluctuations on the S1 and S2 [212].

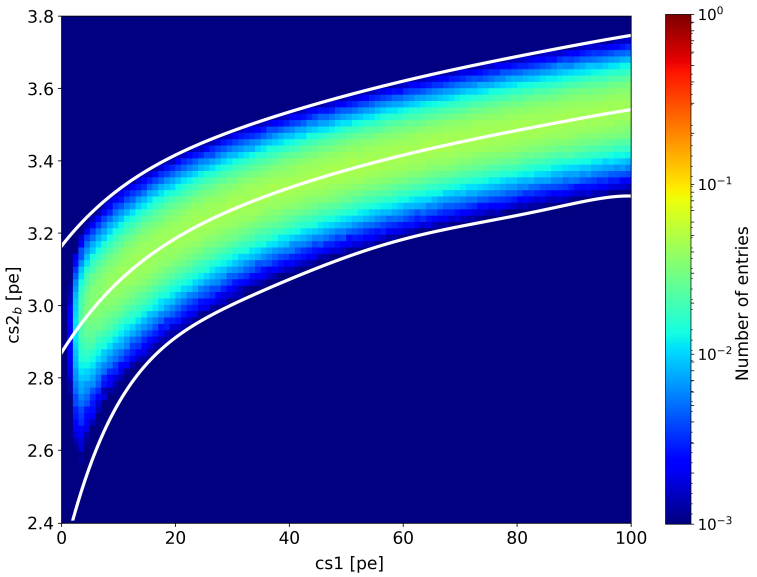

Figure 6.32. ER events selection definition using a $\pm\mathbf{3}\sigma$ quantile from the ER model, consistent with SR0 and SR1 ^{220}Rn calibration data.

Once having this definition in place, as *first* step it was explored to load all data available from SR1. By implementing all the cuts specified from the dark matter search, using as pre-selection a energy selection to only keep events inside the 0-20 keV range and by initially taking the 1T FV cut, Figure 6.33 (**a**) presents all remaining events after this procedure. Specifically, the population of events showed corresponds to all the remaining events after the 20 cuts used (black dots) in terms of their spatial distribution, both in the z vs R^2 and x vs y spaces, while events that were removed by the cuts label as "under investigation" **U.I** (those specified on Table 6.8), are presented as well (red dots). The distribution of the events remaining and removed seems to be uniform in these parameter spaces. Furthermore, Figure 6.33 (**b**) illustrates in the discrimination space more details of what is the consequence of using the cuts U.I. Events in this space can be categorized as being inside or outside the $\pm 3\sigma$ quantile limits from the ER band (dashed gray lines), such that there is a direct discrimination between ERs or other events. From the remaining 1315 events found after all cuts, ERs constitute 977 events (black dots), while events left outside this ER band selection constitute a

population of 338 events (red dots). Furthermore, for these two different regions just specified, the triangular markers represent the events removed by the cuts U.I inside the 3σ ER band (blue) and outside this band selection (green). Thus, without further information yet, it can be noticed that the effect of using the seven cuts discussed is to remove only $\sim 5\%$ of the total ER events (on the contrary, they remove $\sim 53\%$ of the total NR events, which is consistent with comprehension that they were mainly designed to clean the NR band).

Focusing on the cuts U.I removing the found $\sim 5\%$ population of the total ER events, as *second* step, it was explored the possible correlation between the cuts removing these events. The idea was to search for hints that could suggest the importance of using a some cuts over another ones, if given the case, as well as checking the effect of these cuts on the data removed. Thus figure 6.34 illustrates as pie charts what events are being removed and by which specific cuts this happens. This approach was explored in terms of the z vs R^2, x vs y and the discrimination spaces inside the 1T fiducial volume. Several things are found from the 51 events removed. In terms of the amount of events removed per cut, it can be seen that the cuts removing the less amount of events are *Muon Veto* and *Pre-S2Junk* (3 and 1 events respectively). In contrast, the cuts removing most events seem to be *S1MaxPMT*, *PosDiff* and *S1 Area Fraction Top* (above 10 events each one). Most importantly, in terms of in which energy region inside the discrimination space do these cuts influence the selection the most, it is found that:

- *Muon Veto* and *Pre-S2Junk* remove events located exclusively in the control region, between 10-20 keV
- *PosDiff* and *S1 Area Fraction Top* seem to remove events spread through the full range of energy and homogeneously inside the FV
- *S1MaxPMT* and *S1 Pattern Likelihood* seem to remove the majority of the events outside the ROI. For the former cut, 10 out of 12 events (also 10 out of these 12 events are located close to the cathode). For the latter, 8 out of the 9 events.
- Lastly, all 5 events removed by the *Single electron S2* cut are in the ROI and only 7 events from the original 51 have a correlation of being removed by 2 or at the most 3 cuts at the time.

Based on the results from this inspection, as *third* and last step, the last consideration moved to look into the waveforms of the events removed. The examination of these waveforms suggested that those events do not have anything particularly harmful, but rather, they are likely removed as the acceptance of these cuts is not 100%. Thus, the detailed analysis of the cuts used has led as results the final set of cuts summarized in Table 6.9.

Summary of Final Cuts to be Used

Table 6.9 presents a short overview of the set of cuts meant to be used for the annual modulation analysis of XENON1T. Concretely, the majority of these cuts ensure to have ER and NR events having physically meaningful information. However, since this search focuses on the selection of ERs events,

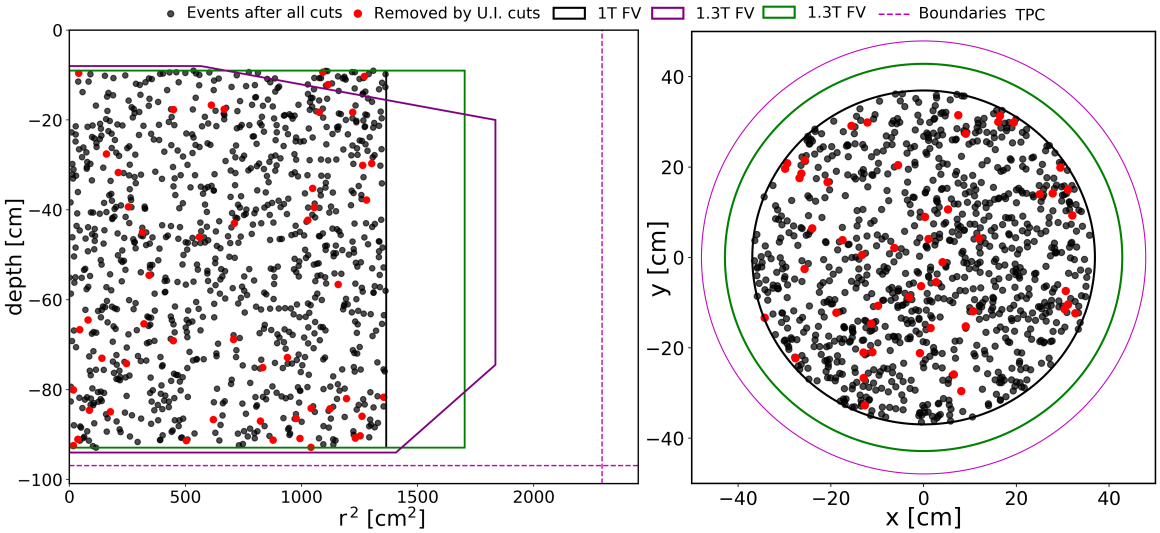

(a) Spatial distribution of events after all cuts have been used

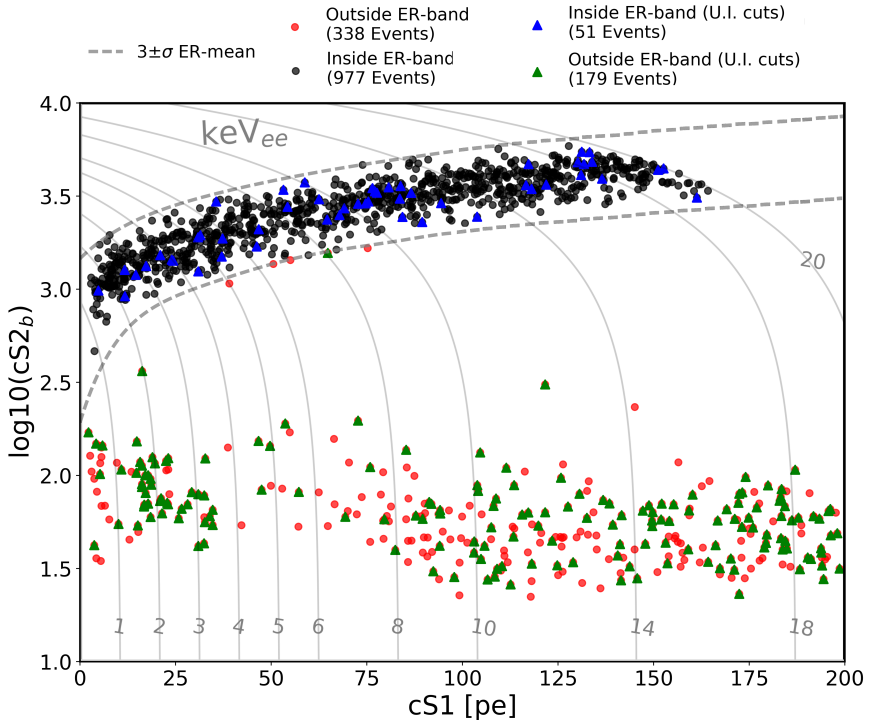

(b) Discrimination space for events after all cuts have been used

Figure 6.33. Inspection of all background data from SR1 under the full set of dark matter search cuts. The events presented are those remaining after applying all cuts. In order to get an inside on the selection used, specifically the effect of the cuts U.I, the distribution of remaining events are characterized in the z vs R^2, x vs y and discrimination spaces. The color code is explained in the text.

the $\pm 3\sigma$ quantile lines from the modeled ER band have been used to further introduce a particle-type event selection. Lastly, in addition to these cuts, the 1T FV used in the SR0 dark matter analysis has

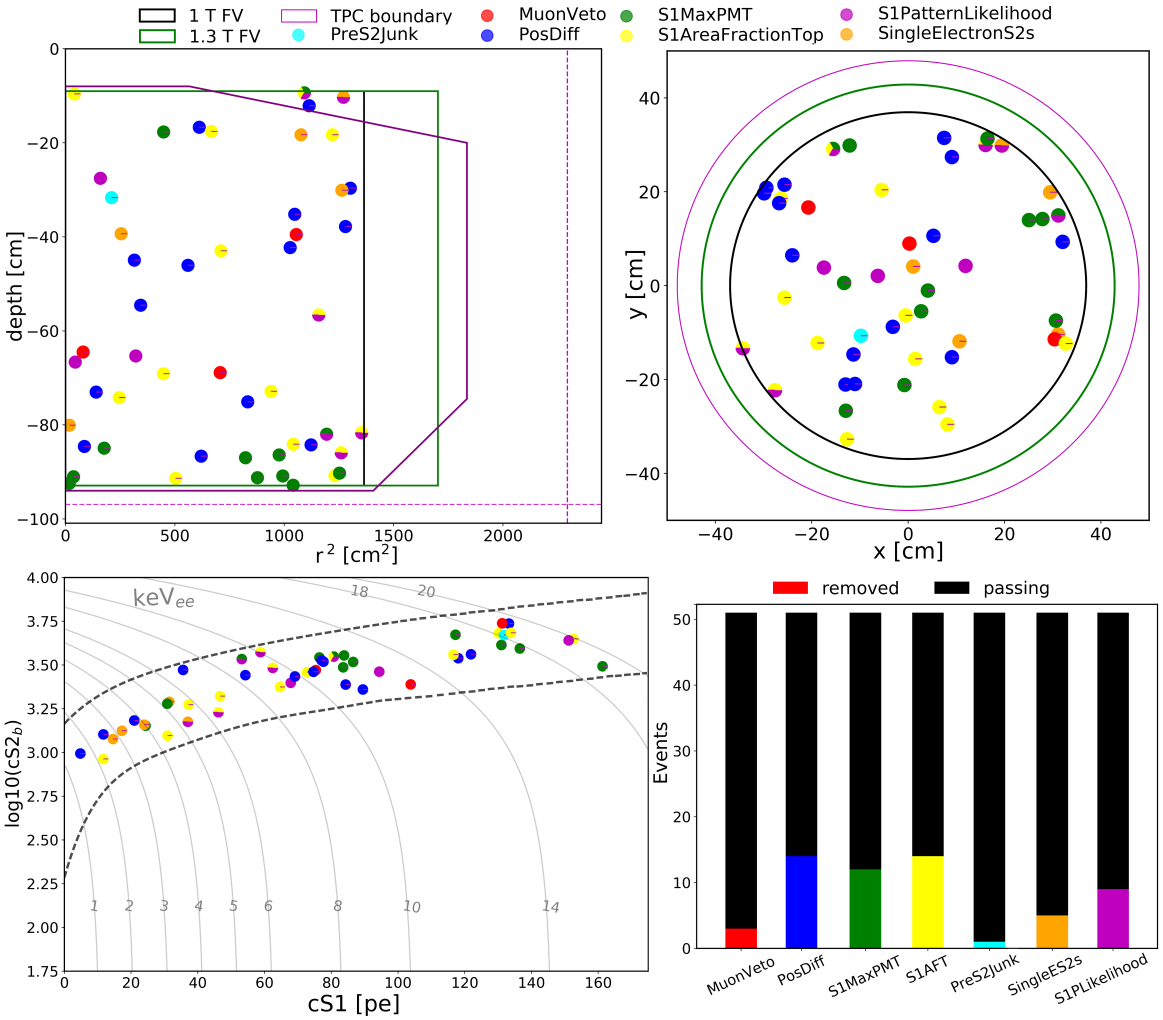

Figure 6.34. Spatial distribution of events removed by "under investigation" cuts. Discrimination space distribution and summary of number of event removed by each cut

been selected because it is extremely well understood and any possible artifact introduced by any field distortion, or charge collection loss close to the TPC walls, is sub-dominant within this inner volume [190].

Cuts Acceptances

An important aspect concerning the selection of events for annual modulation studies has to do with the stability with which cuts efficiently keep/remove good/bad events as function of time. In order to quantify their efficiency, the term *acceptance* is introduced and it refers to the probability that a valid event has to pass a given cut. Therefore, an ideal cut removing all bad events of a sample would have a 100% acceptance. Since a variation in time of number of events selected, given the change in the acceptance of a cut, could directly affect the rate obtained, a detailed study was done in

order to monitor the time evolution stability acceptance of each cut used. This can help to identify both population of events behaving different from the average, or detection artifacts that need to be considered to have a stable selection of events. Once that this acceptance is quantified for all events, the measured rate is scaled by the inverse of the value derived so that it can correctly estimated the actual rate of observed interactions inside the detector. Furthermore, the uncertainties in these acceptances can be included in the statistical analysis used to further improve the significance of discovery of a signal.

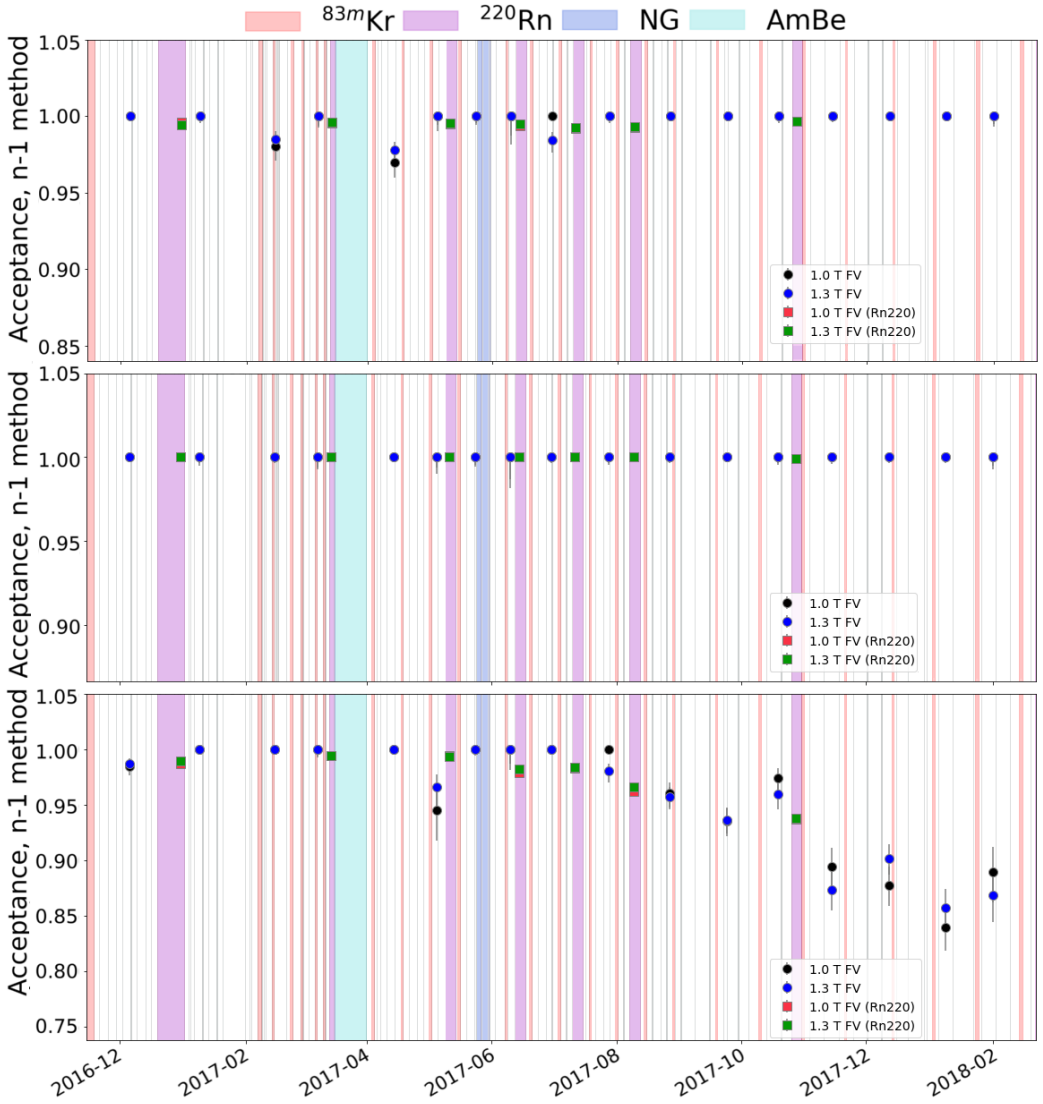

Figure 6.35. N-1 acceptance evolution of several cuts specified in Table 6.9. From top to bottom, the cuts showed are: *S1 Single scatter*, *Flasher* and *S2 Pattern Likelihood*. Circle dots correspond to the acceptance calculated on background data when using a 28 days binning for 1T FV(black) and 1.3 T FV (blue). Squares correspond to the acceptance calculated on ^{220}Rn calibration data for for 1T FV(red) and 1.3 T FV (green).

Technically, the acceptance of a cut can be calculated by using a control sample of only good events and then by computing the fraction of events passing the cut. However, having a good control sample is often a difficult task given that, e.g., defining a sample of dark matter-like events is not something than can be done in practice. Thus, two approaches are often used to estimate this acceptance. On one hand, for some cuts closely following a physics motivated definition or a certain model[15] (such as the S2 width cut based on a diffusion model), the acceptance can be estimated through simulations or based on the fact that the cut don't rely on properties on the events. Nevertheless, on the other hand, for cuts assessing artifacts of detection the difficulty when trying to simulate the events is related to know/predict how the parameters of the simulation evolve in time (if they even do or not), which is in reality complex. Therefore, for these cuts the acceptance is estimated by the so called *N-1 method*, as it was done in XENON100 [261]. Under this method, the acceptance of one cut in a set of N uncorrelated cuts results as the fraction of passing events after having applied the other N-1 cuts. The idea behind in this method is that after having applied N-1 cuts, most of bad events will have been removed, such that the remaining events constitute a good control sample of events (i.e. signal-like) that can then be used to evaluate the acceptance of the N^{th} cut[16]. Following this approach, the acceptance A_{i} for a given cut i is computed as:

$$A_{\text{i}} = N_{\text{all}}/N_{\text{i}}, \tag{6.14}$$

where N_{all} and N_{i} are the numbers of events in the control sample with and without applying the i'th cut, respectively[17]. To estimate the cut acceptance of the different cuts defined for annual modulation, mainly ^{220}Rn calibration data was used since with high statistics it populates completely the ER band, exactly where the selection of events has to focus on. Figure 6.35 presents the N-1 acceptance evolution of several of the cuts used in the search of annual modulation for illustration. From top to bottom, the cuts presented are: *S1 Single scatter*, *Flasher* and *S2 Pattern Likelihood*. The results from ^{220}Rn calibration data suggest that for the three first cuts, the acceptance evolution seems to be constant and in average close to one (results from background data also support this notion in both FVs). However, from all the different cuts used, it was recognized as remarked in the last column of Table 6.9, that the acceptance of the *S2 Pattern Likelihood* cut was deteriorating in time, thus cutting more good events as time passed by than expected. In the next section a new definition for this cut in order to assess this problem is discussed.

S2 Pattern Likelihood Cut

From the different results obtained when monitoring the cut's acceptance stability, it was identified that the S2 Pattern Likelihood cut had a strong time dependency, i.e., its acceptance progressively

[15] This approach is often referred to as an "analytic method".

[16] However, for some cuts that present a strong correlation, this assumption is not valid and different criteria are required to define the control sample.

[17] One of the biggest difficulties has also to do with addressing the correlation between different cuts. Thus a *N-M* approach could be the approach to take, but is not guarantee to solve such a problem.

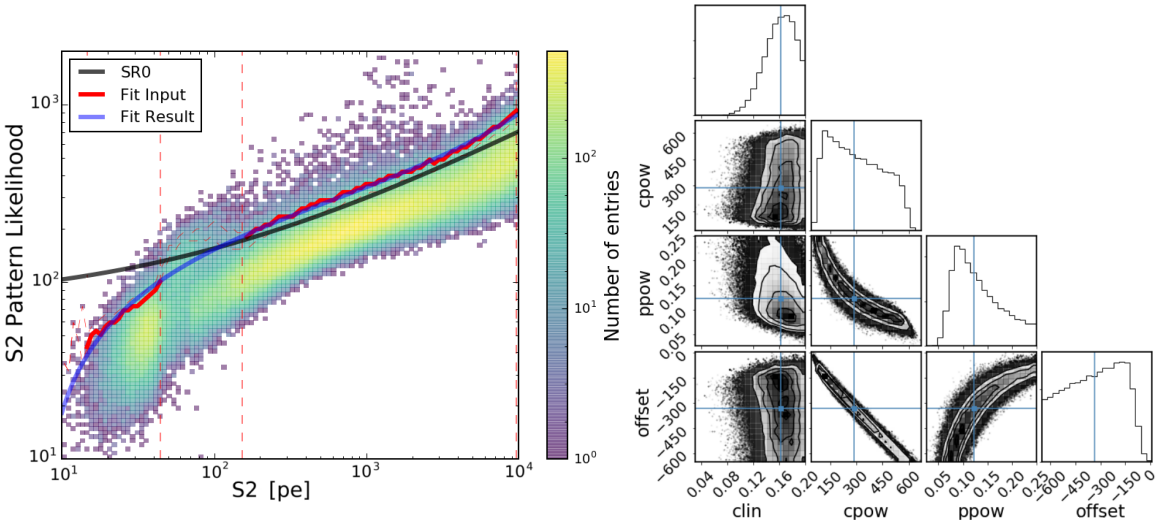

Figure 6.36. Left Visualization of the S2 Pattern Likelihood cut definitions used in SR0 and SR1 **Right** MCMC corner plot illustrating the likelihood fit for every parameter.

deteriorated in time during SR1, particularly after July. Given that up to date no underlying reason has been identified as the reason causing this, a time dependent definition was proposed. To begin with, this cut is motivated on the fact that it is desired to only have one maximum in the S2 hit pattern for an event (this allows to identify and reject multiple scatters). In order to quantify the quality of the hit pattern of a peak, a Poisson likelihood chi-square statistical test [262] is performed and the goodness of fit is translated into the variable called "*S2 pattern likelihood*" [161] (events with unusual high values are identified as anomalous events). Given that this parameter is energy dependent, the strategy is to identify and define if there is a energy dependent boundary in the *S2* vs *S2 Pattern Likelihood* parameters space[18] that can be construct in order to categorize the population of events having a consistent S2 hit pattern for each event.

The cut was defined using all available ^{220}Rn calibration data and it is tested with AmBe data to confirm that it does reject bad events. To select a clean sample, all quality cuts implemented in the dark matter search were used on the ^{220}Rn, except by the 1 ton fiducial volume. As for the sample of AmBe data, also used in order to extend the range of pattern cut to 0 PE, all quality cuts are used but *S2 Single Scatter* (the attention this sample is mainly on the variable *largest other S2s*[19] since contains information of multiple scatters). Figure 6.36 (*left*) illustrates the distribution of the combination of both data samples, where the trend and correlation of the S2 area and the hit pattern likelihood can be seen (data presented was processed with PAX version 6.5.0). Together with the S2 area energy dependency of their pattern likelihood, it can be observed that at S2 = 100 PE the AmBe contribution

[18] Here, instead of S2 it is used $S2_{Top}$ = S2×S2 area fraction top since the area fraction top, even though it has a small effect, helps to introduce an extra smearing from the imperfection of PMT pattern temples, thus making the result more robust.

[19] Associated with the second biggest S2 peak besides the main S2 peak used to pair the event, which in the case of AmBe data is mostly generated by multiple scatters of neutrons, such that this variable provides the perfect handle to test the hit pattern.

introduces some contaminated population having an exceeding S2 pattern likelihood. This is mainly because PAX clustering starts to cluster multi-electron-pile-up peaks into one S2, such that it can happen that several small single electrons end up accidentally summed together. Furthermore, the population below S2 = 70 PE is understood to be mainly composed by piled up of single electrons. With the basic understanding of the trend in the parameter space of these variables, the first step to make a correct definition for the cut was to examining several waveforms for events having a S2 pattern likelihood below/above the 98 percentile for a given S2 area. Since this inspection showed that events above this limit come close to be anomalous, i.e., having not a clear and singular S2 PMT hit pattern, for steps of 5 PE in S2 through the complete range showed, the 98 percentile is calculated. In order to avoid a bias due to the ill-defined population S2 = 100 PE, boundaries masking this region (marked in red dashed lines) have been established. Next, the calculated 98% quantile boundary is fit then with the same function used in SR1:

$$f(S2) = a \cdot S2 + b \cdot S2^{c} + d, \tag{6.15}$$

in order to generalize the energy dependency to different S2 areas. The fit uses the binned likelihood for this distribution, excluding the region specified by the red dashed lines, and it is sampled using an affine invariant Markov Chain Monte Carlo **MCMC** approach (see Figure 6.36 (*right*), where *clin, cpow, ppow* and *offset* correspond to *a, b, c* and *d* in Equation 6.15). Figure 6.36 (*left*) illustrates as well the comparison of the boundary definition used for SR0 (black) and SR1 (blue). These results show an improvement on the cut definition employed in SR0, where the cut did not fully captured the linear increase in the S2 pattern likelihood with increasing S2 observed, and it was also not extended for small S2s. Nevertheless, given that all different seven periods of ^{220}Rn calibration data were used at once to define this boundary, any possible variation of time was overlooked. This explains why the acceptance of this cut through the N-1 method presented shows such a time dependent behavior, given that, as later showed, the S2 pattern likelihood increased with time.

Since the time behavior of this cut was in question, a first cross check when loading ^{220}Rn calibration data taken on March 2017 and separately on October 2017 was done. By calculating and comparing the boundary obtained from the procedure discussed of each of these data sets, as contrasted in Figure 6.37, it was found that while the SR1 previous definition agrees with the fit for the data taken at the beginning of the year (were statistics dominate), for later times in the year the 98 percentile and thus the boundaries of the fit have changed in time, such that more events are being cut by this constant definition. Having recognized this trend, several conditions were inspected in order to understand the change in time of the S2 pattern likelihood with no success (one possible cause yet to explore has to do with considering the contribution from PMT after pulses). Thus a data driven approach was used such that for each of the seven ^{220}Rn calibration data periods in SR1, in addition to an extra period just after SR1 stopped, the 98 percentile boundary was derived and fit, as presented in Figure 6.36 (*c*). In order to capture the time dependent change found, the idea explored was to do a

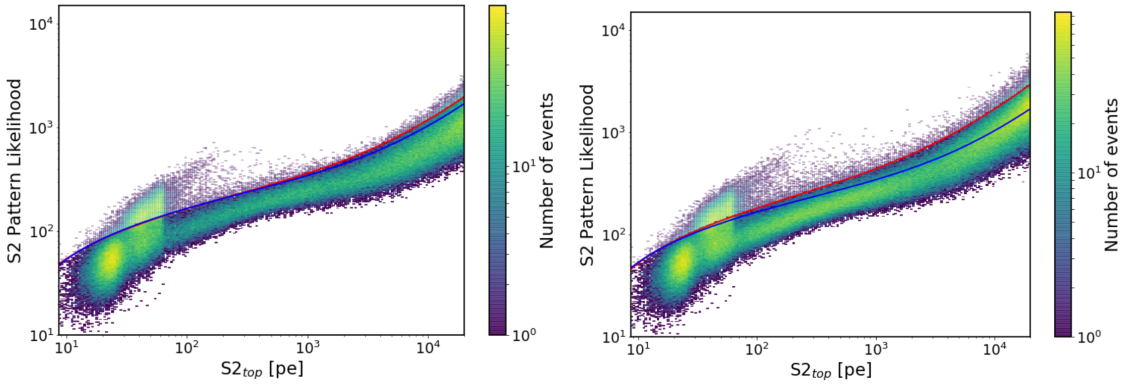

(a) ^{220}Rn calibration data from March 2017

(b) ^{220}Rn calibration data from October 2017

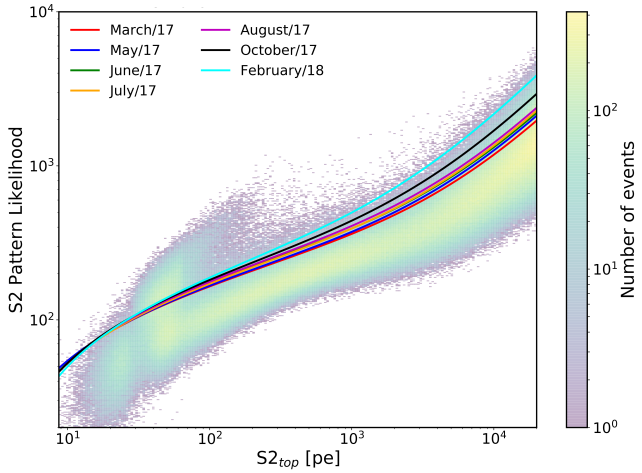

(c) Summary of all boundaries derived for all ^{220}Rn data.

Figure 6.37. S2 Pattern Likelihood cut boundary from SR1 (blue) in comparison with the derived boundary calculated (red) when using ^{220}Rn calibration data only from (**a**) March 2017 (**b**) October 2017 (**c**) Here each different color illustrates the boundary derived for each ^{220}Rn data set.

parametrization in time for the coefficients defying each of the fits obtained, such that a definition generalized continuously in time would enclose all the information derived from data.

Next, Figure 6.38 illustrates the trend and parametrization explored in time of the coefficients associated to each boundary derived. Here the black points correspond to the value of each coefficient, while two different interpolation functions have been explored. On one hand, following the assumption of a linear change between each coefficient, a linear interpolation has been calculated in solid *blue, green, red* and *pink*, corresponding to the parameters *a,b,c* and *d* found in Equation 6.15. On the other hand, the interpolation labeled as "nearest" (solid magenta), does not assume a continuous linear increase but rather follows in a continuous behavior around the data, changing like a step function to the previous or next value half way in time distance to that value. In practice, the implementation of the linear assumption was tested on data, in preference to the unphysical changed of the step-like interpolation approach. The results were satisfactory in terms of the posterior acceptance evolution

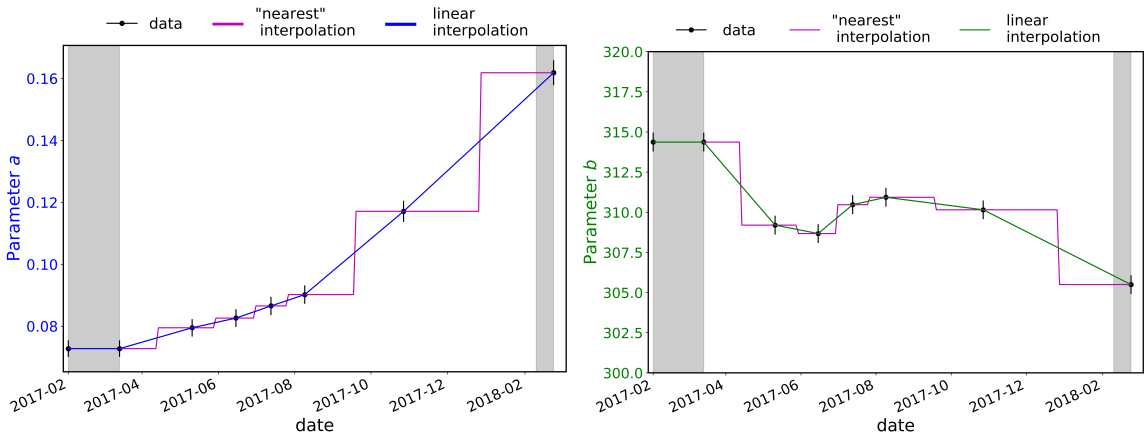

(a) Parameter a

(b) Parameter b

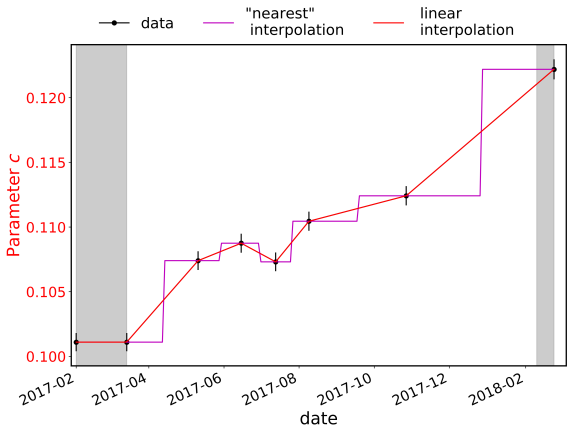

(c) Parameter c

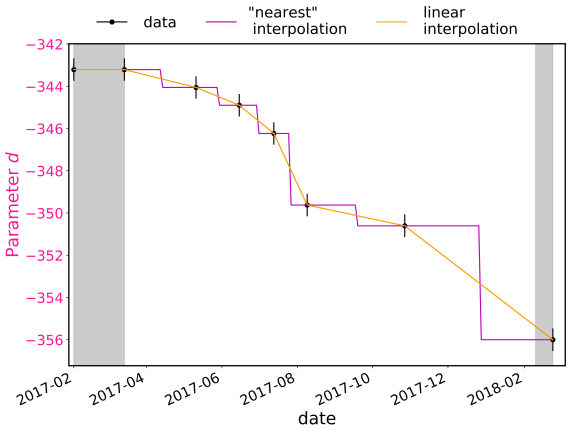

(d) Parameter d

Figure 6.38. Description of time-dependency of each coefficient defined by Equation 6.15, for the boundaries summarized in Figure 6.37 (**c**), calculated for the 8 sets of ^{220}Rn calibration data.

found for this new time dependent and continuous definition describing the S2 Pattern Likelihood boundary needed to find data that could be trusted, as presented in Figure 6.39. For the acceptance evolution trend calculated, by making a linear fit, it is found that the average acceptance using the new cut definition is 0.984, while for the previous definition used it was close to 0.943 (most importantly while having a strong time-dependent drop passed July). As result, this new definition was implemented in the analysis given that opposite to the previous definitions constructed both in SR0 and SR1, this one guaranteed time stability.

6.5.7 Low Energy Rate

Annual modulation studies

An accurate determination of the low energy ER rate inside the detector is a major ingredient for the described annual modulation study that aims for a detection of leptophilic dark matter particles. One

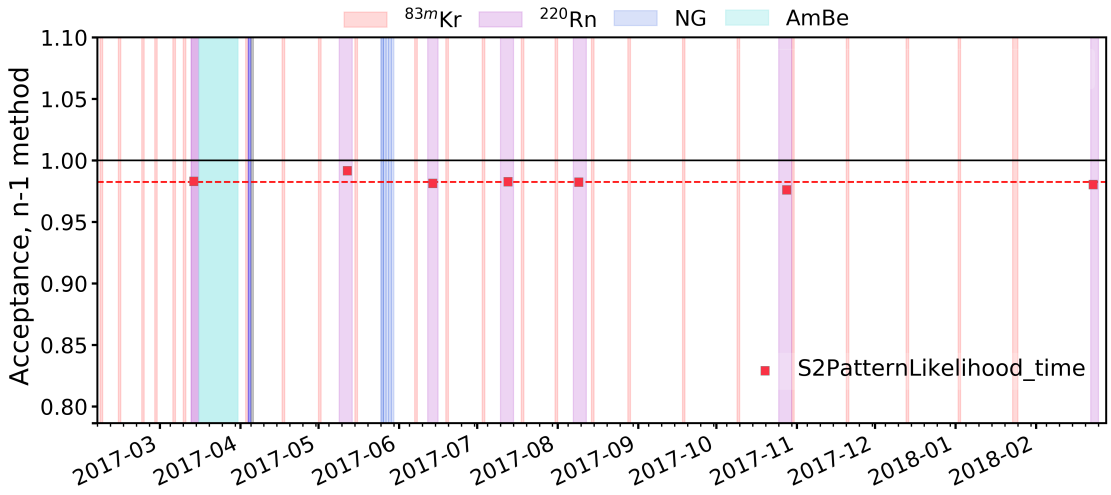

Figure 6.39. Time evolution monitoring of the N-1 acceptance of the new time-dependent *S2 likelihood time-dependent cut*. Opposite to the results found for the previous definition of this cut, see Figure 6.35 (bottom), the acceptance stability requirement required has been demonstrated to be satisfied with the new proposed data-driven definition introduced.

important step in calculating this rate is the cut selection as described in the previous section. It was shown that, with the adopted S2PatternLiklihoodCut, the overall cut acceptances is stable over time. In a next step the absolute value of the integral cut acceptance has to be determined. Subsequently, one can either correct the rate with this total cut acceptance, or, as it will be done in this analysis, the cut acceptance will be considered in the statistical analysis, with which the significance of a potential modulation will be probed. Furthermore, the total cut acceptance is slightly energy depending, in the order of a few percent. This affects the rate, depending on the selected energy range that was chosen. The rates shown in this section do not include this energy dependency of the cut acceptance yet, but the effect is expected to be minor.

After applying all selection cuts, including the one of the $\pm 3\sigma$ quantile ER band selection, the light and charge signals of each event are used to calculate its energy in the CES. In Figure 6.40 (*left*) this was done for an energy range of (0 - 20) keV in 1 t FV. The rate is stably decreasing towards low energies due to a limited detector efficiency for small signal sizes. Around 2.5 keV an upwards fluctuation of the energy spectrum is seen that could be caused by the β-decay of tritium. Tritium can be produced by cosmic activation when the xenon is stored above ground. This hypothesis is currently under investigation by the XENON Collaboration. Apart from this the energy spectrum appears to be flat as expected.

Figure 6.40 (*right*) shows the simulated energy spectrum in 1 t FV, equivalent to the one extracted from data. It serves as illustration of the various ER background contributions as described previously. The largest one is induced by ^{214}Pb from the ^{222}Rn decay chain (red line). In the simulation a level of 10 mBq/kg xenon is assumed, determined by radon emanation measurements of most detector components before the experiment started. From data, the maximum and minimum decay rate of ^{214}Pb

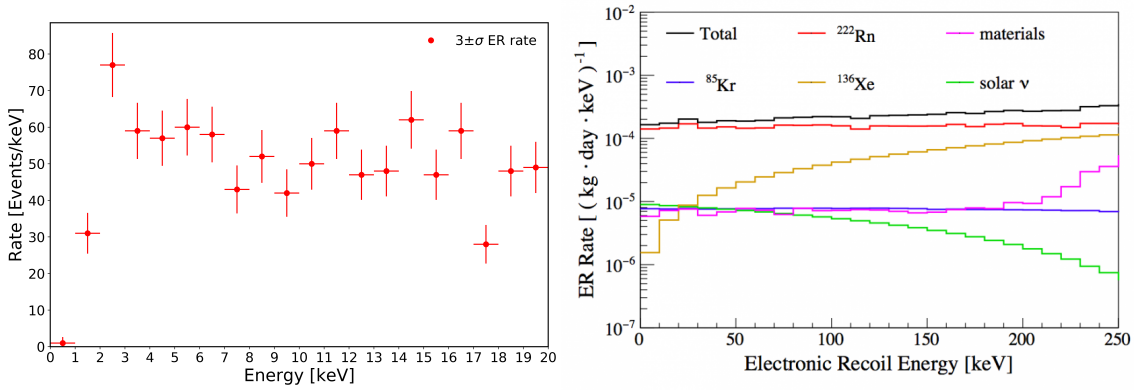

Figure 6.40. Left Energy spectrum in combined energy scale for all ER events after the applying the selection cuts. **Right** Energy spectrum of the total ER background rate in the 1 t fiducial volume (black), and the separate contributions from detector components (purple), 10 mBq/kg of ^{222}Rn (red), 0.2 ppt of ^{nat}Kr (blue), solar neutrinos (green) and ^{136}Xe double-beta decay (brown).

is (12.6 $\pm$ 0.8) and (5.1 $\pm$ 0.5) mBq/kg, determined with the α-decay of ^{218}Po and the time-coincident ^{214}Bi-^{214}Po decays, respectively. In the order of a few percent, the decays of ^{nat}Kr (blue), the detector material (purple), solar neutrinos (green) and ^{136}Xe double-beta decay contribute.

The detailed background study in the framework of the annual modulation analysis is beyond the scope of this thesis and still under investigation by the XENON Collaboration at the time of writing. We just want to summarize the most important background components in the following. For the annual modulation search only time-varying background sources are from interest. Due to its long half-life of (2.17×10^{21}) years, the contribution of ^{136}Xe is constant in the data taking time of XENON1T. Hence, it will not be considered. From the detector materials themselves, mainly the decay of ^{60}Co is important as it, on one hand, presents the largest contribution from material induced background inside the 1 t FV. However, due to the high stopping power of xenon, this contribution is in the order of only one percent. On the other hand, ^{60}Co decays present a time-varying background component as it decays with a half-life of 5.3 years. The amount of ^{nat}Kr is also time depending. During SR0 the concentration was lowered by more than three orders of magnitude. During the second science run it was observed that the concentration is slightly increasing again. This could be caused by the slow diffusion of ^{nat}Kr out of the detector components over time. The interaction of solar neutrinos with the liquid xenon is also only in the order of a few percent in comparison with the ^{214}Pb induced background. It varies over time due to the Earth's motion around the Sun. Another background could arise from the decays of ^{212}Pb, a decay daughter in the ^{220}Rn chain. These decays were monitored over time and are in the order of one percent compared to the ^{214}Pb induced background. Even though the ^{214}Pb contribution is observed to be stable over time, it will be nevertheless considered in the background model as it presents the most dominant background component.

In Figure 6.41 the final low energy ER rate is shown for three different binnings over the time period of SR1. We chose a signal energy range of (1 - 6) keV as dark matter is expected to induce

low-energetic recoils with the atomic electrons. As control region we chose a higher energy window of (6 - 20) keV in which no signal is expected. Thereby, potential detector effects that could mimic an annual modulation signal can be detected. The uncertainty (either Poissonian or Gaussian) on each data point was calculated depending on the underlying amount of events. Average rates of $(2.13 \pm 0.16) \times 10^{-4}$, $(2.22 \pm 0.17) \times 10^{-4}$ and $(2.17 \pm 0.14) \times 10^{-4}$ Events/(kg×day×keV) were found for a binning of 15, 28 and 40 days, respectively. The rates agree among each other within the uncertainties. Furthermore, a rate of $(2.00 \pm 0.11) \times 10^{-4}$ Events/(kg×day×keV) was determined in an energy range of (1 - 12) keV and 1 t FV. This is in agreement with the predicted ER rate based on Figure 6.40 (right) of $(1.80 \pm 0.15) \times 10^{-4}$ Events/(kg×day×keV). This shows that the ER background components in 1 t FV are well understood and that no additional, large background was detected.

From Figure 6.41 it seems as the rate changes periodically during SR1. However, it requires a full profile likelihood analysis, which incorporates the stability of the detector parameters and the ER background model to quantify the significance of periodicity in the time distribution of events. Even though this is beyond the scope of this thesis, it determined the central necessary parameter, the ER rate, along with the proof of a stable cut acceptance over time. Both studies will serve as input for the ongoing annual modulation analysis in XENON1T.

Monitoring main ER background

In this section we show the ER rate in Figure 6.42 (blue) during the commissioning phase of XENON1T in autumn 2016, during SR0 as well as at the beginning of SR1. Additionally, the absolute krypton in xenon concentration measured with RGMS is presented in red. In terms of the ER rate an energy range of (80, 150) keV was used and slightly different cuts as described in the previous sections. This is still sufficient to use the calculated rate as a complementing way to monitor the krypton concentration in xenon, the main goal of Figure 6.42.

During the commissioning phase the krypton rate was the dominant source of background. As the online krypton distillation started, the krypton rate was significantly reduced by more than three orders of magnitude. A simultaneous rate reduction can be also observed in the ER rate. Beginning of December 2016 the low energy rate levels off, despite the further krypton reduction measured via xenon gas samples in the RGMS. This is a clear indication that krypton is no longer the major electronic recoil background. From then on radon became the dominant source of background in XENON1T. Moreover, Figure 6.42 shows that the radon rate did not change significantly during the science runs, as the ER rate is stable over time. This is a sign that no air leak is present as it was partly the case in XENON100.

Table 6.9. Overview of the selection criteria used in Annual Modulation to ensure the quality and consistency of the found events.

Name cut	Description	Time dependency
InteractionPeaks Biggest	Ensures that the main peak is larger than the other peaks	No
S2 Single scatter	Removes neutron background by excluding double/multiple scatters	No
S2 Width	It compares the S2 width expect from the diffusion model to the one measured. It removes several unphysical events: gas events, accidentally coincidences, etc	No
cS2 Area Fraction Top	Designed to remove some of the gas events which get through the S2 width cut	No
DAQ Veto	Computed as a livetime loss, it removes events containing a dead-time trigger. It also checks both busy and high-energy vetos	No
S1 Single scatter	By checking if an alternate interaction exists between the main S2 and an S1 which is not the main S1, reduced a population to only single interactions	No
S2 Tails	Checks if an event is in a tail of a previous S2, and if so, it removes the tail to avoid lots of little S2s which are noisy in general	No
Flasher	Removes events within a PMT flash. In addition, an extended time-window around the flash is removed as well	No
S2 Pattern Likelihood	Rejects poorly reconstructed S2s, multiple scatters or anomalous hit patterns	Yes
MissIdSingle scatter	Removes remaining events from ^{83}Rb contamination where S1s are misclassified as S2s	No
Fiducial Cylinder 1T	$-92.9 < z < -9$ cm $\mid x^2 + y^2 < 36.94^2$ cm^2	No
$\pm 3\sigma$ **ER band** quantiles	Specific cut for electronic recoil events selection	No

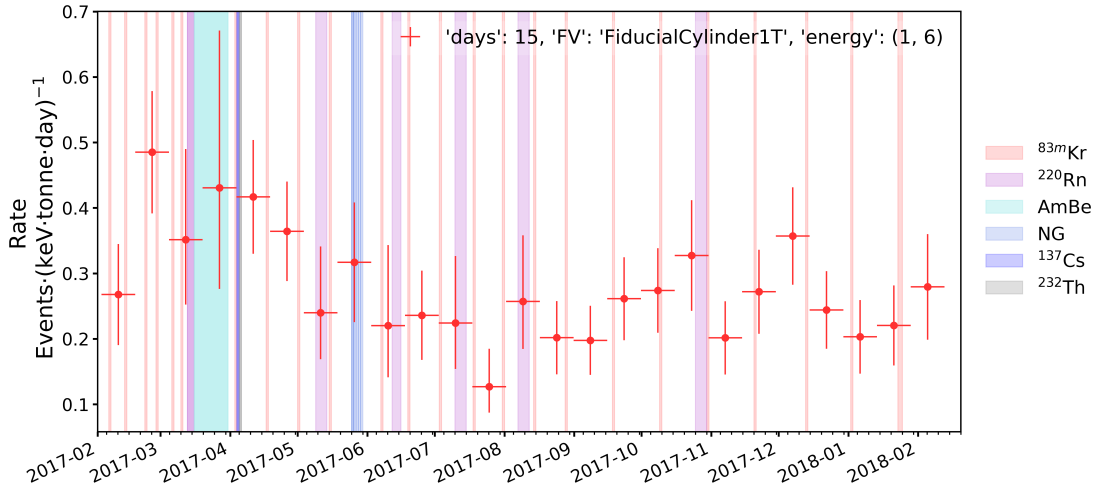

(a) Time binning used: 15 days

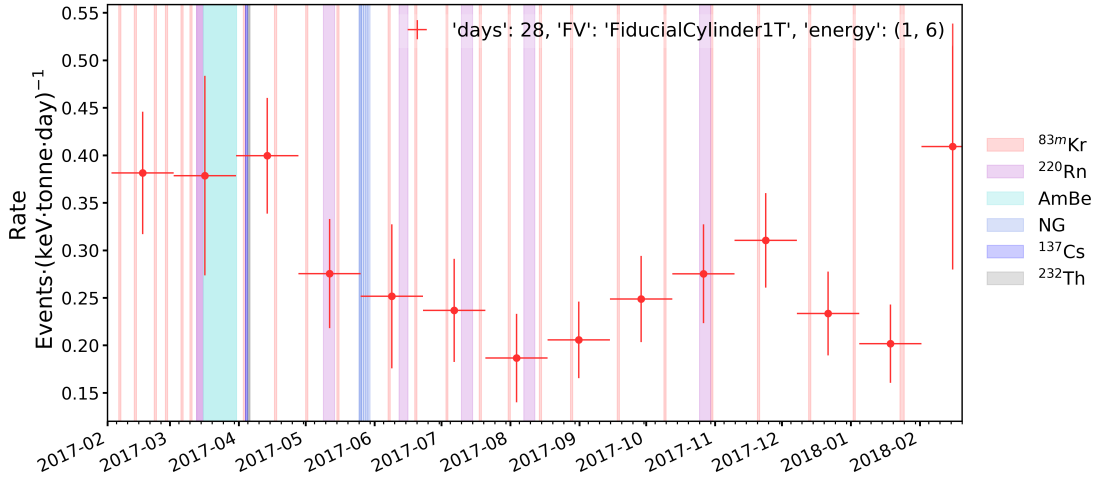

(b) Time binning used: 28 days

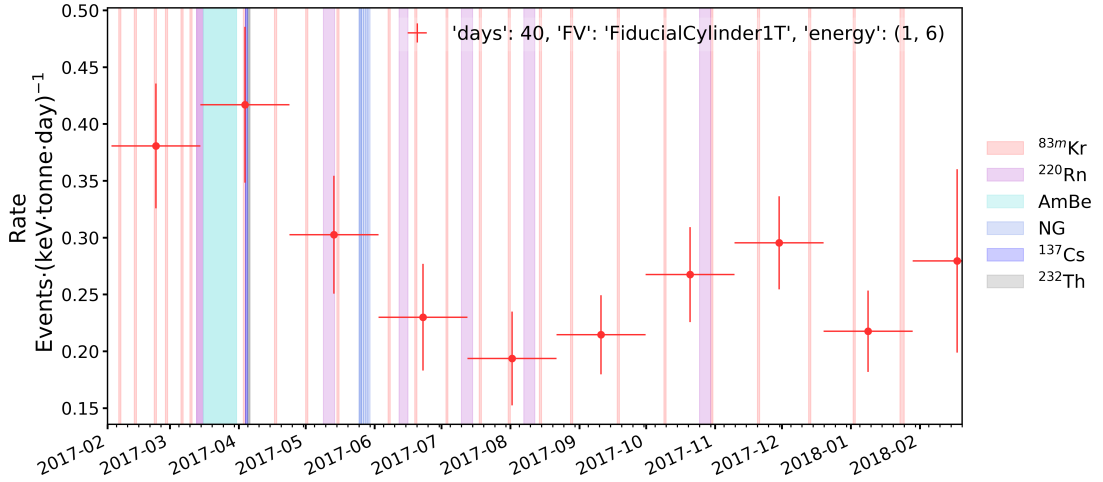

(c) Time binning used: 40 days

Figure 6.41. Monitoring of the ER background in annual modulation studies after the selection of cuts discussed was performed. The results correspond to the ER background rate evolution in time inside 1 t FV for the energy window defined by (1-6) keV. Firthermore, from (*a-c*) the rate was calculating using as temporal binning 15, 28 and 40 respectively.

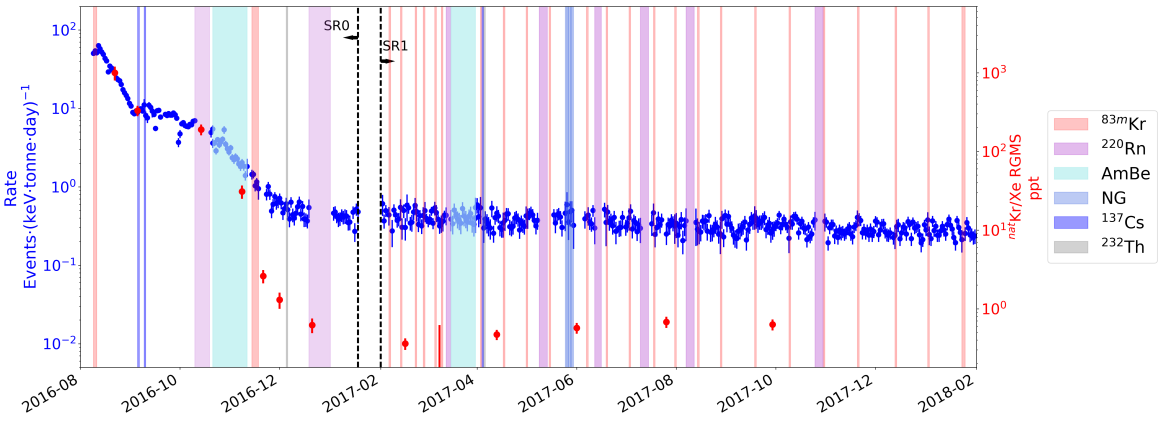

Figure 6.42. Monitoring evolution of the rate of the low energy components of the intrinsic internal backgrounds that are dispersed inside detector. The rate of these components (mainly radon progeny and ^{85}Kr) are presented (blue) together with the corresponding RGMS measurements (red). The rate is calculated taking at least 2 days of live data at the time.

Chapter 7

Beyond WIMPs: Sub-GeV Dark Matter Scattering off electrons

In spite of WIMPs being currently one of the most well-motivated candidates for dark matter, such that most of direct detection experiments are optimized to detect weak-scale $\mathcal{O}(100)$ GeV particles scattering off nuclei from a target, efforts searching for this signature have so far not been able to establish a discovery nor suggest clear hint of a potential signal (see section 2.3). With the reality of exclusion limits continuously getting tighter and t×yr exposure detectors on the verge of becoming sensitive enough to measure neutrino-induced recoil events due to solar, atmospheric, and diffuse supernova neutrinos (referred as the inevitable background from the "neutrino floor" [61]), it is useful to take advantage of well motivated theoretically constructions that explore new alternatives. One of these well-motivated constructions is to consider weakly interacting sub-GeV dark matter with masses in the MeV to GeV range [263–265]. As illustrated in Figure 7.1, this proposal aims on taking advantage of the opportunity to extend the reach of exclusion and discovery for different dark matter masses without changing the technology already developed by several experiments.

Light candidates are motivated by several aspects. On one hand by production mechanisms that go beyond the standard freeze-out, such as asymmetric dark matter [266], bosonic super-WIMPs [267], WIMPless [268], etc. On the other hand since the origin of the dark matter relic density can naturally be addressed by several means that suggest light dark matter interacting with standard model particles via the exchange, for example, of an axion, a light dark photon or through and electromagnetic dipole moment. A natural way to also motivate this approach arises from the fact that direct detection experiments expect an average energy transferred for an elastic nuclear recoil in the order of:

$$E_{\rm NR} = \frac{q^2}{2m_{\rm N}} \leq \frac{2\mu_{\chi{\rm N}}^2 v^2}{m_{\rm N}} \simeq 1 \text{ eV} \times \left(\frac{m_\chi}{100 \text{ MeV}}\right)^2 \left(\frac{20 \text{ GeV}}{m_{\rm N}}\right), \tag{7.1}$$

where $q \sim m_\chi v$ is the momentum transferred, the typical dark matter average velocity is of the order of $v \sim 10^{-3}c$ and $m_{\rm N}$ is the mass of the nucleus. Thus, as illustrated in Figure 7.2 for a diverse of different target materials (gray band), in the case of considering as an example a dark matter

mass of $m_\chi = 20$ GeV scattering with a xenon target ($m_N \sim 120$ GeV), a recoil energy close to $E_{\rm NR} \simeq 6.541$ keV would be expected, enough to obtain a variety of measurable signals in different detector technologies[1] . However, in the context of considering lighter dark matter masses such as m_χ = 100 MeV, the recoil energy of any of those materials considered will drop below the eV level, which is generally way below the detection thresholds of any current direct detection experiments (e.g. XENON1T: 1 keV_{nr} [62], LUX: 1.1 keV_{nr} [270], SuperCDMS: 1.6 keV_{nr} [270]). Consequently, signals below the GeV mass scale for elastic scatterings with the nucleus are not accessible as the feasible recoil energies are below any realistic detection threshold. Nonetheless, the recoil energy available in the case of dark matter scattering off electrons would scale as:

$$E_{\rm e} \leq \frac{1}{2}\mu_{\chi {\rm N} v^2} \simeq \frac{1}{2}\ \text{eV} \times \left(\frac{m_\chi}{\text{MeV}}\right), \tag{7.2}$$

where $E_{\rm e}$ is the energy transferred to the electron, as illustrated in 7.2 (green band). Although some of this energy goes to overcome its binding energy, it turns out that there is left sufficient energy to induce inelastic atomic processes that require energies in the order of a few eV. Thus sub-Gev dark matter masses can be probed since the resulting energy of these processes are in the order of few hundred eVs. If these processes are attribute to sub-GeV dark matter particles scattering with electrons, measurable signals in the form of few electron may result from primary ionized electron or de-excitation photons, which can induce further ionization. Studies on these few ionization signals can be explored in experiments such as XENON1T through analyses such as single-electrons characterization [246] or ionization-only ("S2-only") approach [246, 271].

This chapter is dedicated to explore the premise of sub-GeV dark matter scattering with atomic electrons, as opposed to nuclei. Subsequently, the observable signals from different channels in XENON1T will be used to analyze the sensitivity and the constrain power of this framework. The chapter starts presenting all the details needed to establish the machinery to calculate direct detection rates, along several cross-checks of the framework developed with calculations presented in literature (section 7.1). Next different physical channels of applicability in XENON1T are discussed and preliminary sensitivity studies are presented (section 7.2). Lastly, a neutrino-like MeV dark matter and electron recoil model is explored in connection of the framework developed (section 7.3).

[1] Signals such as phonons, electron from ionization, electronic excitation, molecular disassociation, etc. [269].

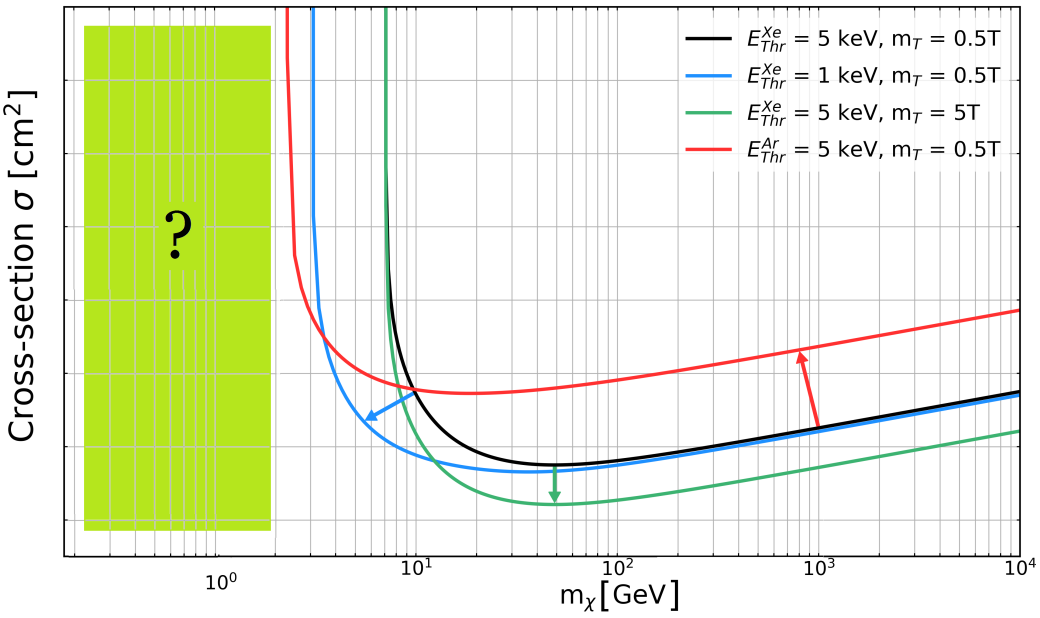

Figure 7.1. Illustration of results from direct dark matter detection derived in terms of the cross-section as function of the WIMP mass. The different colored limits illustrate the variation of an upper limit due to changes in the detector design or properties. Under the approach of considering sub-GeV dark matter scattering off electrons, the green box represents the new space available for probing light dark matter.

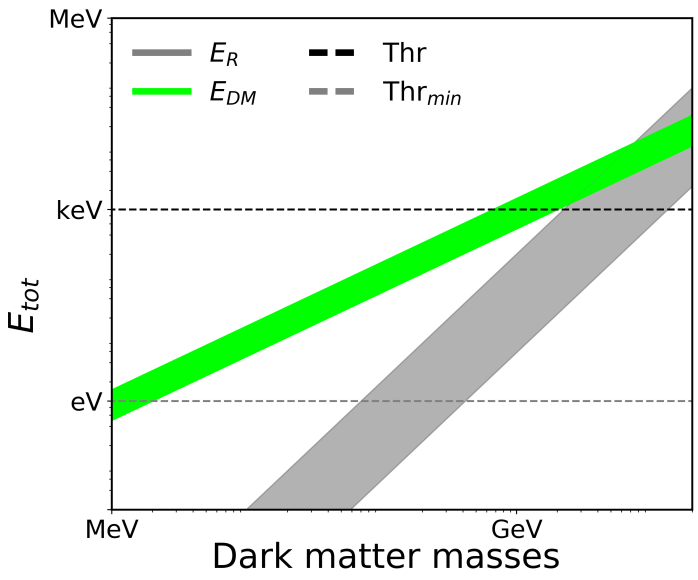

Figure 7.2. Illustration of the elastic scattering in direct detection. Presented are the considerations for nuclear recoils (gray band) together with the available recoil energy in the case of dark matter scattering off electrons (green band). Dashed lines illustrate the typical nuclear recoils detection threshold for many direct detection experiments (black), together with the minimal threshold of detecting dark matter-electron scattering (gray).

7.1 Detection strategy

In contrast with the standard approach already discussed in section 3.1, signatures from processes where dark matter scatters off electrons tend to be dismissed in liquefied noble gas detector techniques. This is because it is assumed that these electrons are at rest and therefore, with typical dark matter average velocities of $v \sim 10^{-3}c$, they could only realize a maximal detectable energy in the order of few eV, something quite challenging in terms of distinguishing a signal from background. However, in reality these electrons are bound to the atom such that even in the case of the atom being at rest, an electron could have a non-negligible momentum[2] p (e.g. bound electrons in Na(TI) have a probability equal to 1.5×10^{-4} to have a momentum $p > 0.5$ MeV/cm). Hence, interactions with these high momentum electrons can give rise to detectable signals having an average energy transfer to the detector proportional to the momentum $E_e \sim pv$. Accordingly, an electron having a momentum $p \sim$MeV would then induce to obtain at least energies of the order of $E_e \sim$keV, something feasible to measure.

The challenge in probing this hypothesis is essentially twofold: on one hand modeling bound electrons in a dense media can be difficult because there is a complicated structure of energy levels. Electrons have typical speeds greater than dark matter particles and also since they have an indefinite momentum (where even large momenta can be found to have non-zero probability). On the other hand, the quantum nature of the initial and final state of the electrons cannot be treated simply classically, as discussed in [273]. In the next subsections the different ingredients needed to calculate a differential ionization event rate will be explained in detail, together with a procedure on how to overcome this challenges.

7.1.1 Scattering kinematics

Unlike the kinematics from a nuclear recoil, in the case of dark matter scattering with electrons, the starting point is to consider a dark matter particle of mass m_χ colliding with a bound electron such that the transferred energy ends up exciting the ground state electron into either a higher energy bound state or into an ionized state (as illustrated in Figure 7.3). Since a bound state electron does not have a definite momentum, and in fact it may have arbitrarily high momentum with low probability, the energy transferred to the electron ΔE_e can be calculated in terms of the momentum lost of the initial dark matter particle momentum $\vec{q}$, as:

$$\begin{aligned}\Delta E_e &= -\Delta E_\chi - \Delta E_N \\ &= -\frac{|m_\chi \vec{v} - \vec{p}|^2}{2m_\chi} + \frac{1}{2}m_\chi \vec{v}^2 - \frac{q^2}{2m_N} \\ &= \vec{q}\cdot\vec{v} - \frac{q^2}{2\mu_N},\end{aligned} \tag{7.3}$$

[2] In fact, the typical velocity of a bound electron is in the order of $v_e \sim Z_{eff}\alpha$, where Z_{eff} is 1 for outer shell electrons and larger for inner shells. Thus these possible velocities are larger that the dark matter average velocities of $v \sim 10^{-3}c$ [272].

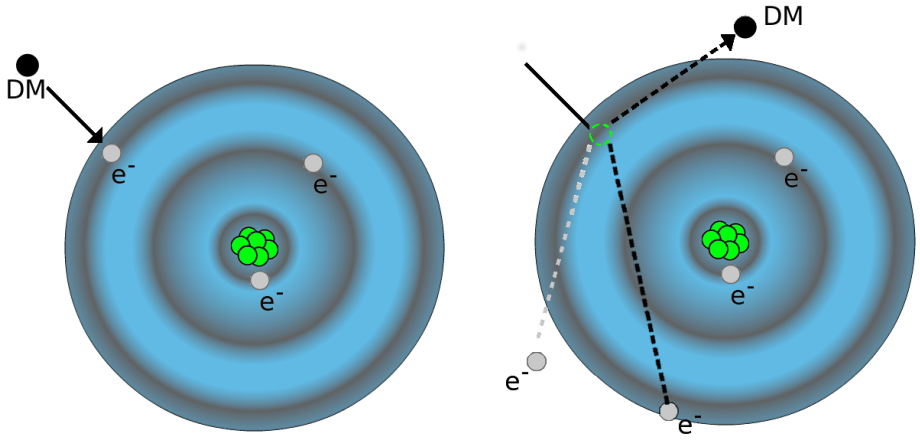

Figure 7.3. Illustration of a dark matter DM particle scattering with a bound electron. The transfer of momentum to the target produces the excitation from ground state electrons into excited states, or with enough energy it can result in an ionized state.

where the ΔE_χ is the change in energy for the dark matter particle and ΔE_{N} accounts for the recoil of the entire atom. Given that in practice the recoil of the atom is relatively small, which also allows to replace μ_{N} with m_χ, the energy transferred to the electron simplifies to:

$$\Delta E_{\mathrm{e}} = -\Delta E_\chi. \tag{7.4}$$

Having now the possibility to consider an arbitrary size momentum transfer to the electron, ΔE_e, this value can be maximized with respect to $\vec{q}$ in order to find what is the largest allowed energy transfer (this energy corresponds to all the kinetic energy of the collision available to excite the electron), which leads to:

$$\Delta E_{\mathrm{e}} \leq \frac{1}{2}\mu_{\mathrm{N}} v^2 \approx \frac{1}{2} m_\chi v^2. \tag{7.5}$$

From Equation 7.3, it is hinted that as long as m_χ is above the bound implied by Equation 7.5:

$$m_\chi \geq 2 \cdot \frac{\Delta E_{\mathrm{e}}}{v^2},$$

the $\vec{q} \cdot \vec{v}$ term will dominate. As consequence, the minimum momentum transfer q_{min} required for an energy transfer of ΔE_{e} can be expressed as:

$$q_{\mathrm{min}} \geq \frac{\Delta E_{\mathrm{e}}}{v}. \tag{7.6}$$

The scaling found in Equation 7.5 indicates as well that in order to cause transitions with more energy than a few eV, a typical momentum on the tail of the electron's momentum space - or probing the tail of the dark matter velocity distribution - is needed. At the same time, the energy transfered to the electron ΔE_{e} will contribute both to overcome the binding energy of the electron in its initial

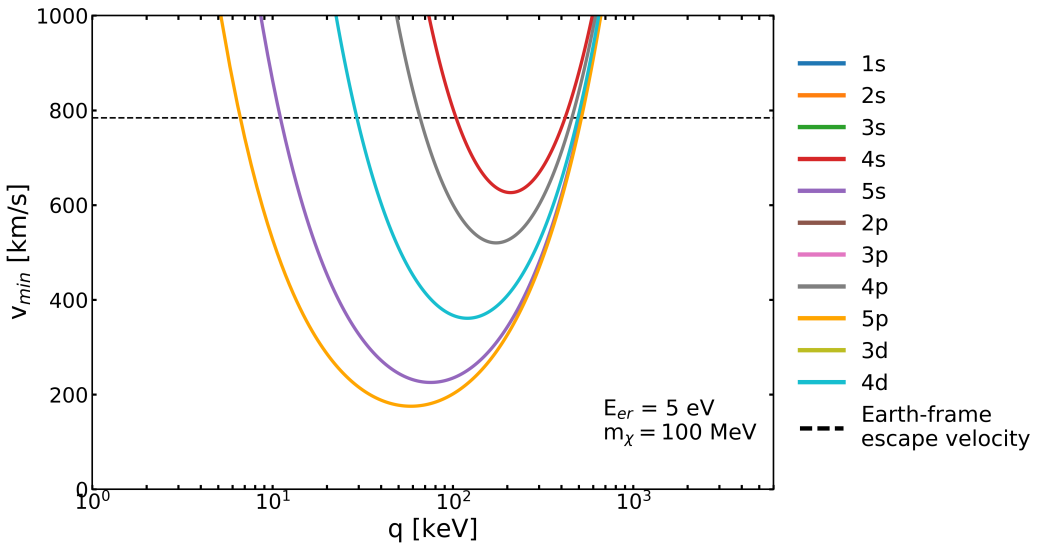

Figure 7.4. Minimum dark matter velocity $v_{\rm min}$ required for an electron to gain an energy $E_{\rm e}$ as function of the momentum transfer q. In different colors are illustrated the kinematical restrictions for different shells with quantum numbers (n,ℓ) for $m_\chi = 100$ MeV and an electron recoil energy $E_{\rm er} = 5$ eV. The Earth's frame escape velocity (dashed line) determines the constrains for the allowed momentum transfered.

bound state (n,ℓ), $E_{\rm B}^{n\ell}$, and to the electron recoil energy $E_{\rm er}$:

$$\Delta E_{\rm e} \equiv E_{\rm e} = E_{\rm B}^{n\ell} + E_{\rm er}. \tag{7.7}$$

Returning to the conservation of energy given by Equation 7.3, but neglecting the recoil of the atom since it is relatively small, one can find an expression for the minimum dark matter velocity required to induce a electron recoil $E_{\rm er}$ by taking the momentum transfer to be parallel to the initial dark matter velocity:

$$E_{\rm B}^{n\ell} + E_{\rm er} = -\frac{(m_\chi v_{\rm min} - q)^2}{2m_\chi} + \frac{1}{2}\frac{(m_\chi v_{\rm min})^2}{m_\chi}. \tag{7.8}$$

Thus, by solving Equation 7.8 for $v_{\rm min}$, one can determine the dependency of this minimum speed in terms of the the momentum transfer and the bound state of energy of the target electron:

$$v_{\rm min} = \frac{E_{\rm B}^{n\ell} + E_{\rm er}}{q} + \frac{q}{2m_\chi}. \tag{7.9}$$

Equation 7.9 embodies all requirement of energy conservation. It contains the information about the minimum dark matter velocity $v_{\rm min}$ required for an electron to gain an energy $E_{\rm e}$ with a momentum transfer q. This is illustrated in Figure 7.4 in the context of xenon for all its different shell states. In this parameter space, by including the physical constrains from the Earth's frame escape velocity (black dashed line), it can be determined the allowed range of momentum transfered for a given electron recoil energy.

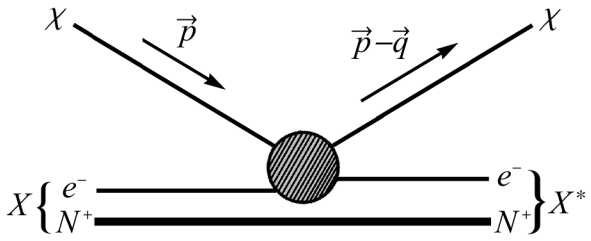

Figure 7.5. Scattering kinematics of a dark matter χ particle with a bound electron. The dark matter momentum transfer $\vec{q}$ to the target material consequently leading to two possibilities: to excite the electron from the ground state X into an excited state X* with a higher bound energy or to produce an ionized state. Adapted from [272].

7.1.2 Velocity-averaged ionization cross-section for electrons

Based on the formalism described in [272], the scattering rate for dark matter-electron interaction can be derived from the standard approach of cross-section calculations in field theory. Starting by considering the electron as being bound in a static background potential (stationary bound state), the transfer of momentum $\vec{q}$ after the scattering may excite the electron from an initial energy level 1 to an excited energy level 2, as shown in Figure 7.5. For a free $2 \rightarrow 2$ scattering, the strength of this interaction can be parameterized in terms of a cross-section as:

$$\sigma v_{\text{free}} = \frac{1}{4E'_\chi E'_e} \int \frac{d^3q}{(2\pi)^3} \frac{d^3k'}{(2\pi)^3} \frac{1}{4E_\chi E_e} (2\pi)^4 \delta(E_i - E_f) \delta^3(\vec{k} + \vec{q} - \vec{k}') |\overline{\mathscr{M}_{\text{free}}(\vec{q})^2}|, \tag{7.10}$$

where $\mathscr{M}_{\text{free}}$ is the field theory invariant amplitude and $|\overline{\mathscr{M}(\vec{q})^2}|$ represents its absolute square averaged over the sum of all possible initial and final spin configurations. In order to account for the bound-state scattering amplitude nature from assuming electrons being bound instead of free, and to account for the different final state phase space for the different electron levels, the *atomic form factor* $f(\vec{q})$ is introduced. Thus, the excitation of an electron from the level 1 to level 2 described by Equation 7.10 can now be written as:

$$\sigma v_{1\rightarrow 2} = \frac{1}{4E'_\chi E'_e} \int \frac{d^3q}{(2\pi)^3} \frac{1}{4E_\chi E_e} (2\pi) \delta(E_i - E_f) |\overline{\mathscr{M}_{\text{free}}(\vec{q})^2}| \times |f_{1\rightarrow 2}(\vec{q})|^2. \tag{7.11}$$

Furthermore, to account for the momentum dependence of this interaction, one can follow the parametrization discussed in [264] and introduce a dark matter form factor $F_{\text{DM}}(q)$ that will describe the underlying dark matter-electron coupling. Explicitly, this dependency is captured by defining the cross-section in terms of the invariant matrix amplitude for dark matter-electron free elastic scattering with a fixed momentum transfer $q = \alpha m_e$ and respectively $\mathscr{M}_{\text{free}}(\alpha m_e)$, such that:

$$\overline{\sigma_e} = \frac{\mu_{\chi e}^2}{16\pi m_\chi^2 m_e^2} \overline{|\mathscr{M}_{\text{free}}(\alpha m_e)|^2}\Big|_{q^2=\alpha^2 m_e^2}, \tag{7.12}$$

such that the input from particle physics is specified by two elements. On one hand by the normalized cross-section $\overline{\sigma_e}$, representing the non-relativistic scattering rate between electrons at a fixed momentum transfer αm_e and dark matter. On the other hand by the form factor $F_{DM}(q)$, that contains the momentum transfer dependence of the field theory invariant amplitude, defined as:

$$|F_{DM}(q)|^2 = \overline{|\mathscr{M}_{free}(\vec{q})|^2}/\overline{|\mathscr{M}_{free}(\alpha m_e)|^2}. \tag{7.13}$$

While the parametrization in terms of $\overline{\sigma_e}$ and $F_{DM}(q)$ offers a model-independent framework, there are several light dark matter models motivated on communicating the dark matter particles, from a dark sector, with the Standard Model **SM**. As discussed in [272], through this chapter there are mainly considered models derived from using a vector-portal that communicates the dark sector with the SM via a $U(1)_D$ gauge boson A', exchanged when dark matter scatters off electrons. The reference cross-section for this scenario is then given by:

$$\overline{\sigma_e} = \frac{16\pi\mu_{\chi e}^2\alpha\varepsilon^2\alpha_D}{(m_{A'}^2+\alpha^2m_e^2)^2} \simeq \begin{cases} \frac{16\pi\mu_{\chi e}^2\alpha\varepsilon^2\alpha_D}{(m_{A'})^4} & m_{A'} \gg \alpha m_e \\ \frac{16\pi\mu_{\chi e}^2\alpha\varepsilon^2\alpha_D}{(\alpha m_e)^4} & m_{A'} \ll \alpha m_e \end{cases}, \tag{7.14}$$

where ε is a kinetic mixing parameter, $\mu_{\chi e}$ is the dark matter-electron reduced mass and $\alpha_D = g_D^2/4\pi$ (with g_D as the $U(1)_D$ gauge coupling). Thus, for these reference cross-sections, the corresponding dark matter form factors are:

$$F_{DM}(q) = \frac{m_{A'}^2+\alpha^2m_e^2}{m_{A'}^2+q^2} \simeq \begin{cases} 1 & m_{A'} \gg \alpha m_e \\ \frac{\alpha^2m_e^2}{q^2} & m_{A'} \ll \alpha m_e \end{cases}, \tag{7.15}$$

where q is the momentum transfered in the scattering between the dark matter particle and the electron and both regimes considered define different parameter spaces that can have different production mechanism. The resulting dark matter form factors $F_{DM}(q) = 1$ and $\alpha^2m_e^2/q^2$ correspond to generic modes having heavy and light mediator models, respectively[3].

Expressing the energies in the non-relativistic regime:

$$\begin{aligned} E_i &= m_\chi + m_e + \frac{1}{2}m_\chi v^2 + E_{e,1} \\ E_f &= m_\chi + m_e + \frac{1}{2}\frac{|m_\chi\vec{v}-\vec{q}|^2}{m_\chi} + E_{e,2}, \end{aligned} \tag{7.16}$$

together with Equation 7.12, the cross-section given by Equation 7.11 simplifies to:

$$\sigma v_{1\to2} = \frac{\overline{\sigma_e}}{\mu_{\chi e}^2}\int\frac{d^3q}{(4\pi)}\delta\left(\Delta E_{1\to2} + \frac{q^2}{2m_\chi} - qv\cos\theta_{qv}\right) \times |F_{DM}(q)|^2|f_{1\to2}(\vec{q})|^2. \tag{7.17}$$

[3]The former can result from a point-like interaction induced by the exchange of a heavy vector mediator or magnetic dipole moment coupling, while the latter can arise from the exchange of a massless or ultra-light vector mediator.

7.1.3 Ionization event rate

From the derived velocity-averaged ionization cross-section for a given transition and a given target electron, Equation 7.17, the rate for dark matter-electron interaction can be obtained in the same way that it was done for dark matter-nucleus in section 3.1.2. That is, by introducing the dark matter density and averaging over the dark matter velocity distribution $f(v,t)$, the rate for a transition from the energy level 1 to the energy level 2 is given by:

$$R_{1\to 2} = \frac{\rho_\chi}{m_\chi} \int d^3v f(v,t)(\sigma v_{1\to 2}). \tag{7.18}$$

Now, by approximating the dark matter velocity to be spherically symmetric, one can integrate out the δ-function as:

$$\begin{aligned} R_{1\to 2} &= \frac{\rho_\chi}{m_\chi} \frac{\overline{\sigma_e}}{\mu_{\chi e}^2} \int \frac{d^3q}{(4\pi)} \int \frac{v^2 dv d\phi_v}{qv} f(v,t)\Theta(v - v_{\min}(q,\Delta E_{1\to 2})) \times |F_{\rm DM}(q)|^2 |f_{1\to 2}(\vec{q})|^2 \\ &= \frac{\rho_\chi}{m_\chi} \frac{\overline{\sigma_e}}{8\pi\mu_{\chi e}^2} \int \frac{d^3q}{q} \eta(v_{\min}(q,\Delta E_{1\to 2}),t) |F_{\rm DM}(q)|^2 |f_{1\to 2}(\vec{q})|^2, \end{aligned} \tag{7.19}$$

where, just as in section 3.1.2, the mean inverse speed function $\eta(v_{\min},t)$ is defined as:

$$\eta(v_{\min},t) = \int \frac{d^3v}{v} f(v,t)\Theta(v - v_{\min}), \tag{7.20}$$

being $v_{\min}$ defined by Equation 7.9. Due to the explicit velocity dependence of the momentum transfer expressed by Equations 7.6 and 7.19, the rate computed will be sensitive to any assumption made on the dark matter velocity distribution. As discussed in studies with the intention of mapping the neutrino floor based on dark matter-electron scattering measured in direct detection experiments [274], the uncertainty in the velocity distribution $f(v,t)$ can have a significant impact on the discovery potential. Furthermore, due to the Sun's motion through the dark matter halo, and the motion of the Earth relative to the Sun, the rate of dark matter particles measured in a direct detection experiment is expected to vary over the year, as discussed in section 6.5.3. Thus, the significance of a signal over a flat background can be also explored under this framework.

7.1.4 Form factor

The only missing component in the rate defined by Equation 7.19 is the information about the target material, which is directly related to the modeling of all the available knowledge about the electron wave-functions in the dense, disordered medium considered (this information is often encode in the ionization form factor). The procedure to specify this information starts by assuming the ionization of atoms with filled shells, bound in isolated spherical atomic potentials. The rate for such an atom is then obtained by summing over all occupied electron shells and integrating over the phase space of all possible ionized states.

Although the resulting ionized electrons after the scattering can be treated as being in one of a continuum of positive energy bound states, which are directly affected by the action of a potential well from the atom, at asymptotically large radii they can be considered to be free particle states having a final state energy $E_{\rm er} = k'^2/2m$. Thus, as described in [272], this leads to include the phase space contribution from the free spherical-wave states:

$$\begin{matrix}\text{ionized electron}\\ \text{phase space}\end{matrix} = \sum_{n'\ell'} \frac{k'^2 dk'}{(2\pi)^3} = \frac{1}{2}\sum_{n'\ell'} \int \frac{k'^3 d\ln E_{\rm R}}{(2\pi)^3}. \tag{7.21}$$

When taking this information into account, the ionization rate becomes:

$$\begin{aligned} R_{\rm ion} = &\frac{\rho_\chi}{m_\chi} \frac{\overline{\sigma_{\rm e}}}{16\pi\mu_{\chi{\rm e}}^2} \times \\ &\sum_{\substack{\text{occupied}\\ \text{states}}} \sum_{\ell' m'} \int \frac{d^3q}{q} \frac{k'^3 d\ln E_{\rm R}}{(2\pi)^3} \eta(v_{\rm min}(q, E_{\rm B}^i + k'^2/2m_{\rm e}), t) |F_{\rm DM}(q)|^2 |f_{i\to k'\ell' m'}(\vec{q})|^2, \end{aligned} \tag{7.22}$$

where $E_{\rm B}^i$ is the corresponding binding energy of the considered occupied state i and the wave-function normalization $\langle \widetilde{\psi}_{k'\ell' m'} | \widetilde{\psi}_{k'\ell' m'} \rangle = (2\pi)^3 \delta_{\ell'\ell} \delta_{m' m} \frac{1}{k^2} \delta(k-k')$ has been adapted.

Under the assumptions, the dimensionless ionization form factor $|f_{i\to k'\ell' m'}(\vec{q})|^2$ represents the likelihood that a given momentum transfer results in a particular electron recoil energy. Technically it is computed by considering the sum over all the final angular variables and degenerated, occupied initial states:

$$\left| f_{\rm ion}^{\rm i}(k', \vec{q}) \right|^2 = \sum_{\substack{\text{occupied}\\ \text{states}}} \sum_{\ell' m'} \left| \int d^3x \; \widetilde{\psi}^*_{k'\ell' m'}(\vec{x}) \psi_{\rm i}(\vec{x}) e^{i\vec{q}\cdot\vec{x}} \right|^2. \tag{7.23}$$

In practice, the exact computation of the unbound wave-functions involved is rather difficult. One approach is to approximate the outgoing electron as a free plane wave such that for spherically symmetric full shells with quantum numbers (n, ℓ), Equation 7.23 reduces to:

$$\left| f_{\rm ion}^{n\ell}(k', \vec{q}) \right|^2 = \frac{(2\ell+1)k'^2}{4\pi^3 q} \int k dk \left| \chi_{n\ell}(k) \right|^2. \tag{7.24}$$

On one hand the momentum space radial wave-function $\chi_{n\ell}(k)$, normalized to $\int k^2 dk |\chi_{n\ell}(k)|^2 = (2\pi)^3$, is obtained by splitting the coordinate space wave-function $\psi_{n\ell m}(\vec{k})$ into its angular part $Y(\theta_k, \phi_k)$ and its radial part $R_{n\ell}(r)$:

$$\begin{aligned} \chi_{n\ell}(k) &= \frac{4\pi}{2\ell+1} \sum_m \psi_{n\ell m}(\vec{k}) Y(\theta_k, \phi_k) \\ &= 2\pi \int dr \; r^2 R_{n\ell}(r) \int d(\cos\theta) P_\ell(\cos\theta) e^{i\cdot p\cdot r\cos\theta} \\ &= 4\pi i^\ell \int dr \; r^2 R_{n\ell}(r) j_\ell(pr), \end{aligned} \tag{7.25}$$

where k is a momentum space vector with modulus k, and arbitrary orientation (θ_k, ϕ_k), and $P_\ell(\cos\theta)$ is a Legendre polynomial. The radial wave-functions $R_{n\ell}(r)$, on the other hand, can be obtained as a linear combination of Slater type orbitals (STOs), as presented in [275], such that:

$$R_{n\ell}(r) = \sum_k c_{n\ell k} \frac{(2Z_{\ell k})^{\mathrm{n}_{\ell k}+1/2}}{a_0^{3/2}\sqrt{2\mathrm{n}_{\ell k}!}} \left(\frac{r}{a_0}\right)^{\mathrm{n}_{\ell k}-1} e^{-Z_{\ell k} r/a_0}. \tag{7.26}$$

where a_0 is the Bohr radius and $c_{n\ell k}$, $Z_{\ell k}$ and $\mathrm{n}_{\ell k}$ are the coefficients from the numerical Roothaan-Hartree-Fock[4] bound wave-functions tabulated in [275] (shown in Table 7.1), used when treating the target electron as single-particles states bound in isolated xenon atoms. Thus by replacing Equation 7.26 into Equation 7.25, and by using the definition of the ${}_2F_1(a,b,c,x)$ hypergeometric function, $\chi_{n\ell}$ can be evaluated analytically as:

$$\begin{aligned}\chi_{n\ell}(k) = \sum_k c_{n\ell k} 2^{-\ell+\mathrm{n}_{\ell k}} \left(\frac{2\pi a_0}{Z_{\ell k}}\right)^{3/2} \left(\frac{i\cdot p\cdot a_0}{Z_{\ell k}}\right)^{\ell} \frac{(1+\mathrm{n}_{\ell k}+\ell)!}{\sqrt{(2\mathrm{n}_{\ell k})!}} \\ \times {}_2F_1\left[\frac{1}{2}(2+\ell+\mathrm{n}_{\ell k}), \frac{1}{2}(3+\ell+\mathrm{n}_{\ell k}), \frac{3}{2}+\ell, -\left(\frac{pa_0}{Z_{\ell k}}\right)^2\right].\end{aligned} \tag{7.27}$$

The second approach to calculate this form factor corresponds to make the numerical evaluation of the atomic matrix element by expanding the factor $e^{i\vec{q}\cdot\vec{x}}$ in spherical harmonics and by rewriting the angular integral over the product of three spherical harmonics in terms of the Wigner-3j symbol. As derived in [276]:

$$\begin{aligned}\int d^3x\ \widetilde{\psi}^*_{n'\ell'm'}(\vec{x})\psi_{n\ell m}(\vec{x})e^{i\vec{q}\cdot\vec{x}} &\equiv \langle n'\ell'm'|e^{i\vec{q}\cdot\vec{x}}|n\ell m\rangle \\ &= 4\pi\int dr\, r^2 R_{n\ell}(r)R_{n'\ell'}(r)\sum_{L,M} j_L(qr)Y_{LM}(\theta_q,\phi_q) \\ &\times \frac{(-1)^m}{\sqrt{4\pi}}\sqrt{(2\ell+1)(2\ell'+1)(2L+1)}\begin{pmatrix}\ell & \ell' & L\\ 0 & 0 & 0\end{pmatrix}\begin{pmatrix}\ell & \ell' & L\\ m & m' & M\end{pmatrix},\end{aligned} \tag{7.28}$$

where j_L is a spherical Bessel function of the first kind and θ_q, ϕ_q are the angular components of q. Thus, by using Equation 7.28, the form factor expressed in Equation 7.23 reduces to be:

$$\begin{aligned}\left|f^{n\ell}_{\mathrm{ion}}(k',\vec{q})\right|^2 = \frac{4k'^3}{(2\pi)^3}\sum_{\ell' L}(2\ell+1)(2\ell'+1)(2L+1)\begin{pmatrix}\ell & \ell' & L\\ 0 & 0 & 0\end{pmatrix}^2 \\ \times\left|\int dr\, r^2 R_{n\ell}(r)R_{n'\ell'}(r)j_L(qr)\right|^2,\end{aligned} \tag{7.29}$$

such that these form factors are evaluated numerically by cutting off the sum at ℓ', L once it converges.

[4] In short, the Hartree-Fock method is a variational, wave-function based many-body approach used to determine the wave-function and the energy of a quantum many-body system in a stationary state.

Table 7.1. Roothan-Hartree-Fock ground-state atomic wave-function coefficients. These are read as following: 1s, 2p, 3p,.. denote the RHF orbital. The orbital coefficients $C_{n\ell k}$ are listed next under each RHF orbital 1s, 2p,... which denotes the Slater-type orbital (STOs) $n_{j\ell}$. Lastly, the orbital exponent $Z_{j\ell}$ are shown following the STO designation. Adapted from [275].

Xenon, Z=54						
		RHF ground state atomic wave-function				
		1s	2s	3s	4s	5s
1S	54.9179	-0.965401	0.313912	-0.140382	0.064020	-0.022510
2S	47.2500	-0.040350	0.236118	-0.125401	0.059550	-0.021077
2S	26.0942	-0.001890	-0.985333	0.528161	-0.251138	0.088978
3S	68.1771	-0.003868	0.000229	-0.000435	0.000152	-0.000081
3S	16.8296	-0.000263	-0.346825	0.494492	-0.252274	0.095199
3S	12.0759	0.000547	0.345786	-1.855445	1.063559	-0.398492
4S	31.9030	-0.000791	-0.120941	0.128637	-0.071737	0.025623
4S	8.0145	0.000014	-0.005057	-0.017980	-0.563072	0.274471
4S	5.8396	-0.000013	0.001528	0.000792	-0.697466	0.291110
5S	14.7123	-0.000286	-0.151508	0.333907	-0.058009	0.011171
5S	3.8555	0.000005	-0.000281	-0.000228	-0.018353	-0.463123
5S	2.6343	-0.000003	0.000134	0.000191	0.002292	-0.545266
5S	1.8124	0.000001	-0.000040	-0.000037	-0.000834	-0.167779
		2p	3p	4p	5p	
2P	58.7712	0.051242	0.000264	0.013769	-0.005879	
2P	22.6065	0.781070	0.622357	-0.426955	0.149040	
3P	48.9702	0.114910	-0.009861	0.045088	-0.018716	
3P	13.4997	-0.000731	-0.952677	0.748434	-0.266839	
3P	9.8328	0.000458	-0.337900	0.132850	-0.031096	
4P	40.2591	0.083993	-0.026340	0.059406	-0.024100	
4P	7.1841	-0.000265	-0.000384	-0.679569	0.267374	
4P	5.1284	0.000034	-0.001665	-0.503653	0.161460	
5P	21.5330	0.009061	0.087491	-0.149635	0.059721	
5P	3.4469	-0.000014	0.000240	-0.014193	-0.428353	
5P	2.2384	0.000006	-0.000083	0.000528	-0.542284	
5P	1.4588	-0.000002	0.000026	-0.000221	-0.201667	
		3d	4d			
3D	19.9787	0.220185	-0.013758			
3D	12.2129	0.603140	-0.804573			
3D	8.6994	0.194682	0.260624			
4D	27.7398	-0.014369	0.007490			
4D	15.9410	0.049865	0.244109			
4D	6.0580	-0.000300	0.597018			
4D	4.0990	0.000418	0.395554			
4D	2.5857	-0.000133	0.039786			

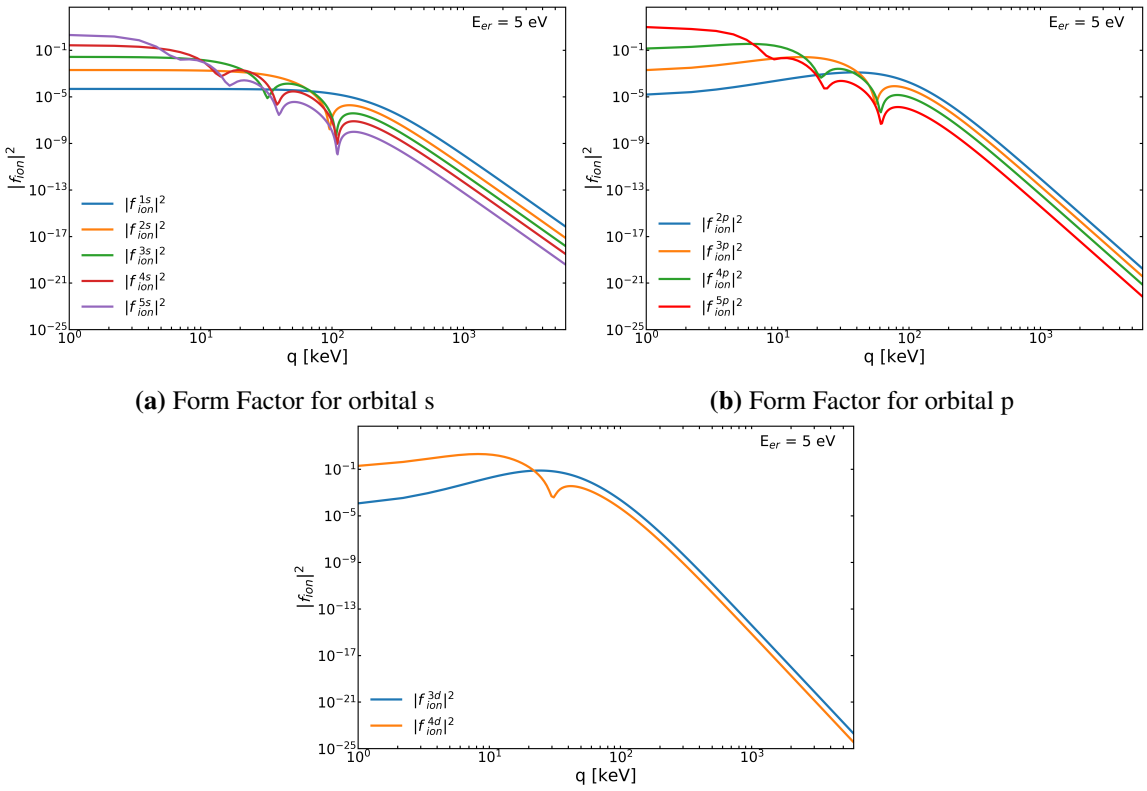

(a) Form Factor for orbital s

(b) Form Factor for orbital p

(c) Form Factor for orbital d

Figure 7.6. In the context of considering a xenon target, the form factors for the orbitals s, p and d are illustrated when taking the energy $E_{\rm er}$ = 5 eV, showing how larger values of momentum transfer q are strongly suppressed since it is unlikely for the atomic electron to be found with such a high momentum.

With a disagreement of less than $\mathcal{O}(5\%)$ between both methods, the first approach has been used in order to compute the form factor for each different xenon orbital, as presented in Figure 7.6. By assuming an energy $E_{\rm er}$ = 5 eV, it is illustrated for the different orbitals of the xenon atom how rates will be suppressed given a momentum transfer, specially for large values. Specifically, these results illustrate that when the momentum q is found to be far above the inverse the Bohr radius, $a_0^{-1} = 3.7$ keV, the scattering rate will receive a strong wave-function suppression from the fact that it is unlikely for the atomic electron to be found with such a high momentum.

7.1.5 Differential scattering rate

With all previous definitions into consideration, the differential ionization rate for $N_{\rm T}$ number of target nuclei, when summing over all possible electron states, can be expressed as:

$$\frac{dR_{\rm ion}}{d\ln E_{\rm er}} = N_{\rm T}\frac{\rho_\chi}{m_\chi}\sum_{n\ell}\frac{\langle\sigma^{n\ell}_{\rm ion}v\rangle}{d\ln E_{\rm er}}, \tag{7.30}$$

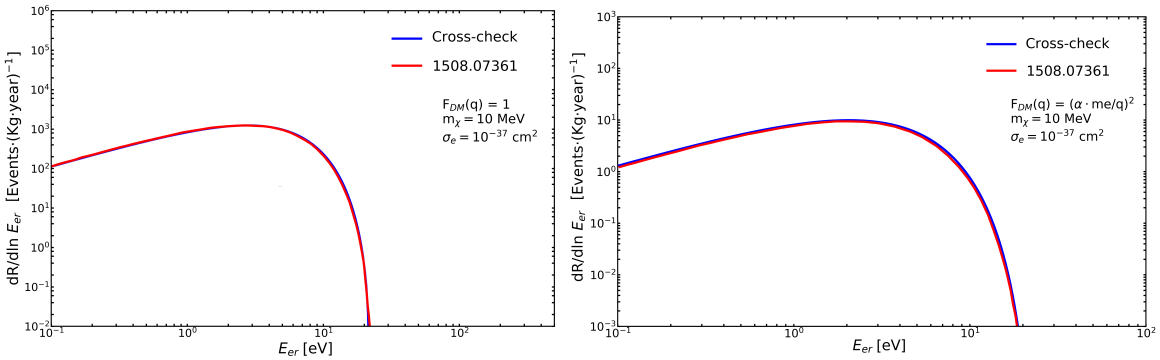

Figure 7.7. Differential event rate for dark matter scattering off electrons as function of the electron recoil energy, for the assumed form factors: $F_{\rm DM} = 1$ *Left* and $F_{\rm DM} = \alpha^2 m_{\rm e}^2/q^2$ **Right**. The rate illustrated with a red (blue) line corresponds to the literature (this framework), when considering as example the dark matter mass $m_\chi = 10$ MeV and a cross-section $\overline{\sigma_{\rm e}} = 10^{-37} cm^2$.

where the thermally averaged differential cross-section has been defined as:

$$\frac{\langle \sigma^{n\ell}_{\rm ion} v \rangle}{d \ln E_{\rm er}} = \frac{\overline{\sigma_{\rm e}}}{8\mu^2_{\chi {\rm e}}} \int q \, |f^{n\ell}_{\rm ion}(k',q)|^2 |F_{\rm DM}(q)|^2 \eta(v_{\rm min},t) \, dq. \tag{7.31}$$

Due to the presence of the charged nucleus, the resulting electron wave-functions treated get deformed, causing the deviation from simple wave-functions of a scattered electron and resulting in the enhancement of the cross-section. This effect can be approximated by combining a plane wave final state with a moment-dependent enhancement factor[5], such that Equation 7.30 is modified by introducing the factor:

$$F(k') = \frac{2\pi\xi}{1 - e^{2\pi\xi}} \quad \text{with} \quad \xi = Z_{\rm eff} \frac{\alpha m_{\rm e}}{k'}, \tag{7.32}$$

where α is the fine-structure constant and $Z_{\rm eff}$ is the effective charge felt by the escaping electron, taken as 1 for the following calculations. In summary, all aspects for considering dark matter scattering electrons have been modeled into a framework that provides a handle to calculate their differential rate, through Equation 7.30.

Before exploring the reach of this framework in the context of XENON1T, the *rate* predictions need to be validated with literature results in order to approve the framework developed. Figure 7.7 shows the differential scattering rate for form factors $F_{\rm DM} = 1$ (*left*) and $F_{\rm DM} = \alpha^2 m_{\rm e}^2/q^2$ (*right*) for $m_\chi = 10$ MeV when assuming a xenon target and a cross-section $\overline{\sigma_{\rm e}} = 10^{-37} cm^2$. At the same time, Figure 7.8 illustrates the result from estimating the 95% confidence level exclusion reach obtained after assuming 1 kg·year of exposure for a xenon target. Thus by integrating the differential rate with respect to the electron recoil energy, the number of event obtained are scaled with the cross-section, such that 3.6 events expected after 1 kg·year are found after considering the background to be composed only by contribution of the irreducible neutrino background [235] (negligible with this

[5]Formally this factor can be understand as the Fermi-factor considered in the standard treatment of β-decay, or in the context of the Sommerfeld enhancement, but related to an outgoing state instead of an incoming one [264].

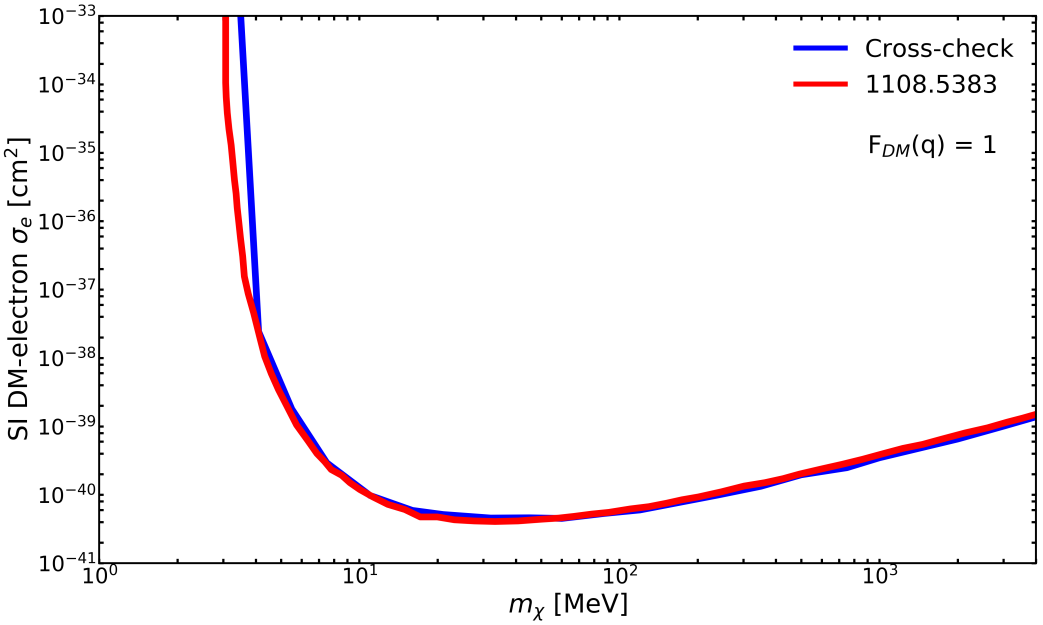

Figure 7.8. Projection of dark matter-electron scattering cross-section $\overline{\sigma_e}$ as a function of the dark matter mass m_χ, for form factors $F_{\rm DM} = 1$. The exclusion limit presented with a red (blue) line corresponds to cross-section limit calculated in literature (this framework) for a xenon target, at 95% C.L. for 1 kg·year of exposure, assuming only the irreducible neutrino background, which is equivalent to expect 3.6 events after 1 kg·year.

exposure). The exclusion limit calculation indicates that on one hand, for small dark matter masses, the reach falls as the energy available approaches the ionization threshold. In the other hand, for larger dark matter masses, at one point the cross-section saturates such that the overall reach falls linearly with decreasing number density. Furthermore, the resulted limit seems to slightly deviate from the calculated in [264], only when reaching small masses. However, in terms of consistency, the minimum mass that should be accessible within this framework has to follow the energy constrain:

$$m_{\chi,\rm min} = \frac{2E_{\rm B}^{n\ell}}{v_{\rm max}^2}, \tag{7.33}$$

where $E_{\rm B}^{n\ell}$ is the binding energy and $v_{\rm max} = v_{\rm esc} + v_{\rm max,\,Earth}$ corresponds to the maximum observed velocity of dark matter, consisting on the is the velocity of escape of the Earth $v_{\rm esc}$ in addition to the maximum velocity from Earth around the Sun $v_{\rm max,\,Earth}$. In terms of the result, the most likely candidates to be ionized and thus defining the lowest reach of the exclusion limit are for xenon the outer-shell electron states: *5p* ($E_{\rm B}^{5p}$ = 12.4 eV), *5s* ($E_{\rm B}^{5s}$ = 25.7 eV) and *4d* ($E_{\rm B}^{4d}$ = 75.6 eV). Hence, the minimum dark matter mass to be probed corresponds to the state *5s*, leading to $m_{\chi,\rm min}$ = 3.62 MeV, consistent with the limit obtained.

In summary, the agreement found succeeds the requirements to proceed without modifying the computational approach. The calculations have considered target detector features through the information contain in the form factors of the atomic electrons and the particle physic conditions

contain in the interaction parametrization. At the same time, dark matter aspects are introduced by means of astrophysical input and its realization through a dark matter form factor. The framework developed containing all previous information has been used to compute differential ionization rates and to estimate exclusion limits. Results suggest that the minimum velocity that dark matter must have depends on the bound state energy of the electron, which in turn depends on the detector target. As consequence, the scattering rate is not only sensible to the detail of electrons binding in the target, or to the dark matter velocity distribution, but also to the energy deposition and threshold of detection. In summary, the interplay of the different elements discussed opens the possibility to explore and test new hypothesis about the nature of dark matter.

7.2 Dark matter-electron scattering in the context of XENON1T

Up to date, xenon TPC based detectors are the most sensitive target materials for dark matter masses $m_\chi \gtrsim 6$ GeV/c^2, given that lighter masses interacting with the xenon nuclei fail to transfer enough energy that can produce detectable S1s. However, the XENON10 experiment [246] has already demonstrated the feasibility to detect ionization of single electrons, probing that there exist approaches that while using the same technology, allow to explore the reach for dark matter particle with masses going as low as a few MeV [277]. This section will explore the sensitivity of XENON1T under the assumption that dark matter scatters off electrons. On one hand, the exposure and the background model from the latest SI dark matter search of XENON1T [62, 212] can be used to estimate the sensitivity to lighter dark matter without having optimized the data selection for ionization signals only. On the other hand, the data can be reanalyzed without requiring the condition of an S1 this time, as previous analyses in the XENON Dark matter project [246, 278, 271]. As result of the latter S2-only data selection, the detection thresholds of both NR and ER signals fall below the keV level, opening the perspective to explore a previously restricted parameter space. Under this approach it is studied the sensitivity reach of XENON1T [279]. Furthermore, it will be briefly described what other possible estimations can be made in the context of characterizing single rate electrons and when exploring an annual modulation signal.

7.2.1 Standard Search

For a first sensitivity study under the assumption that dark matter scatters off electrons, the same 278.8 days of data collected for the SI WIMP-search analysis are used, equivalent to 1.0 t$\times$yr exposure. In order to do this two different aspects need to be detailed. On one hand, a description of the selection of the targeted events and their background modeling has to be specified. That is, to distinguish that ER events are targeted in this approach and therefore a background model containing all the information of their detection efficiency, detection threshold and modeling needs to be taken into consideration. On the other hand, all previous information has to be expressed in terms of deposited energy rather than in units from S1 and S2 signals. Furthermore, since the measurements in this approach are likely

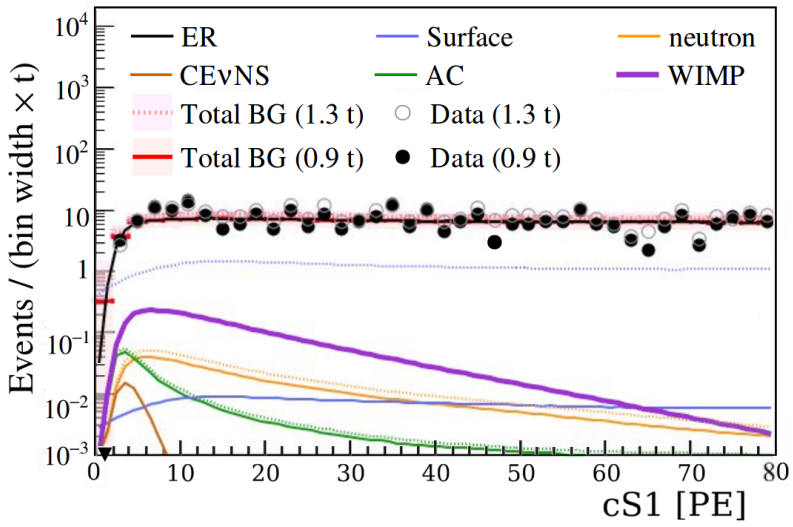

Figure 7.9. Background and signal prediction projected onto the cS1, for the best-fit signal prediction of 200 GeV/c^2 WIMP, assuming $\sigma_{SI} = 4.7 \times 10^{-47} cm^2$. Data from the dark matter search in a 0.9 t (solid lines and markers) and 1.3 t (dotted lines and hollow markers) FV is included. As for the shaded bands, they indicate the 68% Poisson probability region for the total background expectation, while colors illustrate the different components of the total background found.

to be less than the estimated background, the sensitivity can be defined as the average upper limit that would be obtained by an ensemble of experiments having a certain expected background and no true signal. Thus by making use of G. Feldman and R. Cousins formalism to classical statistical analysis of small signals, the sensitivity can be derived given a defined confidence level [235].

In terms of the data selection, two main classes of cuts were applied. The first consist on basic quality cuts used to reject anomalies, noise, selection artifacts or unidentified energy deposition peaks; specifically by demanding a valid S1 and S2 pair, where the S1s are required to contain coincident signals from at least 3 PMTs within 100 ns. The second are consistency cuts. Used as well in the WIMP search, they include technical technical knowledge about the performance and response of the detector, as explained in section 3.3.3. Figure 7.9 shows the spectrum of remaining events after all the selection cuts have been implemented as function of cS1, between 3 and 80 PE. Data of the dark matter search in a 0.9 t (solid lines and markers) and 1.3 t (dotted lines and hollow markers) FV is included, together with the different components of the total background (illustrated in colors). Furthermore, the ER background prediction (solid black line) is also specified, together with the signal prediction of 200 GeV/c^2 WIMP, assuming $\sigma_{SI} = 4.7 \times 10^{-47} cm^2$.

The energy deposited in each interaction has been projected onto the observed S1 signal. In order to translate this detected signal to deposited energy, a PE-keV conversion has to be specified. As it was done in XENON100 [280], one conservative way to do this would correspond to use the Noble element Simulation Technique **NEST** model [139], which takes into consideration community measurements that account for the expected quenching and scintillation efficiency of the measured signals at low energy (done by characterizing, for instance, the 32.1 keV transition line of ^{83m}Kr).

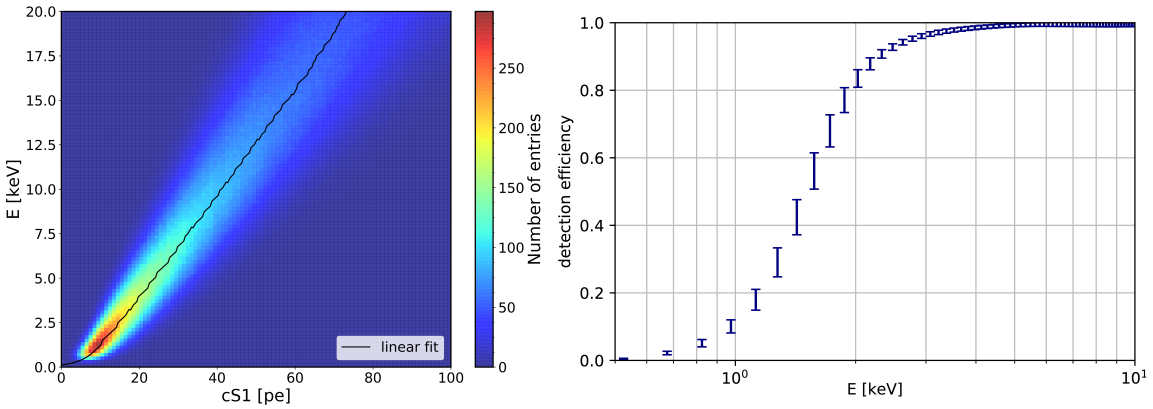

Figure 7.10. Left Conversion function between energy recoil in keV and cS1 in PE, derived by using bbf **Right** Efficiency in energy space, considering S1 efficiency and all systematic uncertainties.

However, XENON1T has been developed a Bayesian Band Fitting **bbf** framework [212] that can be used to characterize the detector response in a more robust way. That is, the bbf is a Bayesian parameter estimation based framework [281] that combines a simulation-based modeling of the signal response, together with all known detector features in XENON1T, the microphysics in liquid xenon and all their known relevant uncertainties[6].

Thus the conversion from a cS1 to the energy space was modeled using the bbf, as presented in Figure 7.10 (*left*). The result showed follow from 1 million events simulated under the response of ERs. Here the solid black line traced corresponds to the linear function fit made to the mean values of the deposited and observed energy. This relation is implemented for the rest of the chapter for the conversion of energies. In addition, Figure 7.10 (*right*) illustrates the efficiency in energy space which can be consider for the background/signal models after taking into account the detector resolution, thus including all systematic uncertainties from the S1 and S2 efficiencies [282]. Next, by making use of the conversion relation derived, the ER background model presented in Figure 7.9 can be now expressed in terms of the deposited energy E in keV units. The result is illustrated in Figure 7.11 (*left*). The translation of the ER background model for the 1.3 t FV is showed (solid green line and markers) together with a linear fit of these values inside the region of interest (solid red line), and an illustration of the total background events obtained after progressively integrating from the start of the region of interest until its end (blue solid line).

The derivation of the sensitivity reach for dark matter-electron scattering in the context of XENON1T follows from putting together the framework used to calculate rates with the ER background model. The procedure starts by fixing the dark matter form factor $F_{\rm DM}(q) = 1$, the realization of the model. Then by specifying the region of interest and the confidence level at which the hypothesis of no true signal given a certain expected background is tested. Figure 7.10 (*right*) illustrates that in terms of detection efficiency, deposited energies below ~ 0.4 keV for the given trigger conditions are not relevant. Thus, that would be the maximum extension of the region of interest. Two different

[6] In fact, the bbf was used to build the background and signal model for SR1 analysis.

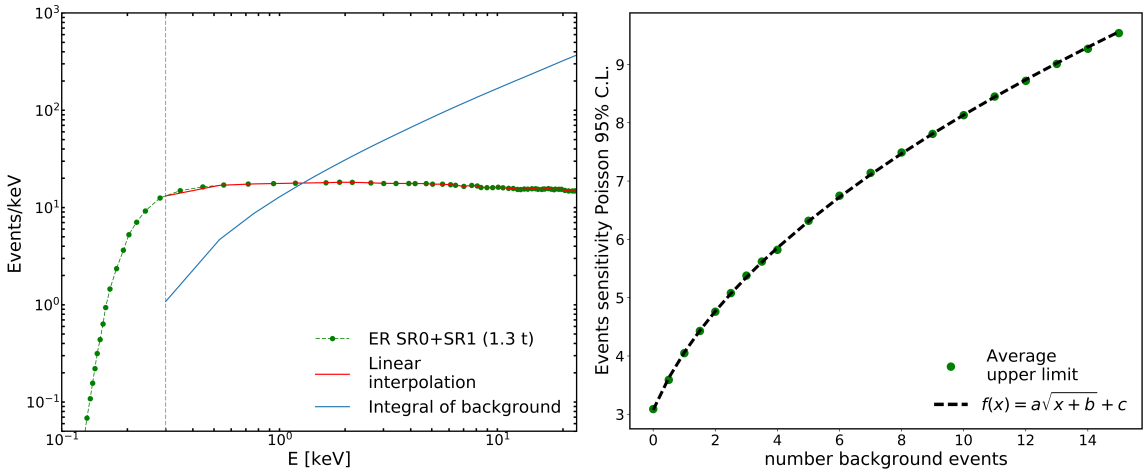

Figure 7.11. Left Background model for SR0 + SR1 within XENON1T for a 1.3 t FV in terms of energy detected, after having used the result from the bbf **Right** Fit to the events expected given the background seen in the context of measurement of a Poisson variable.

thresholds are studied. The same used in SR0 + SR1, corresponding to 2 keV, and a more restrictive due to the detection efficiency of 1 keV. These two thresholds are tested for the expected 95% exclusion reach given the 1 ton$\times$ yr exposure in the context of measurement of a Poisson variable, thus following the expected signals from Table XXII in [235]. In order to generalize these values into a continuous, such that the complete dark matter mass and cross-section space can be scanned, the values in this table were fitted to derive a parametrization of the condition of events expected given the background seen. Figure 7.11 (*right*) illustrates the fit. The function was motivated by following the prescription of Poisson-based detection limit and signal confidence intervals for few total counts.

With the previous tools at hand, the last step corresponds to explore the sensitivity of the accessible rate obtained when considering dark matter scattering off electrons in the context of XENON1T, its background model and a 95% C.L. upper limit condition. This procedure follows the next steps:

1. For a given mass m_χ and a default cross-section, calculate the number of events observed (rate times exposure) inside the region of interest defined
2. Count the background in that region of interest covered by the signal calculated given that fixed mass
3. Use the fit function to the Poisson sensitivity in order to obtain the number of events needed to establish a 95% exclusion limit given the background that was counted
4. Scale the rate by changing the cross-section σ_e such that the number of events expected is satisfied
5. Repeat the same procedure for dark matter masses m_χ in the range of 1 - 1000 MeV.

Figure 7.12 presents the 95% confidence upper limits calculated by employing the standard Poisson method [235] described for the threshold detection condition of 1 and 2 keV (green and

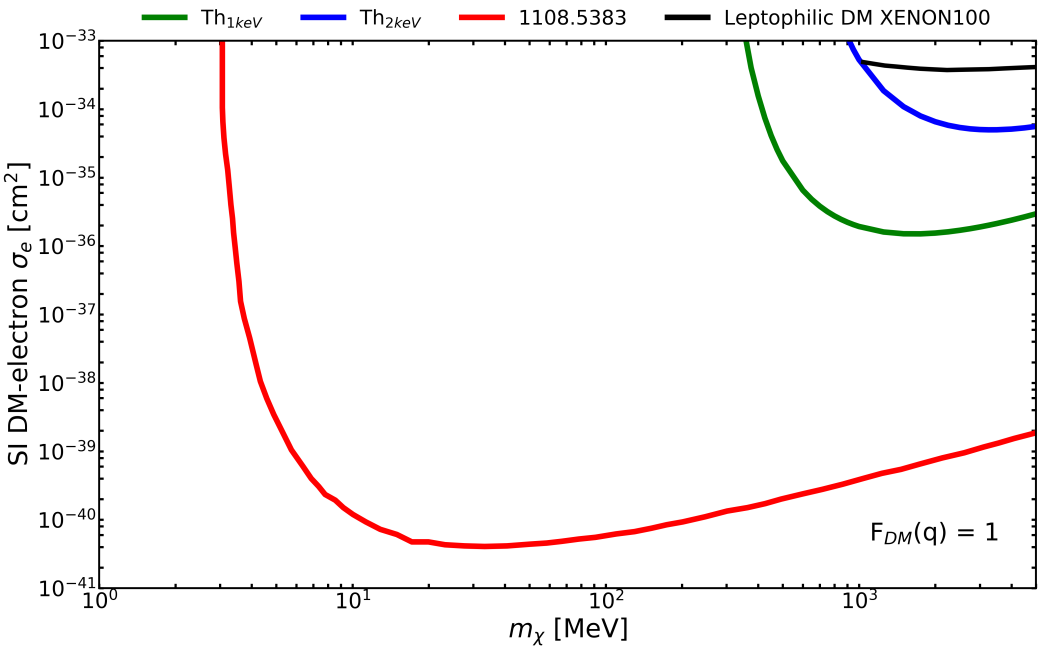

Figure 7.12. 95% confidence upper limits for dark matter scattering scattering off electrons for a detection threshold of 1 and 2 keV (green and blue lines respectively). In addition it is presented at 95% C.L. the limit for 1 kg·year of exposure when there is no background or detection threshold limitation [264] (red), together with the 90% C.L. for tested leptophilic dark matter models from XENON100 [278] (black).

blue lines respectively). Together with these results it is presented the corresponding limit calculated in literature at 95% C.L., for a xenon target having 1 kg·year of exposure when no background or detection threshold limitation is taken into consideration [264] (red). Lastly, the XENON100 Experiment exclusion limit at 90% C.L. for tested leptophilic dark matter models [278] (black). In the most conservative case, when taking the threshold of 2 keV, the result derived confirms that due to the larger exposure and improved background control from XENON1T in comparison to XENON100, stronger exclusion limits for dark matter scattering of electrons are obtained. Even in terms of XENON1T vs XENON100 when using a non-specialized approach to test this hypothesis (i.e. using the same data selection and background model from the SI dark matter search). Furthermore, lowering the threshold to 1 keV illustrates how much reach under this same analysis the approach proposed is able to have.Due to the technical constraints related to have a detection threshold and unavoidable background contributions (despite that XENON1T has the lowest background level in the world for a dark matter experiment), the limits illustrated in red are fully out of reach within this approach. However, in the next section the specific approach of using an S2-only analysis will present the improvements of doing a specialized data selection to test this same hypothesis.

7.2.2 S2-only analysis

An S2-only analysis extends the dark matter exclusion to lower-mass WIMPs given that it removes the requirement of having S1s in events. Thus the detection efficiency at low-energy previously discussed, see Figure 7.10 (*right*), is increased particularly for ER analyses, at the cost of poorer ER/NR discrimination and fiducialization. One of the biggest challenges by removing the requirement of S1s is that despite finding a way to define stronger data quality cuts, the background modeling is limited. As consequence, this restricts any discovery potential. However, world-leading exclusion limits can be establish in complete new parameter space regions, which in turn has strong consequences for multi-GeV leptophilic dark matter phenomenological models []. Specific details of this analysis are fully described in the thesis of Jelle Aalbers [109], who is leading the efforts of an upcoming paper about the S2-only analysis done in XENON1T [279]. Thus only a brief discussion and the preliminary results in the context of considering dark matter scattering of electrons as the signal model are presented in this section.

To begin with, in terms of data selection, the same data from the SR0 + SR1 XENON1T analysis was used, leading to a total livetime of 257 days. One independent part of this data, 30% of the SR1 events, were unblined and used as a *training set* for determining good cuts, while the left 70% was blinded to set the final limit. The overall criteria selection of events this time falls into four different categories:

- **Pre-selection:** Introduced in order to remove incomplete events, tails from PMT flashes, fake S2s from photo-ions, afterpulses and cosmogenic neutrons.

- **Data quality cuts:** Implemented to remove the different observed populations of gas events, single electron pileup, double scatters, merged signals from S1-S2 peaks and cathode, top surface events. These events are discriminated by using information from the hitpattern, the correlation of S2s with large previous S2s, information about the area fraction top, drift time and all knowledge about S1s merging that can potentially create an S2

- **Fiducial volume choice:** The width of the S2 waveform increases with depth due to diffusion of the electron cloud during drift. However, at the same time, giving a depth the S2 width can also increase with S2 size due to a statistical bias. By exploring events from ^{220}Rn and D-D neutron generator calibration sources, both for ERs and NRs, it was observed that wide S2s are consistent with β-decays from contaminants on the cathode wire. At the same time, narrow S2s can similarly originated from contaminants on the anode and gate at the top of detector. Having this information, together with the uncorrected observed radius reconstructed by the NN algorithm introduced the definition of a FV containing all this information, see Figure 7.13 (*left*). The FV defined (purple) avoids the strong effects from the time-dependent field distortion found in the outer region. Additional consideration about the background distribution having a phi-asymmetry were explore in the training data showed. The events passing the S2-only selections (blue dots) have S1s, while the rest do not (red dots)

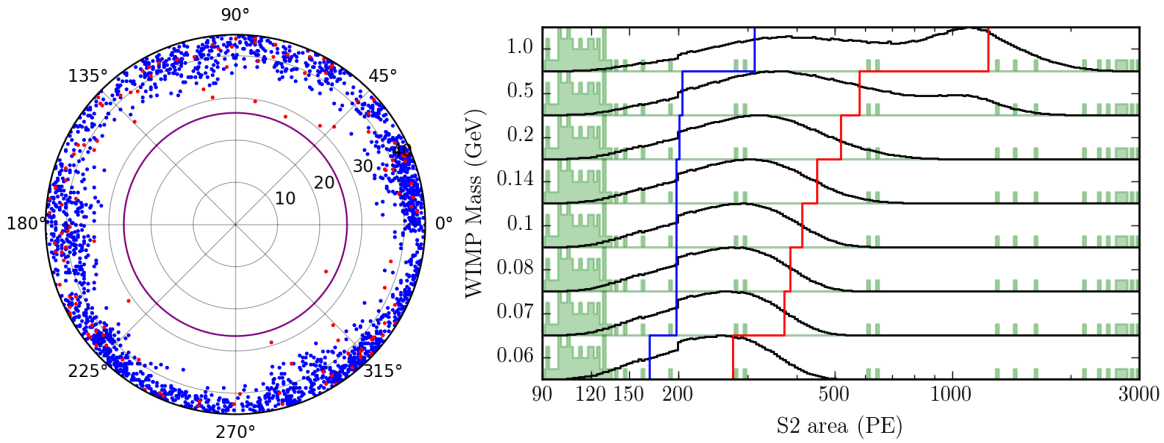

Figure 7.13. Left Background events for training data in (x,y) after all selection criteria. The events passing the S2-only selections (blue dots) have S1s, while the rest do not (red dots) **Right** Illustration of the differential evolution optimizer used in the S2 area vs WIMP mass space to define the best selection boundaries (blue and red) for a given WIMP mass. Adapted from [109].

- **S2 area cut:** This cut defines the region of interest selection and it is characterized because it is fine-tuned to each WIMP model, as showed in Figure 7.13 (*right*), by using a differential evolution optimizer [205] to scan the space of possible cut bounds, with the (biased) WIMP limit on the training sample as the figure of merit. All other cuts are universal to the analysis.

Table 7.2. Overview of backgrounds considered and quantified, affecting the S2-only region of interest.

Component	Identified	Origin known	Quantified
Regular ER events	Yes	Primarily ^{214}Pb betas	Yes
CEνNS	Not in XENON1T	Primarily solar neutrinos	Yes
Cathode events	Yes	^{210}Pb intrinsic to cathode wires	Yes
Gas events	Yes	Rn daughter betas and external radiogens	Partially
Wall events	Yes	^{210}Pb betas	Only in S1-S2
Neutrons	Not yet	Mostly external radiogens	Only in S1-S2
Single electrons pileup	Yes	Previous large S2s	No
Low-width population	Yes	Betas from ^{222}Rn for sure, probably also ^{85}Kr	No

After data selection was done with the previous cuts discussed, and their acceptances were calculated, the further effort to quantify, characterize, model and subtract all possible background

was done. Table 7.2 summarizes the overall knowledge about the various backgrounds in the S2-only analysis. The mainly components are the ER backgrounds from ^{214}Pb (Q-value 1024.11 keV), coherent nuclear scattering of ^{8}B solar neutrinos CEνNS and nearly identical NR background and backgrounds from β-decays of contaminants on the cathode wires. The spectral fit, constraints and rate bounds to each of these backgrounds is fully describe here [279].

Lastly, in terms of the statistical treatment, a one-bin counting experiment approach for every WIMP mass is taken after the unblinding of the initial 70% of data not used. In short, based on count of surviving events after all cuts have been implemented, a 90% Poisson upper limit on the number of expected events above background is set, as discussed in the previous section although this time the detection threshold is down to 0.186 keV. Figure 7.14 presents an estimate for the final result (black solid and dashed lines). These boundaries are determined by different levels of optimistic and pessimistic estimates (i.e. by computing the uncertainties of cuts efficiencies, signal parameters, statistical fluctuations and the limitations of the training data). Furthermore, the results showed correspond to different Q_y assumptions:

- The upper limit (dashed line) uses the same conservative assumption that $Q_y = 0$ below 0.186 keV, since no detector has demonstrated LXe charge yield below this value
- The lower one (solid line) considers that, as often done in the field e.g. in XENON10 [246] and Darkside [283], energy deposition can be computed by extrapolating Q_y to 0. Thus, to get a comparable limit, the bottom curve corresponds to extrapolating Q_y linearly

The limits obtained show to have improved upon previous world-leading constraints for dark matter messes $m_\chi \geq 33$ MeV/c^2, within the context of Sub-GeV dark matter scattering off electrons. In comparison to the result obtained in the previous section, it is worth mention the impact that a specific analysis can have. Having access to ionization signals from ER events down to a threshold of 0.186 keV completely allows to exploit the capabilities of XENON1T. Further improvements will be possible with SR2 data, given the lower background achieved and higher electron lifetime, but also due to the current background mitigation techniques being developed and due to the implemented methods to remove the most dominant sources of background [149, 150].

7.2.3 Annual Modulation

As discussed in section 6.5.3, a potential detection method for dark matter consist on searching for an annual modulating signal related to the Sun's motion through the dark matter halo while the Earth is moving around it. One of the advantages of this signal is that it could potentially discriminate between background and signals, since the former are not expected to modulate. The time-dependent feature in its detection enters in the calculation of the rate when specifying the Earth-frame dark matter velocity distribution $\widetilde{f}(\mathbf{v},t)$, which is determined by the velocity of the Earth with respect to the Sun and also with respect to the Galactic frame. The signal from dark matter-electron scattering consists potentially of three components observed simultaneously [284]:

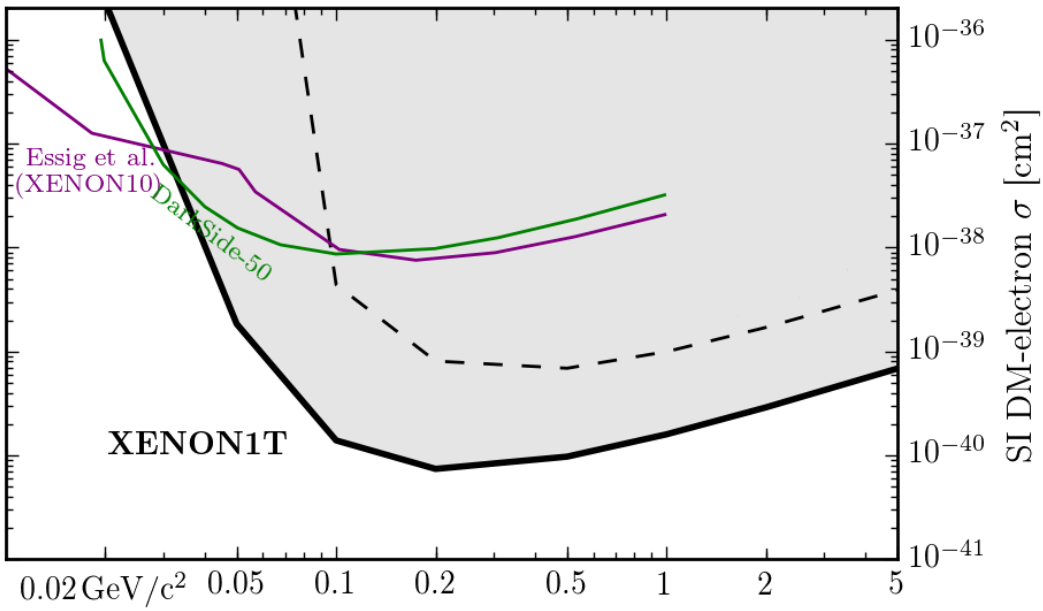

Figure 7.14. Projection limits for dark matter-electron scattering in the context of XENON1T with the S2-only analysis data. The upper limit (dashed line) corresponds to the conservative assumption that Q_y = 0 below 0.186 keV. The lower limit (solid line) corresponds to extrapolating Q_y linearly to 0. The limit obtained is the world-leading constraints for dark matter messes $m_\chi \geq 33$ MeV/c^2 within the context of Sub-GeV dark matter scattering off electrons.

1. The primary electron itself
2. The ER track created by the primary electron as it deposits its kinetic energy
3. Photons emitted as the source atom de-excites, provided an inner-shell electron is hit

The probability of an ejected electron with energy E from shell (n,l) to yield k electrons can be calculated as:

$$n_e = (1 - f_R)\text{Binom}(k-1|N+N_{\text{bonus}}, p = f_e) + f_R \cdot \text{Binom}(k, |N+N_{\text{bonus}}, p = f_e), \tag{7.34}$$

where the first term corresponds to the primary electron surviving and the second to the primary electron recombining. $f_e \approx 0.87\%$ is the fraction of produced ER quanta that survive as electrons (where the numbers are taken from the SR1 bbf nominal fit [212]), $f_R \approx 0.01$ is the recombination fraction, $N = \text{floor}(E/W)$ is the number of quanta produced by the electron in the ER track with $W = 13.8$ eV being the work function. Moreover, N_{bonus} is the additional quanta from de-excitation contribution, which depends on the shell from which the electron originates. Thus Equation 7.34 can be used as a first step to reproduce dark matter-electron rates in terms of number of produced electrons, as showed in Figure 7.15 (*left*), for $F_{\text{DM}} = 1$, m_χ= 100 MeV and $\sigma_e = 5 \times 10^{-39}$ cm^2. At the same time, the annual modulation amplitude of these rates can be estimated given the changes of the Earth's velocity, as illustrated in Figure 7.15 (*right*). Here the modulation amplitude $f_{\text{mod}} =$

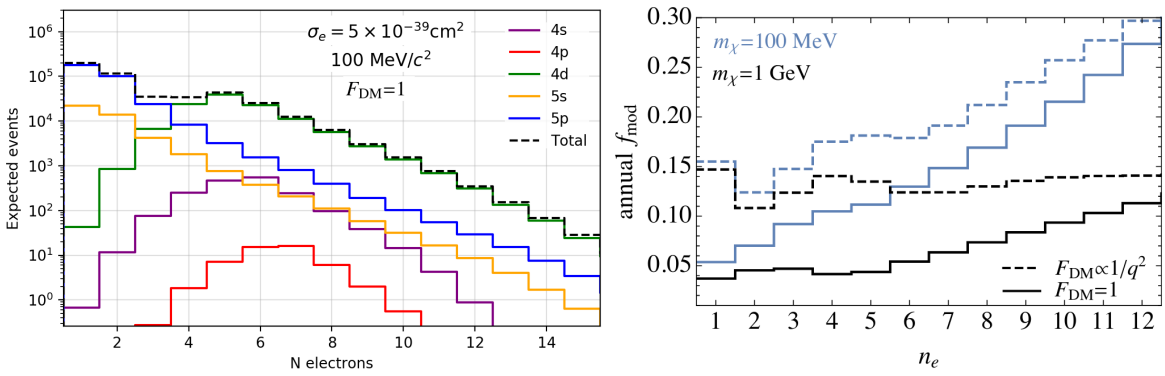

Figure 7.15. Left Dark matter-electron event rates in terms of number of produced electrons according to [284] **Right** Annual modulation amplitude for $F_{\rm DM} = 1$ (solid) and $F_{\rm DM} = \alpha^2 m_{\rm e}^2/q^2$ (dashed) for m_χ= 100 MeV (blue) and 1 GeV (black), adapted from [284].

$(R_{\rm max} + R_{\rm min})/2R_{\rm avg}$ provides a distinctive spectrum that can be used to discriminate backgrounds B from signals S.

In summary, a prescription in the field for studying the reach of this modulation signature require for this signal to have less significance than $\zeta = (f_{\rm mod} S)/\sqrt{S+B}$, such that the expected sensitivity is given by:

$$\overline{\sigma_{\rm e}}^{\rm mod} = \frac{\zeta \times \overline{\sigma_{\rm e,Xe}}}{f_{\rm mod}\sqrt{R_{\rm Xe} \times \varepsilon}}, \tag{7.35}$$

where $R_{\rm Xe}$ is the rate spectrum observed in a detector (such as the one from the S2-only analysis in XENON1T), $\overline{\sigma_{\rm e,Xe}}$ is the cross-section constraint from the observed events given the signal rate and ε is the exposure. At the moment of writing this thesis, as presented in Figure 7.16, only sensitivity studies for XENON10 and XENON100 have been made and therefore, future results will be derived next in the context of the presented results from XENON1T.

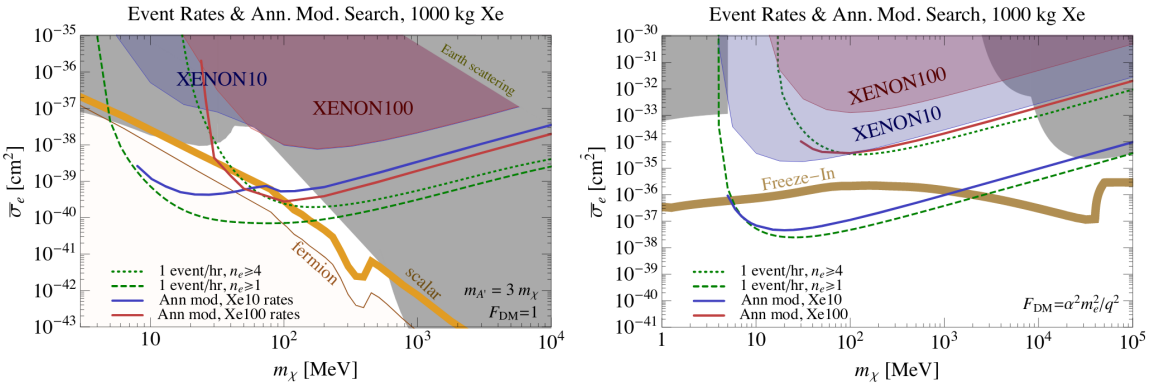

Figure 7.16. Reach for an annual modulation analysis when assuming 1 ton×year exposure, taking the spectrum rate measured by XENON10 (solid blue) and XENON100(solid red). The dark matter-electron scattering rate has been computed as well after assuming 1 electron (4 electrons) as threshold, respectively (dashed and dotted lines). The color regions contain constraints from MiniBooNE [285] and BaBar [286]. Limits calculated for the dark matter form factors: $F_{\rm DM} = 1$ **Left** and $F_{\rm DM} = \alpha^2 m_{\rm e}^2/q^2$ **Right**.Taken from [284].

7.3 Neutrino-like MeV dark matter and electron recoil

Although different candidates explaining the nature of dark matter have prevailed through the years, among them WIMPs, axions, sterile neutrinos, etc., there has been recent interest in exploring the scenario of dark matter-neutrino coupling. In the context of specific models [287], the interaction of neutrinos with MeV dark matter has a possibility to explain the existence of small neutrino masses, in addition to solve the missing satellite and the "too big to fail" problems[7]. This section introduces a minimal extension of the Standard Model where the phenomenological constraints of the radiative generation of neutrino mass through the interaction with dark matter are explored.

7.3.1 Description of the model

One of the simplest finite one-loop radiative model for neutrino mass through dark matter is the scotogenic model introduced by Ernest Ma in 2006 [288]. It extends the Standard Model **SM** with the addition of one scalar doublet η and three singlet Majorana fermions $N_{1,2,3}$, odd under $\mathbb{Z}_2$. The model explored in this work further considers the addition of a complex scalar ρ [289]. These beyond the Standard Model particles are charged under a global $U(1)_{\rm D}$ symmetry that is softly broken to $\mathbb{Z}_2$, such that N can have a Majorana mass and ν gets a one-loop radiative mass, as illustrated in Figure 7.17. At the same time, this complex scalar allows for two scalars at the MeV scale due to the mixing of the neutral component of the doublet with the complex scalar. The components of the new field elements are defined as:

$$\eta = \begin{pmatrix} \eta^+ \\ \frac{1}{\sqrt{2}}(\eta_{\rm R} + i\eta_{\rm I}) \end{pmatrix}, \quad \Phi = \begin{pmatrix} \omega_2^+ \\ \frac{1}{\sqrt{2}}(v + \phi_{\rm R} + i\phi_{\rm I}) \end{pmatrix}, \quad \rho = \frac{1}{\sqrt{2}}(\rho_{\rm R} + i\rho_{\rm I}), \quad N_{1,2}, \tag{7.36}$$

where the subscripts R and I refer to the real and imaginary parts, v is the expectation value, ϕ is the usual Higgs of the SM and χ will be the dark matter candidate from the lightest of the Majorana $N_{1,2}$. With the notation of these elements, the Lagrangian can be expressed as:

$$\begin{aligned} \mathscr{L} = \mathscr{L}_{\rm SM} + \mathscr{L}_{\rm kin} - m_{\rm h}^2 \Phi^\dagger \Phi - m_2^2 \eta^\dagger \eta - m_3^2 \rho^* \rho - \frac{1}{2} m_4^2 \left(\rho^2 + (\rho^*)^2\right) - \frac{1}{2} M_{\rm N}^2 \overline{N^c} N \\ - Y(\eta^\dagger \Phi \rho + h.c.) - \frac{1}{2}\lambda_1 (\Phi^\dagger \Phi)^2 - \frac{1}{2}\lambda_2 (\eta^\dagger \eta)^2 - \frac{1}{2}\lambda_3 (\rho^* \rho)^2 - \lambda_4 (\eta^\dagger \eta)(\Phi^\dagger \Phi) \\ - \lambda_5 (\eta^\dagger \Phi)(\Phi^\dagger \eta) - \lambda_6 (\rho^* \rho)(\Phi^\dagger \Phi) - \lambda_7 (\rho^* \rho)(\eta^\dagger \eta) - (\lambda_8)_{\rm ij} (L_{\rm i}^\dagger \eta N_{\rm j} + h.c.). \end{aligned} \tag{7.37}$$

Here the mass of the SM-like Higgs h and charged Higgs $\eta^\pm$ are defined as:

$$m_h^2 = \lambda_1 v^2, \quad m_{\eta^\pm}^2 = m_2^2 + \frac{1}{2}\lambda_4 v^2. \tag{7.38}$$

[7] The former refers to the discrepancy between the number of satellites predicted in ΛCDM, in contrast to the observed in the Milky Way, while the latter states that the observed satellites of the Milky Way are not massive enough to be consistent with predictions from ΛCDM.

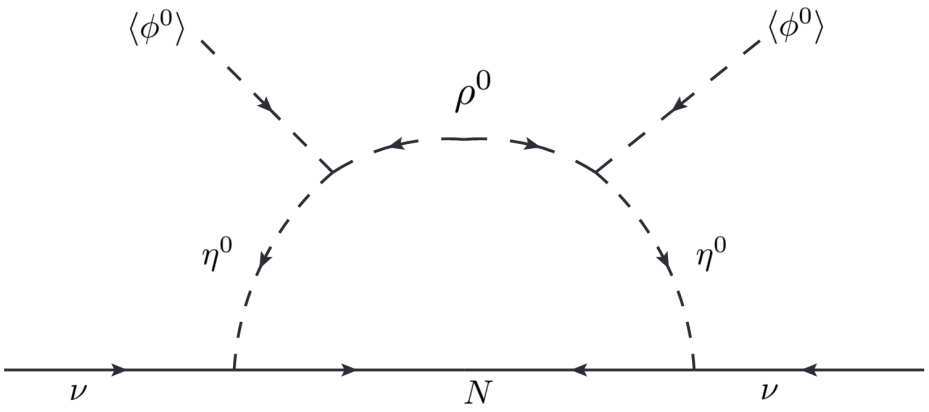

Figure 7.17. One-loop scotogenic neutrino mass generation from the $U(1)_{\mathrm{D}}$ breaking to $\mathbb{Z}_2$. Adapted from [288].

At the same time, and most importantly, the Majorana mass terms for N and the m_4^2 term are responsible of breaking the $U(1)_{\mathrm{D}}$ symmetry to $\mathbb{Z}_2$, generating finite corrections in the normalizable terms for the Lagrangian for small values of m_4^2. Furthermore, the 3×2 matrix $(\lambda_8)_{\mathrm{ij}}$ term is the one that gives masses to neutrinos, mixes generations, influences lepton flavor violation and the electronic recoil. This term is of the form:

$$\lambda_8 = \begin{pmatrix} \lambda_8^{e1} & \lambda_8^{e2} \\ \lambda_8^{\mu 1} & \lambda_8^{\mu 2} \\ \lambda_8^{\tau 1} & \lambda_8^{\tau 2} \end{pmatrix}. \tag{7.39}$$

From Equation 7.37 it can be identified that the Y term of the potential mixes the neutral components of the complex scalar ρ and the doublet η. Thus the mass matrices for the neutral scalars considering $(\eta_{\mathrm{R,I}}, \rho_{\mathrm{R,I}})$ are defined as:

$$M^2_{\mathrm{R,I}} = \begin{pmatrix} m_2^2 + (\lambda_4+\lambda_5)v^2/2 & Yv/\sqrt{2} \\ Yv/\sqrt{2} & m_3^2 + \lambda_6 v^2/2 \pm m_4^2 \end{pmatrix}, \tag{7.40}$$

where the signs + (-) accompanying the m_4^2 stand for the real (imaginary) component from the term $\frac{1}{2}m_4^2\left(\rho^2 + (\rho^*)^2\right)$. This effectively leads to a small mass splitting between the real and imaginary scalars ζ after the mixing. These scalar will be denoted as ζ_{1R}, ζ_{2R}, ζ_{1I}, and ζ_{2I}, where the numbers 2 stands for the lighter ones, while the mixing angles are denoted by θ_R and θ_I. After such parametrization and similar to treatment as the one described in [289], the expression for the neutrino mass

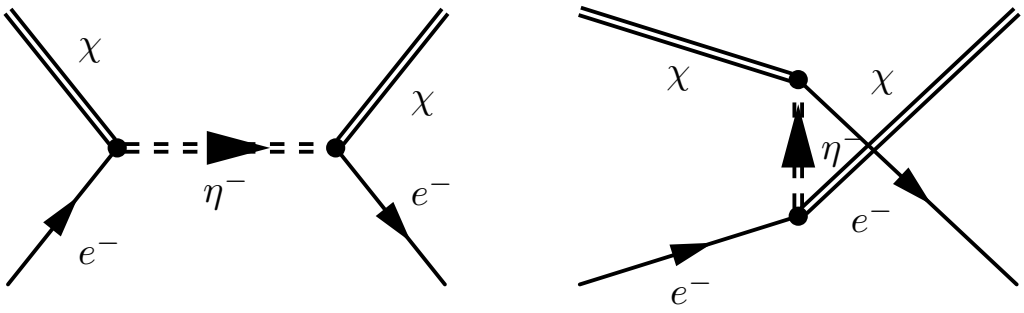

Figure 7.18. Diagram of the electron scattering through the $s-$ and u-channel.

matrix is given by:

$$(M_\nu)_{ij} = \sum_k \frac{(\lambda_8)_{ik}(\lambda_8)_{jk}}{16\pi^2} M_k \left[\frac{\cos^2\theta_R m_{1R}^2}{m_{1R}^2 - M_k^2} \ln \frac{m_{1R}^2}{M_k^2} + \frac{\sin^2\theta_R m_{2R}^2}{m_{2R}^2 - M_k^2} \ln \frac{m_{2R}^2}{M_k^2} \right. \tag{7.41}$$

$$\left. - \frac{\cos^2\theta_I m_{1I}^2}{m_{1I}^2 - M_k^2} \ln \frac{m_{1I}^2}{M_k^2} - \frac{\sin^2\theta_I m_{2I}^2}{m_{2I}^2 - M_k^2} \ln \frac{m_{2I}^2}{M_k^2} \right], \tag{7.42}$$

where M_k are the masses of N_k and the mixing angles θ follow from the potential. Analogous to the scotogenic model, the idea is that the neutrinos obtain their mass at one-loop level. Then the loop diagrams have to be calculated for the real and imaginary parts. As result, 1-loop contribution gives masses to the neutrinos. In this analysis, the Casas-Ibarra parametrization [290] is used to take as input all experimental neutrino data and the parameters in the potential. The procedure returns the dark matter coupling to neutrinos λ_8, such that the desired neutrino masses are guaranteed.

7.3.2 Realization and results

With a leptophilic candidate that is not expected to scatter-off nuclei at tree level, dark matter-electron scattering is motivated. Hence the total cross-section of this scattering can be expressed by factorizing the momentum transfer dependency in terms of the normalized cross-section $\overline{\sigma_e}$ and the dark matter form factor $F_{\rm DM}(q)$, as expressed in Equation 7.12.

Assuming that the realization takes place via an intermediate scalar η heavier than all other particles involved $m_\eta \gg \alpha m_e$, translates in a dark matter form factor to be $F_{\rm DM}(q) = 1$. As illustrated in Figure 7.18, the resulting reference cross-section for $\mathbb{Z}_2$-odd Majorana fermions scattering-off electrons will have contributions from s- and u-channel diagrams. Once evaluated the limit of this mediator mass $m_\eta \gg \alpha m_e$, the reference cross-section is given by:

$$\bar{\sigma}_e = \frac{\mu_{\chi e}^2 g^4}{\pi m_\eta^4}, \tag{7.43}$$

where $\mu_{\chi e}$ is the dark matter-electron reduced mass and $g^2 = 4\pi\alpha$ (the coupling g can be identified as λ_8^{e1} [291]). With this expression at hand, rates are calculated next in order to scan the sensitivity that

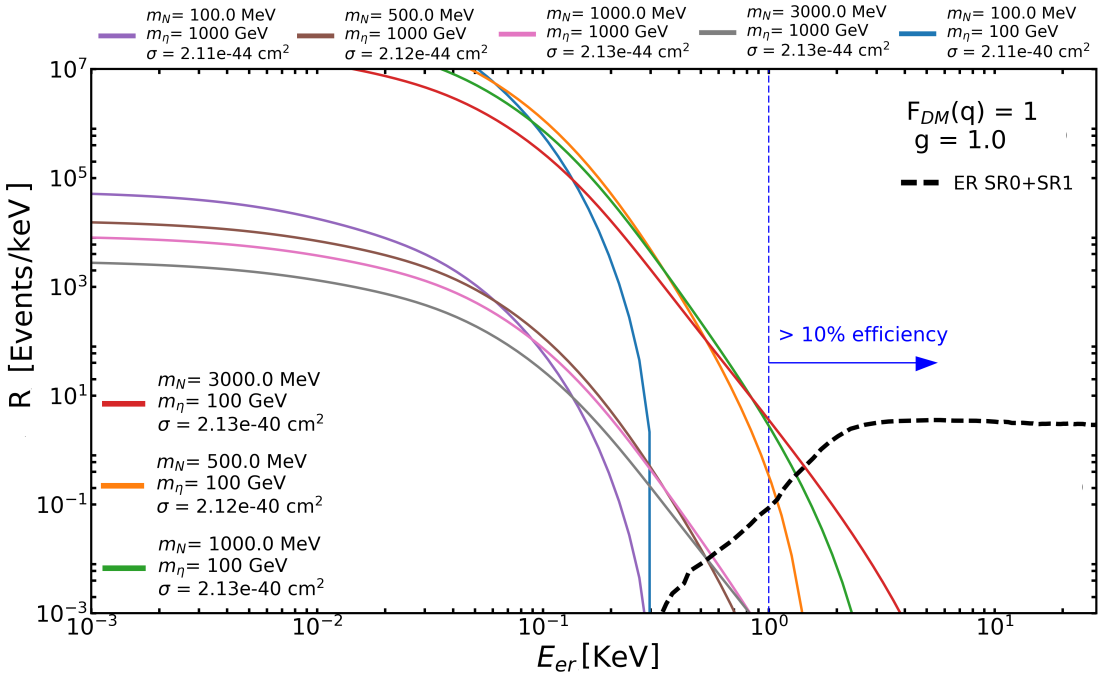

Figure 7.19. Rate calculated for the reference cross-section $\bar{\sigma}_e$ defined by Equation 7.43, for $\mathbb{Z}_2$-odd Majorana fermions scattering-off electrons when taking $g = 1.0$. Eight different mediator cases (solid colors) are illustrated here, along with the ER background model and the SI threshold of XENON1T (dashed black and blue lines).

XENON1T has to measure different mediator and dark matter candidate masses. The scan performed was done fixing $g = 1$ (less suppressed case) considering eight different mediator cases, as presented in Figure 7.19. The rates obtained (solid colors) have been placed along the ER background model and an optimistic SI threshold in XENON1T (dashed black and blue lines).

Results initially seemed to suggest that for the model considered, there could be accessible values that can barely accommodate a measurable rate above the ER background of XENON1T in SR0 + SR1, as it is for masses such as $m_N = 0.5$ GeV (orange), 1 GeV (green) and 3 GeV (red) when fixing $m_\eta = 100$ GeV. However, when further considerations related to ensuring correct neutrino masses and relic density are included, the results indicate that g has to be at most of the order of $\mathcal{O}(10^{-1})$ (if additionally lepton flavor violation is also included, g can at most be $\sim \mathcal{O}(10^{-3})$, which is even much lower). This in turn constraints the reference cross-section to be at least in the order of $\bar{\sigma}_e \sim 10^{-46}$ cm^2, thus inaccessible in XENON1T. All the specific details concerning the numerical analysis and further implications will be discuss in the PhD thesis of Sybrand Zeinstra [291].

Chapter 8

Summary and Outlook

The XENON1T experiment set up a further milestone in the history of the XENON Dark Matter Project. It was the first time that a dual-phase liquid xenon time projection chamber has employed a multi-ton target mass. This large mass combined with a long science data taking time of $\sim$ 280 days enabled XENON1T to set the world leading limit on the WIMP-nucleon spin-independent (SI) elastic scatter cross-section. Furthermore, XENON1T measured the lowest background level ever achieved in a dark matter experiment, arising from background particles interacting with the electrons of the xenon atoms (electronic recoils, ER). However, in order to accomplish these results, several challenges needed to be overcome. Among others, these were the detailed understanding of calibration data for the characterization of the innermost target volume, the precise description of several background components and the modeling and correction of detector effects that are introduced by charge accumulating at the PTFE walls of the TPC. These challenges have been addressed in this thesis. Additionally, the potential scattering of dark matter particles at the xenon atoms' electrons has been studied. Thus, the previously mentioned background rate of electronic recoils was monitored over time, since it is is the key parameter for an event rate modulation search of dark matter interacting with atomic electrons. In the same context, a framework to explore the notion of dark matter scattering-off electrons from the atomic shell was developed and used to calculate the scattering rate and sensitivity reach for different analyses performed in XENON1T.

To recap, Chapter 2 presented a collection of evidences for dark matter at several scales in the Universe, from observation in rotational velocity curves of galaxies, colliding galaxy clusters, gravitational lensing, large-scale structure formation, to the cosmic microwave background. Several well motivated candidates for dark matter were discussed. Among them, attention was placed on Weakly Interacting Massive Particles (WIMPs) as they could explain the observed relic dark matter density under the assumption of an interaction having a cross-section at the order of the weak scale. Furthermore, to test the hypothesis of the potential particle nature of dark matter, different and complementary experimental efforts for its detection were presented, as well as their status. Emphasis was placed on direct detection methods as used in XENON1T. Chapter 3 was dedicated to review in detail the required knowledge to calculate scattering rates of dark matter particles with the xenon

nucleus, the mainly studied interaction channel of XENON1T. Hereby, the scattering kinematics, nuclear physics aspects containing the form factors related to the target used, astrophysical input from the density and velocity distribution of WIMP particles in the galactic halo play a role. It turns out that the element xenon as target material is from advantage as it offers a significant enhancement in the rate for SI WIMP-nucleon cross-section because this rate scales with the atomic number squared A^2.

Next, an introduction to particle detection aspects with liquid xenon followed. The discussion reviewed how light and charge signals are created when a particle deposits energy in the detection medium. One of the most important features found is that charge and light are complementary signals highly anti-correlated. Hence, their precise measurement can be used to deduce the properties of the interacting particle such as its type, deposit energy and reconstructed position. With this arguments it was concluded that liquid xenon dual-phase TPCs are especially well suited to directly detect dark matter. Lastly, an introduction to the XENON1T experiment was presented. Details about the instrument itself, the data processor PAX, the detection of the light S1 and charge S2 signals and a review of the data quality and event selection for analysis was presented.

Chapter4 summarizes the required corrections of the light and charge signals. Thereby, the radioactive element ^{83m}Kr is favored for calibration because of the following advantages: the noble ^{83m}Kr atoms distribute homogeneously within the detector. Due to its short half-life and the decay into a stable element it does not lead to a contamination of the system and its coincident decay transitions (9keV and 32 keV) enables an unique identification. With this characterization,^{83m}Kr data is used to correct the light and charge signals for different detector inefficiencies like incomplete solid-angle PMT coverage, reduced PMT quantum efficiency, the mesh-warping of the anode, the tilt of the detector and light quenching together with charge losses, as consequence of traces of impurities in the medium. For this reason, correction maps for the light collection efficiency and its equivalent for the charge signal were calculated together with the electron lifetime correction.

During the operation of the XENON1T detector it was observed that charges were accumulated on the inner PTFE walls of the TPC, which description is the main focus of Chapter 5. From evidences collected in data and by a developed 3D COMSOL simulation framework, this phenomenon was found to have crucial consequences on the position reconstruction and signal corrections, thus affecting the integrity of the dark matter search analysis. Charges building up predominately on the TPC's sliding PTFE panels were found to introduce time-dependent changes in the applied electric field. As a consequence, these variations induced an inwards bias of the reconstructed positions along the radius of the TPC of up to $\sim 35\%$. Therefore, a 3D time-dependent field distortion correction map had to be designed as counteracting measure. Additionally, local changes of the field over time produced a variation in the S1 and S2 signal generation, which in turn introduced a bias of the initially integral signal corrections themselves. Consequently, a data-driven method to decouple field effects from charge accumulation was presented, resulting in a new time-independent light collection efficiency map that only accounts for geometrical effects, which was subsequently used for the S1 signal correction. Furthermore, a 3D COMSOL framework was used to estimate the average charge density evolution on the PTFE wall during the science run one (SR1). This was achieved

by mapping the position distribution of ^{83m}Kr events in data, that was found to be affected by a specific charge distribution, to the position obtained from simulated particles. Starting by an initial distribution estimation, a Metropolis algorithm designed for sampling from a multi-dimensional charge distributions was used to iteratively redefine the initial estimate, until an agreement in observed and simulated positions was found. Over the course of SR1 an average charge density increase on the PTFE walls of - (0.04 - 0.16) $\mu C/m^2$ was calculated, in addition to a distribution pattern that features a higher charge concentration near the anode of the TPC. These observations are consistent with what was found by the LUX collaboration, that uses a very similar TPC design as XENON1T. The charge accumulation of the PTFE walls limited the accuracy of the position reconstruction in XENON1T and thereby the size of trustworthy volume that was used for the dark matter analysis. Therefore, a reduction of the charge accumulation in the future experiment XENONnT is necessary. The results from this Chapter 5 supported a fundamental understanding of the charge accumulation over time and lead to a redesign of the XENONnT TPC with which the accumulation of charges on the PTFE walls should be significantly reduced in the future.

Studies performed in Chapter 6 provided a better understanding of intrinsic and extrinsic sources of backgrounds potentially reducing the sensitivity of the experiment in detecting WIMPs. On one hand, nuclear recoils (NR) were identified to be induced mainly from cosmogenic neutrons, solar neutrinos undergoing coherent elastic neutrino - nucleus scattering and radiogenic neutrons from materials. On the other hand, electronic recoils were related to solar neutrinos and electron/gamma radiation from sources such as ^{85}Kr, material contamination, ^{136}Xe double-beta decays and the decays of radon progenies. The latter (particularity the decay of ^{214}Pb) induces the main background in XENON1T. Thereby, internally emanating ^{222}Rn distributes homogeneously into the bulk of the liquid xenon target. However, an unexpected kind of background was additionally observed in XENON1T. It is also induced by ^{222}Rn daughters, but in this case from air-born ^{222}Rn that lead to an out-plating of long-lived ^{222}Rn daughters on the PTFE surfaces of the TPC. A partly or completely loss of the generated S2 charge signal from these wall events can cause background events in the experiment. This effect is enhanced by a limited position reconstruction resolution. Studies of this charge-loss near the boundaries of the detector (performed with ^{210}Po and ^{83m}Kr data) motivated a data-driven surface background model that, together with improvements of the position reconstruction algorithms, allowed to enlarge the active volume for the dark matter search used in SR1 by $\sim$ 30 % with respect to SR0. In virtue of selecting data in an enlarged active volume of 1.3 t during 278.8 live days, a 1 t$\times$yr exposure analysis resulted in the most stringent limit to date for WIMP masses above 6 GeV/c^2 and a WIMP-nucleon SI elastic scattering cross-section σ_{SI} at 4.1×10^{-47} cm^2 for a WIMP mass of 30 GeV/c^2.

Additionally to the search of dark matter particles interacting with the xenon nucleus, alternative models could describe dark matter interactions with matter. One of them is based on the potential interaction with the atomic electrons of xenon. A signal would manifest itself in an annual modulation of the total electronic recoil rate. In this thesis this electronic recoil rate was monitored and determined, given that it is the key parameters for the described study. Therefore, the data selection criteria and

their efficiencies were investigated over the entire period of SR1. An electronic recoil rate of (1.80 $\pm$ 0.15) $\times 10^{-4}$ Events/(kg$\times$day$\times$keV) were expected in a range of [1,12] keV and one ton fiducial volume. This is in agreement with the rate of (2.00 $\pm$ 0.11) $\times 10^{-4}$ Events/(kg$\times$day$\times$keV) in the same energy range and fiducial volume, measured in the context of this thesis. This rate represents the world leading lowest electronic recoil level in a dark matter experiment. The studies on the low energy rate will serve as input of the subsequent statistical analysis in terms of a rate modulation search with XENON1T. Chapter 7 explored as well the premise of sub-GeV dark matter scattering with atomic electrons. Therefore, a framework that considered target detector features (e.g. form factors of the atomic electrons), particle physics input (e.g. interactions parametrization) and dark matter aspects (e.g. astrophysical inputs) was developed and used to initially reproduce differential ionization rates and exclusion limits from literature. Using this framework together with the exposure and background model of the XENON1T SI dark matter search, the 95% confidence upper limit was calculated and it was found to have stronger exclusion limits that previous leptophilic dark matter results from XENON100. Similarly, with the input from a new S2-only analysis (ionization only) performed in XENON1T, sensitivity studies concluded in new 90% confidence exclusion limit estimates for dark matter-electron scattering. The constraints derived have the potential of establishing the world-leading exclusion limit for dark matter masses $m_\chi \geq 33$ MeV/c^2, within the context of direct dark matter detection experiments. The new excluded parameter space has in turn strong consequences for multi-GeV leptophilic dark matter phenomenological models. Therefore, the framework was additionally used to investigate the detectability of MeV dark matter-neutrino coupling through electron recoils.

Within the two years of operating the XENON1T experiment the most stringent SI WIMP-nucleon cross-section was determined but no dark matter was so far discovered. This is now up to the next generation of dark matter detectors like XENONnT. The detector is currently built at the time of writing and the commissioning phase should start end of 2019. It will feature a total liquid xenon mass of 8 tons, from which around 4 tons will be used as innermost ultra-pure fiducial target. In terms of background, many improvements are foreseen. The main background in XENON1T, induced by ^{222}Rn should be reduced by a factor of ten. Besides a careful material selection of new components for the detector system, this can be achieved by exchanging components that are known for a high radon emanation rate. By replacing the XENON1T recirculation pumps with a single magnetic pump (after SR1) the radon level was already reduced by $\sim$ 50%. For a further reduction a high-throughput radon distillation system has been developed. As already applied in XENON100 and XENON1T, the ^{85}Kr contamination can be similarly reduced by a 2-Phase distillation system to the required XENONnT purity of 100 ppq. Furthermore, an active neutron veto based on Gd loaded water will be installed to reduced neutron background in XENONnT. Thus, an expected maximum sensitivity of around $\sim 10^{-48}$ cm^2 for SI WIMP-nucleon cross-section will be probed in XENONnT or, optimistically, finally dark matter particles discovered.

References

[1] F. Zwicky. Die rotverschiebung von extragalaktischen nebeln. *Physica Acta 6*, pages 110–127, 1933.

[2] W. K. Ford Jr. V. C. Rubin, N. Thonnard. *ApJ*, 225:L107–L111, 1978.

[3] W. K. Ford Jr. V. C. Rubin, N. Thonnard. *ApJ*, 159:379, 1970.

[4] Carlos S. Frenk and Simon D.M. White. Dark matter and cosmic structure. *Ann. Phys*, 524:507, 2012.

[5] M. Milgrom. *ApJ 270*, pages 365–370, 1983.

[6] J. D. Bekenstein. *Phys. Rev. D 70 (8)*, page 083509, 2004.

[7] E. Verlinde. Emergent gravity and the dark universe. *arXiv: 1611.02269v2*, 2016.

[8] P. van Dokkum at all. A galaxy lacking dark matter. *Nature*, 555:629–632, 2018.

[9] H. Lee & H. Ford (Johns Hopkins U.) Credit: NASA, ESA. Giant cluster bends, breaks images. image consulted in:https://apod.nasa.gov/apod/ap090823.html. 2009.

[10] P. Salucci and A. Borriello. The intriguing distribution of dark matter in galaxies. *arXiv:astro-ph/0203457*, 2002.

[11] A. Bosma W. J. de Blok, S. S. McGaugh and V. C. Rubin. Mass density profiles of lsb galaxies. *arXiv:astro-ph/0103102*, 2001.

[12] Petrosian V. Lynds R. Bergmann, A.G. *ApJ*, 350:23–35, 1990.

[13] K. Garrett and G. Duda. Dark matter: a primer. *Advances in Astronomy*, 2011.

[14] Maxim Markevitch. Chandra observation of the most interesting cluster in the universe. *arXiv:astro-ph/0511345*, 2005.

[15] Douglas Clowe, Marusa Bradac, Anthony H. Gonzalez, Maxim Markevitch, Scott W. Randall, Christine Jones, and Dennis Zaritsky. A direct empirical proof of the existence of dark matter. *Astrophys. J.*, 648, 2006.

[16] Rhodes J. Ellis R. et al. Massey, R. Dark matter maps reveal cosmic scaffolding. *Nature*, 445:286–290, 2007.

[17] David Harvey, Richard Massey, Thomas Kitching, Andy Taylor, and Eric Tittley. The non-gravitational interactions of dark matter in colliding galaxy clusters. *Science*, 347:1462–1465, 2015.

[18] J. P. Ostriker, P. J. E. Peebles, and A. Yahil. The size and mass of galaxies, and the mass of the universe. *Astrophys. J.*, 193:L1–L4, 1974.

[19] Simon D. M. White and M. J. Rees. Core condensation in heavy halos: A Two stage theory for galaxy formation and clusters. *Mon. Not. Roy. Astron. Soc.*, 183:341–358, 1978.

[20] William H. Press and Paul Schechter. Formation of galaxies and clusters of galaxies by selfsimilar gravitational condensation. *Astrophys. J.*, 187:425–438, 1974.

[21] Alan H. Guth. The Inflationary Universe: A Possible Solution to the Horizon and Flatness Problems. *Phys. Rev.*, D23:347–356, 1981.

[22] Andrei D. Linde. A New Inflationary Universe Scenario: A Possible Solution of the Horizon, Flatness, Homogeneity, Isotropy and Primordial Monopole Problems. *Phys. Lett.*, 108B:389–393, 1982.

[23] Alan H. Guth and S. Y. Pi. Fluctuations in the New Inflationary Universe. *Phys. Rev. Lett.*, 49:1110–1113, 1982.

[24] Huchra J. Latham D. W. Tonry J. Davis, M. A survey of galaxy redshifts. II - The large scale space distribution. *Astrophysical Journal*, 253:423–445, 1982.

[25] Margaret J. Geller and John P. Huchra. Mapping the universe. *Science*, 246:897–903, 1989.

[26] Carlos S White Simon D. M. Springel, Volker. Frenk. The large-scale structure of the Universe. *Nature*, 440:1137–1144, 2006.

[27] V. et al. Springel. Simulations of the formation, evolution and clustering of galaxies and quasars. *Nature*, 435:629–636, 2005.

[28] Sutherland W. J. Maddox S. J. Efstathiou, G. The cosmological constant and cold dark matter. *Nature*, 116:705–707, 1990.

[29] Carlos S. Frenk, August E. Evrard, Simon D. M. White, and F. J. Summers. Galaxy dynamics in clusters. *Astrophys. J.*, 472:460, 1996.

[30] Katherine Freese, Mariangela Lisanti, and Christopher Savage. Colloquium: Annual modulation of dark matter. *Rev. Mod. Phys.*, 85:1561–1581, 2013.

[31] Adam G. at al. Riess. Observational evidence from supernovae for an accelerating universe and a cosmological constant. *Astron. J.*, 116:1009–1038, 1998.

[32] George F. Smoot et al. Structure in the COBE differential microwave radiometer first year maps. *Astrophys. J.*, 396:L1–L5, 1992.

[33] P. A. R. Ade et al. Planck 2015 results. XIII. Cosmological parameters. *Astron. Astrophys.*, 594:A13, 2016.

[34] Roberto Trotta. *Cosmic microwave background anisotropies*. PhD thesis, Geneva U., 2004.

[35] David N. Spergel. The dark side of cosmology: Dark matter and dark energy. *Science*, 347:1100–1102, 2015.

[36] Bruce A. Bassett and Renee Hlozek. Baryon Acoustic Oscillations. 2009.

[37] Lars Bergström. Nonbaryonic dark matter: Observational evidence and detection methods. *Rept. Prog. Phys.*, 63:793, 2000.

[38] J. R. Bond, G. Efstathiou, and J. Silk. Massive Neutrinos and the Large Scale Structure of the Universe. *Phys. Rev. Lett.*, 45:1980–1984, 1980.

[39] C. Weinheimer. Direct measurements of neutrino mass. *Nuovo Cim.*, C037(03):89–94, 2014.

[40] C. Patrignani et al. (Particle Data Group). Neutrinos in Cosmology by J. Lesgourgues and L. Verde. *Chin. Phys. C*, 26:1–15, 2017.

[41] S. Tremaine and J. E. Gunn. Dynamical Role of Light Neutral Leptons in Cosmology. *Phys. Rev. Lett.*, 42:407–410, 1979.

[42] Simon D. M. White, C. S. Frenk, and M. Davis. Clustering in a Neutrino Dominated Universe. *Astrophys. J.*, 274:L1–L5, 1983.

[43] C. Alcock et al. The MACHO project: Microlensing results from 5.7 years of LMC observations. *Astrophys. J.*, 542:281–307, 2000.

[44] Robert J. Scherrer and Michael S. Turner. On the Relic, Cosmic Abundance of Stable Weakly Interacting Massive Particles. *Phys. Rev.*, D33:1585, 1986.

[45] Jonathan L. Feng. Dark Matter Candidates from Particle Physics and Methods of Detection. *Ann. Rev. Astron. Astrophys.*, 48:495–545, 2010.

[46] J. Wess and B. Zumino. Supergauge Transformations in Four-Dimensions. *Nucl. Phys.*, B70:39–50, 1974.

[47] Gerard Jungman, Marc Kamionkowski, and Kim Griest. Supersymmetric dark matter. *Phys. Rept.*, 267:195–373, 1996.

[48] Gianfranco Bertone, Dan Hooper, and Joseph Silk. Particle dark matter: Evidence, candidates and constraints. *Phys. Rept.*, 405:279–390, 2005.

[49] K. A. Olive et al. Review of Particle Physics. *Chin. Phys.*, C38:090001, 2014.

[50] J. at al Beringer. Review of particle physics. *Phys. Rev. D*, 86:010001, 2012.

[51] R. D. Peccei and Helen R. Quinn. CP Conservation in the Presence of Instantons. *Phys. Rev. Lett.*, 38:1440–1443, 1977.

[52] Georg G. Raffelt. Astrophysical axion bounds. *Lect. Notes Phys.*, 741:51–71, 2008.

[53] Jihn E. Kim. Weak Interaction Singlet and Strong CP Invariance. *Phys. Rev. Lett.*, 43:103, 1979.

[54] Michael Dine, Willy Fischler, and Mark Srednicki. A Simple Solution to the Strong CP Problem with a Harmless Axion. *Phys. Lett.*, 104B:199–202, 1981.

[55] Q. R. Ahmad et al. Direct evidence for neutrino flavor transformation from neutral current interactions in the Sudbury Neutrino Observatory. *Phys. Rev. Lett.*, 89:011301, 2002.

[56] L. Wolfenstein. Neutrino Oscillations in Matter. *Phys. Rev.*, D17:2369–2374, 1978.

[57] Y. Fukuda et al. Evidence for oscillation of atmospheric neutrinos. *Phys. Rev. Lett.*, 81:1562–1567, 1998.

[58] Scott Dodelson and Lawrence M. Widrow. Sterile-neutrinos as dark matter. *Phys. Rev. Lett.*, 72:17–20, 1994.

[59] P. Cushman et al. Working Group Report: WIMP Dark Matter Direct Detection. *Lect. Notes Phys.*, 2013.

[60] Guillaume Plante. *The XENON100 Dark Matter Experiment: Design, Construction, Calibration and 2010 Search Results with Improved Measurement of the Scintillation Response of Liquid Xenon to Low-Energy Nuclear Recoils*. PhD thesis, Columbia U. (main), 2012.

[61] Louis E. Strigari. Neutrino Coherent Scattering Rates at Direct Dark Matter Detectors. *New J. Phys.*, 11:105011, 2009.

[62] E. Aprile et al. Dark Matter Search Results from a One Tonne$\times$Year Exposure of XENON1T. 2018.

[63] D. S. Akerib et al. The Large Underground Xenon (LUX) Experiment. *Nucl. Instrum. Meth.*, A704:111–126, 2013.

[64] Xiang Xiao et al. Low-mass dark matter search results from full exposure of the PandaX-I experiment. *Phys. Rev.*, D92(5):052004, 2015.

[65] P. Agnes et al. Results From the First Use of Low Radioactivity Argon in a Dark Matter Search. *Phys. Rev.*, D93(8):081101, 2016.

[66] P. A. Amaudruz et al. DEAP-3600 Dark Matter Search. *Nucl. Part. Phys. Proc.*, 273-275:340–346, 2016.

[67] Hiroyuki Iwasaki, Takeshi K. Komatsubara, and Yasuhiro Sugimoto. Technology and instrumentation in particle physics. Proceedings, 1st International Conference, TIPP09, Tsukuba, Japan, March 12-17, 2009. *Nucl. Instrum. Meth.*, A623:pp.1–646, 2010.

[68] E. Aprile and Xenon Collaboration. The XENONnT Dark Matter Experiment. In *APS April Meeting Abstracts*, January 2017.

[69] J. Aalbers et al. DARWIN: towards the ultimate dark matter detector. *JCAP*, 1611:017, 2016.

[70] D. S. Akerib et al. LUX-ZEPLIN (LZ) Conceptual Design Report. 2015.

[71] M. Bravin et al. The CRESST dark matter search. *Astropart. Phys.*, 12:107–114, 1999.

[72] Z. Ahmed et al. Search for Axions with the CDMS Experiment. *Phys. Rev. Lett.*, 103:141802, 2009.

[73] Ke-Jun Kang et al. Introduction to the CDEX experiment. *Front. Phys.(Beijing)*, 8:412–437, 2013.

[74] J. Barreto et al. Direct Search for Low Mass Dark Matter Particles with CCDs. *Phys. Lett.*, B711:264–269, 2012.

[75] S. Scorza. The EDELWEISS-II experiment. 2008.

[76] R. Agnese et al. Search for Low-Mass Weakly Interacting Massive Particles with SuperCDMS. *Phys. Rev. Lett.*, 112(24):241302, 2014.

[77] R. Bernabei et al. First Model Independent Results from DAMA/LIBRA-Phase2. *Universe*, 4(11):116, 2018.

[78] C. Amole et al. Dark Matter Search Results from the PICO-2L C_3F_8 Bubble Chamber. *Phys. Rev. Lett.*, 114(23):231302, 2015.

[79] Teresa Marrodan Undagoitia and Ludwig Rauch. Dark matter direct-detection experiments. *J. Phys.*, G43(1):013001, 2016.

[80] Carsten Rott. Status of Dark Matter Searches (Rapporteur Talk). *PoS*, ICRC2017:1119, 2018.

[81] Andrea Silvestri. Results from the AMANDA experiment. *Mod. Phys. Lett.*, A22:1769–1778, 2007.

[82] M. G. Aartsen et al. The IceCube Neutrino Observatory: Instrumentation and Online Systems. *JINST*, 12(03):P03012, 2017.

[83] M. Ageron et al. ANTARES: the first undersea neutrino telescope. *Nucl. Instrum. Meth.*, A656:11–38, 2011.

[84] Benjamin Zitzer. The VERITAS Dark Matter Program. *PoS*, ICRC2017:904, 2018.

[85] Nicola. Turini. The Magic Experiment. pages 61–68, 2007.

[86] Axel Donath, Francois Brun, Ryan C. G. Chaves, Christoph Deil, Vincent Marandon, and Regis Terrier. The H.E.S.S. galactic plane survey. *AIP Conf. Proc.*, 1792(1):040001, 2017.

[87] A. A. Lutovinov, R. A. Krivonos, I. A. Mereminsky, S. Yu Sazonov, S. S. Tsygankov, E. M. Churazov, and R. A. Sunyaev. Hard X-ray surveys with the INTEGRAL observatory. pages 101–110, 2017.

[88] Charles Meegan et al. The Fermi Gamma-Ray Burst Monitor. *Astrophys. J.*, 702:791–804, 2009.

[89] Emiliano Mocchiutti et al. The PAMELA Space Experiment. pages 317–324, 2009.

[90] W. B. Atwood et al. The Large Area Telescope on the Fermi Gamma-ray Space Telescope Mission. *Astrophys. J.*, 697:1071–1102, 2009.

[91] Andrei Kousine. AMS Experiment on the International Space Station. Proceedings, 32nd International Cosmic Ray Conference Gamma-Ray Astronomy (ICRC 2011): Beijing, China, August 11-18. C:1–5, 2011.

[92] Belinda J. Wilkes et al. The SWIRE/Chandra Survey: The X-ray Sources. *Astrophys. J. Suppl.*, 185:433–450, 2009.

[93] Jennifer M. Gaskins. A review of indirect searches for particle dark matter. *Contemp. Phys.*, 57(4):496–525, 2016.

[94] Lyndon Evans and Philip Bryant. LHC Machine. *Journal of Instrumentation*, 3(08):S08001, 2008.

[95] R. Turlay. LEP, CERN'S LARGE ELECTRON POSITRON COLLIDER: THE EXPERIMENTAL PROGRAM. *Europhys. News*, 20:75–79, 1989.

[96] Daniel Bauer et al. Dark Matter in the Coming Decade: Complementary Paths to Discovery and Beyond. *Phys. Dark Univ.*, 7-8:16–23, 2015.

[97] Paul A. Abell et al. LSST Science Book, Version 2.0. 2009.

[98] D. Spergel et al. Wide-Field InfraRed Survey Telescope-Astrophysics Focused Telescope Assets WFIRST-AFTA Final Report. 2013.

[99] Anatoly A. Klypin, Andrey V. Kravtsov, Octavio Valenzuela, and Francisco Prada. Where are the missing Galactic satellites? *Astrophys. J.*, 522:82–92, 1999.

[100] Miguel Rocha, Annika H. G. Peter, James S. Bullock, Manoj Kaplinghat, Shea Garrison-Kimmel, Jose Onorbe, and Leonidas A. Moustakas. Cosmological Simulations with Self-Interacting Dark Matter I: Constant Density Cores and Substructure. *Mon. Not. Roy. Astron. Soc.*, 430:81–104, 2013.

[101] Patrick McDonald et al. The Lyman-alpha forest power spectrum from the Sloan Digital Sky Survey. *Astrophys. J. Suppl.*, 163:80–109, 2006.

[102] Sebastian Arrenberg et al. Working Group Report: Dark Matter Complementarity. 2013.

[103] J. D. Lewin and P. F. Smith. Review of mathematics, numerical factors, and corrections for dark matter experiments based on elastic nuclear recoil. *Astropart. Phys.*, 6:87–112, 1996.

[104] Katherine Freese and Christopher Savage. Dark Matter collisions with the Human Body. *Phys. Lett.*, B717:25–28, 2012.

[105] Jo Bovy and Scott Tremaine. On the local dark matter density. *The Astrophysical Journal*, 756(1):89, 2012.

[106] Konrad Kuijken and Gerard Gilmore. The galactic disk surface mass density and the galactic force k(z) = 1.1-kpc. *Submitted to: Astrophys. J. Lett.*, 1990.

[107] Anne M Green. Astrophysical uncertainties on the local dark matter distribution and direct detection experiments. *J. Phys.*, G44(8):084001, 2017.

[108] J. I. Read. The local dark matter density. *J. Phys.*, G41, 2014.

[109] J. Aalbers. *Dark matter search with XENON1T*. PhD thesis, Universiteit van Amsterdam, 2018.

[110] V. Chepel and H. Araujo. Liquid noble gas detectors for low energy particle physics. *JINST*, 8:R04001, 2013.

[111] Cristina Marcos, Miguel Peiro, and Sandra Robles. On the importance of direct detection combined limits for spin independent and spin dependent dark matter interactions. *JCAP*, 1603(03):019, 2016.

[112] E. Aprile and T. Doke. Liquid Xenon Detectors for Particle Physics and Astrophysics. *Rev. Mod. Phys.*, 82:2053–2097, 2010.

[113] J. B. Albert et al. Search for Neutrinoless Double-Beta Decay with the Upgraded EXO-200 Detector. *Phys. Rev. Lett.*, 120(7):072701, 2018.

[114] A. I. Bolozdynya E. Aprile, A. E. Bolotnikov and T. Doke. Noble Gas Detectors. Wiley-VCH Verlag GmbH and Co. KGaA. 2006.

[115] M. Scharff J. Lindhard, V. Nielsen and P. V. Thomsen. Integral equations governing radiation effects. *33 Mat. Fys. Medd. Dan. Vid. Selsk*, page 1, 1963.

[116] Estimation of fano factors in liquid argon, krypton, xenon and xenon-doped liquid argon. *Nuclear Instruments and Methods*, 134(2):353–357, 1976.

[117] T. Takahashi, S. Konno, T. Hamada, M. Miyajima, S. Kubota, A. Nakamoto, A. Hitachi, E. Shibamura, and T. Doke. Average energy expended per ion pair in liquid xenon. *Phys. Rev. A*, 12:1771–1775, 1975.

[118] S. Kubota, A. Nakamoto, T. Takahashi, T. Hamada, E. Shibamura, M. Miyajima, K. Masuda, and T. Doke. Recombination luminescence in liquid argon and in liquid xenon. *Phys. Rev. B*, 17:2762–2765, 1978.

[119] J. P. Biersack J. F. Ziegler and M. D. Ziegler. SRIM – The Stopping Power and Range of Ions in Matter. *SRIM Co*, page Available at http://www.srim.org, 2008.

[120] O. Hilt, W. F. Schmidt, and A. G. Khrapak. Ionic mobilities in liquid xenon. *IEEE Transactions on Dielectrics and Electrical Insulation*, 1(4):648–656, 1994.

[121] G. Jaffé. Zur Theorie der Ionisation in Kolonnen, Annalen der Physik (Leipzig). page 303–344, 1913.

[122] M. I. Lopes and V. Chepel. Rare gas liquid detectors, in electronic excitations in liquefied rare. *American Scientific Publishers*, pages 331–388, 2005.

[123] J. Lindhard, V. Nielsen, M. Scharff, and P.V. Thomsen. Integral equations governing radiation effects. (notes on atomic collisions, iii). *Kgl. Danske Videnskab., Selskab. Mat. Fys. Medd.*, Vol: 33: No. 10, 1963.

[124] M. Miyajima, T. Takahashi, S. Konno, T. Hamada, S. Kubota, H. Shibamura, and T. Doke. Average energy expended per ion pair in liquid argon. *Phys. Rev. A*, 9:1438–1443, 1974.

[125] Tadayoshi Doke, Akira Hitachi, Jun Kikuchi, Kimiaki Masuda, Hiroyuki Okada, and Eido Shibamura. Absolute Scintillation Yields in Liquid Argon and Xenon for Various Particles. *Jap. J. Appl. Phys.*, 41:1538–1545, 2002.

[126] Brian Lenardo, Kareem Kazkaz, Aaron Manalaysay, Jeremy Mock, Matthew Szydagis, and Mani Tripathi. A Global Analysis of Light and Charge Yields in Liquid Xenon. *IEEE Trans. Nucl. Sci.*, 62(6):3387–3396, 2015.

[127] V. Y. Chepel, M. I. Lopes, R. F. Marques, and A. J. P. L. Policarpo. Primary scintillation yield and alpha, beta ratio in liquid xenon. pages 52–55, 1999.

[128] Scintillation efficiency of nuclear recoil in liquid xenon. *Nuclear Instruments and Methods in Physics Research Section A: Accelerators, Spectrometers, Detectors and Associated Equipment*, 449(1):147–157, 2000.

[129] D. Akimov et al. Measurements of scintillation efficiency and pulse shape for low-energy recoils in liquid xenon. *Phys. Lett.*, B524:245–251, 2002.

[130] E. Aprile, K. L. Giboni, P. Majewski, K. Ni, M. Yamashita, R. Hasty, A. Manzur, and D. N. McKinsey. Scintillation response of liquid xenon to low energy nuclear recoils. *Phys. Rev. D*, 72:072006, 2005.

[131] E. Aprile, L. Baudis, B. Choi, K. L. Giboni, K. Lim, A. Manalaysay, M. E. Monzani, G. Plante, R. Santorelli, and M. Yamashita. New measurement of the relative scintillation efficiency of xenon nuclear recoils below 10 kev. *Phys. Rev. C*, 79:045807, 2009.

[132] G. Plante, E. Aprile, R. Budnik, B. Choi, K.-L. Giboni, L. W. Goetzke, R. F. Lang, K. E. Lim, and A. J. Melgarejo Fernandez. New measurement of the scintillation efficiency of low-energy nuclear recoils in liquid xenon. *Phys. Rev. C*, 84:045805, 2011.

[133] A. Manzur, A. Curioni, L. Kastens, D. N. McKinsey, K. Ni, and T. Wongjirad. Scintillation efficiency and ionization yield of liquid xenon for monoenergetic nuclear recoils down to 4 kev. *Phys. Rev. C*, 81:025808, 2010.

[134] E. Aprile, C. E. Dahl, L. de Viveiros, R. J. Gaitskell, K. L. Giboni, J. Kwong, P. Majewski, K. Ni, T. Shutt, and M. Yamashita. Simultaneous measurement of ionization and scintillation from nuclear recoils in liquid xenon for a dark matter experiment. *Phys. Rev. Lett.*, 97:081302, 2006.

[135] E. et al. Aprile. Response of the xenon100 dark matter detector to nuclear recoils. *Phys. Rev. D*, 88:012006, 2013.

[136] P. Sorensen et al. The scintillation and ionization yield of liquid xenon for nuclear recoils. *Nucl. Instrum. Meth.*, A601:339–346, 2009.

[137] M. Horn et al. Nuclear recoil scintillation and ionisation yields in liquid xenon from ZEPLIN-III data. *Phys. Lett.*, B705:471–476, 2011.

[138] A. Manalaysay et al. Spatially uniform calibration of a liquid xenon detector at low energies using 83m-Kr. *Rev. Sci. Instrum.*, 81:073303, 2010.

[139] Szydagis et al M. Nest: a comprehensive model for scintillation yield in liquid xenon. *Journal of Instrumentation*, 6(10):P10002, 2011.

[140] J. Seguinot, T. Ypsilantis, G. Passardi, and J. Tischhauser. Liquid xenon ionization and scintillation: Studies for a totally active vector electromagnetic calorimeter. *Nucl. Instrum. Meth.*, A323:583–600, 1992.

[141] T. Shutt, Carl E. Dahl, J. Kwong, A. Bolozdynya, and P. Brusov. Performance and Fundamental Processes at Low Energy in a Two-Phase Liquid Xenon Dark Matter Detector. *Nucl. Instrum. Meth.*, A579:451–453, 2007.

[142] A. S. Barabash and A. I. Bolozdynya. How to Detect the Dark Matter of the Galaxy if It Is Made Up of Weakly Interacting Neutral Particles With Masses 1GeV/c^2 - 10GeV/c^2. *JETP Lett.*, 49:356–359, 1989.

[143] E. Aprile et al. Design and performance of the xenon10 dark matter experiment. *Astropart. Phys.*, 34:679–698, 2011.

[144] E. Aprile et al. The xenon100 dark matter experiment. *Astropart. Phys.*, 35:573–590, 2012.

[145] E. Aprile et al. The XENON1T Dark Matter Experiment. *Eur. Phys. J.*, C77(12):881, 2017.

[146] Lutz Althüser. Light collection efficiency simulations of the xenon1t experiment and comparison to data. Master's thesis, University of Münster, 2017.

[147] M. Aglietta et al. Muon Depth intensity relation measured by LVD underground experiment and cosmic ray muon spectrum at sea level. *Phys. Rev.*, D58:092005, 1998.

[148] E. Aprile et al. Material radioassay and selection for the XENON1T dark matter experiment. *Eur. Phys. J.*, C77(12):890, 2017.

[149] E. Aprile et al. Removing krypton from xenon by cryogenic distillation to the ppq level. *Eur. Phys. J.*, C77(5):275, 2017.

[150] Ethan Brown et al. Magnetically-coupled piston pump for high-purity gas applications. *Eur. Phys. J.*, C78(7):604, 2018.

[151] J. Aalbers and C. Tunnell. The Pax Data Processor v6.4.2. Zenodo, Feb. 19 doi: 10.5281/zenodo.546239. url: https://zenodo.org/record/546239.WZWq1CdLfb0. 2017.

[152] E. Aprile et al. Observation and applications of single-electron charge signals in the XENON100 experiment. *J. Phys.*, G41:035201, 2014.

[153] Peter Sorensen. Electron train backgrounds in liquid xenon dark matter search detectors are indeed due to thermalization and trapping. 2017.

[154] Jeremy Mock, Nichole Barry, Kareem Kazkaz, Matthew Szydagis, Mani Tripathi, Sergey Uvarov, Michael Woods, and Nicholas Walsh. Modeling Pulse Characteristics in Xenon with NEST. *JINST*, 9:T04002, 2014.

[155] M. Moongweluwan. The Impact of Photon Flight Path on S1 Pulse Shape Analysis in Liquid Xenon Two-phase Detectors. *JINST*, 11(02):C02036, 2016.

[156] A. Baldini et al. Absorption of scintillation light in a 100 l liquid xenon gamma ray detector and expected detector performance. *Nucl. Instrum. Meth.*, A545:753–764, 2005.

[157] Yichen Li et al. Measurement of Longitudinal Electron Diffusion in Liquid Argon. *Nucl. Instrum. Meth.*, A816:160–170, 2016.

[158] Peter Sorensen. Anisotropic diffusion of electrons in liquid xenon with application to improving the sensitivity of direct dark matter searches. 2011.

[159] J. Angle et al. First Results from the XENON10 Dark Matter Experiment at the Gran Sasso National Laboratory. *Phys. Rev. Lett.*, 100:021303, 2008.

[160] C. M. B. Monteiro, L. M. P. Fernandes, J. A. M. Lopes, L. C. C. Coelho, J. F. C. A. Veloso, J. M. F. dos Santos, K. Giboni, and E. Aprile. Secondary Scintillation Yield in Pure Xenon. *JINST*, 2:P05001, 2007.

[161] Bart Pelssers. Position reconstruction and data quality in xenon. 2015.

[162] J. Alme et al. The ALICE TPC, a large 3-dimensional tracking device with fast readout for ultra-high multiplicity events. *Nucl. Instrum. and Meth. A*, 622:316–367, 2010.

[163] Performance of the delphi detector. *Nuclear Instruments and Methods in Physics Research Section A: Accelerators, Spectrometers, Detectors and Associated Equipment*, 378(1):57–100, 1996.

[164] A. De Min et al. Performance of the HPC calorimeter in DELPHI. *IEEE Trans. Nucl. Sci.*, 42:491–498, 1995.

[165] D. Buskulic et al. Performance of the ALEPH detector at LEP. *Nucl. Instrum. Meth.*, A360:481–506, 1995.

[166] Johannes Stiller. Gain calibration of the alice trd using the decay of 83mkr by internalconversion1. *Nuclear Instruments and Methods in Physics Research Section A: Accelerators, Spectrometers, Detectors and Associated Equipment*, 706:20–22, 2013.

[167] V. Eckardt et al. Calibration of the STAR forward time projection chamber with krypton-83m. 2001.

[168] A. I. et al Belesev. Investigation of space-charge effects in gaseous tritium as a source of distortions of the beta spectrum observed in the troitsk neutrino-mass experiment. *Physics of Atomic Nuclei*, 71(3):427–436, 2008.

[169] J. Angrik et al. KATRIN design report 2004. KATRIN. 2005.

[170] L. W. Kastens, S. B. Cahn, A. Manzur, and D. N. McKinsey. Calibration of a Liquid Xenon Detector with Kr-83m. *Phys. Rev.*, C80, 2009.

[171] E.A. McCutchan. Nuclear data sheets for a = 83. *Nuclear Data Sheets*, 125:201–394, 2015.

[172] D. S. Akerib et al. ^{83m}Kr calibration of the 2013 LUX dark matter search. *Phys. Rev.*, D96(11):112009, 2017.

[173] E. Aprile et al. XENON1T data Analysis: Signal Reconstruction, Calibration and Event Selection. In preparation. 2019.

[174] V. Hannen et al. Limits on the release of Rb isotopes from a zeolite based 83mKr calibration source for the XENON project. *JINST*, 6, 2011.

[175] D. Venos et al. ^{83m}Kr radioactive source based on ^{83}Rb trapped in cation-exchange paper or in zeolite. *Appl. Radiat. Isot*, 63:323–327, 2005.

[176] KGaA Germany Merck. Zeolite molecular sieve, CAS no 1318-02-1. 2000.

[177] XENON1T. Waveform simulator (fax) for xenon experiment. https://xe1t-wiki.lngs.infn.it/doku.php?id=xenon:xenon1t:analysis:firstresults:waveform_simulator. 2017.

[178] Dan Alexander Ted Berger. 83mkr event selection and physics for xenon1t flushing mode. https://xe1t-wiki.lngs.infn.it/lib/exe/fetch.php?media=xenon:xenon1t:berget2:xe1t_kr83m_eventselect.html. 2016.

[179] Daniel Mayani. Ion identification through afterpulsing. https://xe1t-wiki.lngs.infn.it/doku.php?id=xenon:xenon1t:dsg:sensors:r11410:ion_id_afterpulses. 2016.

[180] E. et al Aprile. Physics reach of the XENON1T dark matter experiment. *JCAP*, 1604(04):027, 2016.

[181] Pietro Di Gangi Ted Berger. Summery note on s1 lce correction for xenon1t. https://xe1t-wiki.lngs.infn.it/doku.php?id=xenon:xenon1t:berget2:s1_lce_summary. 2017.

[182] D. Foreman-Mackey, D.W. Hogg, D. Lang, and J. Goodman. emcee: The MCMC Hammer. 125:306, March 2013.

[183] Zach Greene. Electron lifetime modeling. https://xe1t-wiki.lngs.infn.it/doku.php?id=greene:electron_lifetime_attempts. 2018.

[184] Christopher Geis. Detector leveling using s2 width and s2 width vs. liquid level. https://xe1t-wiki.lngs.infn.it/doku.php?id=xenon:xenon1t:analysis:chg:s2width_leveling&s[]=warping&s[]=anode. 2016.

[185] E. Aprile et al. Dark Matter Results from 225 Live Days of XENON100 Data. *Phys. Rev. Lett.*, 109:181301, 2012.

[186] Adam Brown. S2 xy correction summary. https://xe1t-wiki.lngs.infn.it/doku.php?id=xenon1t:analysis:firstresults:s2-xy-correction-summary. 2017.

[187] Jingqiang Ye. *In preparation.* PhD thesis, University of California. UC San Diego., 2021.

[188] Jialing Fei and Christian Wittweg. Overview page for g1 and g2 in sr1. https://xe1t-wiki.lngs.infn.it/doku.php?id=xenon:xenon1t:analysis:sciencerun1:g1_g2_overview. 2018.

[189] D. S. Akerib et al. 3D Modeling of Electric Fields in the LUX Detector. *JINST*, 12(11):P11022, 2017.

[190] E. Aprile and others. First dark matter search results from the xenon1t experiment. *Phys. Rev. Lett.*, 119:181301, 2017.

[191] Steffen Nissen and others. Fast artificial neural network library. consulted in:http://leenissen.dk/fann/wp/. 2003.

[192] S. Agostinelli and others. Geant4-a simulation toolkit. *Nuclear Instruments and Methods in Physics Research Section A: Accelerators, Spectrometers, Detectors and Associated Equipment*, 506(3):250–303, 2003.

[193] M Szydagis et al. Noble Element Simulation Technique v2.0. doi:10.5281/zenodo.1314669. Jul 2014.

[194] D. S. Akerib and others. Results from a search for dark matter in the complete lux exposure. *Phys. Rev. Lett.*, 118:021303, 2017.

[195] R.D. Andresen, E.-A. Leimann, and A. Peacock. The nature of the light produced inside a gas scintillation proportional counter. *Nuclear Instruments and Methods*, 140(2):371–374, 1977.

[196] I. Kanik. Far ultraviolet emission spectrum of xenon induced by electron impact at 100 ev. *Chemical Physics Letters*, 258(3):455–459, 1996.

[197] Kazuhiko Seki, Hiroshi Tanaka, Toshiaki Ohta, Yuriko Aoki, Akira Imamura, Hitoshi Fujimoto, Hiromichi Yamamoto, and Hiroo Inokuchi. Electronic structure of poly(tetrafluoroethylene) studied by ups, vuv absorption, and band calculations. *Physica Scripta*, 41(1):167, 1990.

[198] Munsoo Yun, Katsumi Yoshino, Yoshio Inuishi, and Motoo Kawatsu. Photoconduction in polytetrafluoroethylene induced by vacuum-ultraviolet light. *Japanese Journal of Applied Physics*, 21(11R):1592, 1982.

[199] Guan-Jun Zhang, Kai Yang, Wen-Bin Zhao, and Zhang Yan. On the surface trapping parameters of polytetrafluoroethylene block. *Applied Surface Science*, 253(4):1995–1998, 2006.

[200] McCarty and Whitesides. Electrostatic Charging Due to Separation of Ions at Interfaces: Contact Electrification of Ionic Electrets. 47(12):2188–2207, 2008.

[201] R. Kressmann, G. M. Sessler, and P. Gunther. Space-charge electrets. *IEEE Transactions on Dielectrics and Electrical Insulation*, 3(5):607–623, 1996.

[202] G. Ascarelli. Electric field dependence of the capture rate constant of electrons by sf6 and o2 dissolved in either liquid ar or xe. *The Journal of Chemical Physics*, 74(5):3085–3086, 1981.

[203] Comsol Multiphysics. COMSOL AB, Stockholm, Sweden. http://www.comsol.com. , 2001-.

[204] Junji Naganoma. Field distortion correction for sr1. *https://xe1t-wiki.lngs.infn.it/doku.php?id=xenon:xenon1t:junji:comsol:dir5:fine_tune_science1*, 2017.

[205] Eric Jones, Travis Oliphant, Pearu Peterson, et al. SciPy: Open source scientific tools for Python. http://www.scipy.org/, 2001-.

[206] Michael Wigard. Modeling electric fields inside the xenon1t tpc and comparison to data. Master's thesis, University of Münster, 2018.

[207] Yuan Mei. *Direct Dark Matter Search with the XENON100 Experiment*. PhD thesis, Rice University, 2011.

[208] Kathrin Valerius. *Spectrometer-related background processes and their suppression in the KATRIN experiment.* PhD thesis, University of Münster, 2009.

[209] Ferenc Gluck, Guido Drexlin, Benjamin Leiber, Susanne Mertens, Alexander Osipowicz, Jan Reich, and Nancy Wandkowsky. Electromagnetic design of the large-volumes air coil system of the KATRIN experiment. *New J. Phys.*, 15:083025, 2013.

[210] Julien W. Xenon1t 3d field simulation. *https://xe1t-wiki.lngs.infn.it/doku.php?id=xenon:xenon1t:julien:xenon1t_3d_field_simulation*, 2018.

[211] Knoche Richard. *Signal corrections and calibrations in the LUX Dark Matter detector*. PhD thesis, University of Maryland, 2016.

[212] E. Aprile et al. Analysis of XENON1T data for dark matter search: Signal & Background Models and Statistical Inference. 2019.

[213] D. S. Akerib et al. Low-energy (0.7-74 keV) nuclear recoil calibration of the LUX dark matter experiment using D-D neutron scattering kinematics. 2016.

[214] D. S. at all Akerib. Signal yields, energy resolution, and recombination fluctuations in liquid xenon. *Phys. Rev. D*, 95:012008, 2017.

[215] S. Behnel, R. Bradshaw, C. Citro, L. Dalcin, D.S. Seljebotn, and K. Smith. Cython: The best of both worlds. *Computing in Science Engineering*, 13(2):31–39, 2011.

[216] Sebastian Lindemann. Ptfe reflectors: Notches and holes for charge collection. *https://xe1t-wiki.lngs.infn.it/doku.php?id=xenon:xenonnt:dsg:tpc:notch_and_holes_for_charge_collection*, 2018.

[217] E. Aprile et al. Intrinsic backgrounds from Rn and Kr in the XENON100 experiment. *Eur. Phys. J.*, C78(2):132, 2018.

[218] Sebastian Lindemann. *Intrinsic Kr-85 and Rn-222 Backgrounds in the XENON Dark Matter Search*. PhD thesis, University of Heidelberg, 2013.

[219] Glen Cowan. *Statistical Data Analysis*. Clarendon (Oxford), Oxford, 1998.

[220] Sebastian Lindemann and Hardy Simgen. Krypton assay in xenon at the ppq level using a gas chromatographic system and mass spectrometer. *Eur. Phys. J.*, C74:2746, 2014.

[221] Xiangyi Cui et al. Dark Matter Results From 54-Ton-Day Exposure of PandaX-II Experiment. *Phys. Rev. Lett.*, 119(18):181302, 2017.

[222] M et al Be. Table of radionuclides. 8, 2016.

[223] Natascha Rupp. *In preparation.* PhD thesis, MPIK Heidelberg, 2019.

[224] E. Aprile et al. Online^{222} Rn removal by cryogenic distillation in the XENON100 experiment. *Eur. Phys. J.*, C77, 2017.

[225] P. et al Amaudruz. First results from the deap-3600 dark matter search with argon at snolab. *Phys. Rev. Lett.*, 121:071801, Aug 2018.

[226] R. et al Agnese. Improved wimp-search reach of the cdms ii germanium data. *Phys. Rev. D*, 92:072003, Oct 2015.

[227] M Wojcik and G Zuzel. 226ra, 210pb, 210bi and 210po deposition and removal from surfaces and liquids. *Journal of Radioanalytical and Nuclear Chemistry*, 296, 2012.

[228] Michael Murra. *Intrinsic background reduction by cryogenic distillation for the XENON1T dark matter experiment*. PhD thesis, University of Münster, 2018.

[229] Eric S. Morrison, Therese Frels, Eric H. Miller, Richard W. Schnee, and Joseph Street. Radon Daughter Plate-out onto Teflon. *AIP Conf. Proc.*, 1921(1):090002, 2018.

[230] A. J. Anderson. Phonon-Based Position Determination in SuperCDMS iZIP Detectors. *J. Low Temp. Phys.*, 176, 2014.

[231] Sander Breur. *Backgrounds in XENON1T*. PhD thesis, University of Amsterdam, 2019.

[232] M. Reginatto. Overview of spectral unfolding techniques and uncertainty estimation. *Radiation Measurements*, 45(10):1323–1329, 2010.

[233] Lee Chang. *Mitigation of Backgrounds for the Large Underground Xenon Dark Matter Experiment*. PhD thesis, Case Western Reserve University, 2015.

[234] R. F. Lang, J. Pienaar, E. Hogenbirk, D. Masson, R. Nolte, A. Zimbal, S. Rottger, M. L. Benabderrahmane, and G. Bruno. Characterization of a deuterium-deuterium plasma fusion neutron generator. *Nucl. Instrum. Meth.*, A879:31–38, 2018.

[235] Gary J. Feldman and Robert D. Cousins. A Unified approach to the classical statistical analysis of small signals. *Phys. Rev.*, D57, 1998.

[236] Nadav Priel, Ludwig Rauch, Hagar Landsman, Alessandro Manfredini, and Ranny Budnik. A model independent safeguard against background mismodeling for statistical inference. *JCAP*, 1705(05):013, 2017.

[237] S.P. Ahlen, F.T. Avignone, R.L. Brodzinski, A.K. Drukier, G. Gelmini, and D.N. Spergel. Limits on cold dark matter candidates from an ultralow background germanium spectrometer. *Physics Letters B*, 195(4):603–608, 1987.

[238] David N. Spergel. Motion of the earth and the detection of weakly interacting massive particles. *Phys. Rev. D*, 37:1353–1355, 1988.

[239] Matthew J. Lewis and Katherine Freese. The Phase of the annual modulation: Constraining the WIMP mass. *Phys. Rev.*, D70:043501, 2004.

[240] R. Bernabei et al. The DAMA/LIBRA apparatus. *Nucl. Instrum. Meth.*, A592:297–315, 2008.

[241] C. E. Aalseth et al. CoGeNT: A Search for Low-Mass Dark Matter using p-type Point Contact Germanium Detectors. *Phys. Rev.*, D88, 2013.

[242] R. Bernabei et al. Dark matter search. *Riv. Nuovo Cim.*, 26N1:1–73, 2003.

[243] R. Bernabei et al. Final model independent result of DAMA/LIBRA-phase1. *Eur. Phys. J.*, C73:2648, 2013.

[244] L. Hehn et al. Improved EDELWEISS-III sensitivity for low-mass WIMPs using a profile likelihood approach. *Eur. Phys. J.*, C76(10):548, 2016.

[245] R. Agnese et al. Low-mass dark matter search with CDMSlite. *Phys. Rev.*, D97(2):022002, 2018.

[246] J. Angle et al. A search for light dark matter in XENON10 data. *Phys. Rev. Lett.*, 107:051301, 2011.

[247] J Amare et al. The ANAIS-112 experiment at the Canfranc Underground Laboratory. 2017.

[248] Emily Shields, Jingke Xu, and Frank Calaprice. Sabre: A new nai(tl) dark matter direct detection experiment. *Physics Procedia*, 61:169–178, 2015.

[249] G. Adhikari et al. Initial Performance of the COSINE-100 Experiment. *Eur. Phys. J.*, C78(2):107, 2018.

[250] G at al. Adhikari. An experiment to search for dark-matter interactions using sodium iodide detectors. *Nature*, 564:83–86, 12 2018.

[251] Jonathan H. Davis. Fitting the annual modulation in DAMA with neutrons from muons and neutrinos. *Phys. Rev. Lett.*, 113:081302, 2014.

[252] Davide D'Angelo. Seasonal modulation in the Borexino cosmic muon signal. 4:26–29, 2011.

[253] Enrique Fernandez-Martinez and Rakhi Mahbubani. The Gran Sasso muon puzzle. *JCAP*, 1207:029, 2012.

[254] G. Bellini et al. Final results of Borexino Phase-I on low energy solar neutrino spectroscopy. *Phys. Rev.*, D89(11), 2014.

[255] J. P. et al Cravens. Solar neutrino measurements in super-kamiokande-ii. *Phys. Rev. D*, 78, Aug 2008.

[256] Daniel Ferenc, Dan Ferenc Segedin, Ivan Ferenc Segedin, and Marija Segedin Ferenc. Helium migration through photomultiplier tubes - the probable cause of the dama seasonal variation effect. 2019.

[257] E. Aprile et al. Search for Electronic Recoil Event Rate Modulation with 4 Years of XENON100 Data. *Phys. Rev. Lett.*, 118(10), 2017.

[258] D. S. Akerib et al. Search for annual and diurnal rate modulations in the LUX experiment. *Phys. Rev.*, D98(6):062005, 2018.

[259] K. Abe et al. Direct dark matter search by annual modulation with 2.7 years of XMASS-I data. *Phys. Rev.*, D97(10), 2018.

[260] Yun Zhang. Summary on xenon1t sr1 data selection based on detector parameters stability. https://xe1t-wiki.lngs.infn.it/doku.php?id=xenon:xenon1t:analysis:sciencerun1:sc_summary. 2017.

[261] Luke Walker Goetzke. *Low-Energy Electronic Recoils in Liquid Xenon: Search for Annual Modulation with XENON100, Measurement of Charge and Light Yield with neriX, and Measurement of Krypton in Xenon with ATTA*. PhD thesis, University of Columbia, 2015.

[262] Steve Baker and Robert D. Cousins. Clarification of the use of chi-square and likelihood functions in fits to histograms. *Nuclear Instruments and Methods in Physics Research*, 221(2):437–442, 1984.

[263] Haipeng An, Maxim Pospelov, Josef Pradler, and Adam Ritz. Directly Detecting MeV-scale Dark Matter via Solar Reflection. *Phys. Rev. Lett.*, 120(14), 2018.

[264] Rouven Essig, Jeremy Mardon, and Tomer Volansky. Direct Detection of Sub-GeV Dark Matter. *Phys. Rev.*, D85:076007, 2012.

[265] B. M. Roberts, V. A. Dzuba, V. V. Flambaum, M. Pospelov, and Y. V. Stadnik. Dark matter scattering on electrons: Accurate calculations of atomic excitations and implications for the DAMA signal. *Phys. Rev.*, D93(11), 2016.

[266] David E. Kaplan, Markus A. Luty, and Kathryn M. Zurek. Asymmetric Dark Matter. *Phys. Rev.*, D79:115016, 2009.

[267] Maxim Pospelov, Adam Ritz, and Mikhail B. Voloshin. Bosonic super-WIMPs as keV-scale dark matter. *Phys. Rev.*, D78:115012, 2008.

[268] Jonathan L. Feng and Jason Kumar. The WIMPless Miracle: Dark-Matter Particles without Weak-Scale Masses or Weak Interactions. *Phys. Rev. Lett.*, 101:231301, 2008.

[269] Rouven Essig, Jeremy Mardon, Oren Slone, and Tomer Volansky. Detection of sub-GeV Dark Matter and Solar Neutrinos via Chemical-Bond Breaking. *Phys. Rev.*, D95(5):056011, 2017.

[270] Liu Jianglai. *A Search of Spin-Independent WIMP-NucleonInteractions using the PandaX-I and PandaX-II*. PhD thesis, Shanghai Jiao Tong University, 2017.

[271] E. Aprile et al. Low-mass dark matter search using ionization signals in XENON100. *Phys. Rev.*, D94, 2016.

[272] Rouven Essig, Marivi Fernandez Serra, Jeremy Mardon, Adrian Soto, Tomer Volansky, and Tien-Tien Yu. Direct Detection of sub-GeV Dark Matter with Semiconductor Targets. *JHEP*, 05:046, 2016.

[273] Stephen Derenzo, Rouven Essig, Andrea Massari, Adrían Soto, and Tien-Tien Yu. Direct Detection of sub-GeV Dark Matter with Scintillating Targets. *Phys. Rev.*, D96(1):016026, 2017.

[274] Jason Wyenberg and Ian M. Shoemaker. Mapping the neutrino floor for direct detection experiments based on dark matter-electron scattering. *Phys. Rev.*, D97(11), 2018.

[275] C. F. Bunge, J. A. Barrientos, and A. V. Bunge. Roothaan-Hartree-Fock Ground-State Atomic Wave Functions: Slater-Type Orbital Expansions and Expectation Values for Z = 2-54. *Atom. Data Nucl. Data Tabl.*, 53:113–162, 1993.

[276] Joachim Kopp, Viviana Niro, Thomas Schwetz, and Jure Zupan. DAMA/LIBRA and leptonically interacting Dark Matter. *Phys. Rev.*, D80:083502, 2009.

[277] Rouven Essig, Aaron Manalaysay, Jeremy Mardon, Peter Sorensen, and Tomer Volansky. First Direct Detection Limits on sub-GeV Dark Matter from XENON10. *Phys. Rev. Lett.*, 109, 2012.

[278] E. Aprile et al. Exclusion of Leptophilic Dark Matter Models using XENON100 Electronic Recoil Data. *Science*, 349, 2015.

[279] E. Aprile et al. Light dark matter search with ionization signals in xenon1t. in preparation. 2019.

[280] E. Aprile et al. First Axion Results from the XENON100 Experiment. *Phys. Rev.*, D90, 2014.

[281] F. Beaujean, A. Caldwell, D. Kollar, K. Kroninger, and S. Pashapour. Signal discovery in sparse spectra: a Bayesian analysis. Proceedings, PHYSTAT 2011 Workshop on Statistical Issues Related to Discovery Claims in Search Experiments and Unfolding. 2011.

[282] Evan Shockley. Detection efficiency for lower analysis. *https://xe1t-wiki.lngs.infn.it/doku.php?id=xenon:shockley:lower:detection_efficiency_update*, 2018.

[283] P. Agnes et al. Constraints on Sub-GeV Dark-Matter-Electron Scattering from the DarkSide-50 Experiment. *Phys. Rev. Lett.*, 121, 2018.

[284] Rouven Essig, Tomer Volansky, and Tien-Tien Yu. New Constraints and Prospects for sub-GeV Dark Matter Scattering off Electrons in Xenon. *Phys. Rev.*, D96(4), 2017.

[285] A. A. Aguilar-Arevalo et al. Dark Matter Search in a Proton Beam Dump with MiniBooNE. *Phys. Rev. Lett.*, 118, 2017.

[286] J. P. Lees et al. Search for Invisible Decays of a Dark Photon Produced in e^+e^- Collisions at BaBar. *Phys. Rev. Lett.*, 119, 2017.

[287] Yasaman Farzan. Minimal model linking two great mysteries: Neutrino mass and dark matter. *Phys. Rev. D*, 80:073009, 2009.

[288] Ernest Ma. Verifiable radiative seesaw mechanism of neutrino mass and dark matter. *Phys. Rev.*, D73, 2006.

[289] Abdesslam Arhrib, Celine Bahm, Ernest Ma, and Tzu-Chiang Yuan. Radiative Model of Neutrino Mass with Neutrino Interacting MeV Dark Matter. *JCAP*, 1604, 2016.

[290] J. A. Casas and A. Ibarra. Oscillating neutrinos and muon —> e, gamma. *Nucl. Phys.*, B618, 2001.

[291] Sybrand Zeinstra. *In preparation.* PhD thesis, University of Muenster, 2022.